Applied Electromagnetic Methods for Geothermal Exploration in northern México: 3D forward and inverse modeling of Magnetotelluric data

Inaugural-Dissertation

zur Erlangung des Doktorgrades
der Mathematisch-Naturwissenschaftlichen Fakultät
der Universität zu Köln

vorgelegt von

Diego Ruiz Aguilar

aus Chiapas (México)

Köln 2018

Gutachter:

Prof. Dr. B. Tezkan
Prof. Dr. A. Junge

Tag der mündlichen Prüfung: 20.04.2018

Abstract

The main focus of this thesis is the application of electromagnetic (EM) methods for the exploration of geothermal resources in San Felipe's area, which it is located in northern México. A regional geophysical field survey was carried out in 2014 where Magnetotellurics (MT) and Transient Electromagnetics (TEM) methods were applied. Conventional 1D inversion techniques are firstly performed to the TEM data. Afterwards, a Spatially Constrained Inversion (SCI) scheme is applied to the TEM data and thus, a pseudo-3D resistivity model of the shallow part of San Felipe's subsurface is achieved. The SCI results are correlated to the hydrogeological information and a description of the shallow aquifer of San Felipe is given.

The acquired magnetotelluric data are processed with robust statistics techniques. A dimensionality analysis of San Felipe MT data suggests a 1D and 3D subsurface structure. The effect of the static shift in MT data is corrected based on the TEM information. Prior to the inversion of the MT data, 3D MT modeling studies are carried out to investigate the detectability of geothermal anomalies and the influence of the field survey configuration applied in San Felipe. Due to the proximity of the survey area to the gulf of California, a possible coast effect in the MT data is also investigated. Later on, one-dimensional inversions of MT data are carried out and the uncertainty of the inverse models is evaluated. To perform a 3D inversion of San Felipe MT data, trials are firstly performed by systematically varying the input parameters and their impact on the inversion models is appraised. Thus, the inversion input parameters suitable for San Felipe data set are applied and a 3D inversion model is derived. Although the dimensionality analysis only suggests a 1D and 3D subsurface structure, two-dimensional inversions are applied to the MT data in order to compare the results with the 1D and 3D inversion models.

The derived TEM information is incorporated into the 3D MT inversion scheme to stabilize the inversion process. On the one hand, a 3D MT constrained inversion model is achieved using the information of TEM inversion models as constraints. On the other hand, the features from the pseudo-3D resistivity model generated with the SCI of TEM data is incorporated as *a priori* information into the 3D inversion scheme of MT data. The second approach shows better results and therefore its output is taken as the preferred inversion model. A conductive structure is imaged in the central part of the survey area which is interpreted as a sedimentary basin at its shallow part and as a fault zone with geothermal fluids at depths greater than 1.5 km.

Zusammenfassung

Die vorliegende Arbeit befasst sich mit der geothermischen Untersuchung der Gegend um San Felipe im nördlichen Mexiko mittels elektromagnetischer Verfahren. Während einer Feldkampagne in 2014 kamen hierbei magnetotellurische (MT) und transient-elektromagnetische (TEM) Verfahren zum Einsatz. In einem ersten Schritt wurden konventionelle 1D Inversionsverfahren auf die TEM Felddaten angewendet. Anschliessend wurden die TEM Daten mittels einer sogenannten Spatially Constrained Inversion (SCI) untersucht und hieraus ein Pseudo-3D-Modell des oberflächennahen Untergrundes abgeleitet. Die SCI Ergebnisse wurden mit hydrogeologischen Informationen abgeglichen und es folgt eine Beschreibung des oberflächennahen Aquifers bei San Felipe.

Die gemessenen MT Daten wurden mit der *robust statistics* Methode prozessiert. Eine Dimensionalitätsanalyse dieser Daten deutet auf eine 1D and 3D Untergrundstruktur hin und der Static Shift Effekt wurde mithilfe der TEM Daten korrigiert. Der Inversion der MT Daten gingen 3D Modellstudien voraus um die Detektierbarkeit von geothermischen Anomalien und der Einfluss der in San Felipe gewählten Messkonfiguration zu untersuchen. Des Weiteren wurde ein möglicher Einfluss des nahegelegenen Golf von Kalifornien auf die MT Daten modelliert. Die MT Daten wurden anschliessend mit 1D Verfahren invertiert und die erhaltenen Ergebnismodelle bzgl. ihrer Fehler und Genauigkeit diskutiert. Im Zuge einer 3D Inversion dieser Daten wurden die zugehörigen Inversionparameter systematisch variiert und deren Einfluss auf die Ergebnismodelle studiert. Darauf aufbauend wurden mithilfe passender Inversionsparameter eine 3D Inversion durchgeführt und somit ein 3D Untergrundmodell abgeleitet. Obwohl die o.g. Dimensionalitätsanalyse lediglich auf eine 1D und 3D Untergrundstruktur hindeutete wurden ebenfalls 2D Inversionen durchgeführt mit dem Ziel, deren Resultate mit denen der 1D und 3D Inversionen zu vergleichen.

Die TEM Inversionsmodelle wurden zur Verbesserung der Ergebnisse in den 3D MT Inversionsprozess miteinbezogen. Zum einen dienten die TEM Modelle als Zwangsbedingung für eine sogenannte 3D MT constrained Inversion. Zum anderen flossen das Pseudo-3D-Modell der SCI als a priori Information in die 3D Inversion der MT Daten mit ein. Hierbei verspricht die letztgenannte Herangehensweise bessere Ergebnisse, daher wird deren Resultat als das bevorzugte Inversionsmodell betrachtet. In den zentralen Lagen des Untersuchungsgebietes bildet sich eine leitfähige Struktur ab, die sich oberflächennah als Sedimentationsbecken und in größeren Tiefen > 1.5 km als geologische Verwerfung mit geothermischem Bezug interpretieren lässt.

Contents

Chapter No. 1

Introduction

Geothermal energy is a recurrent alternative around the world to produce and supply electricity. The following definition of geothermal energy is adopted in this thesis: that part of the Earth's heat that can, or could be, recovered and exploited by man (Dickson and Fanelli, 2004). The total installed capacity from worldwide geothermal power plant up to 2015 is of 12,635 MW (Bertani, 2015), representing thus an increment of 1700 MW since the last report in 2010 (Bertani, 2010). In Mexico, the installed geothermal-electric capacity was of 958 MW in 2010 (Gutiérrez-Negrín et al., 2010) and 1017 MW in 2015 (Bertani, 2015). Large exploration campaigns have been carried out to find new geothermal resources in the country during the last years (Flores-Armenta et al., 2014). Besides these campaigns, recent studies have focused on evaluating the potential of known and new geothermal areas at Baja California peninsula (Fig. 1.1), in the north of Mexico (Arango-Galván et al., 2015). The high geothermal potential of Baja California is well known. In fact, two geothermal fields located on the Peninsula (Cerro Prieto and Las Tres Vírgenes; Fig. 1.1) are generating up to 730 MW (Quijano and Gutiérrez-Negrín, 2005; Gutiérrez-Negrín et al., 2015). One of the new proposed geothermal areas of Baja California is San Felipe, located in the northeastern part of the Peninsula. San Felipe's area shows evidences of hydrothermal alteration, recent volcanism, and surface manifestations. There are hot springs along the coast from the town of San Felipe to the south and water wells with high temperature in the San Felipe valley. In addition, important NE-SW and NW-SE strike-slip faults exist in the San Felipe area (Arango-Galván et al., 2015). The chemical composition of water acquired from surface manifestations indicates temperatures that vary from 124 to 254°C which are adequate to consider San Felipe as a geothermal prospect (Arango-Galván et al., 2015). Based on all this information, a regional geophysical survey was carried out in San Felipe's area in order to describe the geothermal system with the help of applied electromagnetic (EM) methods, specifically Magnetotellurics (MT) and Transient Electromagnetic (TEM) techniques.

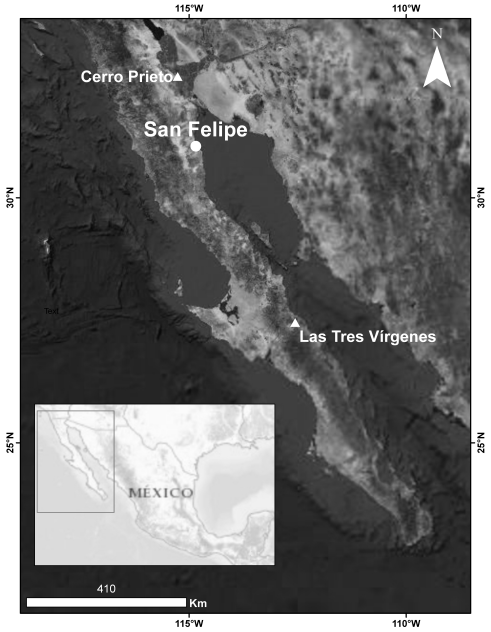

FIGURE 1.1: *Location of San Felipe in the Baja California peninsula. Cerro Prieto and Las Tres Vírgenes geothermal fields are also marked. Figure taken from Ruiz-Aguilar et al. (2018).*

Applied electromagnetic methods have been mainly utilized for mining and hydrocarbon exploration. During the last decades, however, they have also been applied for environmental investigations due to their improved spatial resolution and low costs (Tezkan, 1999). In the geothermal industry, applied EM methods have been widely used for imaging hydrothermal systems. A review of case studies where EM methods have been utilized for imaging geothermal systems can be found in Muñoz (2014). Williams et al. (2011) defines geothermal system as: any localized geological setting where portions of the Earth's thermal energy may be extracted from natural or artificially induced circulating fluids transported to a point of use. Geothermal systems are normally located in regions composed of faults and fractures filled with thermal fluids and hydrothermal alteration products that show low resistivity signature, therefore they are attractive targets for applied EM methods (Muñoz, 2014). Pellerin et al. (1996) showed with numerical models how magnetotellurics (MT), controlled-source audio magnetotellurics (CSAMT), long-offset time-domain (LOTEM) and transient electromagnetic (TEM) can effectively delineate the conductive clay cap generally presented in geothermal systems. Due to its cost-effectiveness, MT has become the most applied technique for geothermal exploration. In addition, acquisition of TEM soundings is often requested by geothermal companies to correct the possible static shift effect on MT data (Cumming and Mackie, 2010; Pellerin and Hohmann, 1990).

1.1 Guideline of the Thesis

This thesis is organized through the following structure. The theoretical aspects of the applied electromagnetic (EM) methods are given in Chapter 2. The inversion theory of geophysical data is described in Chapter 3, focusing in the inversion algorithms used in this thesis. In Chapter 4, the field survey is introduced and the main geological aspects of San Felipe's area are described. All the procedures applied to the acquired data before the subsequent inversion are explained in Chapter 5. A theoretical overview of the algorithm used to process MT data is also given in this chapter. Three-dimensional MT modeling investigations are carried out in Chapter 6, where an overview of 3D MT forward modeling is firstly given. In Chapter 7, one-dimensional inversion of TEM data is described and a geological interpretation of the shallow part of San Felipe's subsurface is presented. The 1D and 2D inversion of MT data are also described in this chapter. In Chapter 8, the 3D inversion scheme applied to the magnetotelluric data acquired in San Felipe is explained, but a theoretical overview of the used inversion algorithm is firstly given. Furthermore, it is described how the acquired TEM data is incorporated into the 3D inversion scheme of MT data and the preferred 3D inversion model is correlated to the geological information. Finally a conclusion and outlook of the presented work is given in Chapter 9.

Chapter No. 2

Theory of applied EM methods

The theoretical aspects of applied Electromagnetic (EM) methods are presented in the following chapter, emphasizing the basics of the techniques that are utilized in this thesis: Magnetotellurics (MT) and Transient Electromagnetics (TEM). Applied EM methods are based on the Maxwell equations to describe the propagation and diffusion of electromagnetic waves. Therefore, the derivation of the diffusion equation is firstly explained. Subsequently, an introduction to the Magnetotelluric method is given and its transfer functions and main features are described. Finally, the main aspects of the Transient Electromagnetic technique are explained.

Vectors are presented in lower case, bold, italic characters. An exception are the vector fields $\boldsymbol{E}$, $\boldsymbol{B}$, $\boldsymbol{H}$, $\boldsymbol{D}$, which are displayed similar to matrices in upper case, bold, italic characters.

2.1 Maxwell's equations

All the electromagnetic phenomena are based on the Maxwell's equations which describe the relation between the time varying electric and magnetic fields. They are the fundamental equations in electromagnetism (Ward and Hohmann, 1988) and are expressed in differential form as follows:

$$\nabla \times \boldsymbol{E} = -\frac{\partial \boldsymbol{B}}{\partial t} \tag{2.1}$$

$$\nabla \times \boldsymbol{H} = \frac{\partial \boldsymbol{D}}{\partial t} + \boldsymbol{j} \tag{2.2}$$

$$\nabla \cdot \boldsymbol{B} = 0 \tag{2.3}$$

$$\nabla \cdot \boldsymbol{D} = q \tag{2.4}$$

Where $\boldsymbol{E}$ is the electric field in V/m, $\boldsymbol{B}$ is the magnetic flux density in Vs/m^2 , $\boldsymbol{H}$ is the magnetic field in A/m, $\boldsymbol{D}$ is the electric displacement field in As/m^2, $\boldsymbol{j}$ is the current density in A/m^2 and q is the electric charge density in As/m^3. All the above mentioned fields are functions of position $\boldsymbol{r} = (x, y, z)$ in meters (m) and of time t in seconds (s).

Equation 2.1 represents Faraday's law which indicates that the induced electric field is equal to the time rate of change of the magnetic flux. Ampere's law is represented in eq. 2.2 and it relates the magnetic field with the electric current density and the electric displacement field. Equation 2.3 is representing Gauss's law for magnetism and states that magnetic monopoles do not exist. Gauss's law for electricity is expressed in eq. 2.4 and shows that the electric field is the result of the distribution of electric charges. Equation 2.1 through 2.4 are coupled with the earth physical properties trough the following constitutive relations and Ohm's law:

$$\boldsymbol{B} = \mu \boldsymbol{H} \tag{2.5}$$

$$\boldsymbol{D} = \varepsilon \boldsymbol{E} \tag{2.6}$$

$$\boldsymbol{j} = \sigma \boldsymbol{E} \tag{2.7}$$

Thus, magnetic flux density $\boldsymbol{B}$ is connected to the magnetic field $\boldsymbol{H}$ by the magnetic permeability μ (eq. 2.5). Whereas the electric displacement field $\boldsymbol{D}$ is connected to the electric field $\boldsymbol{E}$ through the electric permittivity ε (eq. 2.6). Equation 2.7 represents Ohm's law and it connects the current density $\boldsymbol{j}$ with the electric field $\boldsymbol{E}$ via the conductivity σ (in S/m). For an isotropic media, σ, μ and ε are reduced to scalar quantities. In addition, the magnetic permeability μ equals the vacuum permeability μ_0 for most of the subsurface materials. The free space constants are $\mu_0 = 4\pi \cdot 10^{-7}$ Vs/Am and $\varepsilon_0 = 8.85 \cdot 10^{-12}$ As/Vm.

2.1.1 Telegraph and Helmholtz equation

Telegraph or wave equations are derived following the assumptions that outside of external sources and in regions of homogeneous conductivity no free charges exist[1], and the current density is source free in homogeneous regions[2]. In this way, Maxwell equations can be transformed by taking the curl of eq. 2.1 and $\boldsymbol{B}$ is eliminated using 2.5 and subsequently 2.2, resulting in a second order differential equation for the electric field.[3] The vector identity $\nabla \times \nabla \times \boldsymbol{\mathcal{F}} = \nabla\nabla \cdot \boldsymbol{\mathcal{F}} - \Delta\boldsymbol{\mathcal{F}}$ is considered and thus the telegraph equations are:

$$\Delta\boldsymbol{\mathcal{F}} - \mu\sigma\frac{\partial}{\partial t}\boldsymbol{\mathcal{F}} - \mu\varepsilon\frac{\partial^2}{\partial t^2}\boldsymbol{\mathcal{F}} = 0 \qquad\qquad \boldsymbol{\mathcal{F}} \in \{\boldsymbol{E}, \boldsymbol{H}\} \tag{2.8}$$

[1] $\nabla \cdot \boldsymbol{E} = 0$

[2] $\nabla \cdot \boldsymbol{j} = 0$

[3] An equation for the magnetic field $\boldsymbol{H}$ is derived in a similar way.

By applying a Fourier transformation to the telegraph equation, the Helmholtz equation is obtained:

$$\Delta \boldsymbol{\mathcal{F}} - \underbrace{i\omega\mu\sigma\boldsymbol{\mathcal{F}}}_{\text{conduction}} + \underbrace{\mu\varepsilon\omega^2\boldsymbol{\mathcal{F}}}_{\text{displacement}} = 0 \qquad \boldsymbol{\mathcal{F}} \in \{\boldsymbol{E}, \boldsymbol{H}\} \tag{2.9}$$

With the wavenumber k: $k^2 = \mu\varepsilon\omega^2 - i\mu\sigma\omega$, which implies the physical properties of the media; ω is the angular frequency in $1/\mathrm{s}$.

2.1.2 Quasi static approximation

In the quasi static approximation ($\mu\varepsilon\omega^2 \ll \mu\sigma\omega$) the Telegraph equation (2.8) and Helmholtz equation (2.9) are reduced to:

$$\Delta \boldsymbol{\mathcal{F}} - \mu\sigma\partial_t \boldsymbol{\mathcal{F}} = 0 \qquad \boldsymbol{\mathcal{F}} \in \{\boldsymbol{E}, \boldsymbol{H}\} \tag{2.10}$$

$$\Delta \boldsymbol{\mathcal{F}} - i\omega\mu\sigma\boldsymbol{\mathcal{F}} = 0 \qquad \boldsymbol{\mathcal{F}} \in \{\boldsymbol{E}, \boldsymbol{H}\} \tag{2.11}$$

This approximation is valid when the conducting currents ($\sigma\boldsymbol{E}$) are much larger than the displacement currents ($\partial\boldsymbol{D}/\partial t$), as it is the case for typical conductivities found in the subsurface and most of the frequencies used by the instruments in the applied EM induction methods[4]. Equations 2.10 and 2.11 are the diffusion equations in time and frequency domain, respectively.

A solution of equation 2.10 is a positive downward decaying EM field with a harmonic time dependence $e^{i\omega t}$ in a uniform conductor with conductivity σ (Ward and Hohmann, 1988):

$$\begin{aligned} \boldsymbol{\mathcal{F}}(z,t) &= \boldsymbol{\mathcal{F}}_0^+ e^{i\omega t} e^{-ikz} \\ &= \boldsymbol{\mathcal{F}}_0^+ e^{i\omega t} e^{-i\sqrt{\frac{\mu\sigma\omega}{2}}z} e^{-\sqrt{\frac{\mu\sigma\omega}{2}}z} \qquad \boldsymbol{\mathcal{F}} \in \{\boldsymbol{E}, \boldsymbol{H}\} \end{aligned} \tag{2.12}$$

Where $\boldsymbol{\mathcal{F}}_0^+$ is the initial amplitude of the EM field and k is the wavenumber that in the quasi static approximation is given by:

$$k = \sqrt{-i\mu\sigma\omega} = (1-i)\sqrt{\frac{\mu\sigma\omega}{2}} \tag{2.13}$$

The depth at which the EM wave reduces its amplitude by a factor of $1/e$ is defined as skin depth δ:

$$\delta = \sqrt{\frac{2}{\mu\sigma\omega}} \tag{2.14}$$

In addition, a solution of the time domain diffusion equation for an impulse EM field at $z = 0$ is (Ward and Hohmann, 1988):

$$\left\{ \begin{array}{c} \boldsymbol{E}(z,t) \\ \boldsymbol{H}(z,t) \end{array} \right\} = \left\{ \begin{array}{c} \boldsymbol{E}_0^+ \\ \boldsymbol{H}_0^+ \end{array} \right\} \frac{\sqrt{\mu\sigma}z}{2\pi^{\frac{1}{2}}t^{\frac{3}{2}}} e^{-\frac{\mu\sigma z^2}{4t}} \tag{2.15}$$

[4]Ground-penetrating radar is an exception.

By calculating the derivative of eq. 2.15 with respect to z and setting it to zero, the diffusion depth is obtained:

$$\delta_{TD} = \sqrt{\frac{2t}{\mu\sigma}} \tag{2.16}$$

This equation describes the depth of the maximum wave amplitude to a certain time t (Ward and Hohmann, 1988). In addition, the velocity of the maximum field amplitude within a conductive media is given by the derivative of equation 2.16 with respect to time (Ward and Hohmann, 1988):

$$v = \partial_t \delta_{TD} = \frac{1}{\sqrt{2\mu\sigma t}} \tag{2.17}$$

Spies (1989) studied the depth of investigation of frequency and time domain EM soundings. He concluded that for MT measurements a buried inhomogeneity can be detected under about 1.5 skin depth and for TEM under about one diffusion depth. Moreover, the depth of investigation for TEM is dependent on the transmitter moment, noise levels and conductivity of the subsurface structure (Spies, 1989). For TEM soundings in the near zone:

$$z_{max} \approx 0.55 \left(\frac{IA_{Tx}}{\sigma\eta_v} \right)^{\frac{1}{5}} \tag{2.18}$$

where I is the transmitter current (in A), A_{Tx} is the area of the transmitter loop (in m^2) and η_v is the voltage noise level (in V).

2.2 Magnetotellurics

Magnetotellurics (MT) is an electromagnetic method which uses natural variations of the electric and magnetic fields measured at the Earth's surface to image the electrical conductivity structure of the subsurface. The method was introduced separately by Cagniard (1953) and Tikhonov (1950). MT is a passive method and uses naturally generated electromagnetic field variations in the period range of 10^{-3} s to 10^5 s. These electromagnetic fields have two main sources (Vozoff, 1991): lightning discharge (spherics) and interaction of the solar wind with the earth's magnetosphere (micropulsations). For periods shorter than 1 s, the major source mechanism is the propagation of electromagnetic energy from distant thunderstorms which occur primarily in the equatorial regions. The energy propagates in the spherical cavity wave guide formed by the earth's atmosphere. Whereas at periods longer than 1 s the major source mechanism for natural EM fields come from interactions of the charged particles in the solar wind with the earth's magnetic field and charged particles in the ionosphere. An excitation minimum exists between these two ranges of period, called as dead band (from 0.1 to 10 s) and it leads to significantly lower signal to noise ratios (Simpson and Bahr, 2005). MT is capable to image the subsurface structure at depths from several tens of meters to more than 100 km depending on the resistivity ρ ($\rho = 1/\sigma$) of the structure and frequency contents of the EM field.

2.2.1 Transfer functions

The measured variations of the horizontal electric and magnetic field components are linearly related through the magnetotelluric impedance tensor $\boldsymbol{Z}$, which is written in the frequency domain as follows:

$$\begin{pmatrix} E_x \\ E_y \end{pmatrix} = \begin{pmatrix} Z_{xx} & Z_{xy} \\ Z_{yx} & Z_{yy} \end{pmatrix} \cdot \begin{pmatrix} B_x \\ B_y \end{pmatrix} \tag{2.19}$$

The complex impedances can be described as apparent resistivity (ρ_a) and phase (ϕ) values through (Cagniard, 1953):

$$\rho_{a,ij} = 0.2T \left| \frac{E_i}{B_j} \right|^2 = 0.2T|Z_{ij}|^2 \tag{2.20}$$

$$\phi_{ij} = \arctan\left(\frac{Im(Z_{ij})}{Re(Z_{ij})} \right) \tag{2.21}$$

where $i, j = x, y$ and $T = 2\pi/\omega$ is the period in s. The electric field is measured in mV/km and the magnetic field in nT. Apparent resistivity represents an average of the electrical resistivity within the induction volume of the EM fields. For a homogeneous half-space, the apparent resistivity reflects the true resistivity of the subsurface and ϕ = 45° (Kaufman and Keller, 1981).

The vertical magnetic transfer function $\boldsymbol{T}$ or also called Tipper, is a linear relationship between the vertical magnetic component and the horizontal magnetic field components:

$$B_z = \begin{pmatrix} T_{zx} & T_{zy} \end{pmatrix} \cdot \begin{pmatrix} B_x \\ B_y \end{pmatrix} \tag{2.22}$$

The vertical magnetic transfer functions (VTF) can be represented as induction vectors or also called induction arrows, whose amplitude and angle of their real part in the Wiese convention (Wiese, 1962) are calculated as follows:

$$amplitude: \qquad \sqrt{Re(T_{zx})^2 + Re(T_{zy})^2} \tag{2.23}$$

$$angle: \qquad \arctan\left(\frac{Re(T_{zy})}{Re(T_{zx})} \right) \tag{2.24}$$

The induction vectors are used for identifying lateral contrasts in the conductivity of the subsurface. In the Wiese convention (Wiese, 1962), the real induction vectors give the direction of the lateral resistivity gradient.

In addition, the phase relation of the impedance tensor can be expressed by the phase tensor Φ as follows (Caldwell et al., 2004):

$$\Phi = \boldsymbol{X}^{-1}\boldsymbol{Y} \tag{2.25}$$

where $\boldsymbol{X}$ and $\boldsymbol{Y}$ are real and imaginary parts of the impedance tensor $\boldsymbol{Z}$. Φ is a real second rank tensor which is characterized by a direction and three independent scalar coordinate invariants. It has the advantage that no additional

information about the dimensionality of the subsurface is required and it is not affected by near surface heterogeneities which produce galvanic distortion. As coordinate invariants Caldwell et al. (2004) suggested to use the maximum Φ_{max} and minimum Φ_{min} tensor values and the tensor skew β which is defined as:

$$\beta = \frac{1}{2}\arctan\left(\frac{\Phi_{xy} - \Phi_{yx}}{\Phi_{xx} + \Phi_{yy}}\right) \tag{2.26}$$

The phase tensor can be now written as:

$$\Phi = \boldsymbol{R}^T(\alpha - \beta)\begin{pmatrix}\Phi_{max} & 0\\ 0 & \Phi_{min}\end{pmatrix}\boldsymbol{R}(\alpha + \beta) \tag{2.27}$$

where $\boldsymbol{R}(\alpha + \beta)$ is the rotation matrix:

$$\boldsymbol{R}(\alpha + \beta) = \begin{pmatrix}\cos(\alpha + \beta) & \sin(\alpha + \beta)\\ -\sin(\alpha + \beta) & \cos(\alpha + \beta)\end{pmatrix} \tag{2.28}$$

and the angle α which reflects the dependence of the tensor on the coordinate system is computed:

$$\alpha = \frac{1}{2}\arctan\left(\frac{\Phi_{xy} + \Phi_{yx}}{\Phi_{xx} - \Phi_{yy}}\right) \tag{2.29}$$

Phase tensor data are usually depicted as ellipses (Fig. 2.1). The lengths of the major and the minor axis are determined by Φ_{max} and Φ_{min}, respectively. Whereas $\alpha - \beta$ defines the orientation of the major axis. The information about the dimensionality of the subsurface structure can be obtained from the phase tensor invariants: $\beta = 0$ indicates that the subsurface structure is 1D or 2D. Additionally, $\Phi_{max} = \Phi_{min}$ indicates that the structure is one-dimensional.

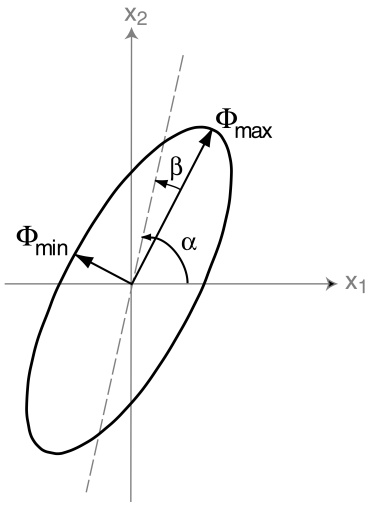

FIGURE 2.1: *Graphical representation of the phase tensor. The angle $\alpha - \beta$ gives the orientation of the major axis of the ellipse in the observer's coordinate system. Figure taken from Caldwell et al. (2004).*

2.2.2 Galvanic effect

As it has been earlier mentioned, the impedance tensor can be visualized through the apparent resistivity and phase. The apparent resistivity might be distorted by small scale near surface heterogeneities if the skin depth is significantly larger than the dimensions of the small anomalies (Simpson and Bahr, 2005). This situation is referred as galvanic distortion, and it influences the measured electric field. The galvanic distortion of the electric field is caused by an accumulation of electric charges at the boundaries of the near surface heterogeneities (Jiracek, 1990).

Considering a small anomaly below the MT station, the measured electric field $\boldsymbol{E}$ is given by:

$$\boldsymbol{E} = \boldsymbol{D}\boldsymbol{E}_R = \boldsymbol{D}\left(\boldsymbol{Z}_R\boldsymbol{B}_R\right) = \left(\boldsymbol{D}\boldsymbol{Z}_R\right)\boldsymbol{B} \tag{2.30}$$

Where $\boldsymbol{D}$ is a distortion tensor, $\boldsymbol{E}_R$, $\boldsymbol{B}_R$ and $\boldsymbol{Z}_R$ are the regional electric field, magnetic field and impedance tensor in absence of the anomaly, respectively. The horizontal magnetic field components are not severely affected, so that the distortion in the magnetic field can be neglected ($\boldsymbol{B} = \boldsymbol{B}_R$). Thus, the observed impedance is also distorted:

$$\boldsymbol{Z} = \boldsymbol{D}\boldsymbol{Z}_R \tag{2.31}$$

The galvanic distortion is also named as static because the deflection of a regional electric current by small scale electric charges is period-independent (Jiracek, 1990). When the near surface heterogeneities are more conductive than the regional background, the measured electric field is reduced. In contrast, the measured electric field is increased when the heterogeneities are more resistive.

2.2.3 Dimensionality

For a 1D subsurface structure, the conductivity (σ) only varies with depth and the main diagonal elements of the impedance tensor are zero:

$$Z_{xx} = Z_{yy} = 0 \tag{2.32}$$

Whereas the off-diagonal components have opposite signs but identical magnitude:

$$Z_{xy} = -Z_{yx} \tag{2.33}$$

The phase tensor is visually represented with a circle ($\Phi_{max} = \Phi_{min}$). With the absence of lateral conductivity contrasts, $T_{zx} = T_{zy} = 0$.

For a 2D subsurface structure, the conductivities of the earth vary in the vertical and one horizontal directions. Assuming that the geo-electric strike direction coincides with x-axis: $\sigma = \sigma(z, y)$, the Maxwell equations are decoupled in two different sets of equations with independent polarizations:

$$\frac{\partial B_z}{\partial y} - \frac{\partial B_y}{\partial z} = \mu_0 \sigma E_x \tag{2.34}$$

$$-\frac{\partial E_x}{\partial z} = i\omega B_y \tag{2.35}$$

$$\frac{\partial E_x}{\partial y} = i\omega B_z \tag{2.36}$$

These three equations represent the TE mode. Whereas:

$$\frac{\partial E_y}{\partial z} - \frac{\partial E_z}{\partial y} = i\omega B_x \tag{2.37}$$

$$\frac{\partial B_x}{\partial z} = \mu_0 \sigma E_y \tag{2.38}$$

$$-\frac{\partial B_x}{\partial y} = \mu_0 \sigma E_z \tag{2.39}$$

are the TM mode. For the E-polarization or TE mode, $\boldsymbol{E}$ points in the strike

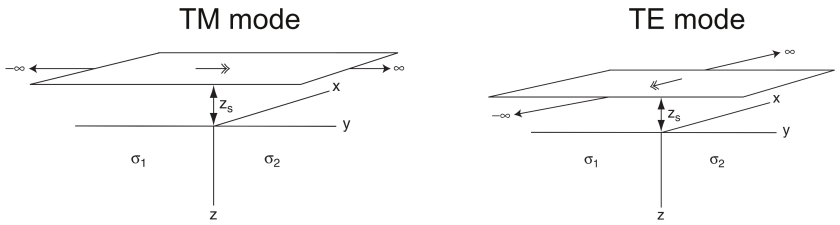

FIGURE 2.2: *Simple models for the source electric currents for TM and TE modes. Figure taken from Chave and Weidelt (2012).*

direction and $\boldsymbol{B}$ lies in the plane orthogonal to the strike. Whereas for the B-polarization or TM, $\boldsymbol{B}$ is parallel to the strike and $\boldsymbol{E}$ is in the horizontal plane orthogonal to the strike (Chave and Weidelt, 2012). Figure 2.2 illustrates the TM and TE modes. For a 2D subsurface structure, the main diagonal impedances are equal in magnitude but with different sign:

$$Z_{xx} = -Z_{yy} \tag{2.40}$$

And the anti-diagonal elements are different:

$$Z_{xy} \neq Z_{yx} \tag{2.41}$$

The impedance tensor can be rotated into the strike direction through:

$$\boldsymbol{R}_z \boldsymbol{E} = \boldsymbol{R}_z \boldsymbol{Z} \boldsymbol{R}_z^{-1} \boldsymbol{R}_z \boldsymbol{B} \tag{2.42}$$

Where $\boldsymbol{R}_z$ is the rotation matrix:

$$\boldsymbol{R}_z = \begin{pmatrix} \cos\theta & \sin\theta \\ -\sin\theta & \cos\theta \end{pmatrix} \tag{2.43}$$

The rotation angle θ can be estimated as follows (Swift, 1967):

$$\theta = \frac{1}{4}\arctan\left(\frac{2Re\left(\left(Z_{xx}-Z_{yy}\right)\left(Z_{xy}-Z_{yx}\right)\right)}{\left|Z_{xx}-Z_{yy}\right|^2-\left|Z_{xy}+Z_{yx}\right|^2}\right) \tag{2.44}$$

Thus, the main diagonal impedances become zero and the decoupling into the TE and TM mode can be done. However, it is challenging to obtain a direction where the main diagonal elements are exactly zero due to noise, galvanic distortion or because the subsurface structure is 3D.

The phase tensor is graphically represented by an ellipse where the maximum principal axis of the ellipse is either perpendicular or parallel to the regional strike direction. The real part of the induction vectors is oriented perpendicular to the strike direction and points away from conductors (in the Wiese convention).

Finally, in a 3D subsurface structure, the conductivity varies in three directions ($\sigma(x,y,z)$). All the components of the impedance tensor are different and non-zero values:

$$Z_{xx} \neq Z_{yy} \tag{2.45}$$

$$Z_{xy} \neq Z_{yx} \tag{2.46}$$

The phase tensor is non-symmetric leading to a skew angle β different from zero.

2.3 Transient Electromagnetics

Transient Electromagnetics (TEM) is an active EM method and it operates in time domain. TEM technique has been developed and refined most intensively since the mid-1980's (Christiansen et al., 2006). The method consists of an ungrounded loop as a transmitter coil where a current is driven and abruptly turned off at time t_0. Due to the abrupt change of the primary magnetic field, eddy currents are induced in the ground and are dissipated with progressing time. A receiver coil measures the rate of change of the secondary magnetic field due to such induced eddy currents.

Figure 2.3a illustrates a bipolar transmitter current waveform $I(t)$ with a 50 % duty cycle. An entire cycle period T consists of two current switch-off and two switch-on pulses. Two decay voltage curves measured after a current switch-off at distinct time gates t_i are shown in Fig. 2.3b. It can be distinguished that for a conductive subsurface the transient decays smoother than for a resistive medium. The induced voltage $U_{ind}(t)$ measured with a wire loop as a receiver is[5]:

$$U_{ind} = -\partial_t \int_{A_{rx}} \boldsymbol{B}\cdot\boldsymbol{n} \quad dA_{rx} \tag{2.47}$$

Where A_{rx} is the receiver area and $\boldsymbol{n}$ is the surface normal. Measurements of the magnetic field are referred to as step response and the measurements of its time

[5]The induced voltage is termed as the time derivative of the magnetic field $\partial_t B$.

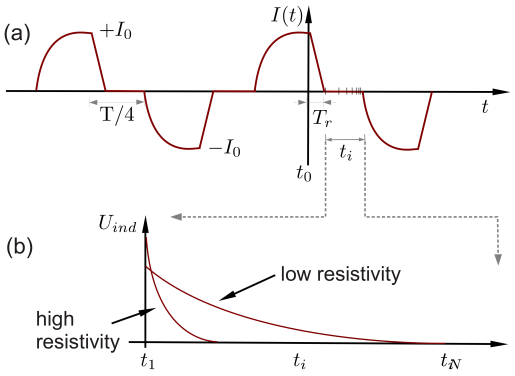

FIGURE 2.3: *(a) Bipolar transmitter current waveform $I(t)$. T_r is the ramp time and t_i the different acquisition times. (b) Theoretical receiver decay voltage curves for the case of a resistive and conductive subsurface. Figure taken from Yogeshwar (2014).*

derivative are named impulse response (Yogeshwar, 2014). As it was already mentioned, the induced voltage is measured after the current turn-off, but this turn-off is not instant at t_0. Due to the non-zero loop inductance and transmitter characteristics a finite amount of time is required to turn the current off (Fitterman and Anderson, 1987). This finite time is known as ramp time T_r and it is marked in Fig. 2.3a. The turn-off time effect is another parameter that must be taken into account for proper data interpretation (Fitterman and Anderson, 1987).

2.3.1 Solution for a half-space

Assuming a horizontal loop with radius a and current I located at $z = 0$, the vertical component of the magnetic field $\dot{H}_z$ at the center of the loop due to a step excitation is given by (Ward and Hohmann, 1988):

$$\dot{H}_z = \frac{-I}{\sigma\mu_0 a^3}\left[3erf\left(\Theta a\right) - \frac{2}{\sqrt{\pi}}\Theta a\left(3 + 2\Theta^2 a^2\right)e^{-\left(\Theta^2 a^2\right)}\right] \tag{2.48}$$

where Θ is:

$$\Theta = \sqrt{\frac{\mu_0\sigma}{4t}} \tag{2.49}$$

and the Gauss error function is:

$$erf\left(x\right) = \frac{2}{\sqrt{\pi}}\int_0^x e^{-\tau^2}d\tau \tag{2.50}$$

For early times after current switch-off, equation 2.48 is reduced to:

$$\dot{H}_{z,et} = -\frac{3I}{\sigma\mu_0 a^3} \tag{2.51}$$

whereas for late times:

$$\dot{H}_{z,lt} = -\frac{Ia^2}{20\sqrt{\pi}}\left(\mu_0\sigma\right)^{\frac{3}{2}} t^{-\frac{5}{2}} \tag{2.52}$$

Rearranging the terms of equation 2.51, the early time apparent resistivity is given by:

$$\rho_{a,et} = -\frac{\mu_0 a^3}{3I}\dot{H}_{z,et} \tag{2.53}$$

Similarly, rearranging the terms of equation 2.52 the late time apparent resistivity is:

$$\rho_{a,lt} = -\left[\frac{I^2 a^4}{20^2 \pi t^5}\right]^{\frac{1}{3}} \mu_0 \dot{H}_{z,lt}^{-\frac{2}{3}} \tag{2.54}$$

The early time approximation is valid for far zone soundings. While the late time approximation works for near zone soundings, where the induction number is less than one. The induction number in frequency domain is given by (Spies and Frischknecht, 1991):

$$B_{FD} = \sqrt{\frac{\mu_0 \sigma \omega}{2}} r \tag{2.55}$$

and for time domain (Spies and Frischknecht, 1991):

$$B_{TD} = \sqrt{\frac{\mu_0 \sigma}{4t}} r \tag{2.56}$$

where r is the source-receiver separation.

2.3.2 Solution for a 1D layered earth

The induced voltage $U_{z,ind}$ obtained in a receiver loop generated by a horizontal electric dipole (HED) sourced at $z = 0$ is defined as (Weidelt, 1986):

$$U_{z,ind}(t,r) = \frac{1}{2\pi}\int_{-\infty}^{\infty} \mu A_{rx} e^{i\omega t} \frac{D_0 \sin\phi}{4\pi} \int_0^{\infty} \frac{B_E(k) - k}{B_E(k) + k} k J_1(kr)\, dk d\omega \tag{2.57}$$

where A_{rx} is the receiver area and the dipole moment is: $D_0 = Idl$. $B_E(k)$ is the reciprocal impedance obtained at surface, k is the wave number and J_1 is a Bessel function of the first kind, order one. r and ϕ are the distance and angle (respectively) between the receiver loop and dipole. The solution for a rectangular transmitter loop is obtained by superposition of the response of elementary dipoles with moment $m = Idl$. For an accurate solution, the length of such elementary dipoles is determined by the induction number. Thus, more dipoles are required in the near zone than in the far zone soundings. Equation 2.57 is solved for one dipole and the rest of the solutions are calculated by a coordinate transformation (Yogeshwar, 2014).

Equation 2.57 involves the calculation of a Bessel integral of the form:

$$g(r) = \int_0^{\infty} f(k) J_\nu(kr)\, dk \qquad \nu = 1 \tag{2.58}$$

These kind of integrals can be numerically evaluated with the fast Hankel transform (Key, 2012).

Chapter No. 3

Inversion theory

In applied EM geophysics, the aim of the inversion problem is to derive the subsurface structure of the earth. Essentially, the inversion of an electromagnetic data set aims to find model parameters that can explain the measured data. This chapter deals with the inversion theory of the different algorithms used for the inversion of the San Felipe field data. The Marquardt and Occam inversion schemes implemented in the software Emuplus (Scholl, 2005) are explained. The theoretical aspects of the Spatially Constrained Inversion (Viezzoli et al., 2008) applied to TEM data are defined. The Non-Linear Conjugate Gradients is also described, which was used for the 2D and 3D inversion of MT data. Many of the described inversion theoretical principles are found in Menke (1984) and Meju (1994). Vectors are presented in lower case, bold, italic characters and matrices in upper case, bold, italic characters.

3.1 Problem formulation

For a given EM data set, the data vector $\boldsymbol{d}$ contains N observations:

$$\boldsymbol{d} = (d_1, ..., d_N)^T \tag{3.1}$$

Usually the observed data are contaminated with errors, which are contained in the data error vector:

$$\delta\boldsymbol{d} = (\delta d_1, ..., \delta d_N)^T \tag{3.2}$$

Assuming a model vector $\boldsymbol{m}$ that contains M model parameters:

$$\boldsymbol{m} = (m_1, ..., m_M)^T \tag{3.3}$$

The objective of the inversion process is to find a model $\boldsymbol{m}$ that explains the observed data $\boldsymbol{d}$ within their errors $\delta\boldsymbol{d}$. Introducing now the forward modeling operator $\boldsymbol{F}$ which is function of $\boldsymbol{m}$:

$$\boldsymbol{F}(\boldsymbol{m}) = \boldsymbol{d} \tag{3.4}$$

The model parameter vector $\boldsymbol{m}$ is thus related to the data vector $\boldsymbol{d}$ trough equation 3.4. The operator $\boldsymbol{F}(\boldsymbol{m})$ generates the calculated or synthetic data $\boldsymbol{d}'$:

$$\boldsymbol{d}' = \boldsymbol{F}(\boldsymbol{m}) \tag{3.5}$$

When the number of measured data and model parameters are identical $N = M$, the problem is *even-determined* and one exact solutions exits. For the case that more model parameters are available than observed data points $N < M$, the problem is named *under-determined* and infinite solutions exist. Whereas if more data than model parameters are available $N > M$, the problem is *over-determined* and no unique solutions exists. In applied EM geophysics, the problems are *ill-posed*, implying that some model parameters are well resolved with the given data set and others model parameters are not.

Essentially, the inversion tries to minimize the misfit between measured $\boldsymbol{d}$ and synthetic data $\boldsymbol{d}'$. In a least-square sense, the function to minimize is named as cost-function or misfit-function, which is defined as follows:

$$\boldsymbol{\Phi}_d = \left(\boldsymbol{d} - \boldsymbol{d}'\right)^T \boldsymbol{W}_d^2 \left(\boldsymbol{d} - \boldsymbol{d}'\right) = \boldsymbol{\epsilon}^T \boldsymbol{W}_d^2 \boldsymbol{\epsilon}. \tag{3.6}$$

where $\boldsymbol{\epsilon} = (\boldsymbol{d} - \boldsymbol{d}')$ is called residual vector. $\boldsymbol{W}_d$ is the diagonal error weighting matrix:

$$\boldsymbol{W}_d = \begin{pmatrix} \frac{1}{\delta d_1} & & 0 \\ & \ddots & \\ 0 & & \frac{1}{\delta d_N} \end{pmatrix} \tag{3.7}$$

The data fit is estimated through:

$$\chi = \sqrt{\frac{\Phi_d}{N}} = \sqrt{\frac{1}{N} \sum_{i=1}^{N} \frac{\left(d_i - d_i'\right)^2}{\delta d_i^2}} \tag{3.8}$$

In this thesis, however, the root mean square (RMS) is termed as χ. It means that the RMS is calculated through equation 3.8 ($RMS = \chi$). A data-fit of RMS=1 indicates an optimal fit within the data errors. Values less than one refers to an over-fit, the mean deviation between observed and calculated data is smaller than the data error. Whereas RMS values greater than 1 indicate an under-fit, the mean deviation between measured and calculated data is larger than the data errors.

For the simplest case, a model can be derived through a direct inversion scheme: $\boldsymbol{m} = \boldsymbol{F}^{-1}\boldsymbol{d}$. Applied EM geophysical problems, however, are non-linear (Meju, 1994) and therefore the function $\boldsymbol{F}(\boldsymbol{m})$ must be firstly linearized. The problem is linearized through a Taylor approximation of first order around a model and consequently an iterative procedure is applied to improve the model.

3.1.1 Non-linear problem strategies

During the inversion process, an initial model $\boldsymbol{m}_0$ is perturbed iteratively. In each iteration k, the model update $\Delta \boldsymbol{m}_k$ is determined and the model of the current

iteration is updated:

$$\boldsymbol{m}_{k+1} = \boldsymbol{m}_k + \Delta \boldsymbol{m}_k \tag{3.9}$$

The problem is linearized through the Taylor approximation of first order:

$$\boldsymbol{F}\left(\boldsymbol{m}_k + \Delta \boldsymbol{m}_k\right) = \boldsymbol{F}\left(\boldsymbol{m}_k\right) + \frac{\partial \boldsymbol{F}(\boldsymbol{m}_k)}{\partial \boldsymbol{m}_k} \Delta \boldsymbol{m}_k + \cdots \approx \boldsymbol{F}\left(\boldsymbol{m}_k\right) + \boldsymbol{J} \Delta \boldsymbol{m}_k \tag{3.10}$$

where $\boldsymbol{J}$ is the NxM Jacobian or sensitivity matrix:

$$\boldsymbol{J} = \begin{pmatrix} \frac{\partial F_1(\boldsymbol{m})}{\partial m_1} & \cdots & \frac{\partial F_1(\boldsymbol{m})}{\partial m_M} \\ \vdots & \ddots & \vdots \\ \frac{\partial F_N(\boldsymbol{m})}{\partial m_1} & \cdots & \frac{\partial F_N(\boldsymbol{m})}{\partial m_M} \end{pmatrix} \tag{3.11}$$

Each entry of the Jacobian matrix $\boldsymbol{J}$ describes the sensitivity of a data point with respect to a small perturbation in the model parameters. The cost function takes now the form:

$$\Phi_d\left(\Delta \boldsymbol{m}_k\right) = \left(\boldsymbol{d} - \boldsymbol{F}\left(\boldsymbol{m}_k\right) - \boldsymbol{J}\boldsymbol{\Delta}\boldsymbol{m}_k\right)^T \boldsymbol{W}_d^2 \left(\boldsymbol{d} - \boldsymbol{F}(\boldsymbol{m}_k) - \boldsymbol{J}\boldsymbol{\Delta}\boldsymbol{m}_k\right) \tag{3.12}$$

To find the minimum of the cost-function, the derivative of equation 3.12 with respect to the model update $\Delta \boldsymbol{m}_k$ is computed and set to zero. Thus, a least-square solution for the model update is:

$$\Delta \boldsymbol{m}_k = \left(\boldsymbol{J}^T \boldsymbol{W}_d^2 \boldsymbol{J}\right)^{-1} \boldsymbol{J}^T \boldsymbol{W}_d^2 \left(\boldsymbol{d} - \boldsymbol{F}(\boldsymbol{m}_k)\right) \tag{3.13}$$

This equation (eq. 3.13) is known as the Gauss-Newton or unconstrained least square solution. This iteratively inversion process is truncated at the k-th iteration if $\boldsymbol{m}_k$ gives an acceptable data fit or the number of desired iterations is reached. The convergence of this Gauss-Newton algorithm is very slow due to two main facts: a suitable initial model $\boldsymbol{m}_0$ is needed and, the matrix $\boldsymbol{J}^T \boldsymbol{W}_d^2 \boldsymbol{J}$ may be singular and the inverse does not exist, therefore equation 3.13 would not have a solution. To avoid the ill-posed problem in the Gauss-Newton method, constraints are often imposed on the normal equations, *e.g.* the model must consider *a priori* information in the form of model $\left(\min \|\boldsymbol{m} - \boldsymbol{m}^{apriori}\|^2\right)$. Thus, a penalty function that considers the original minimization problem exposed with equation 3.6 and one constraint can be defined as follows:

$$\boldsymbol{\Phi} = \boldsymbol{\Phi}_d + \lambda \boldsymbol{\Phi}_m \tag{3.14}$$

where λ is the so-called regularization or trade-off parameter. An optimal value for λ must be found to avoid that neither the data cost function $\boldsymbol{\Phi}_d$ nor the model cost function $\boldsymbol{\Phi}_m$ dominates in the total cost function $\boldsymbol{\Phi}$.

3.2 Marquardt inversion

Levenberg (1944) introduced a possibility to prevent divergence of the solution to the normal equation 3.13 and it was enhanced by Marquardt (1963). Equation 3.13 is modified to:

$$\Delta \boldsymbol{m}_k = \left(\boldsymbol{J}^T \boldsymbol{W}_d^2 \boldsymbol{J} + \beta^2 \boldsymbol{I} \right)^{-1} \boldsymbol{J}^T \boldsymbol{W}_d^T \boldsymbol{W}_d \left(\boldsymbol{d} - \boldsymbol{F}\left(\boldsymbol{m}_k\right) \right) \tag{3.15}$$

where the additional term limits the length of the model update vector depending on the chosen damping factor β. $\boldsymbol{I}$ is the identity matrix and β is a Lagrange multiplier. This method is know as Marquardt-Levenberg inversion or damped least squares inversion. This scheme is used for inversion problems with very few model parameters. A drawback of the Marquardt inversion scheme is that the output strongly depends on the chosen starting model (Petry, 1987).

3.2.1 Singular Value Decomposition

To calculate the inverse in equation 3.15, singular value decomposition (SVD) is often utilized. This methods states that any NxM matrix can be split as follows (Menke, 1984):

$$\boldsymbol{G} = \boldsymbol{U} \boldsymbol{\Lambda} \boldsymbol{V}^T \tag{3.16}$$

where:

- The orthogonal matrix $\boldsymbol{U} \in \mathbb{R}^{N \times N}$ consists of eigenvectors that span the data space. The individual eigenvectors of $\boldsymbol{G}\boldsymbol{G}^T$ are contained in $\boldsymbol{U}$.
- The orthogonal matrix $\boldsymbol{V} \in \mathbb{R}^{M \times M}$ spans the model space and consists of the eigenvectors from $\boldsymbol{G}^T\boldsymbol{G}$.
- $\boldsymbol{\Lambda} \in \mathbb{R}^{N \times M}$ is a diagonal eigenvalue matrix. The diagonal elements λ_i are non-negative and they are called singular values. These singular values are arranged in decreasing order.

If matrix $\boldsymbol{G}$ is rank$(\boldsymbol{G}) = p \leq min(M, N)$, then p number of non-zero singular values exist. The SVD is applied to the weighted Jacobian $\boldsymbol{J}_w = \boldsymbol{W}_d \boldsymbol{J}$ and equation 3.15 can be expressed as (Lines and Treitel, 1984):

$$\begin{aligned} \Delta \boldsymbol{m}_k &= \boldsymbol{V} \underbrace{\left(\boldsymbol{\Lambda}^2 + \beta^2 \boldsymbol{I} \right)^{-1} \boldsymbol{\Lambda}^T \boldsymbol{\Lambda}}_{\boldsymbol{Q}} \boldsymbol{\Lambda}^{-1} \boldsymbol{U}^T \boldsymbol{W}_d \left(\boldsymbol{d} - \boldsymbol{F}(\boldsymbol{m}_k) \right) \\ &= \boldsymbol{V} \boldsymbol{Q} \boldsymbol{\Lambda}^{-1} \boldsymbol{U}^T \boldsymbol{W}_d \left(\boldsymbol{d} - \boldsymbol{F}(\boldsymbol{m}_k) \right) \end{aligned} \tag{3.17}$$

where the diagonal damping matrix $\boldsymbol{Q}$ has the values:

$$Q_{ii} = \frac{\lambda_i^2}{\lambda_i^2 + \beta^2} \tag{3.18}$$

If it is normalized by the maximal singular value λ_{max}:

$$\hat{Q}_{ii} = \frac{\lambda_i^2/\lambda_{max}^2}{\lambda_i^2/\lambda_{max}^2 + \hat{\beta}^2} \tag{3.19}$$

The term $\hat{\beta} = \dfrac{\beta}{\lambda_{max}}$ is the singular value threshold and it marks the boundary beyond which a singular value is damped. Note that a value of $\beta^2 = 0$ results in the Gauss-Newton method.

3.2.2 Importances

The resolution of the model parameters can be investigated through the normalized damping matrix $\hat{\boldsymbol{Q}}$. The model parameter resolution matrix $\boldsymbol{R}$ is defined (Menke, 1984):

$$\boldsymbol{R} = \boldsymbol{V}\hat{\boldsymbol{Q}}\hat{\boldsymbol{Q}}^T\boldsymbol{V}^T \tag{3.20}$$

The importance of the model parameter $\boldsymbol{m}_i$ is obtained:

$$imp_i = \sqrt{R_{ii}} \tag{3.21}$$

with values that range between 0 and 1. The closer the importance is to 1, the better the model parameter is resolved.

3.2.3 Equivalent models

Besides the importances, the equivalent models can be used to asses the resolution of the model parameters. Two models are equivalent if their response is identical within a certain error bound (Spies and Frischknecht, 1991). Scholl (2005) implemented a hybrid Marquardt-Montecarlo[1] inversion scheme to calculate equivalent models. Model parameters of the Marquardt inverse model are randomly perturbed within a few percent. If the data misfit is within an acceptable range, the model is saved. If not, a new Marquardt inversion routine is performed but with the perturbed model as starting model and the steps are repeated. The result is an ensemble of models representing the equivalent models (Scholl, 2005). Thus, these equivalent models are used to evaluate the resolution of the model parameters: if the equivalent models show high variability within a model parameter, this model parameter is not well resolved. In contrast, if the equivalent models display low variability, the corresponding model parameter is well resolved.

3.3 Occam inversion

This inversion scheme was introduced for EM problems by Constable et al. (1987). Occam inversion scheme imposes a smoothness constraint on the model and the

[1]Methods that incorporate random elements are named Monte Carlo (Mosegaard and Sambridge, 2002).

idea is to find the smoothest model that fits the data within a reasonable tolerance. For a 1D case, the subsurface is divided into M layers with fixed thickness and M resistivity values ρ_i. The model vector is only dependent on the resistivity values of the individual layers. Constraints in form of roughnesses are defined as the first (R_1) and second (R_2) order derivative of $\rho(z)$ with respect to depth:

$$R_1 = \int \left(\frac{\partial \rho(z)}{\partial z} \right)^2 dz \qquad \text{and} \qquad R_2 = \int \left(\frac{\partial^2 \rho(z)}{\partial z^2} \right)^2 dz \tag{3.22}$$

and in the discrete form:

$$R_1 = \sum_{i=2}^{M} (\rho_i - \rho_{i-1})^2 \qquad \text{and} \qquad R_2 = \sum_{i=2}^{M-1} (\rho_{i+1} - 2\rho_i + \rho_{i-1})^2 \tag{3.23}$$

In matrix notation, $\boldsymbol{R}_1$ and $\boldsymbol{R}_2$ are:

$$\boldsymbol{R}_1 = \begin{pmatrix} 0 & 0 & 0 & \cdots & 0 \\ -1 & 1 & 0 & \ddots & \vdots \\ 0 & \ddots & \ddots & \ddots & 0 \\ \vdots & \ddots & -1 & 1 & 0 \\ 0 & \cdots & 0 & -1 & 1 \end{pmatrix} \qquad \text{and} \qquad \boldsymbol{R}_2 = \boldsymbol{R}_1^T \boldsymbol{R}_1 \tag{3.24}$$

Thus, the model update is expressed as:

$$\Delta \boldsymbol{m}_k = \left(\boldsymbol{J}^T \boldsymbol{W}_d^2 \boldsymbol{J} + \lambda \boldsymbol{R}_{1,2}^T \boldsymbol{R}_{1,2} \right)^{-1} \left[\boldsymbol{J}^T \boldsymbol{W}_d^2 (\boldsymbol{d} - \boldsymbol{F}(\boldsymbol{m}_k)) - \lambda \boldsymbol{R}_{1,2}^T \boldsymbol{R}_{1,2} \boldsymbol{m}_k \right] \tag{3.25}$$

The regularization parameter λ is a trade-off between data fit and smoothness of the obtained model. For large λ values, a smoother model is expected with a higher data misfit. Whereas if $\lambda \to 0$, the data fit dominates during the inversion process. At each iteration, a λ that minimizes the data misfit is searched (Constable et al., 1987). In practice, an initial high λ value is selected and it decreases during the iterations of the inversion process, however the decrease should be limited between iterations to avoid additional structure in the model (Farquharson and Oldenburg, 2004). In this sense, Scholl (2005) implemented in Emuplus software the restriction of λ as follows: if at k-iteration λ_k was set to $c\lambda_{k-1}$ and the resulting model would meet the chosen convergence criteria, c ($0.01 \leq c \leq 0.5$) is divided by two for such iteration. This restriction of λ makes the results very dependent to its initial value (Scholl, 2005). When applying the roughness R_1, the inverse model is normally very smooth. Whereas with R_2, it leads in a small curvature of the model parameters (*i.e.* the resistivity contrast is uniform).

Additional comments: the roughness can be formulated as a smoothing operator $\boldsymbol{C}_m$ as follows (Menke, 1984):

$$(\boldsymbol{C}_m)^{-1} = \boldsymbol{R}_2 = \boldsymbol{R}_1^T \boldsymbol{R}_1 \tag{3.26}$$

Thus, the smoothing operator $\boldsymbol{C}_m$ is interpreted as the covariance of the model parameters and it provides *a priori* constraints on the magnitude and spatial smoothness of conductivity variations (Egbert, 2006; Meqbel, 2009). This smoothing operator is used in many others inversion schemes, therefore it was here defined.

3.4 Calibration Factor

Newman (1989) investigated the influence of near surface conductive bodies in the LOTEM method and concluded that the transients are shifted at late times when a conductor is close to the transmitter. He therefore proposed to include a Calibration Factor (CF) in the inversion process to account for such shifts. Originally, the calibration factor was introduced to correct errors due to wrong transmitter current or receiver area estimations (Scholl, 2005). After Newman (1989), the CF concept was also used in the inversion of TEM data. In TEM, an error can occur while setting up the transmitter or receiver. The CF is introduced to the inversion process as an additional model parameter and allows to fit shifted transients. The starting value for CF is 1, meaning that the data is not shifted. The calibration factor parameter can be fixed or allowed to vary during the inversion. When CF is not fixed during the inversion process, it is desirable that it stays close to 1. In this thesis, the calibration factor is fixed to 1 in the inversion of the acquired TEM data.

3.5 Spatially Constrained Inversion

The Spatially Constrained Inversion (SCI) is a least-squares inversion of a layered earth regularized through spatial constraints and aims to produce reliable pseudo-3D models. SCI was introduced by Viezzoli et al. (2008) and it is an extension of the Laterally Constrained Inversion (LCI) scheme which was developed by Auken and Christiansen (2004). In SCI scheme, *a priori* information is included in the inversion process and formalized via regularizing terms. The minimization of the model update is expressed by:

$$\begin{aligned}\Delta \boldsymbol{m}_k \;=\; & \left(\boldsymbol{J}^T \boldsymbol{C}_{obs}^{-1} \boldsymbol{J} + \beta^{-1} \boldsymbol{R}_p^T \boldsymbol{C}_R^{-1} \boldsymbol{R}_p + \lambda \boldsymbol{I}\right)^{-1} \\ & \cdot [\boldsymbol{J}^T \boldsymbol{C}_{obs}^{-1} (\boldsymbol{d} - \boldsymbol{F}(\boldsymbol{m}_k)) + \beta^{-1} \boldsymbol{R}_p^T \boldsymbol{C}_R^{-1} \left(-\boldsymbol{R}_p \boldsymbol{m}_k\right)]\end{aligned} \tag{3.27}$$

where $\boldsymbol{C}_{obs}^{-1}$ is a covariance matrix specifying the data errors [2]: $\boldsymbol{C}_{obs}^{-1} = \boldsymbol{W}_d^2$. The matrix $\boldsymbol{C}_R^{-1} = \boldsymbol{Q}_p^T \boldsymbol{Q}_p$ defines the strength of the regularizing constraints. $\boldsymbol{Q}_p$ is a weighting diagonal matrix in the model space which entries are inversely proportional to the model variance (σ_i) and specify the different degrees of variability associated with the spatial constraints. β is a diagonal matrix which entries are all set to unity and controls the relative importance between the data and the stabilizer. λ is the Marquardt damping parameter that is iteratively updated to stabilize the minimization process. $\boldsymbol{R}_p$ is the roughness matrix for SCI and is defined:

$$\boldsymbol{R}_p = \begin{pmatrix} S^1 & 0 & \cdots & 0 & -1 & 0 & \cdots & 0 & -1 & 0 & \cdots & 0 & 0 & 0 \\ 0 & S^2 & 0 & \cdots & 0 & -1 & 0 & \cdots & 0 & -1 & 0 & \cdots & 0 & 0 \\ \vdots & & & & & & \vdots & & & & & \vdots & & \\ 0 & 0 & 0 & \cdots & 0 & S^j & 0 & \cdots & 0 & -1 & 0 & \cdots & 0 & -1 \end{pmatrix} \tag{3.28}$$

[2] Note that the terminology is changed here to be consistent with the published paper about SCI.

where S^j is the number of models that the j-th model parameter is constrained to. The strength of the constraints which is written in the covariance matrix $\boldsymbol{C}_R^{-1}$ has non-zero entries in the same locations as $\boldsymbol{R}_p$. The strength of the constraints is defined by:

$$C_{SCI}(d) = 1 + (A-1)\left(\frac{d}{B}\right)^a \tag{3.29}$$

where d represents the distance between two constrained soundings, B the reference distance and A the reference constraint value. The exponent a determines how the constraints loosen up with distance. The reference distance is set to the mean sounding spacing. The soundings are connected via Delaunay triangulation (Delaunay, 1934). Thus for each data point, the immediate nearest neighbors connected by the Delaunay triangles are used to constrain the model parameters.

3.6 Nonlinear Conjugate Gradient Inversion

The Non-linear Conjugate Gradient (NLCG) algorithm is often used because it avoids the explicit computation of the Jacobian matrix. NLCG have been used to solve the inversion problem in 2D (Rodi and Mackie, 2001) and 3D (Kelbert et al., 2014) MT and numerical tests have shown that NLCG is more efficient than Gauss-Newton methods in terms of computation requirements. Since NLCG is closely related to the Conjugate Gradient (CG) method, CG is explained before proceeding with the description of NLCG scheme.

Solution of the normal equation with Conjugate Gradient

Considering the normal equation 3.15, for sake of simplicity it can be now written as:

$$\boldsymbol{A}\boldsymbol{x} = \boldsymbol{b} \tag{3.30}$$

where $\boldsymbol{A} = \boldsymbol{J}^T\boldsymbol{W}_d^2\boldsymbol{J} + \beta^2\boldsymbol{I}$, $\boldsymbol{x} = \Delta\boldsymbol{m}_k$ and $\boldsymbol{b} = \boldsymbol{J}^T\boldsymbol{W}_d^T\boldsymbol{W}_d\left(\boldsymbol{d} - \boldsymbol{F}\left(\boldsymbol{m}_k\right)\right)$. The equation system of 3.30 can be solved by applying a standard equation system solver. The equation system solvers can be divided in direct and iterative solvers (Meqbel, 2009). Cholesky and LU decompositions are examples of direct solvers. Whereas conjugate gradient (CG) method is an example of an iterative solver. Conjugate Gradient method generates a sequence of approximated solutions by iterative minimization, thus for solving the equation system of eq. 3.30:

$$\boldsymbol{\Phi}(\boldsymbol{x}) = \frac{1}{2}\boldsymbol{x}^T\boldsymbol{A}\boldsymbol{x} - \boldsymbol{b}^T\boldsymbol{x} \tag{3.31}$$

along a sequence of conjugate search directions $\boldsymbol{p}$:

$$\begin{aligned} \boldsymbol{p}_0 &= 0 \\ \boldsymbol{p}_{k+1} &= \boldsymbol{g}_{k+1} - \gamma_k\boldsymbol{p}_k \end{aligned} \tag{3.32}$$

where $\boldsymbol{g}_{k+1}$ is the gradient of equation 3.31:

$$\boldsymbol{g}_{k+1} = \frac{\partial}{\partial\boldsymbol{x}_k}\left(\frac{1}{2}\boldsymbol{x}_k^T\boldsymbol{A}\boldsymbol{x}_k - \boldsymbol{b}^T\boldsymbol{x}_k\right) = \boldsymbol{A}\boldsymbol{x}_k - \boldsymbol{b} \tag{3.33}$$

The scalar γ_k is calculated as:

$$\gamma_k = \frac{\boldsymbol{g}_{k+1}\boldsymbol{A}\boldsymbol{p}_k}{\boldsymbol{p}_k^T\boldsymbol{A}\boldsymbol{p}_k} \tag{3.34}$$

This scalar (γ_k) ensures that the search direction $\boldsymbol{p}_k$ is conjugate to all other previous search directions. The solution of $\boldsymbol{x}_{k+1}$ is:

$$\boldsymbol{x}_{k+1} = \boldsymbol{x}_k - \beta_{k+1}\boldsymbol{p}_{k+1} \tag{3.35}$$

where β_{k+1} is the scalar step size:

$$\beta_{k+1} = \frac{\boldsymbol{p}_{k+1}^T\boldsymbol{g}_{k+1}}{\boldsymbol{p}_{k+1}^T\boldsymbol{A}\boldsymbol{p}_{k+1}} \tag{3.36}$$

NLCG description

In the NLCG method, the gradient of equation 3.14 is calculated:

$$\nabla\boldsymbol{\Phi} = \nabla\boldsymbol{\Phi}_d + \lambda\nabla\boldsymbol{\Phi}_m \tag{3.37}$$

the function $\boldsymbol{\Phi}_m = \|\boldsymbol{L}\boldsymbol{m}^2\|$, therefore:

$$\nabla\boldsymbol{\Phi}_m = 2\boldsymbol{L}^T\boldsymbol{L}\boldsymbol{m} \tag{3.38}$$

And the gradient of equation 3.6:

$$\nabla\boldsymbol{\Phi}_d = -2\boldsymbol{J}^T\boldsymbol{W}_d^2\left(\boldsymbol{d} - \boldsymbol{d}'\right) \tag{3.39}$$

In a uniform grid, the term $\boldsymbol{L}\boldsymbol{m}$ is defined as the Laplacian of the model parameters that describes the differences between adjacent model parameters (Rodi and Mackie, 2001). Thus, the NLCG scheme minimizes the cost function $\boldsymbol{\Phi}$ but with respect to the step size β.

The minimization problem is:

$$\boldsymbol{\Phi}\left(\boldsymbol{m}_k + \beta_k\boldsymbol{p}_k\right) = \min_{\beta}\Phi\left(\boldsymbol{m}_k + \beta\boldsymbol{p}_k\right) \tag{3.40}$$

The NLCG approach generates a sequence of models that are determined:

$$\boldsymbol{m}_{k,j} = \boldsymbol{m}_k + \beta_{k,j}\boldsymbol{p}_k \tag{3.41}$$

where the step size β:

$$\begin{aligned}\beta_{k,0} &= 0\\ \beta_{k,j+1} &= \beta_{k,j} - \frac{\boldsymbol{g}_{k,j}^T\boldsymbol{p}_k}{\boldsymbol{p}_k^T\tilde{\boldsymbol{H}}_{k,j}\boldsymbol{p}_k}\end{aligned} \tag{3.42}$$

The vector $\boldsymbol{g}$ is the gradient: $\boldsymbol{g} = -2\boldsymbol{J}^T\boldsymbol{W}_d^2\left(\boldsymbol{d}-\boldsymbol{d}'\right) + 2\lambda\boldsymbol{L}^T\boldsymbol{L}\boldsymbol{m}$. Whereas the approximate Hessian matrix $\tilde{\boldsymbol{H}}$ is: $\tilde{\boldsymbol{H}} = 2\boldsymbol{J}^T\boldsymbol{W}_d^2\boldsymbol{J} + 2\lambda\boldsymbol{L}^T\boldsymbol{L}$. The conjugate gradient direction $\boldsymbol{p}_k$ is determined by the steepest descent direction:

$$\begin{aligned}\boldsymbol{p}_0 &= -\boldsymbol{C}_0\boldsymbol{g}_0 \\ \boldsymbol{p}_k &= -\boldsymbol{C}_k\boldsymbol{g}_k + \gamma_k\boldsymbol{p}_{k-1}\end{aligned} \tag{3.43}$$

using the Polak-Ribiere technique (Polak, 1971):

$$\gamma_k = \frac{\boldsymbol{g}_k^T\boldsymbol{C}_k\left(\boldsymbol{g}_k - \boldsymbol{g}_{k-1}\right)}{\boldsymbol{g}_{k-1}^T\boldsymbol{C}_{k-1}\boldsymbol{g}_{k-1}} \tag{3.44}$$

The preconditioner $\boldsymbol{C}_k$ is given by:

$$\boldsymbol{C}_k = \left(\eta_k\boldsymbol{I} + \lambda\boldsymbol{L}^T\boldsymbol{L}\right)^{-1} \tag{3.45}$$

where the term η_k is a specified scalar. The application of the preconditioner is effective in steering the gradient vector into a productive search direction (Rodi and Mackie, 2001). The NLCG algorithm keeps track of the best model encountered in the line search:

$$\boldsymbol{m}_{k,best} = \boldsymbol{m}_k + \beta_{k,best}\boldsymbol{p}_k \tag{3.46}$$

The final result of the k-th line search is taken as the best model found:

$$\boldsymbol{m}_{k+1} = \boldsymbol{m}_{k,best} \tag{3.47}$$

Thus, a starting model $\boldsymbol{m}_0$ is given and the next model $\boldsymbol{m}_{k+1}$ can be obtained using the step size $\beta_{k,j}$ in search direction $\boldsymbol{p}_k$. Because the problem is non linear, the line search process is introduced instead of finding only the step length parameter as in the CG method. This line search process avoids computing a large Hessian matrix ($\tilde{\boldsymbol{H}}$ in equation 3.42). A drawback of the NLCG scheme is that it requires more iterations to converge. As it was exposed, the NLCG and CG are closely related, the main difference is that CG method minimizes quadratic cases (*e.g.* equation 3.31) and NLCG non-quadratic cases. Both algorithms avoid the explicitly computation of the Jacobian matrix, only a product of $\boldsymbol{J}$ or $\boldsymbol{J}^T$ with an arbitrary vector is required. As in the NLCG, a preconditioner can also be used in the CG method to speed up the algorithm.

Chapter No. 4

Field Survey

In this chapter the field survey is described. The data set is introduced and the field setup of the applied EM methods is explained. A geological description of San Felipe is summarized. The main tectonic events that occurred in the survey area are also given in this section. Moreover, the hydrogeological background is briefly described.

4.1 Data set

As first stage of the geothermal exploration in San Felipe, a regional geophysical survey was carried out in 2014 within the framework of the project SENER-CONACYT 152823: Evaluation of potential geothermal systems in Baja California. The geophysical survey consisted of Magnetotelluric (MT) and Transient Electromagnetic (TEM) measurements. In total, 17 MT and 17 TEM soundings were recorded, along 4 different profiles (Fig. 4.1; green dots). The coordinates of the soundings can be found in Appendix A (Table A.1). The stations distribution was decided considering the locations of the geothermal surface manifestations and orientation of the geological faults (Fig. 4.1). The manifestations along the shoreline are hot springs and the rest are water wells with high temperature. The distance between neighboring soundings is roughly 4 km. Both methods -MT and TEM- were acquired at the same sites to be able to correct the possible static shift effect on MT data. However, TEM data are also used to map the shallow part of San Felipe subsurface and as constraints for the 3D MT inversion.

Additionally, 5 MT measurements that were acquired in 2007 are also used (Fig. 4.1; purple dots). These 5 MT soundings are already published in a master thesis (Pamplona-Pérez, 2007), where a 2D MT inversion model is derived. Therefore, these additional 5 MT measurements are only included in the 3D MT inversion scheme. Furthermore, field setup of these 5 extra MT stations are not described in this thesis.

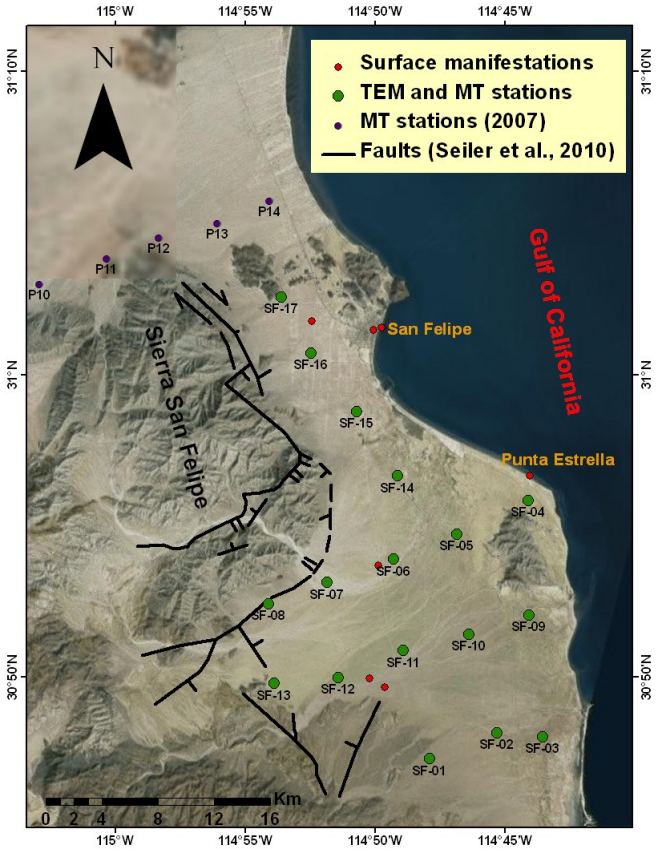

FIGURE 4.1: *Survey area. Location of MT and TEM sites acquired in 2014 are marked with green dots. Red dots represent the geothermal surface manifestations. The 5 additional MT stations taken from Pamplona-Pérez (2007) are marked with purple dots. Geological faults are also shown in the figure. (Map was created with ArcGIS)*

4.1.1 Field setup

The MT soundings were recorded with Metronix/ADU-07 devices (Fig. 4.2). Metronix induction-coil magnetometers and non-polarizable $Pb/PbCl_2$ electrodes with horizontal dipole lengths of 100 m were deployed (Fig. 4.3).

FIGURE 4.2: *Photographies of the devices used during the field campaign. On the left, a Metronix/ADU-07 device is displayed. The right image shows the TerraTEM instrument.*

The TEM measurements were done with a TerraTEM device from Monex Geoscope Ltd (Fig. 4.2). Transient responses were measured between a range from 0.1 ms to 70 ms. A single loop configuration was used, where the same wire works as receiver (Rx) while transmitter (Tx) is off (Nabighian and Macnae, 1991). The effective area of Tx and Rx was of 50 x 50 m^2. The injected current by the transmitter was 9 A.

FIGURE 4.3: *Photographies of the field work. The left image shows the MT setup at the first site, where all the field crew is getting used to the technique. On the right, an induction-coil magnetometer is being deployed. (Photos taken by Martin Pacheco)*

4.2 Geological setting

The basement of survey area is composed by Paleozoic to Mesozoic metamorphic rocks that have been intruded by large volumes of granodioritic to tonalitic batholiths during the Cretaceous (Seiler et al., 2010). These intrusive materials conform the Batholith of Baja California, which are exposed at Sierra San Felipe and Sierra San Pedro Mártir (Fig.4.4).The metamorphic basement and batholitic intrusions were eroded during the Eocene and the Oligocene. The generated sediments and conglomerates from this erosion are overlain by 19-12 Ma old basaltic flows and the San Felipe Tuff Formation (Seiler et al., 2010). These basaltic flows and tuffs are product of volcanic events that occurred during the Miocene. Later on, these units were covered by sediments interlayered with Pleistocene volcanic rocks (Seiler et al., 2010).

4.2.1 Tectonic background

Two important tectonic events took place in the survey area. First one consists of a change from subduction to continental extension during the Miocene, which generated the Gulf of California (Martín-Barajas, 2000). Moreover, the Baja California peninsula was transferred from the North American plate to the Pacific

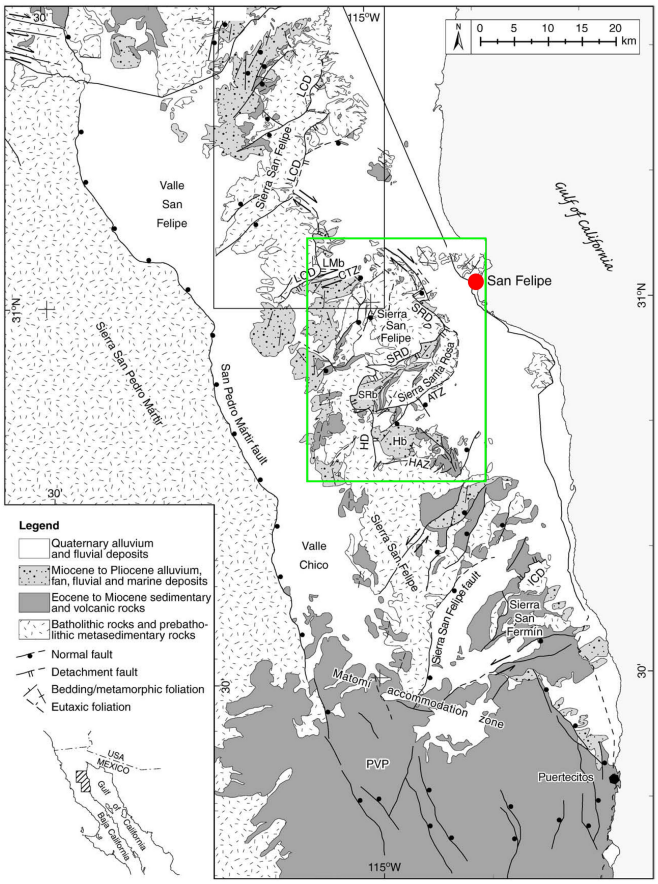

FIGURE 4.4: *Geological map of the survey area, taken from Seiler et al. (2010). San Felipe town is marked with the red dot. The Santa Rosa detachment is abbreviated as SRD and located inside the green box.*

plate (Fletcher et al., 2007). The second event involves the subduction of the Farallon plate under the North America plate during the Oligocene (Atwater, 1970).

The extensional regime caused normal faulting which originated horst and grabens structures, such as Valle San Felipe (Fig.4.4). This basin is delimited by San Felipe fault, on the western part of Sierra San Felipe (Seiler et al., 2010). Figure 4.4 shows the Santa Rosa detachment structure which comprises a normal faulting system that controls the terrain of the eastern area of Sierra San Felipe (Seiler et al., 2010). The detachment juxtaposed the metamorphic basement of Sierra San Felipe under the sediments and volcanic rocks from the Miocene-Pliocene (Seiler et al., 2010).

4.2.2 Hydrogeology

The aquifer located in the survey area is named as San Felipe-Punta Estrella (Fig.4.5). San Felipe-Punta Estrella is an unconfined aquifer and consists of Cenozoic alluvial sediments underlain by intrusive rocks that represent the bedrock

(CONAGUA, 2015).

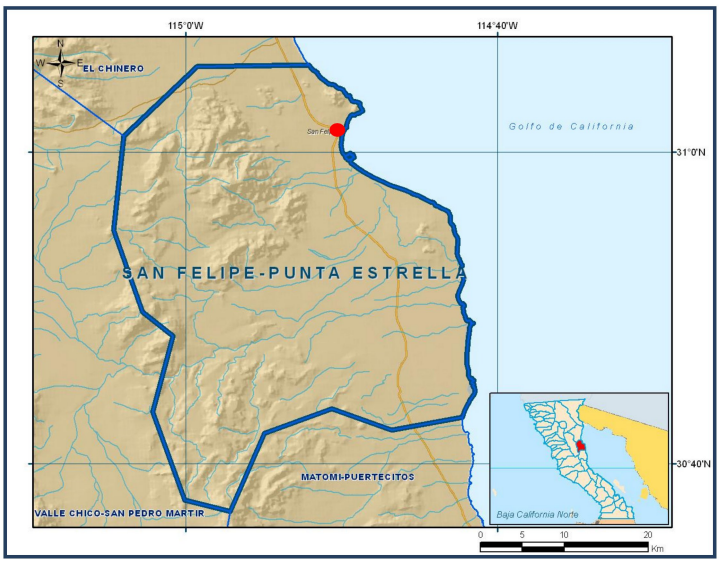

FIGURE 4.5: *Map with the location of San Felipe-Punta Estrella aquifer, taken from CONAGUA (2015). San Felipe town is marked with the red dot.*

According to petrophysical properties of the sediments, the aquifer can be divided into three units (CONAGUA, 2015):

- impermeable unit, consisting of the volcanic intrusive rocks that built the bedrock
- semipermeable unit formed by sediments of fine clayed grains and extrusive igneous rocks
- permeable unit with sediments of different grain sizes, mainly coarse grains

A majority of the wells are pumping the water from the permeable unit which has a thickness from 100 to 150m and lateral continuity (CONAGUA, 2015).

Chapter No. 5

Data processing and analysis

This chapter deals with the processing of measured data. At first, all the procedures applied to TEM data before the subsequent inversion are explained. In regards to the MT data, all the steps that involve the estimation of the Transfer Functions are outlined. A detailed explanation of the used robust processing scheme is given. Dimensionality and directionality analysis of the MT data are also described in this chapter. Finally, static shift effect in the recorded MT data is discussed and corrected.

5.1 Processing of TEM data

The processing steps of TEM data depend of the acquisition characteristics and the used systems. In this regards, the TerraTEM device has an internal stacking algorithm which averages the transient response of a single positive current turn-off and a single negative current turn-off. A maximum of 1024 measurements were stacked at each station.

In Fig. 5.1 a transient is displayed at station SF-03 as an example to demonstrate the data quality. Due to the lack of noise measurements in the survey area, a synthetic error floor is also plotted which is inversely proportional to the square root of the time and approaching 1e-9 V/Am^2 at 1 ms (Swidinsky et al., 2012). This form of noise dependence is common for transient electromagnetics data that are processed and binned in logarithmic time (Munkholm and Auken, 1996). Therefore, data points that reach the error floor were removed before the inversion, *e.g.* t>20 ms at station SF-03 (Fig. 5.1).

As it was mentioned in section 2.3, the current turn-off is not instant. The finite time required to turn the current off is named as ramp-time T_r and it depends primarily on the current, loop size, turns and cable diameter. With the applied acquisition characteristics, the ramp times range from 115 to 120 μs.

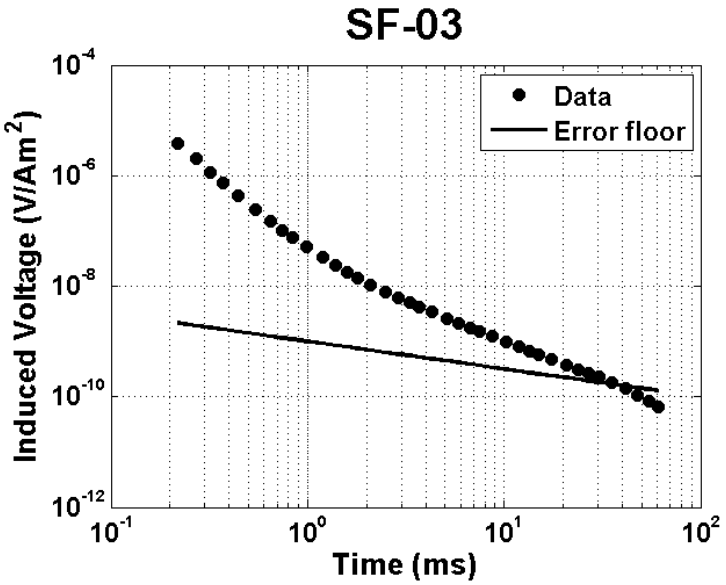

FIGURE 5.1: *Measured induced voltage at station SF- 03. An error floor is also shown, which is inversely proportional to the square root of the time, approaching 1e-9 V/Am2 at 1 ms. Figure taken from Ruiz-Aguilar et al. (2018).*

The current turn-off function is approximated through a linear ramp:

$$I'(t) = I_0(1 - \frac{t}{T_r}), \qquad 0 < t < T_r \tag{5.1}$$

where I_0 is the current before the turn-off. The time derivative of the current ramp is (Fitterman and Anderson, 1987):

$$\frac{\partial I'(t)}{\partial t} = \frac{-I_0}{T_r}, \qquad 0 < t < T_r \tag{5.2}$$

where $\partial_t I'(t)$ is a box car function with width T_r. Thus, the response $U't$ due to a non-ideal turn-off $I'(t)$ is obtained by a convolution of the time derivative of the current ramp function with the unaffected earth response $U(t)$ (Fitterman and Anderson, 1987):

$$U'(t) = \int_{-\infty}^{t} \frac{\partial I'(\tau)}{\partial t} U(t-\tau)d\tau \tag{5.3}$$

The current is normalized by the current I_0, so that $\partial_t I'(t) = -1/T_r$ and therefore:

$$U'(t) = -\frac{1}{T_r}\int_{0}^{T_r} U(t-\tau)d\tau \tag{5.4}$$

Thereby, the effect of the non-zero turn-off time must be considered for a proper data interpretation (Fitterman and Anderson, 1987). For San Felipe data, such effect is considered during the inversion process, where the predicted data is convolved with the ramp function at each inversion step according to the Equation 5.4.

5.2 Processing and analysis of MT data

In this project, the recorded time series at the 17 MT stations were processed with EMERALD software (Ritter et al., 1998; Weckmann et al., 2005; Krings, 2007). The 5 additional MT stations acquired in 2007 were already processed and analyzed by Pamplona-Pérez (2007). As it has been earlier mentioned, the MT data were acquired with Metronix/ADU-07 systems, therefore the data files were translated from the original format to the EMERALD format through a MATLAB script which was implemented on the framework of this thesis.

In general, the processing steps of magnetotelluric data can be summarized as follows:

1. Digital filters are applied to the time series in order to remove cultural noise.
2. If remote reference station exists, synchronization with the time series of such station.
3. Time series of the five components are bandpass filtered into narrow frequency bands.
4. Frequency bands are divided into short segments of a fixed length.
5. Fourier transformation is applied to the segments.
6. Correction for instrument response.
7. Division into different frequency bands around center frequencies that are equally distributed on a logarithmic scale.
8. Averaging of Fourier coefficients in each sub-band.
9. Computation of auto and cross spectra at each event and sub-band.

An inspection of the raw time series must be firstly done to corroborate that all the channels were properly recording and any problem existed (*e.g.* an animal could disconnect the electrodes or coils). Figure 5.2 shows the time series of a selected station where the red box highlights the correlation between B_x and E_y components and the anti-correlation between B_y and E_x components.

Figure 5.3 displays the spectra calculated at one selected station. The strong 60 Hz peak and its harmonics due to the power lines can be distinguished. Hence the importance to apply digital filters in order to remove such noise (*e.g.* notch filter). The time series are bandpass filtered into narrow frequency bands and divided into short segments of a fixed length (*e.g.* 128 samples). Fourier transformation is applied to the segments (events), but they should be previously multiplied by a window function to minimize the spectral leakage effects. After the Fourier transformation, a correction by the instrument response functions is done. The

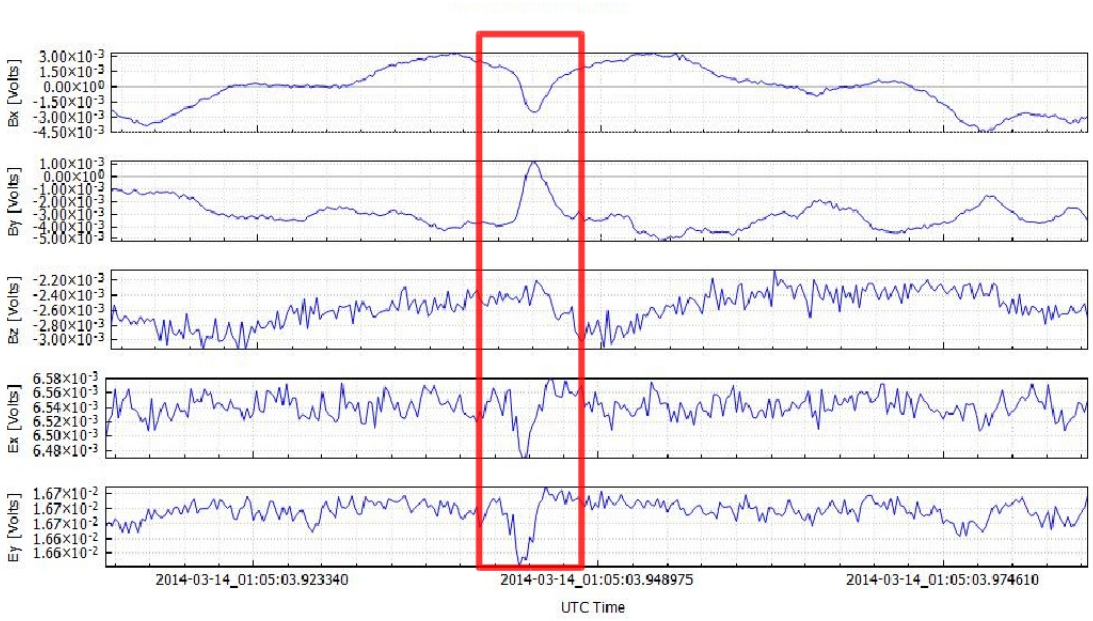

FIGURE 5.2: *Unfiltered time series recorded at station SF-07. The red box highlights the correlation between B_x and E_y components and the anti-correlation between B_y and E_x components.*

Fourier coefficients are divided into different frequency bands around center frequencies that are equally distributed on a logarithmic scale. Finally, the cross and auto spectra are calculated and averaged in each band.

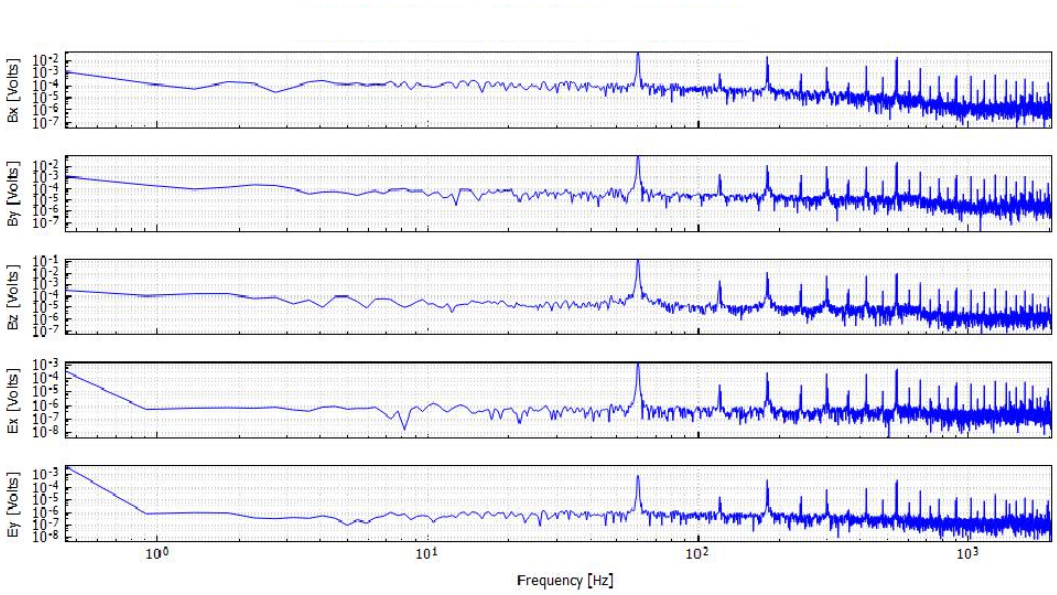

FIGURE 5.3: *Spectra of unfiltered time series recorded with a sampling rate of 4096 Hz at station SF-11. The 60 Hz peak and its harmonics due to the power lines can be distinguished.*

5.2.1 Theoretical aspects of MT data processing

Single site processing

Since the time series are segmented in events, several transfer functions estimations are done. The statistical significance of individual estimates can be improved by calculus of observations, which can be achieved by applying a linear regression in a least square (Krings, 2007).

The equations to calculate the impedance tensor with an additional noise term are:

$$E_x = Z_{xx}B_x + Z_{xy}B_y + \delta E_x \tag{5.5}$$

$$E_y = Z_{yx}B_x + Z_{yy}B_y + \delta E_y \tag{5.6}$$

where E_x, E_y, B_x and B_y are the Fourier spectra of the time series at one frequency. The terms δE_x and δE_y represent the noise on the output channels E_x and E_y. The input channels B_x and B_y are assumed to be free of noise.

Considering the observations of several events, equation 5.5 changes to[1]:

$$\boldsymbol{E}_x = \boldsymbol{B} \cdot \boldsymbol{Z}_x + \delta \boldsymbol{E}_x \tag{5.7}$$

where[2]

$$\boldsymbol{E}_x = \begin{pmatrix} E_{x_1} \\ E_{x_2} \\ \vdots \\ E_{x_n} \end{pmatrix}, \boldsymbol{B} = \begin{pmatrix} B_{x_1} & B_{y_1} \\ B_{x_2} & B_{y_2} \\ \vdots & \vdots \\ B_{x_n} & B_{y_n} \end{pmatrix}, \boldsymbol{Z}_x = \begin{pmatrix} Z_{xx} \\ Z_{xy} \end{pmatrix} \tag{5.8}$$

The problem to minimize is:

$$\min_x \left\| \boldsymbol{B}\boldsymbol{Z}_x - \boldsymbol{E}_x \right\|_2^2 \tag{5.9}$$

where the subscript 2 represents the Euclidean norm. The solution to the minimization problem is given by the least squares estimator:

$$\boldsymbol{Z}_x = \left(\boldsymbol{B}^{T*}\boldsymbol{B} \right)^{-1} \boldsymbol{B}^{T*}\boldsymbol{E}_x \tag{5.10}$$

where T represents the matrix transpose and the asterisk (*) the conjugate complex. After resolving and rearranging the terms, the transfer functions Zxx and Zxy are given by[3]:

$$Z_{xx} = \frac{< B_y^* B_y >< B_x^* E_x > - < B_x^* B_y >< B_y^* E_x >}{< B_x^* B_x >< B_y^* B_y > - < B_x^* B_y >< B_y^* B_x >} \tag{5.11}$$

[1] Similar procedure can also be applied to equation 5.6.

[2] Note that although $\boldsymbol{Z}_x$ is a vector, it is presented in uppercase, bold-italic character.

[3] $< B_x^* B_x >$ is the notation used for cross and auto spectra respectively. These equations are the ones used by EMERALD algorithm.

$$Z_{xy} = \frac{- < B_y^* B_x >< B_x^* E_x > + < B_x^* B_x >< B_y^* E_x >}{< B_x^* B_x >< B_y^* B_y > - < B_x^* B_y >< B_y^* B_x >} \tag{5.12}$$

Similarly for Zyx and Zyy:

$$Z_{yx} = \frac{< B_y^* B_y >< B_x^* E_y > - < B_x^* B_y >< B_y^* E_y >}{< B_x^* B_x >< B_y^* B_y > - < B_x^* B_y >< B_y^* B_x >} \tag{5.13}$$

$$Z_{yy} = \frac{- < B_y^* B_x >< B_x^* E_y > + < B_x^* B_x >< B_y^* E_y >}{< B_x^* B_x >< B_y^* B_y > - < B_x^* B_y >< B_y^* B_x >} \tag{5.14}$$

And for the vertical magnetic transfer functions:

$$T_x = \frac{< B_y^* B_y >< B_x^* B_z > - < B_x^* B_y >< B_y^* B_z >}{< B_x^* B_x >< B_y^* B_y > - < B_x^* B_y >< B_y^* B_x >} \tag{5.15}$$

$$T_y = \frac{- < B_y^* B_x >< B_x^* B_z > + < B_x^* B_x >< B_y^* B_z >}{< B_x^* B_x >< B_y^* B_y > - < B_x^* B_y >< B_y^* B_x >} \tag{5.16}$$

Remote reference processing

Sometimes the transfer functions estimated with the single site processing scheme show various outliers and therefore cannot be further interpreted. In this regards, if B and E are assumed to be affected by noise:

$$B := B_{signal} + B_{noise} \tag{5.17}$$

$$E := E_{signal} + E_{noise} \tag{5.18}$$

the auto spectra of B is:

$$\begin{aligned} < B^* B > &=< (B_{signal}^* + B_{noise}^*)(B_{signal} + B_{noise}) > \\ &=< B_{signal}^* B_{signal} + B_{noise}^* B_{noise} + \underbrace{B_{signal}^* B_{noise}}_{=0} + \underbrace{B_{noise}^* B_{signal}}_{=0} > \\ &=< B_{signal}^* B_{signal} + B_{noise}^* B_{noise} > \end{aligned} \tag{5.19}$$

where the last two terms are canceled because signal and noise are uncorrelated. The equations 5.11-5.16 are biased by the term $(B_{noise}^* B_{noise})$, causing transfer functions with several outliers. Moreover, the cross spectra between B and E is:

$$\begin{aligned} < B^* E > &=< (B_{signal}^* + B_{noise}^*)(E_{signal} + E_{noise}) > \\ &=< B_{signal}^* E_{signal} + B_{noise}^* E_{noise} + \underbrace{B_{signal}^* E_{noise}}_{=0} + \underbrace{B_{noise}^* E_{signal}}_{=0} > \\ &=< B_{signal}^* E_{signal} + B_{noise}^* E_{noise} > \end{aligned} \tag{5.20}$$

This issue can be minimized by using a remote MT site as a reference for the local MT station (Gamble et al., 1979). The remote reference station has to be placed far away from the local noise source, but it has to be located close enough to validate the normal incidence plane wave assumption. Thereby, equations 5.11-5.16 can be expressed as:

$$Z_{xx} = \frac{< B^*_{yR} B_y >< B^*_{xR} E_x > - < B^*_{xR} B_y >< B^*_{yR} E_x >}{< B^*_{xR} B_x >< B^*_{yR} B_y > - < B^*_{xR} B_y >< B^*_{yR} B_x >} \tag{5.21}$$

$$Z_{xy} = \frac{- < B^*_{yR} B_x >< B^*_{xR} E_x > + < B^*_{xR} B_x >< B^*_{yR} E_x >}{< B^*_{xR} B_x >< B^*_{yR} B_y > - < B^*_{xR} B_y >< B^*_{yR} B_x >} \tag{5.22}$$

$$Z_{yx} = \frac{< B^*_{yR} B_y >< B^*_{xR} E_y > - < B^*_{xR} B_y >< B^*_{yR} E_y >}{< B^*_{xR} B_x >< B^*_{yR} B_y > - < B^*_{xR} B_y >< B^*_{yR} B_x >} \tag{5.23}$$

$$Z_{yy} = \frac{- < B^*_{yR} B_x >< B^*_{xR} E_y > + < B^*_{xR} B_x >< B^*_{yR} E_y >}{< B^*_{xR} B_x >< B^*_{yR} B_y > - < B^*_{xR} B_y >< B^*_{yR} B_x >} \tag{5.24}$$

$$T_x = \frac{< B^*_{yR} B_y >< B^*_{xR} B_z > - < B^*_{xR} B_y >< B^*_{yR} B_z >}{< B^*_{xR} B_x >< B^*_{yR} B_y > - < B^*_{xR} B_y >< B^*_{yR} B_x >} \tag{5.25}$$

$$T_y = \frac{- < B^*_{yR} B_x >< B^*_{xR} B_z > + < B^*_{xR} B_x >< B^*_{yR} B_z >}{< B^*_{xR} B_x >< B^*_{yR} B_y > - < B^*_{xR} B_y >< B^*_{yR} B_x >} \tag{5.26}$$

where the subscript R denotes the remote site.

Coherency and phase criteria

A data rejection criteria is based on the bivariate quadratic coherence, which is the ratio of predicted to measured signal energy and is expressed through[4]:

$$r^2 = \frac{Z_{xx} < B_x E^*_x > + Z_{xy} < B_y E^*_x >}{< E_x E^*_x >} \tag{5.27}$$

Coherence values are between 0 and 1, where an ideal coherence is equal to one. In this sense, a coherence limit is given (*e.g.* 0.95) and thus, all the events that are not within the coherence threshold are rejected. In addition, a phase criteria can also be applied to exclude events. For 1D & 2D structures and without noise, the phases of the Z_{xy} component should be in the first quadrant, *i.e.* $0 < \phi_{xy} < \pi/2$ and the phases of Z_{yx} in the third quadrant, *i.e.* $\pi < \phi_{yx} < 3\pi/2$ (Weidelt and Kaikkonen, 1994). Out-of-quadrant phases are interpreted as due to 3D conductive bodies (Ichihara and Mogi, 2009; Thiel et al., 2009; Piña-Varas and Dentith, 2017), electrical anisotropy (Heise and Pous, 2003) and galvanic distortion (Lilley and Weaver, 2003).

[4]For *Ex* as an example.

Robust processing scheme

MT data is normally affected by noise, mainly when the measurements are carried out near to populated areas and therefore the estimated transfer functions show outliers. Junge (1996) defines noise as the part of the data which cannot be explained by a theory. Robust statistics is an useful technique to single out moderate number of data that are not normally distributed (Ritter et al., 1998), and its use in Magnetotellurics leads to estimations of transfer functions with better quality.

The robust processing algorithm implemented in EMERALD software is based in Junge (1990, 1992, 1994) and Ritter et al. (1998). Moreover, Krings (2007) implemented the robust remote reference processing scheme in the software. The main robust estimation is done with two successive algorithms: χ^2 criterion and consistency criterion. Both algorithms minimize the square residual δZ_l for each event l. The initial bivariate equation can be written as:

$$Z_l = a_l X_l + b_l Y_l + \delta Z_l \tag{5.28}$$

where X_l, Y_l and Z_l are the measured components and a_l and b_l the coefficients to be estimated. Thus, the squared residual is given by:

$$|\delta Z_l|^2 = |Z_l - a_l X_l - b_l Y_l|^2 \tag{5.29}$$

The χ^2 criterion

Since δZ_l are normally distributed, $|\delta Z_l|^2$ is described by a χ^2-distribution. Thus, the variance is given by (Junge, 1990):

$$\sigma_{|\delta Z_l|^2} = \sqrt{\frac{2}{v_l - 4}} \cdot \text{median}(|\delta Z_l|^2) \tag{5.30}$$

where v_l is the number of degrees of freedom (*i.e.* number of independent observations). The median-estimator is used as an initial guess for the mean value of $|\delta Z_l|^2$. Then, Huber weights (Huber, 1981) are applied and a new variance of the data is calculated, using the weighted mean instead of the median. Since Huber weights are not sufficient to eliminate the outliers, Tukey weights (Beaton and Tukey, 1974) are also applied.

A linear regression between the logarithm of the residual spectra and the logarithm of the sum of input spectra is computed to obtain a scaling parameter m through:

$$log(|\delta Z_l|^2) = m \cdot log(X_l X_l^* + Y_l Y_l^*) + n \tag{5.31}$$

Thus, m is used to correct the original residuals:

$$|\delta Z_l'|^2 = |\delta Z_l|^2 \cdot (X_l X_l^* + Y_l Y_l^*)^{-m} \tag{5.32}$$

A subsequent calculation of a new weighted mean and variance is done to better estimate the degrees of freedom for the distribution of the squared residuals:

$$v_{\chi^2} = 2\left(\frac{\overline{<\delta Z_l'^2>}}{\sigma}\right) + 4 \tag{5.33}$$

In addition, z-transformation of the bivariate coherence (eq. 5.27) is calculated through Junge (1994):

$$\begin{aligned} z_r &= \operatorname{arctanh}(r) \\ &= \operatorname{arctanh}\left(\sqrt{\frac{a_l < X_l^R Z_l^* > + b_l < Y_l^R Z_l^* >}{Z_l Z_l^*}}\right) \end{aligned} \tag{5.34}$$

with the variance:

$$\sigma_{zr}^2 \approx \frac{1}{v-4} \tag{5.35}$$

The z-transformed values are weighted by Huber and Tukey weights. The degrees of freedom of the original distribution are estimated through the variance $\sigma_{\frac{2}{z_r}}$, which is calculated from the weighted distribution by:

$$v_{ztr} = \frac{1}{\sigma_{\frac{2}{z_r}}} + 4 \tag{5.36}$$

If the number of degrees of freedom in an estimation is high, the approximation can be close to undisturbed distribution. Therefore a weights selection is done either from the χ^2 criterion or from the z-transformation, depending which procedure yields in a higher value of degrees of freedom (Krings, 2007). The results of the robust sum of auto and cross spectra are calculated using the selected weights through:

$$< X^* Y >_{robust} := \sum_{i=1}^{N} (w_l X_i^* Y_i) \tag{5.37}$$

where the w_l are the Tukey weights calculated at each event l.

Consistency criterion

To distinguish the actual induction processes and correlated noise, a consistency criterion is applied. Thereby, the residuals are now calculated by:

$$< |\delta Z_l|^2 > = < |Z_l - aX_l - bY_l|^2 > \tag{5.38}$$

The transfer functions are globally estimated, *i.e.* they are averaged over all events. Huber weights and subsequent adjustments of auto and cross spectra with the predicted values after Egbert and Booker (1986) are applied. Thus, the transfer functions are robust estimated with the new spectra. If the relative difference of the transfer functions before and after the robust adjustment is above a given threshold, the steps are repeated up to a maximum number of iterations (Krings, 2007). The Tukey weights are applied at least in one iteration, if the maximum number of iterations is not reached yet (Krings, 2007).

5.2.2 Transfer Functions

Due to logistical reasons, a proper remote reference MT site was impossible to settle down during the field survey. However, three stations were always recorded at the same time and therefore a robust remote reference (RR) processing scheme was possible to apply. Depending of the affection by noise of the MT station used as remote reference, data processed with RR scheme sometimes showed better quality than data processed with single site scheme. In this way, the transfer functions used for further interpretations were either estimated with robust remote reference or single site scheme.

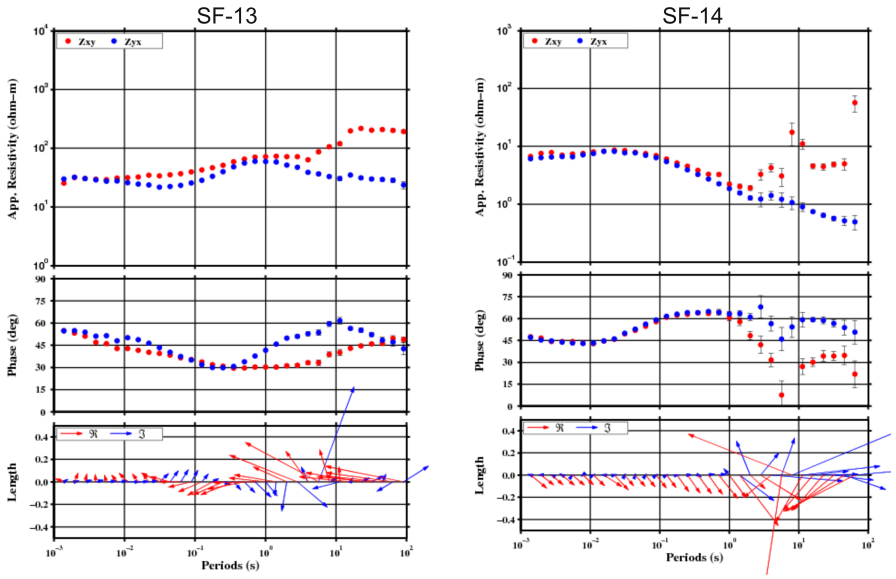

FIGURE 5.4: *Transfer functions obtained after processing the time series at stations SF-13 and SF-14. SF-13 data was processed with a robust single site scheme and SF-14 data with a robust remote reference scheme.*

Results of the robust processing scheme are shown in Fig. 5.4 at two selected stations to illustrate the data quality. Apparent resistivity and phase curves of the off-diagonal impedance tensor elements and induction vectors are displayed. Data of station SF-13 were processed with single site scheme, whereas data of station SF-14 with remote reference scheme. At SF-13, a slight noise affection can be distinguished around 10 s. At SF-14, the affection by noise in the so-called dead band is clearly visible. In general, the MT stations located at the western part of the survey area are less affected by cultural noise (*e.g.* SF-13). Because of the closeness to San Felipe town, the MT sites located at the northern part are the most affected by noise (*e.g.* SF-14).

Figure 5.5 displays the real part of the induction vectors at all stations for 4 different periods. Since a vertical magnetic field component occurs only in the vicinity of horizontal electrical conductivity gradients, the induction vectors can be used to indicate the presence or absence of lateral variations in conductivity (Weaver, 1994). In this thesis, the real part of the induction vectors are plotted in the Wiese

convention (Wiese, 1962), therefore they point away from a conductor where the electric currents have their maximum concentration.

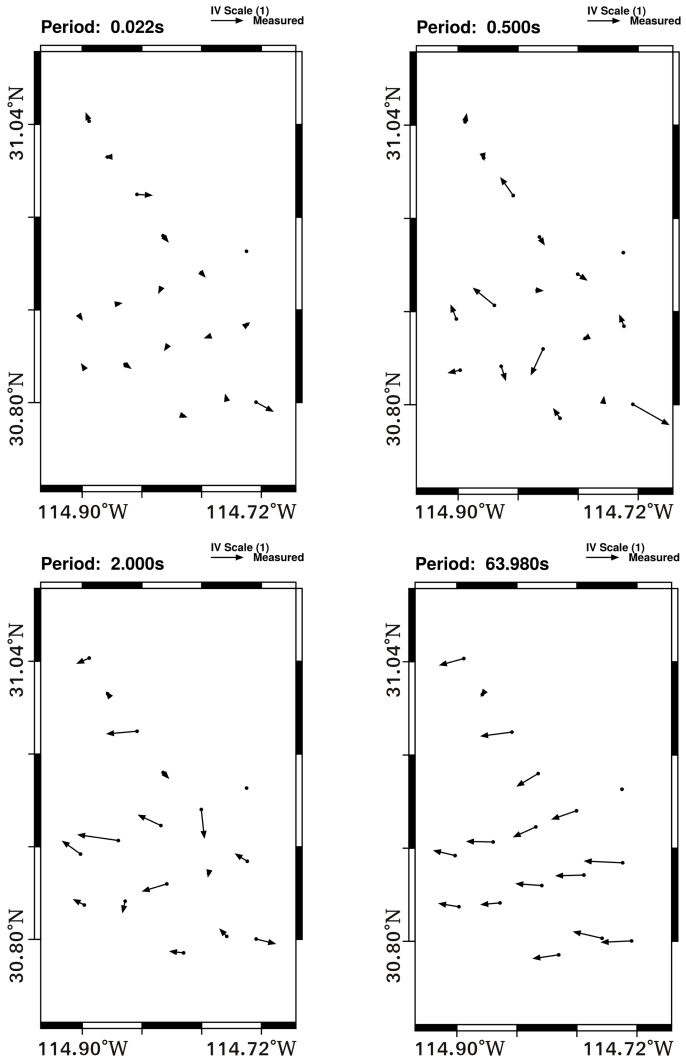

FIGURE 5.5: *Real part of the induction vectors at the acquired stations for different periods using Wiese convention. The dot represents station SF-04, which is masked because it is severely affected by noise.*

At shorter periods (< 0.022 s) the length of the induction vectors is almost zero at all stations, except for a few of them that might be affected by local features and/or noise. From 0.5 to 2 s, the amplitude of the induction vectors increase and they seem to be pointing away from a conductor located in the central part of the survey area. Moreover, the induction vectors at the southeastern station have roughly the same direction than at shorter periods, which indicate that they are pointing away from a conductor. This conductor has a NE-SW orientation at shorter periods (*e.g.* at 0.022 and 0.5 s) and N-S at longer periods (*e.g.* 2 s). At periods > 63.98 s, the induction vectors at all stations are pointing to the west, indicating the presence of the conductive Gulf of California and its underlying

sediments.

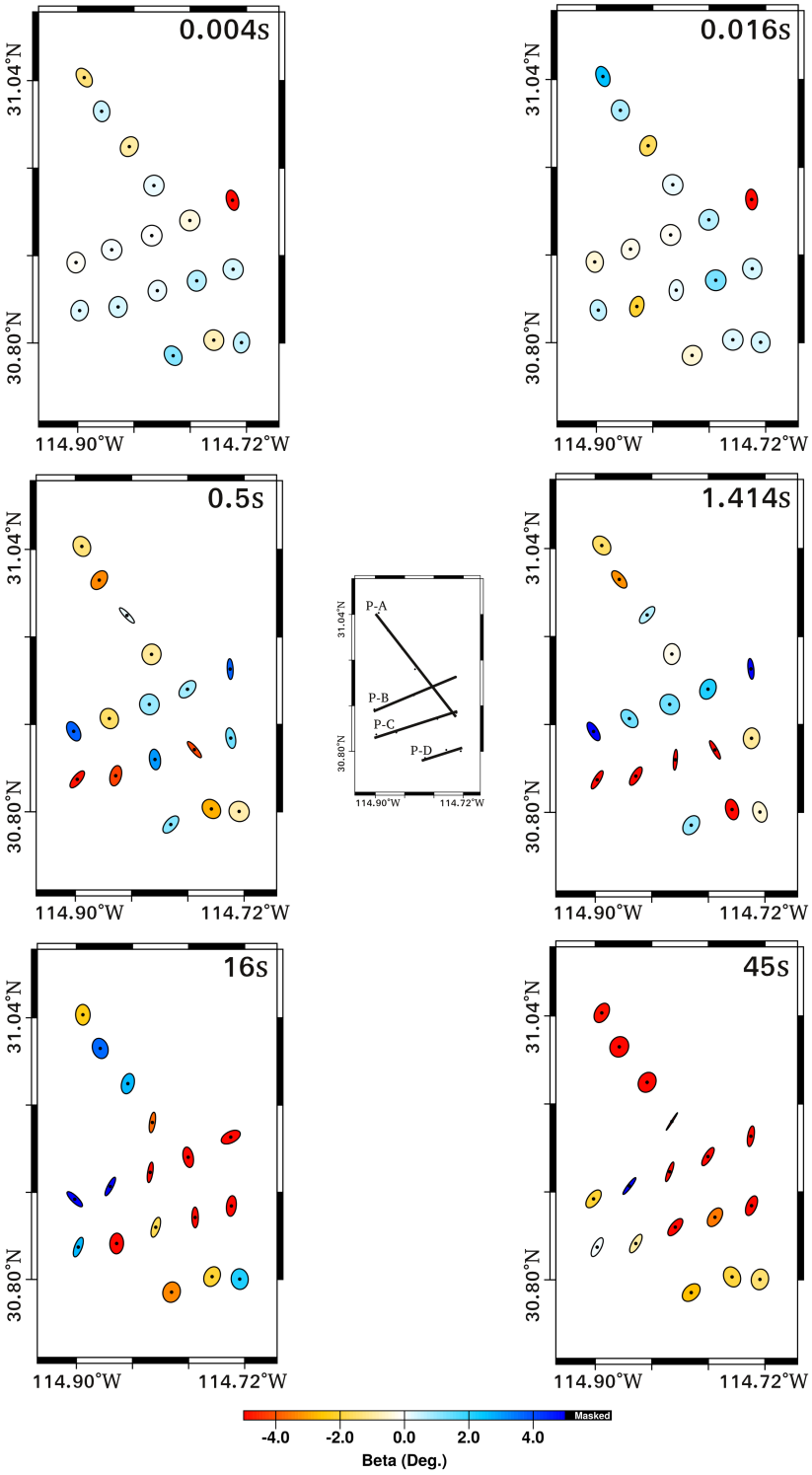

FIGURE 5.6: *Phase tensors at all acquired stations for different periods.*

5.2.3 Dimensionality analysis

In order to analyze the dimensionality of subsurface structures the Magnetotelluric phase tensor was used, which is not affected by galvanic distortion (Caldwell et al., 2004). The β -value and the ellipticities of the phase thensor can define the dimensionality. In fig. 5.6, the phase tensors at all the stations are displayed for six different periods. A circle represents that the subsurface structure is 1D. A two dimensional structure is represented by an ellipse with $\beta = 0$; the principal axis of the ellipse is either perpendicular or parallel to the regional strike direction. For a 3D case, the phase tensor is also represented by an ellipse, but β deviates from zero. In this thesis, values of $\beta < -2$ & $\beta > 2$ are used to determine if the structure is 3D.

To clearly analyze and explain the phase tensors, the stations are grouped in four different profiles which can be seen in the central map of Fig. 5.6. At 0.004 s of period, all phase tensors are represented approximately as circles, indicating a 1D structure. At 0.016 s of period, phase tensors of profile A (P-A) suggest a 1D structure. The profile B (P-B) phase tensors are represented as circles, indicating a 1D structure. Phase tensors of profile C (P-C) are primordially suggesting a 1D structure. The profile D (P-D) phase tensors indicate a 1D structure due to their circular shapes as well. At the rest of periods, all the phase tensors are mainly represented by ellipses with $\beta < -2$ & $\beta > 2$, therefore they indicate a 3D structure.

Basically the dimensionality analysis shows that at all the profiles, phase tensors indicate a 1D structure for periods < 0.5 s and a 3D structure for periods > 0.5 s.

5.2.4 Geo-electric strike analysis

Although the dimensionality analysis exposed that subsurface structures are mainly 1D and 3D, a subsequent strike angle analysis is done to decouple the impedance tensor in TE and TM mode. This analysis is essential for a 2D interpretation where data is rotated into the strike direction to set the measurement axis parallel and normal to the geo-electric strike. Phase tensors were also used to estimate the strike angle which dominates at each profile. The location of the profiles is shown in the central map of Fig. 5.6. To resolve the $\pm 90°$ ambiguity, induction vectors information was used.

Figures 5.7 and 5.8 display the parameters estimated from the phase tensors as functions of periods and grouped by profiles. Outliers were masked. For ellipticities greater than 0.15, the azimuth of phase tensor maximum is calculated. At profile A (Fig. 5.7), azimuth values from -45° to -35° are distinguished between 0.1 and 10 s of period. A value of -38° was chosen and after resolving its ambiguity, a strike direction of 52° is estimated. At profile B (Fig. 5.7), azimuth values around 45° are displayed between 1 and 100 s. After resolving the ambiguity, a strike direction of -47° was estimated. At profile C (Fig. 5.8), azimuth values around 45° are distinguished between 0.1 and 1 s. Comparable to profile B, a strike direction of -48° was estimated. At profile D (Fig. 5.8), azimuth values around 45°

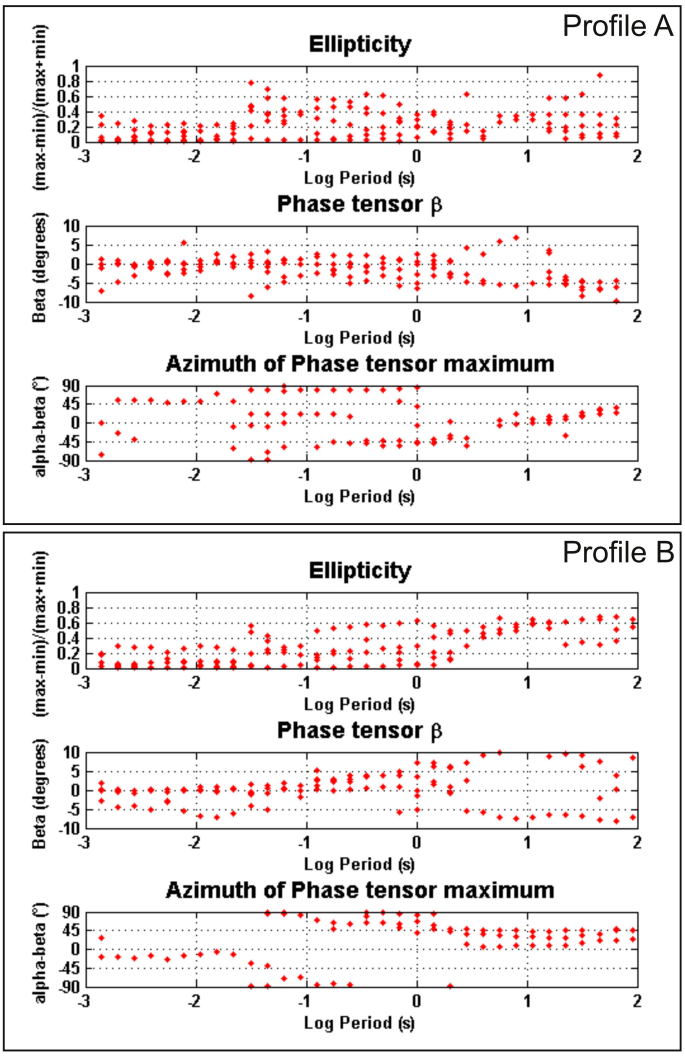

FIGURE 5.7: *Parameters calculated from the phase tensors at profiles A and B. The strike direction is obtained from the azimuth of phase tensor maximum.*

exist between 0.1 and 1 s. Therefore, a strike direction of -40° was estimated after resolving the ambiguity.

5.2.5 Static shift correction

A common problem in Magnetotellurics is the static shift effect due to shallow heterogeneities, which can lead to a misinterpretation of the MT data. Static shift effect causes a shift of the apparent resistivity curves by a scale factor. Phase curves are not affected because the static shift effect is time-independent and produces only a reduction or amplification of the total electric field without changing its phase. One method for measuring the static shift is a controlled-source measurement of the magnetic field because unlike the electric field, the magnetic field is relatively unaffected by surface heterogeneities (Sternberg et al., 1988). Sternberg et al. (1988) & Pellerin and Hohmann (1990) proposed the use of transient

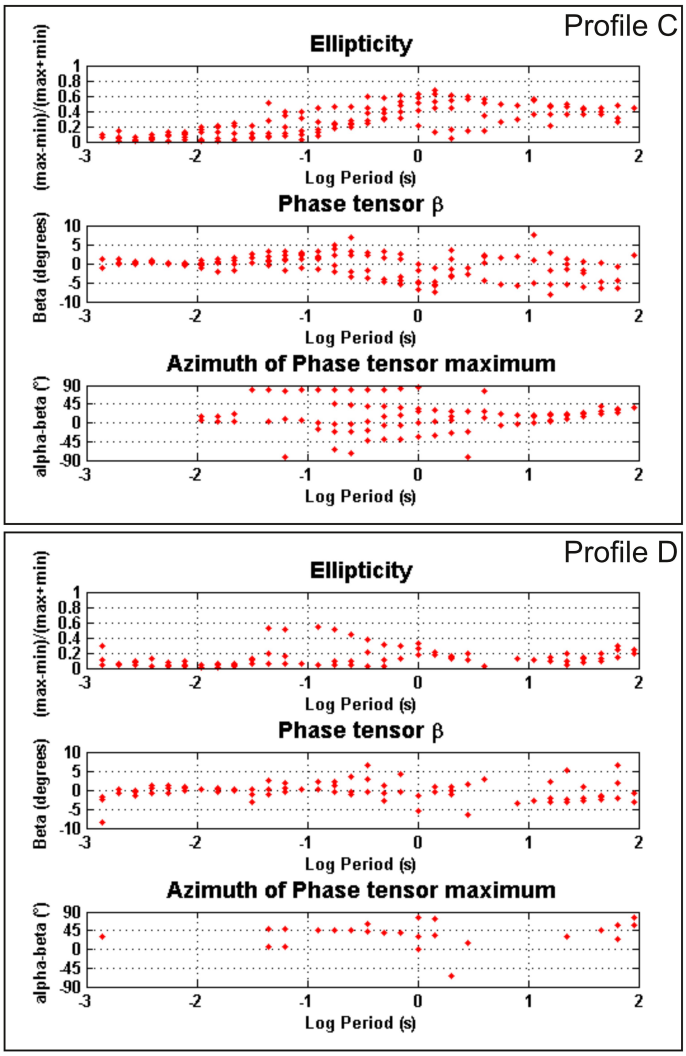

FIGURE 5.8: *Parameters calculated from the phase tensors at profiles C and D. The strike direction is obtained from the azimuth of phase tensor maximum.*

electromagnetic (TEM) data to correct the static shift effect in the MT data. However, Cumming and Mackie (2010) demonstrated that TEM can be an ineffective method of correcting MT static shift in areas where thick, resistive rocks cover most of the surface. Nevertheless, San Felipe surface is mainly cover of alluvial sediments which do not show such high resistivities. Hence TEM data was acquired at the same MT locations for the static shift correction on the frame of this project.

To correct the static shift effect, 1D inversion is firstly applied to TEM data. Thus, a 1D MT Forward calculation is done to the inverse model which was obtained after the inversion of TEM data. These synthetic data are now compared to the MT data. Finally, the observed apparent resistivity curves are shifted to the same position of the synthetic apparent resistivity curves. Figure 5.9 illustrates the static shift correction at one selected station. The non-corrected apparent resis-

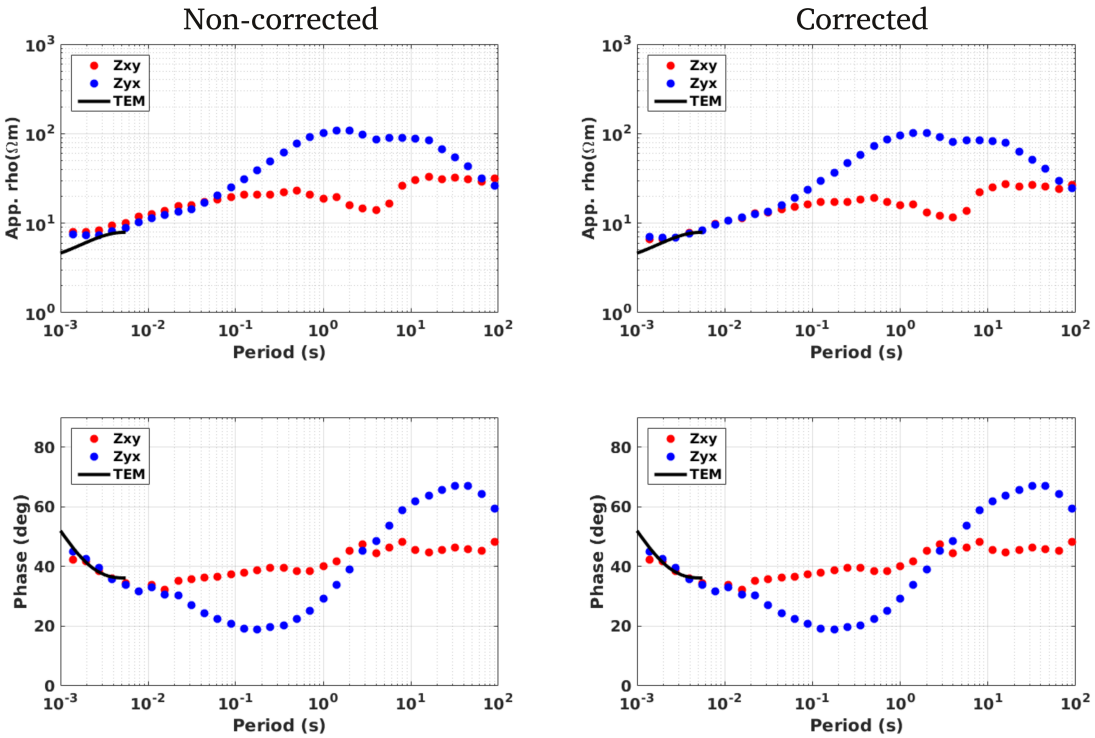

FIGURE 5.9: *Example of static shift correction at station SF-09. Apparent resistivity and phase curves before the static shift correction (left panel) and after applying the static shift correction (right panel).*

tivity curves (top image) are slightly shifted from each other at shorter periods (< 0.01 s). The synthetic apparent resistivity calculated from the 1D TEM inversion model is also plotted. To select the minimum frequency for applying the MT forward calculation, depths of investigation after Spies (1989) were taking into account. In this case, the 1D MT Forward calculation was done for frequencies between 1000 and 180 Hz. A slight shift exists between the observed apparent resistivity curves (both components) and the synthetic (TEM) apparent resistivity curve in Fig. 5.9 (left panel). In Fig. 5.9 (right panel), the corrected apparent resistivity curves are shown; the xy component was shifted by a factor of 0.832, while the yx component by a factor of 0.942.

Chapter No. 6

3D Modeling studies

This chapter treats with 3D MT modeling investigations using ModEM software (Kelbert et al., 2014). Synthetic model studies are important tools for testing newly developed modeling and inversion codes, configuring field studies and analyzing the efficiency of geophysical methods for exploration projects (Erdoğan and Candansayar, 2017). In this regards, modeling studies were carried out to investigate the detectability of geothermal anomalies with Magnetotellurics and for testing the influence of the field survey configuration applied in San Felipe. A possible coast effect in MT data of San Felipe is also investigated due to the proximity of the survey area to the gulf of California. Furthermore, the impact of the input parameters for the 3D MT inversion with ModEM software is analyzed with synthetic data. Additional modeling investigations are described in the Appendix G.

6.1 3D MT forward modeling

In the 3D induction problem, it is assumed that the source field is horizontal and uniform, although theoretically the source field can have an arbitrary geometry (Meqbel, 2009; Weaver, 1994). In a 3D case, the conductivity of the earth varies in three directions $\sigma(x, y, z)$. The solution of Maxwell's equations in 3D is numerically obtained from (Egbert and Kelbert, 2012):

$$\nabla \times \nabla \times \boldsymbol{E} + i\omega\mu\sigma\boldsymbol{E} = 0 \tag{6.1}$$

or in terms of magnetic fields (Egbert and Kelbert, 2012):

$$\nabla \times \frac{1}{\sigma}\nabla \times \boldsymbol{H} + i\omega\mu\boldsymbol{H} = 0 \tag{6.2}$$

The solution to these equations is obtained for the three components of the vector field, either (E_x, E_y, E_z) or (H_x, H_y, H_z). Staggered grid finite difference (FD) or

finite element (FE) are the most commonly used methods for solving equation 6.1. In ModEM algorithm, the solution is done for $\boldsymbol{E}$ with FD. The finite differences method is used to numerically solve Maxwell's equations on a staggered Yee-grid (Yee, 1966). A primitive cell of a Yee-grid is displayed in Fig. 6.1. The total 3D grid of the model space is constructed by a number of $M = N_x \cdot N_y \cdot N_z$ cells, where N_x, N_y and N_z represent the discretization along x, y and z, respectively. This leads to a system of $3M$ complex-valued linear equations with respect to the electric field values along the mesh edges.

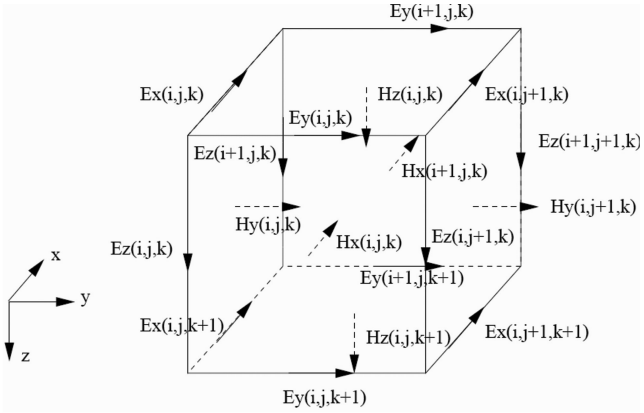

FIGURE 6.1: *Primitive cell of the staggered Yee-grid used in the finite difference method to solve the 3-D MT forward problem. The discrete electric field vector components are defined along the edges, whereas the magnetic components are defined on the cell faces. Figure taken from Kelbert et al. (2014).*

After the grid discretization, the application of finite differences technique yields a system of equations for a given period or frequency (Siripunvaraporn, 2011):

$$\boldsymbol{S}\boldsymbol{e} = \boldsymbol{b} \tag{6.3}$$

where $\boldsymbol{e}$ represents the unknown internal electric fields and $\boldsymbol{b}$ is a vector containing the terms associated with the boundary electric fields. For 3D problems, the coefficient matrix $\boldsymbol{S}$ is relatively large and almost impossible to solve with any direct methods (Streich, 2009). Therefore, it is usually solved with iterative solvers, as the quasi minimum residual method (Siripunvaraporn et al., 2002; Kelbert et al., 2014). A divergence correction is intermittently imposed inside the iterative solver. After obtaining the interior electric fields, the surface impedance responses can be obtained from a linear combination of a vector associated at a measurement site and the computed electric fields (Siripunvaraporn, 2011).

6.2 Geothermal resistivity anomaly

The classical conceptual model of a geothermal reservoir has been proposed and investigated by Pellerin et al. (1996). In that publication, a numerical 3D forward modeling was done to demonstrate the effectiveness of Magnetotellurics to

characterize such types of anomalies. In this sense, a similar investigation is presented. Moreover, the capability of 3D MT inversion to reconstruct the geothermal anomalies is investigated.

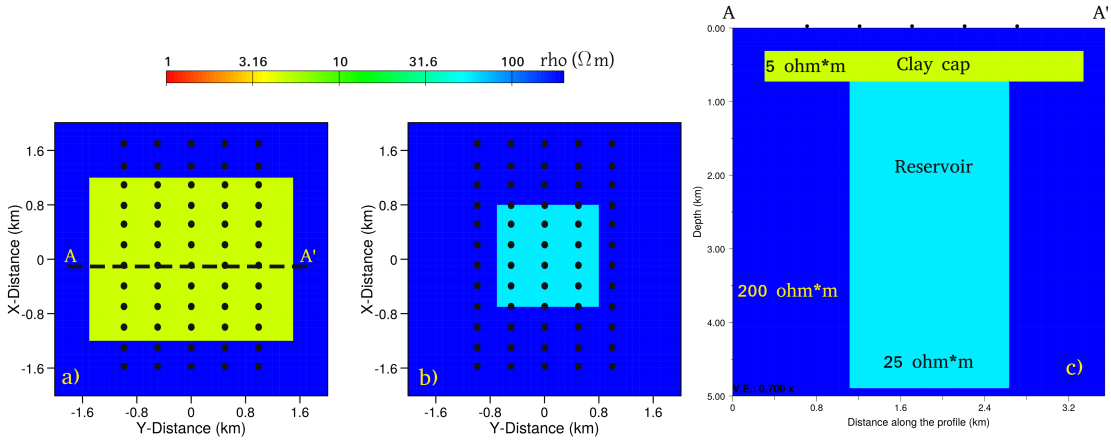

FIGURE 6.2: *Geometry of the geothermal model. MT stations are marked with black dots. (a)Plan view of the clay cap. (b)Plan view of the reservoir. (c)Cross section.*

In Fig. 6.2, the 3D resistivity model simulating the classical conceptual geothermal reservoir is shown. The 3D model consists of a 5 Ωm clay cap over a 25 Ωm reservoir, embedded in a 200 Ωm half-space. The clay cap has dimensions of 2 x 3 x 0.415 km and the reservoir of 1.5 x 1.5 x 4.167 km (Fig.6.2). A total of 60 MT stations were located along 5 different N-S profiles. The separation between stations is of 300 m and 500 m in the N-S and E-W direction, respectively. The 3D finite difference grid used for the model discretization contains 54 x 50 x 46 nodes in the x, y and z directions, respectively. In the central portion of the mesh, the cells were 100 m sided. The first vertical layer has a thickness of 15 m and the subsequent layers were increased by a factor of 1.2. Thus, a 3D MT forward modeling was applied to the described model. The four components of the impedance tensor and the two VTF components were calculated for 25 frequencies between 1000 Hz and 0.001 Hz.

The calculated data was used to perform a 3D inversion. Data errors were set to 5% of $|Zxy * Zyx|^{1/2}$ for the impedance tensor elements and a constant value of 0.05 for the VTF. A 100 Ωm starting model was used for the inversion, with the same discretization utilized for calculating the synthetic data. The result of the 3D inversion can be seen in Fig.6.3 as resistivity depth slices, where the actual position of the clay cap and reservoir are outlined with the white lines. The final RMS is of 0.999. The figure clearly shows that the 3D inversion detects the clay cap structure at depths from 0.312 to 0.727 km. However, the reservoir is not well delimited. At depths from 0.727 to 1.922 km, the influence of the conductive clay cap can still be seen. The slightly more resistive reservoir can only be assumed at depths from 1.922 to 3.375 km. The actual reservoir is located up to a depth of 4.894 km. However the inversion could not recover it at greater depths than

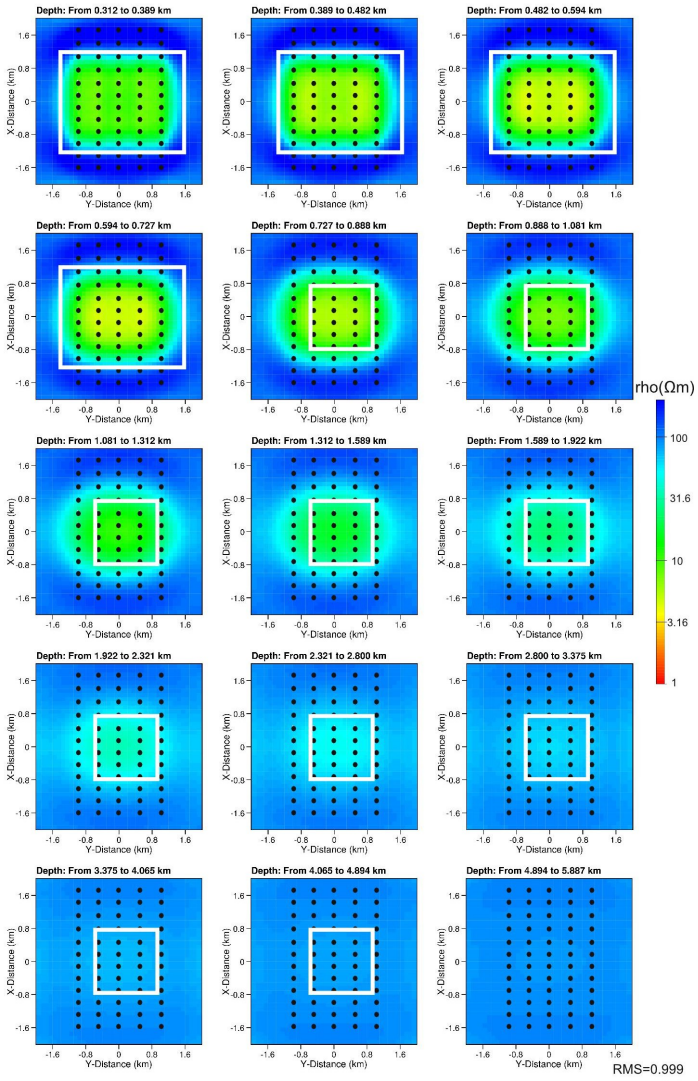

FIGURE 6.3: *Results of the 3D inversion to the synthetic data shown as resistivity depth slices. MT stations are marked with black dots. White lines represent the actual position of the clay cap and reservoir.*

3.375km.

Figure 6.4 displays a profile extracted from the 3D inversion model, actual position of the clay cap and reservoir are again shown with white lines. The figure demonstrates that Magnetotellurics is not capable to detect the whole geothermal reservoir. Nevertheless, MT can map the conductive clay cap and the transition to the reservoir. Moreover, the electrical anomaly arising from a deep, hot reservoir is caused by electric charge accumulation at resistivity boundaries (Pellerin et al., 1996). The above mentioned can be distinguished in the central part of the profile and at depths from $\sim$ 0.5 to $\sim$ 2 km, where a resistivity transition between $\sim$ 3 and $\sim$ 70 Ωm is observed.

In addition, a forward calculation was done to an identical synthetic model but without reservoir. A comparison between MT responses of the models with and

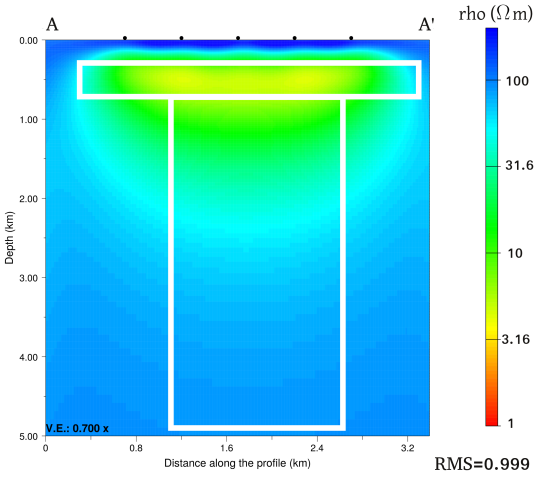

FIGURE 6.4: *Cross section extracted from the 3D resistivity inverse model. Location of the profile can be seen in Fig.6.2. MT stations are marked with black dots. White lines represent the actual position of the clay cap and reservoir.*

without reservoir is shown in Fig. 6.5 for a site located at the central part of the clay cap. Differences are more notorious in the apparent resistivity curves, where the relative difference is 5.94% at the xy component and 6.46% at the yx component. Whereas the phases show a relative difference of $\sim$ 1% at both components. It can be concluded, therefore, that the reservoir does not have a significant effect on the MT data.

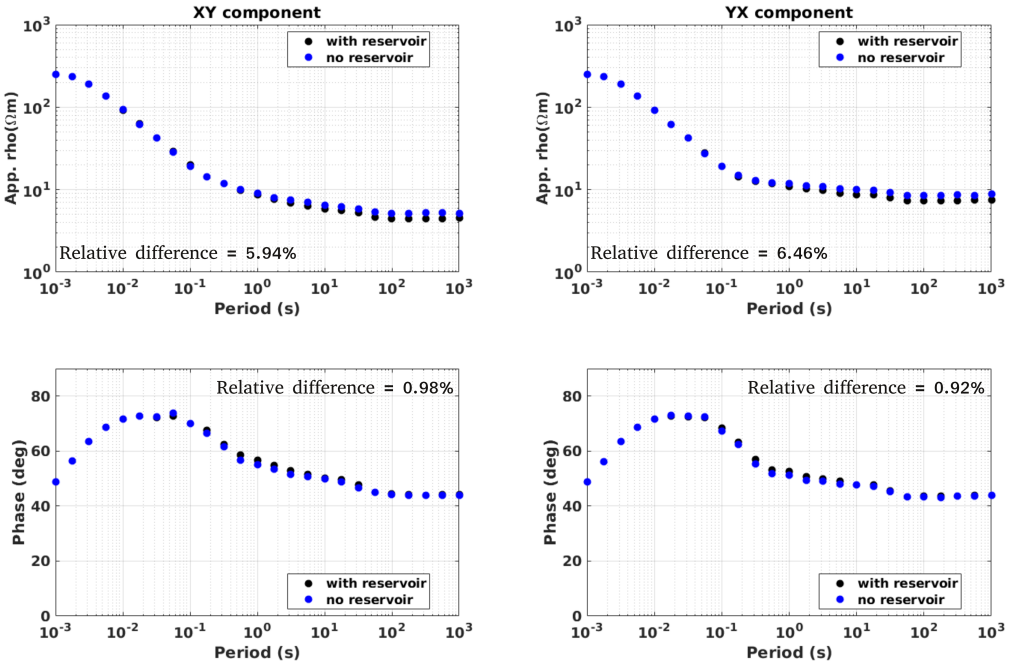

FIGURE 6.5: *Comparison of the MT transfer functions obtained from a forward calculation of the synthetic model with reservoir (see Fig. 6.2) and without reservoir, at a MT station located in the central part of the clay cap.*

Despite the poor detection of the reservoir structure, this modeling investigation shows that Magnetotellurics can characterize a geothermal anomaly. Furthermore, its ability to accurately image the clay cap is important to determine upflow and outflow areas, and thus, locate a suitable drilling site.

6.3 Different grid discretization

This study was motivated to investigate the influence of the grid discretization when the separation between the MT stations is wide and irregular, as is the case for the acquired data (4 km of separation). In this sense, a simple 3D resistivity model was created where a 1 Ωm conductive block structure is embedded in a 100 Ωm host geology (Fig.6.6c).

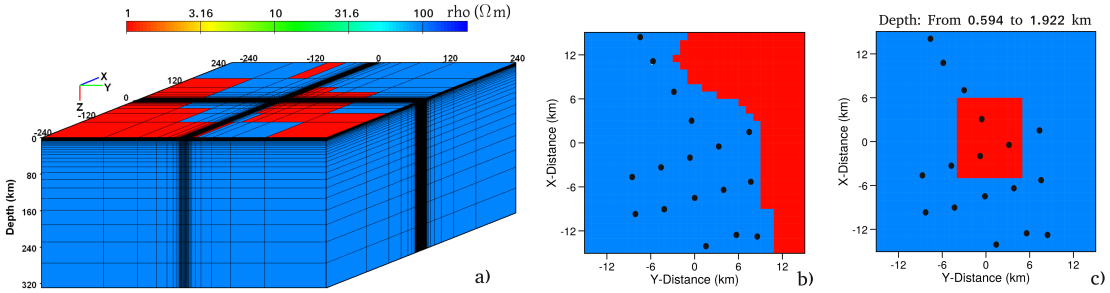

FIGURE 6.6: *(a)Entire model overview, where the Pacific ocean (left side) and gulf of California (right side) are included with a resistivity of 0.3 Ωm. (b)Plan view of the survey area at the sea level. gulf of California can be distinguished in the right part. (c)Plan view of the conductive block structure (1 Ωm) embedded in a 100 Ωm host geology.*

The conductive body has dimensions of 11 x 9 x 1.328 km. In order to represent the same conditions that exist in San Felipe area, the gulf of California and Pacific ocean are included in the model (Fig.6.6a-b), whose bathymetry was taken from the American agency NOAA (National Oceanic and Atmospheric Administration). MT sites were placed at the actual coordinates of the acquired stations. The 3D model consists of 46 x 34 x 46 nodes, in the x, y and z directions, respectively. The grid cells containing the stations are 1000 m sided. The first vertical layer has a thickness of 15 m and the subsequent layers were increased by a factor of 1.2. Thereby, a 3D forward modeling was applied to the described model. The full impedance tensor elements and VTF components were calculated for 21 frequencies in the range from 1000 Hz to 0.01 Hz.

Afterwards, the synthetic data were used to perform 3D inversion with three starting models which were differently discretized in the central part, where the MT sites are located. Thus, starting models were 200, 500 and 1000 m sided. All of them consist of a 10 Ωm half-space including the resistivity of Pacific ocean

and gulf of California (0.3 Ωm). Data errors were set to 5% of $|Zxy * Zyx|^{1/2}$ for the impedance tensor elements and a constant value of 0.05 for the VTF. Same input parameters and dataset were used for the three inversion runs.

Figure 6.7 displays the 3D inversion results of the model with 200 m sided cells, as resistivity depth slices. The actual position of the conductive block is marked with white lines. The obtained RMS was of 1.009. The figure shows that the

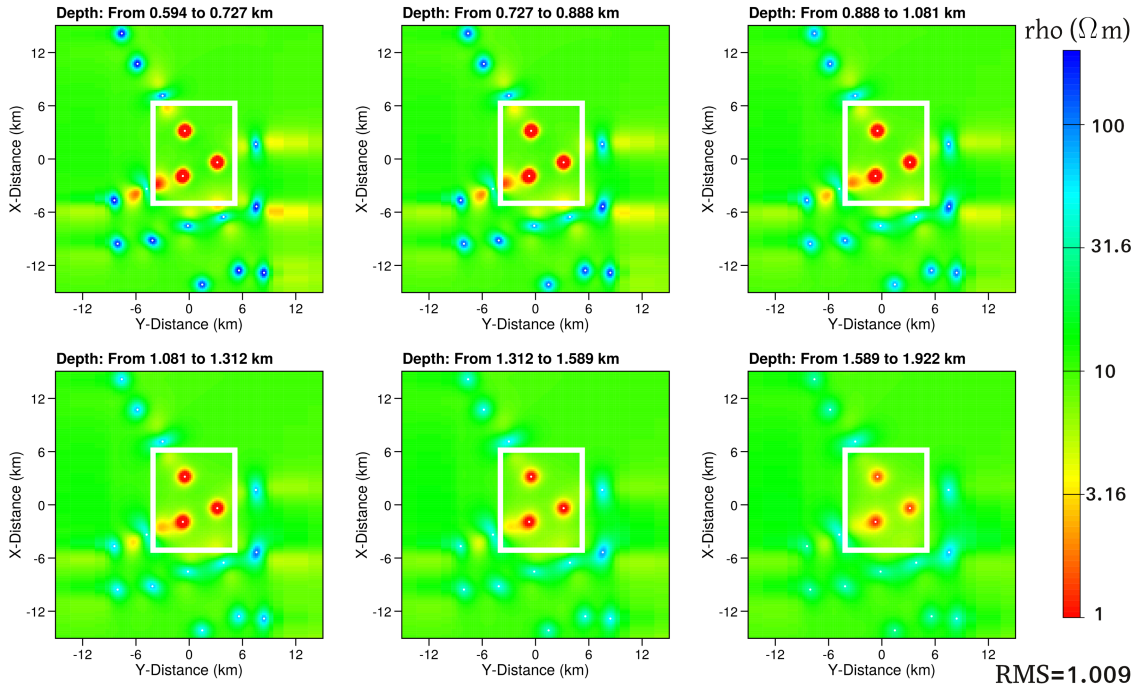

FIGURE 6.7: *Results of the 3D inversion to the model with cells 200 m sided presented as resistivity depth slices. MT sites are marked with white dots. White lines represent the actual position of the conductive block body.*

conductive body was not retrieved. Instead, three small conductors under the stations where the anomaly is located (white lines) can be distinguished. Besides, small resistive bodies can also be seen under the rest of stations in place of the host geology.

In Fig. 6.8, the results of the 3D inversion to the model with cells 500 m sided are shown, as resistivity depth slices. Reached RMS is 0.981. The white lines indicate the actual position of the conductive anomaly. In this case, the conductor was partially recovered, but still can be distinguished that three structures of 1 Ωm are obtained under the MT sites. Resistive bodies are detected under the rest of stations instead of the totality of host geology, but they are bigger than in the inverse model with cells 200 m sided.

The 3D inversion results of the model with cell 1000 m sided are displayed in Fig. 6.9, also as resistivity depth slices with a RMS of 1.03. The actual position of the conductive block is represented with white lines. With this discretization, it was possible to better retrieve the conductive anomaly. Only the northeast corner of

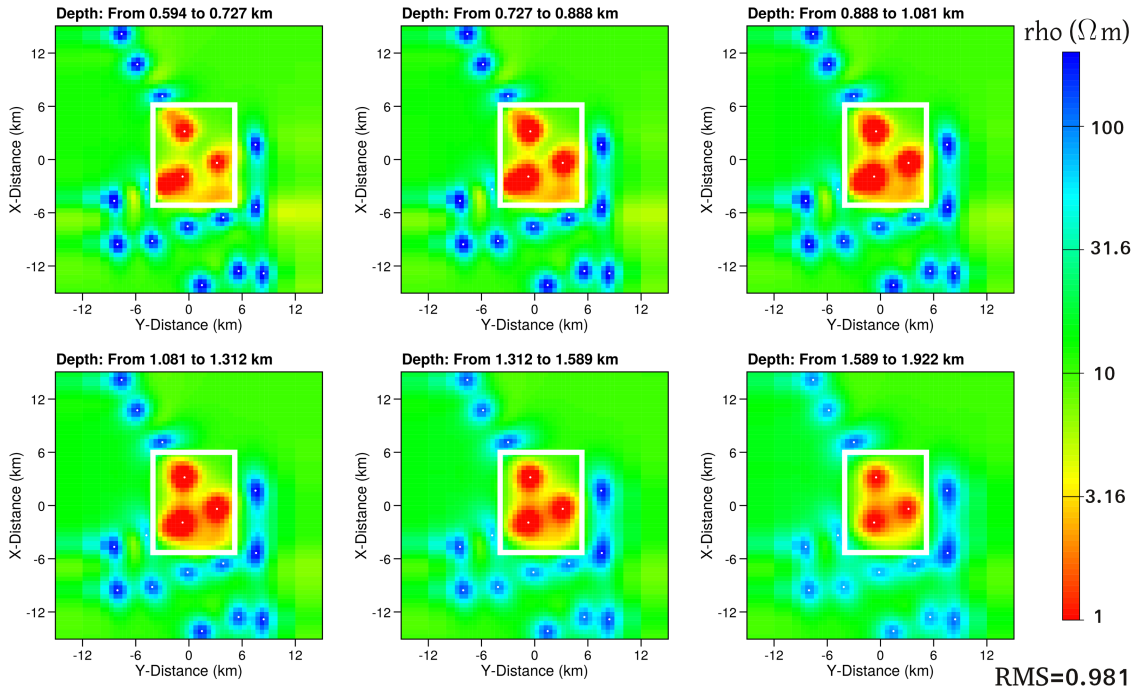

FIGURE 6.8: *Results of the 3D inversion to the model with cells 500 m sided presented as resistivity depth slices. MT sites are marked with white dots. White lines represent the actual position of the conductive block body.*

the structure was not recovered due to the absence of a station in this area. The resistive structures can also be distinguished under the rest of stations, but they are now connected mainly along the profiles directions, better representing the host geology.

These modeling studies show the importance of determining a proper discretization by taking into account the MT sites separation. Moreover, a fine discretization is not necessary when the separation of stations is considerably large; it does not increase the inverse model resolution nor detect small-scale the structures. Another disadvantage of using fine discretization (when separation of stations is great) is that the resistivity of the starting model prevail in the area between soundings, causing possible misinterpretations. An explanation is that the penetrating EM waves at a MT site are not interconnected to the ones of the neighboring site at such shallow depths. Regarding to the RMS, the three different inversion routines obtained a desirable value. Consequently, this confirms that it is not enough to consider only the RMS as a measure of inversion quality for such kind of complex models (Grayver, 2013).

6.4 Different distribution of stations

Normally, a regular grid of stations is desirable to successfully characterize geophysical anomalies. However, this is often impossible to achieve due to field

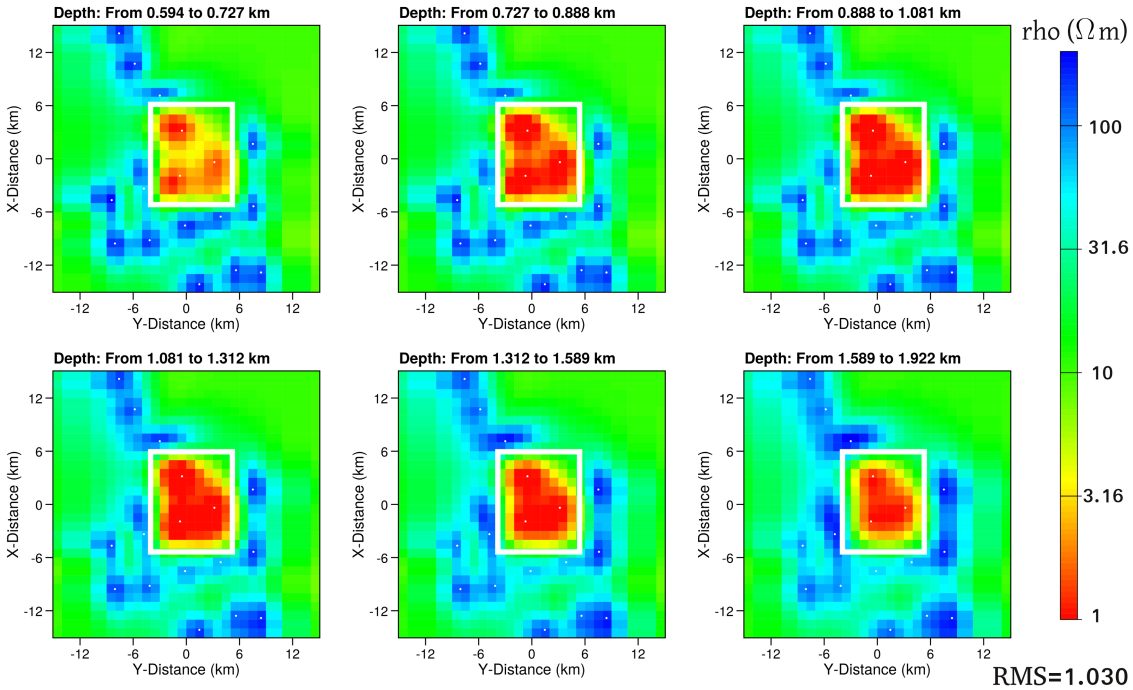

FIGURE 6.9: *Results of the 3D inversion to the model with cells 1000 m sided presented as resistivity depth slices. MT sites are marked with white dots. White lines represent the actual position of the conductive block body.*

obstacles that could exist, such as inaccessibility to some areas, land permissions and abrupt topography. Therefore, the next modeling studies are designed to determine the detectability of resistivity structures using different survey layouts. In particular, the survey layout of San Felipe is tested for a conductive block embedded in a resistive host.

Three different station distributions are tested (Fig. 6.10): a regular (Experiment A; Fig. 6.10a) and an irregular station distribution (Experiment B; Fig. 6.10b), and the original acquired survey layout (Experiment C; Fig. 6.10c). For Experiment A, 20 MT sites are evenly spaced along 5 N-S profiles and with a mean spacing of 4 km (Fig. 6.10a). In the Experiment B, 20 MT stations are irregular spaced by randomly varying the MT locations of Experiment A (Fig. 6.10b). Experiment C was done with the MT locations of the San Felipe survey (Fig. 6.10c). The same model described in section 6.3 was used for the three experiments, where a 1 Ωm block structure is embedded in a 100 Ωm host geology. Dimensions of the conductive body are of 11 x 9 x 1.328 km. As in the previous 3D modeling studies, same conditions that in San Felipe's area were set, where gulf of California and Pacific ocean are included. Thus, a 3D forward modeling was applied for the three experiments. The full impedance tensor elements and VTF components were calculated for 21 frequencies in the range from 1000 Hz to 0.01 Hz.

Subsequently, the calculated data were used as input to perform 3D inversion. For the three experiments, a 10 Ωm starting model was utilized (including the

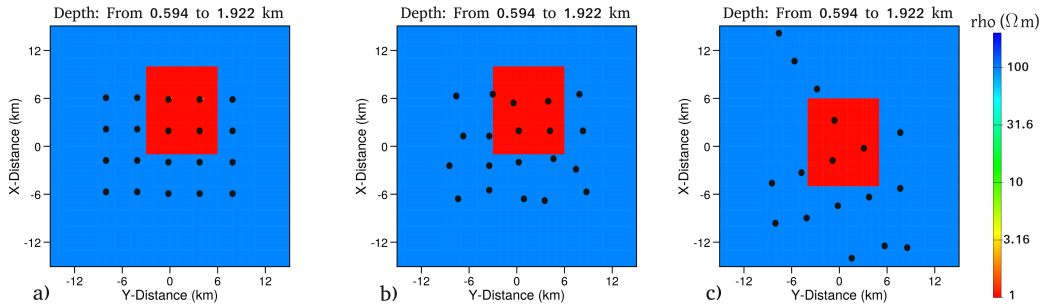

FIGURE 6.10: *Plan views of the 3D model where a conductive block structure (1 Ωm) is embedded in a 100 Ωm host geology. MT sites are marked with black dots. (a)MT stations are distributed in a regular grid. (b)MT stations are distributed in an irregular grid. (c)MT stations are distributed as in the original survey layout.*

0.3 Ωm of Pacific ocean and gulf of California). Data errors were set to 5% of $|Zxy * Zyx|^{1/2}$ for the impedance tensor elements and a constant value of 0.05 for the VTF. Identical input parameters were used for the three experiments.

Figure 6.11 shows the 3D inversion results of Experiment A, as resistivity depth slices. White lines represent the actual position of the conductive structure and white dots the MT sites.

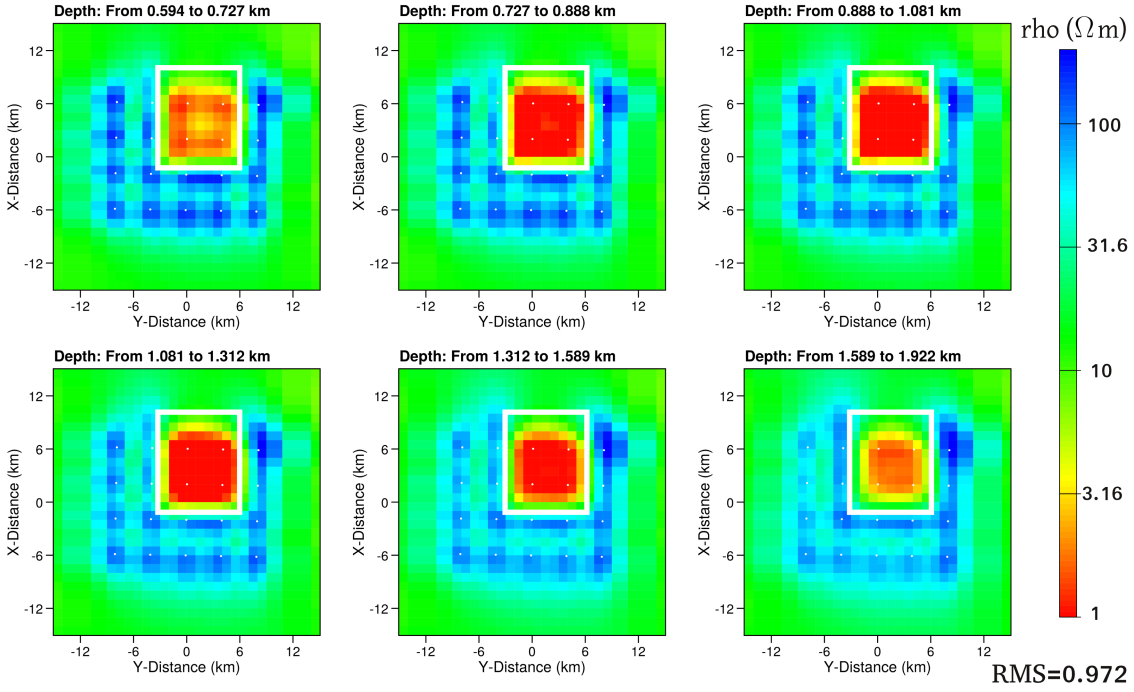

FIGURE 6.11: *3D inversion results of the model with MT soundings regularly distributed , presented as resistivity depth slices. MT sites are marked with white dots. White lines represent the actual position of the conductive block.*

The final RMS was of 0.972. At depths from 0.594 km to 0.727 km the inversion routine was not able to recover all the conductive block, same as at depths from

1.589 to 1.922 km. While at depths nearer to center of the structure, the inversion could better retrieve it, showing the best image at depths from 0.888 to 1.081 km. Nevertheless, the northern part of the conductive block is not mapped because of the lack of MT sites in this region. Approximately, an area of 9 x 9 km was possible to recover. The 100 Ωm host geology were recovered by the inversion, mainly in the zones under stations. Gaps in the host geology resistivity can be seen between the MT sites because of the great stations separation. Furthermore, the 3D inversion mapped the conductive block and host geology as structures with uniform shapes. This is expected due to the regular distribution of MT sites.

The 3D inversion results of the *experiment B* are displayed in Fig. 6.12, as resistivity depth slices as well. White lines show the actual position of the conductive block and the white dots represent the MT sites. The obtained RMS was of 1.049. Similar to Experiment A, the top and bottom of the conductive structure are poorly retrieved for the case of an irregular distribution of sites; in fact the conductor was worse resolved at depths from 1.589 to 1.922. At depths of 0.888 to 1.081 km, the best inversion image of the conductive block is obtained. In this case, not only the northern part of the conductor was not retrieved, but also the northeast corner. This is because of the position of the MT site in that area, it is located more to the central part of the conductor compared to Experiment A. In general less area of the structure was recovered, approximately 8 x 9 km.

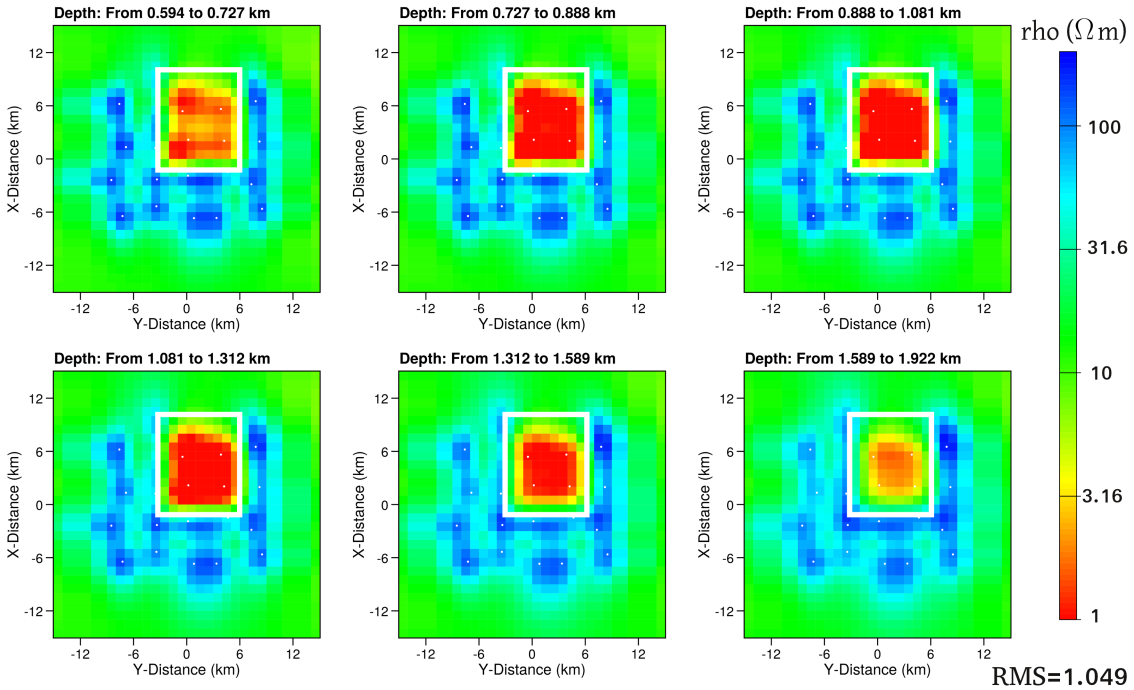

FIGURE 6.12: *3D inversion results of the model with MT soundings irregularly distributed, presented as resistivity depth slices. MT sites are marked with white dots. White lines represent the actual position of the conductive block.*

Regarding the 100 Ωm host geology, it was also retrieved but with an uneven

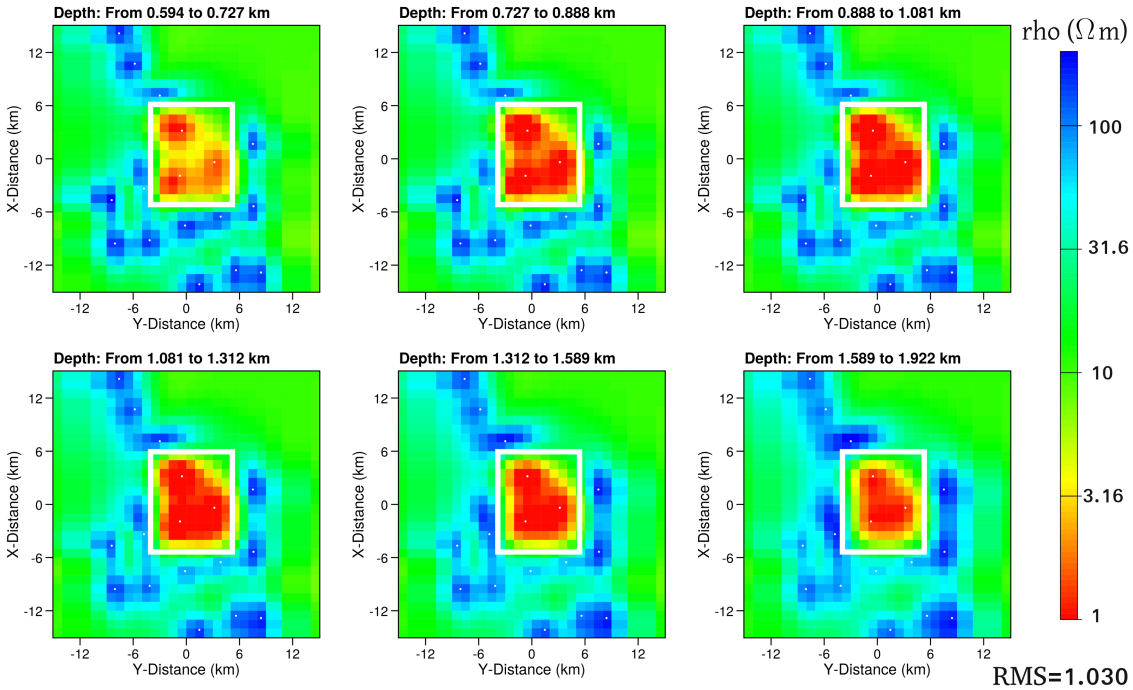

FIGURE 6.13: *3D inversion results of the model with MT soundings distributed as in the original survey layout, presented as resistivity depth slices. MT sites are marked with white dots. White lines represent the actual position of the conductive block.*

shape and mainly under the stations. Due to the MT sites layout, gaps can be observed in the resistivity distribution of the host geology within the stations coverage. The most notorious gap is in the northwestern corner of the survey area, where resistivities of 10 Ωm can be seen instead of the 100 Ωm of the host geology.

In Fig. 6.13, the 3D inversion results of Experiment C are shown, as resistivity depth slices too. The white lines represent the actual position of the conductive block and MT sites are marked with white dots. The reached RMS was of 1.03. Compared to the other two experiments, the 3D inversion better retrieved the central part of conductive structure, *i.e.*, from 0.888 to 1.081 km. The northeast corner of the conductor was not recovered, which make senses because a station is missing in that area. Moreover, only three MT sites are located over the target structure in this case, but they are better spread out along the conductor's area than in experiments A and B. Therefore more area of the conductive structure was possible to retrieve, approximately 10 x 9 km. On the other hand, the resistive host geology was mapped in an uneven shape, similar to Experiment B. In addition, gaps in the resistivity distribution of the host geology can be distinguished in the central-west and south zones of the station coverage.

These modeling studies show the distribution of MT sites can affect the imaging of structures in the 3D inversion. On the one hand, if the stations are regularly

distributed, 3D inversion derive the target structures with uniform shapes. On the other hand, the target structures can be distorted with an irregular distribution of stations.

6.5 Coast effect

The survey area is only a few kilometers away from the gulf of California (right image of Fig. 6.14), therefore a coast effect was expected to be observed in the MT data. Such effect was assumed to be detected due to the behavior of the induction vectors obtained at periods > 60 s (central image of Fig. 6.14), as it was earlier mentioned in this thesis. In this sense, a modeling investigation is carried out in this section to confirm whether or not the gulf of California is causing an effect in the MT data.

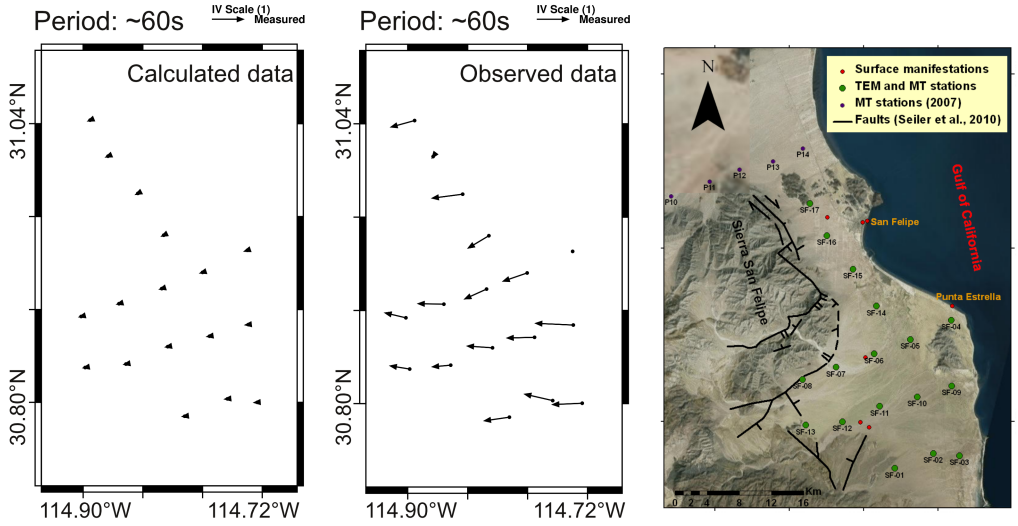

FIGURE 6.14: *The left image displays the induction vectors (Wiese convention) obtained from a synthetic model consisting of a 10 Ωm homogeneous half-space with the gulf of California and Pacific ocean embedded. On the central panel, the induction vectors (Wiese convention) obtained from the field data are shown. The right image shows the location of the survey area and the gulf of California. Note that only the induction vectors of the MT stations acquired in 2014 are displayed (green dots).*

Firstly, a forward calculation was applied to a model consisting of a 10 Ωm half-space with the gulf of California and the Pacific ocean embedded. The two VTF components were calculated for 25 periods from 0.001 to 1000 s at the same locations of the 17 MT sites that were acquired in 2014. The left image of figure 6.14 shows the induction vectors obtained from the synthetic data at ~ 60 s. Whereas the central image (Fig. 6.14) displays the induction vectors obtained from the field data at ~ 60 s too. At both images, Wiese convention is followed. The synthetic induction vectors slightly show a coast effect because they are pointing away

from the conductive gulf of California, although their lengths are not comparable to the ones of the induction vectors generated from the field data. Moreover, the northern part of the gulf of California has depths that range from a few meters to 200 m, consequently the sea itself might not be causing such a great effect noticed in the behavior of the induction vectors. Often, it is not only the ocean/sea which causes an effect in the MT data but also the conductive sediments that are underlain. Therefore, a conductive layer under the gulf of California was added to the above mentioned synthetic model to simulate such conductive sediments. The thickness of this 0.3 Ωm conductive layer was varied to reach depths from 200 m to 10 km. Thus, forward modeling was applied to these synthetic models. Vertical magnetic components were calculated for the same frequencies.

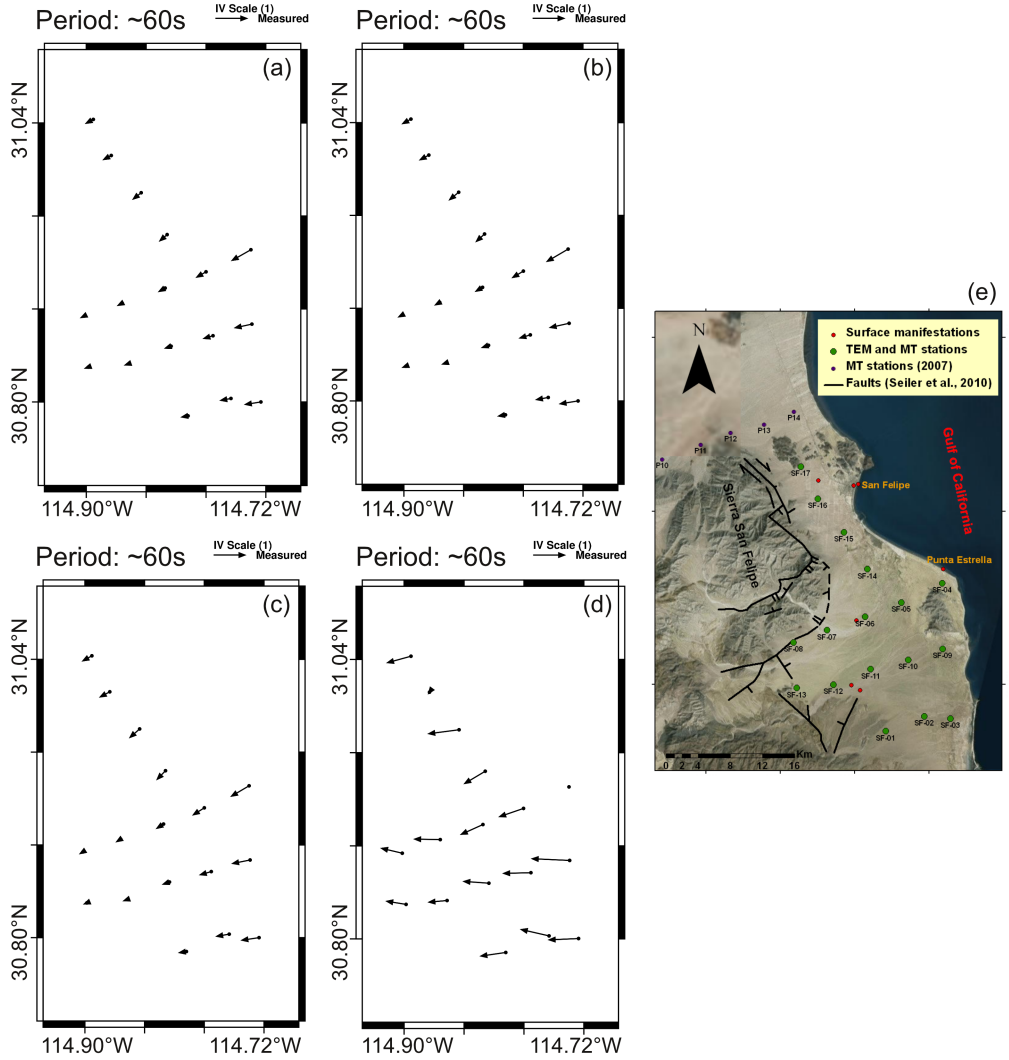

FIGURE 6.15: *Induction vectors (Wiese convention) obtained from a synthetic model with a conductive structure under the gulf of California up to depths of: (a) 600 m,(b) 1.1 km,(c) 5.89 km. (d)Induction vectors (Wiese convention) obtained from the field data. (e)Map of the survey area. Note that only the induction vectors of the MT stations acquired in 2014 are displayed (green dots).*

Figure 6.15(a-c) displays the induction vectors (Wiese convention) obtained from three synthetic models with a conductive structure under the gulf of California up to depths of 600 m, 1.1 km and 5.89 km, respectively. When such conductor is located up to depths of 600 m (Fig. 6.15-a), the induction vectors point away from the sea region. Although their lengths are longer than the ones of the induction vectors obtained if it is only the gulf of California considered (left image of Fig. 6.14), they are still shorter in comparison to the ones obtained from the field data (Fig. 6.15-d). When the conductive structure under the gulf is located up to 1.1 km (Fig. 6.15-b), the lengths of the induction vectors increase. The subsequent increments of the conductor's thickness do not affect the length of the induction vectors. For instance, figure 6.15-c displays the induction vectors obtained from a model with the conductor up to depths of 5.89 km and their lengths do not show any increment. Thereby, the conductor under the gulf of California should at least be located up to depths of 1.1 km in order to cause a similar effect to the one observed in the induction vectors obtained from the field data.

6.6 Input parameters of the 3D MT inversion

The 3D inversion of MT data is a strongly ill-posed problem, therefore this section deals with the impact of the input parameters of the 3D inversion software ModEM. In this way, inversion trials were done with different values for the regularization parameter λ, model covariance α and data errors. Thus, the influence of the chosen parameters on the inversion models are discussed. In this regard, the synthetic model described in section 6.2 is used which simulates the classical conceptual geothermal reservoir model. The 3D model consists of a 5 Ωm clay cap over a 25 Ωm reservoir, embedded in a 200 Ωm half-space (Fig. 6.2). A total of 60 MT stations were deployed, with separations of 300 m and 500 m in the N-S and E-W direction respectively. The detailed characteristics of this synthetic model can be seen in section 6.2. A 3D MT forward modeling was applied to the above mentioned model, where the four components of the impedance tensor and the two VTF components were calculated for 25 frequencies between 1000 Hz and 0.001 Hz.

Afterwards, the calculated data were used to perform 3D inversion trials with different input parameters. In order to avoid redundancy, the influence of the regularization and smoothing parameters is only discussed while inverting the off-diagonal elements. Furthermore, similar results were obtained when λ and α were varied at the inversion trials of the different possible datasets. In contrast, the effect of the data errors is described on the inversion of the off-diagonal, full impedance tensor and VTF components.

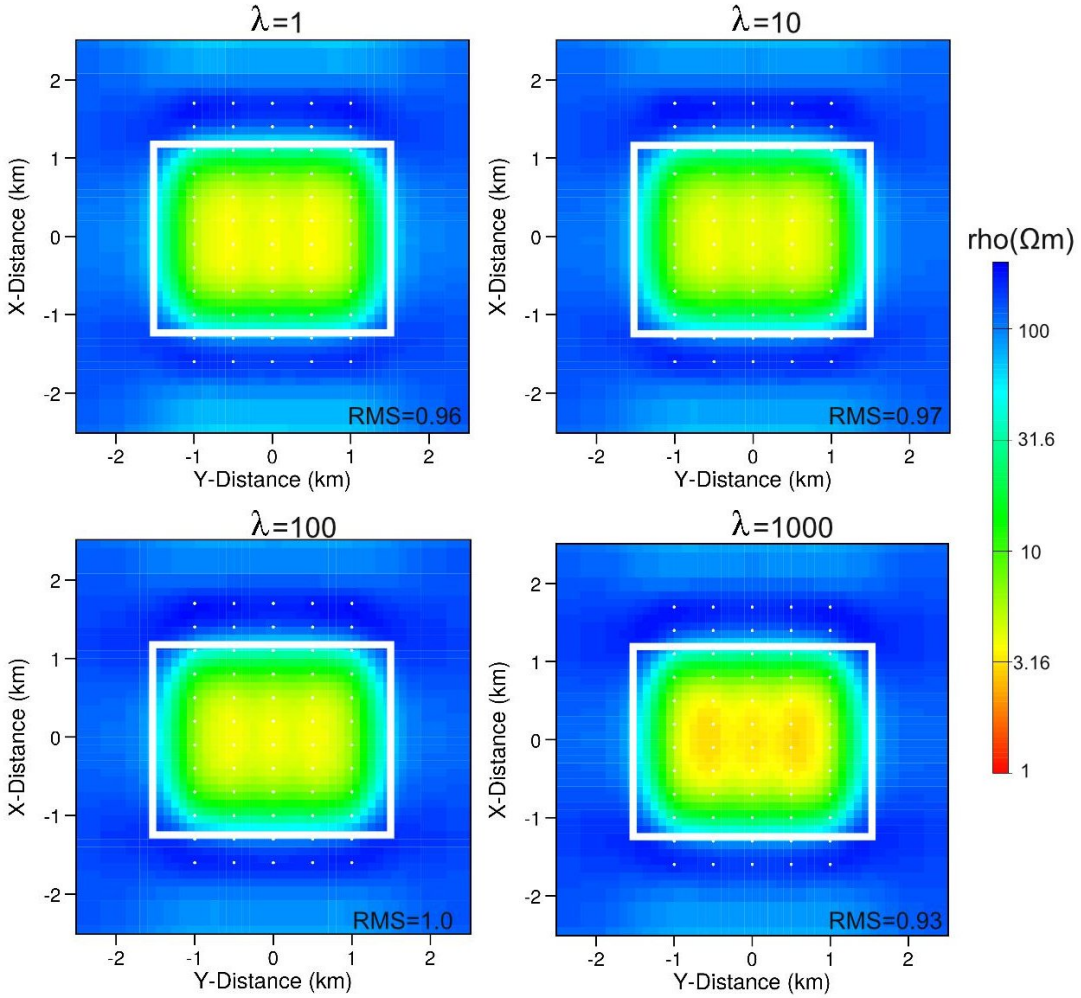

FIGURE 6.16: *Inversion models presented as slices at depths of ∼ 500 m for the four different λ values. The actual position of the conductive clay cap structure is represented with the white lines. The MT stations are marked with white dots.*

6.6.1 Regularization parameter λ

The regularization parameter λ defines the balance between data fit and model smoothness (see section 8.1). This trade-off parameter is selected by the user and it decreases during the inversion routine. Thus, the model smoothness dominates during the first iterations, whereas the data misfit is dominant towards the end of the inversion. In this sense, trials with initial λ values of 1, 10, 100 and 1000 were carried out to assess the different results. A 100 Ωm half-space starting model was utilized at all the runs. Data errors were set to 5% of $|Zxy * Zyx|^{1/2}$. The rest of the input parameters were identical for all the trials.

Figure 6.16 shows the results of the four different inversion trials, as resistivity slices at depths of ∼ 500 m. The actual position of the clay cap structure is marked with the white lines. The main difference is noticed on the resistivity distribution of the central area of the clay cap. At smaller λ values the structure is

more heterogeneous and has resistivities between 3 and 10 Ωm. Whereas at increased λ values (*e.g.* $\lambda = 1000$) the clay cap structure is more homogeneous and a greater area shows resistivities closer to 5 Ωm, which is the value set at the synthetic model. These results make sense because the model smoothness dominates during more iterations when an initial high λ is selected, resulting on a smoother inverse model. In contrast, the data misfit is mainly dominating when an initial low λ is set and therefore, the resulted inverse model is less smooth.

6.6.2 Model Coviarance parameter

The model covariance α describes the model smoothness and can be independently defined along the three different directions (see section 8.1). The implemented spatial smoother is a recursive auto-regressive covariance operator with a quasi Gaussian smoothing kernel (Kelbert et al., 2014). The smoothing parameter can be defined between a range from 0 to 1, where higher values derive smoother models. To evaluate the impact of the smoothing parameter, trials with α values of 0.1, 0.3, 0.5, 0.7 and 0.9 were performed. A 100 Ωm half-space starting model was utilized at all the trials. The trade-off parameter λ was set to an initial value of 100. Data errors were set to 5% of $|\mathrm{Zxy} * \mathrm{Zyx}|^{1/2}$.

The inversion results of all the trials are displayed in Fig. 6.17 as resistivity slices at depths of $\sim$ 500 m. The real position of the conductive clay cap is represented with white lines. For the inversion trials with α=0.1, 0.3 and 0.5, the area of the clay cap was recovered with resistivities between 3 and 10 Ωm. The inversion model of $\alpha = 0.1$ shows local bodies nearby the stations mainly in the central part of the clay cap, with resistivities closer to the real conductivity of the structure. At the inverse model of $\alpha = 0.3$, the central area is recovered with the real resistivity distribution but some gaps can still be distinguished. These gaps are mainly in the Y-direction (E-W) and is caused by greater distances between the stations in such direction. This issue can be overcome by increasing the smoothing parameter of the Y-direction. At the inversion model with $\alpha = 0.5$, the clay cap is better retrieved. The smoothing parameter was high enough to connect the majority of the model parameters of the central part from the clay cap structure. Finally, the inversion trials with $\alpha = 0.7$ and $\alpha = 0.9$ failed to retrieve the clay cap.

6.6.3 Data errors

The data error settings is also an important inversion input parameter that must be systematic tested to define the most suitable for the given data set. In this thesis, the data errors were set relative to the mean of the off-diagonal elements $|\mathrm{Zxy} * \mathrm{Zyx}|^{1/2}$ (Meqbel, 2009; Patro and Egbert, 2011; Tietze, 2012) for the impedance tensor components and constant values for the VTF elements.

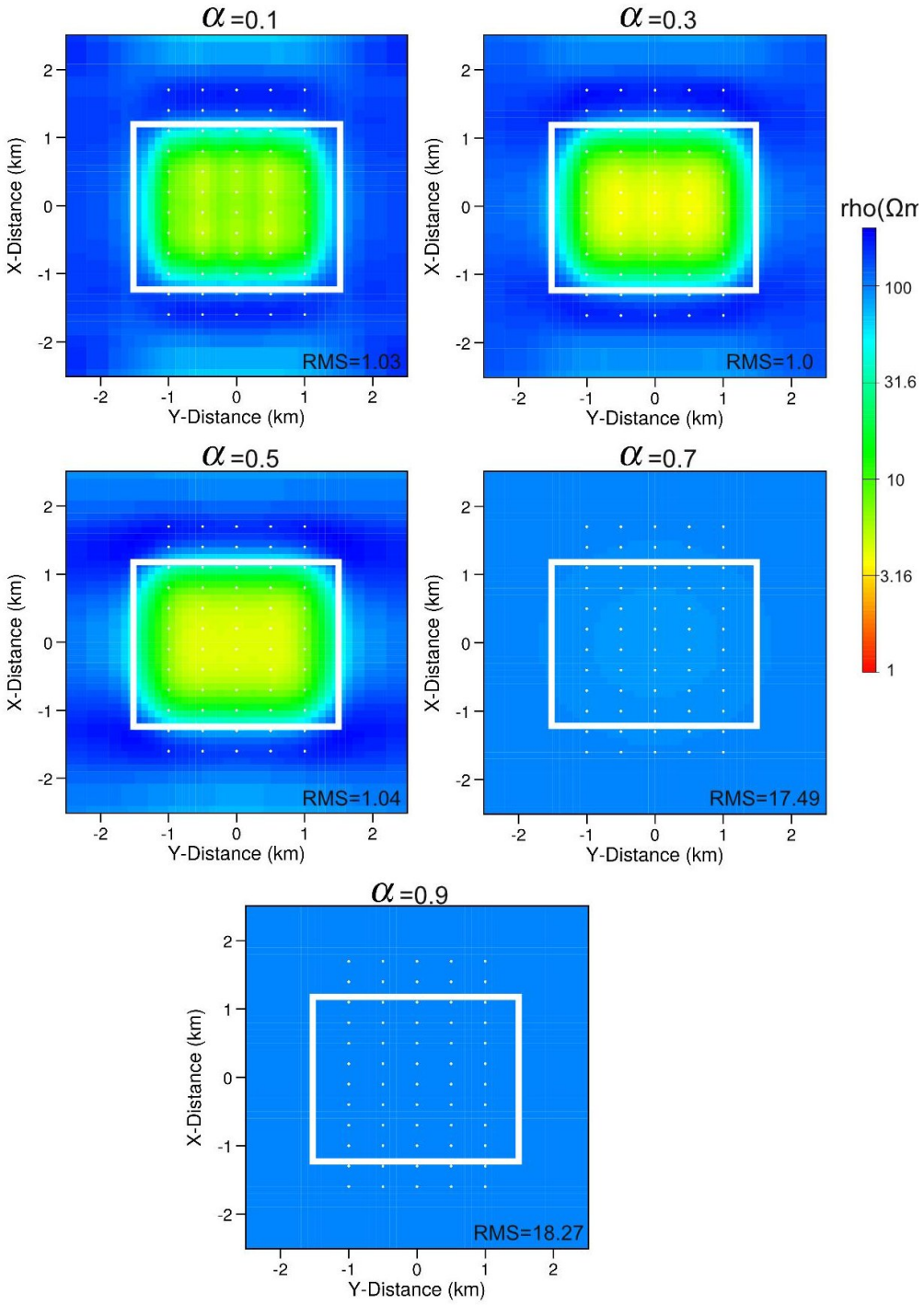

FIGURE 6.17: *Inversion models presented as slices at depths of ∼ 500 m for the five different α values. The actual position of the conductive clay cap structure is represented with the white lines. The MT stations are marked with white dots.*

Off-diagonal elements inversion

Firstly, the influence of the data errors is analyzed on the 3D inversion of the off-diagonal elements. In this way, trials with different data errors were carried

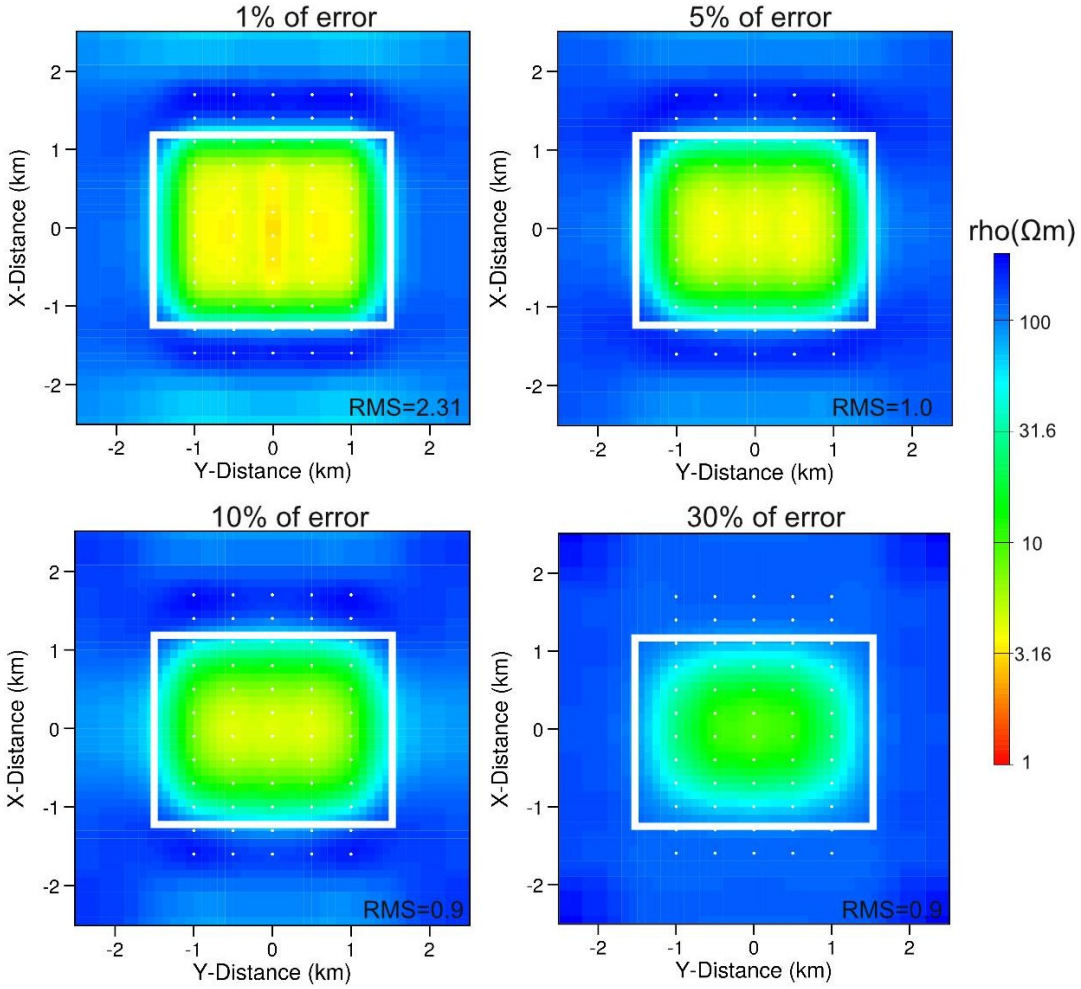

FIGURE 6.18: *Results of the off-diagonal elements inversion with different data error settings, presented as resistivity slices at depths of ∼ 500 m. The actual position of the conductive clay cap structure is represented with the white lines. The MT stations are marked with white dots. Note that data errors were set relative to the mean of the off-diagonal impedances* $|\mathrm{Zxy} * \mathrm{Zyx}|^{1/2}$.

out, which were varied from 1% to 30% of $|\mathrm{Zxy} * \mathrm{Zyx}|^{1/2}$. Identical inversion input parameters were set at all the inversion runs: a trade-off parameter of 100, smoothing parameter of 0.3 and a 100 Ωm starting model.

Figure 6.18 displays the obtained inversion models as resistivity slices at depths of ∼ 500 m. The actual position of the conductive clay cap is marked with white lines. It is clear that the structure is better retrieved at the inversion with data errors set to 1%. It shows a greater area with resistivities closer to the real one. However, this inverse model shows two regions with decreased resistivities outside of the data coverage (in the northern and southern areas). These areas have resistivities of ∼ 25 Ωm, which is four times smaller than the resistivity of the starting model. At the rest of the inversion trials, less weight was assigned to the data which causes a loss of information. This loss of information is not only

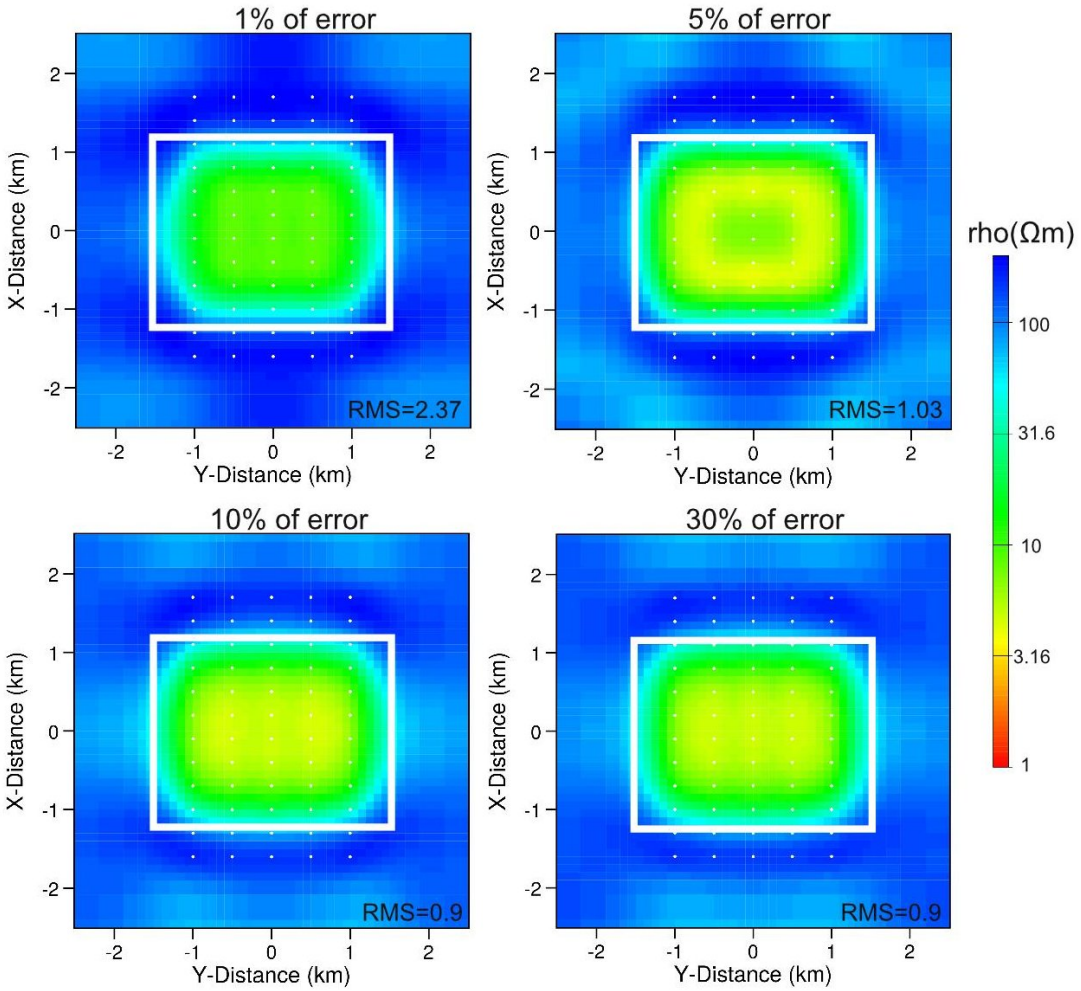

FIGURE 6.19: *Results of the full impedance tensor inversion with different data error settings, presented as resistivity slices at depths of ∼ 500 m. The actual position of the conductive clay cap structure is represented with the white lines. The MT stations are marked with white dots. Note that data errors were set relative to the mean of the off-diagonal impedances* $|\mathrm{Zxy} * \mathrm{Zyx}|^{1/2}$ *and only the errors for the main diagonal components were varied.*

distinguished by the poorer recovering of the clay cap, but also in the increment of the resistivities from the two regions outside of the stations coverage. It is not expected that the anti-diagonal impedances have information of structures outside of the data coverage. On the contrary, the main diagonal components are the important ones for imaging off profile structures (Siripunvaraporn et al., 2005).

Full impedance tensor inversion

The influence of the data errors is now investigated on the inversion of the full impedance tensor elements. At this investigation, only the data errors of the main diagonal elements were varied from 1 to 30 % of $|\mathrm{Zxy} * \mathrm{Zyx}|^{1/2}$, whereas the off-diagonal components were set to 5 % at all the inversion trials. Four of all the

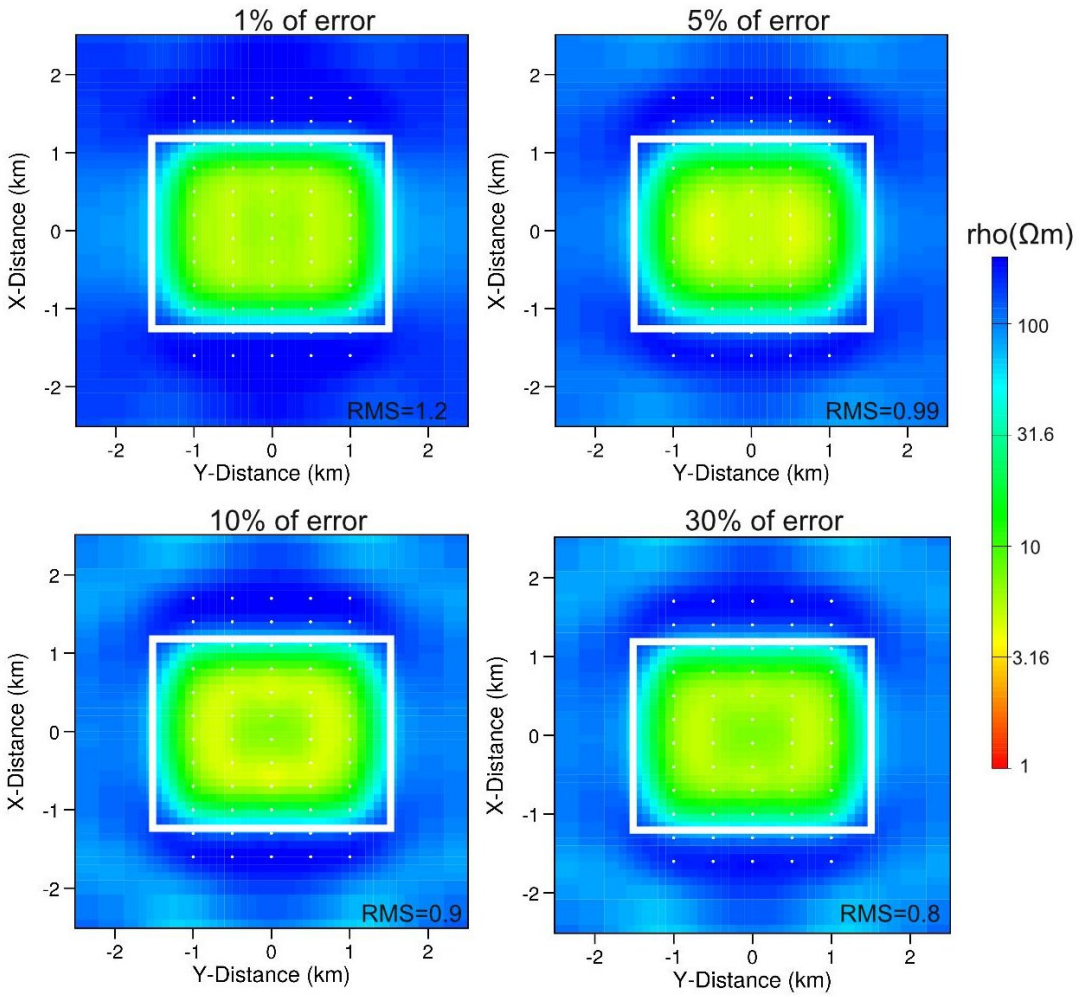

FIGURE 6.20: *Results of the full impedance tensor and VTF elements inversion with different data error settings, presented as resistivity slices at depths of ∼ 500 m. The actual position of the conductive clay cap structure is represented with the white lines. The MT stations are marked with white dots. Note that only the data errors of the VTF elements were varied and set to constant values.*

inversion trials results are presented as resistivity slices at depths of ∼ 500 m in Fig. 6.19. The real position of the clay cap structure is marked with the white lines. The poorest inversion result was obtained when the errors of the main diagonal elements were set to 1%. The clay cap conductivity distribution was poorly retrieved, which it was expected due to the downweighting of the off-diagonal components. Therefore, the information of the main diagonal elements prevailed. At the inversion model with 5% of data errors, a greater area displays the real resistivity (5 Ωm), however, a gap in such a conductivity distribution can be distinguished in the central part of the anomaly. This gap is not noticed anymore at the inversion models with data errors of 10% and 30%. In contrast, less area displays resistivities close to ∼ 5 Ωm, which is the resistivity of the clay cap.

Full impedance tensor and VTF elements inversion

Finally, the influence of the data errors is analyzed on the inversion of the full impedance tensor and VTF elements. At this investigation, only the data errors of the VTF elements were varied from 1 to 30%, whereas all the components of the impedance tensor were set to 5 % of $|Zxy * Zyx|^{1/2}$ at all the inversion trials. Four of all the inversion trials results are presented as resistivity slices at depths of $\sim$ 500 m in Fig. 6.20. The real position of the clay cap structure is represented with the white lines. At the inverse model with 1% of data errors, it can be slightly distinguished an area with resistivities closer to 5 Ωm. This 5 Ωm zone is more evident at the inversion model with 5% of data errors. When the VTF elements are downweighted (*e.g.*10 and 30 % of error), a gap in the central area of the clay cap resistivity distribution is noticed and regions with decreased resistivities outside of the data coverage showed up.

6.7 Summary of the 3D Modeling studies

The described 3D Modeling studies provided useful insights regarding the utilization of Magnetotellurics in geothermal exploration and practical issues of 3D inversion. The results of this chapter are summarized as follows:

- Magnetotellurics cannot properly image a volcanic-type geothermal reservoir. However, it can successfully characterize the clay cap structure and the transition area between this one and the reservoir.
- When a considerable great separation between MT sites exists, a fine discretization is not necessary to perform 3D inversion.
- Desirable RMS values can be obtained with different kinds of discretization in the 3D starting model, but without adequate reconstructing the target structures.
- In order to derive undistorted target structures with 3D MT inversion, a distribution of stations as a regular grid is needed.
- A conductor under the gulf of California is required in order to cause an effect on the MT data comparable to the one observed on the field data of San Felipe.
- All the input parameters for the 3D MT inversion must be systematically tested in order to find out the most appropriated ones for the given data set. Particularly the smoothing parameter α and the data errors showed to have more influence on the output of the inversion, therefore they must be effectively assigned according to the data set.

Chapter No. 7

1D & 2D inversion of field data

This chapter is focused to describe the one and two-dimensional inversion schemes that were applied to the acquired data. The first part deals with the inversion of TEM data. In that respect, two different conventional 1D inversion methods were firstly applied in order to avoid geological misinterpretations. Model parameter uncertainties of the best fit 1D inverse models are discussed. Moreover, a pseudo-3D conductivity model is constructed with TEM information and thus, a geological interpretation of the shallow part of the subsurface from San Felipe is described. In the second part, the 1D inversion of MT data is presented. The resolution of the model parameters of the best fit 1D inversion model is appraised. Although the dimensionality analysis of MT data suggested a 1D and 3D subsurface structure, a 2D inversion of the magnetotelluric data is performed. The geological interpretation based on the MT data is given in the subsequent chapter, where the applied 3D inversion scheme to MT data from San Felipe is described.

7.1 1D inversion of TEM data

As a first approach, two different conventional 1D inversion schemes were performed to the TEM data: Occam and Marquardt techniques. First, the Occam inversion scheme is performed. Subsequently, the resulting resistivity model is utilized to derive the starting model for the Marquardt inversion. It is well known that the Marquardt inversion is more dependent on the starting model than the Occam inversion. Therefore, it is advisable to perform both regularizations of the Occam method beforehand. Here, it is important to mention that both inversion schemes were performed in EMUPLUS software, which has implemented a numerical forward calculation for a central loop TEM configuration. However, TEM data of this project were acquired with a single loop configuration. Hence, a comparison was done with a second software -JOINTEM (Pirttijärvi, 2010)- which has implemented a forward solution for a single loop configuration and no important

differences were noticed (see Appendix B). After performing conventional 1D inversion schemes, a Spatially Constrained Inversion (SCI) was applied to TEM data to derive a pseudo-3D resistivity model. The resulting model is used for a geological interpretation.

The applied inversion schemes are error weighted. Therefore, data errors must be included. A common approach is to use the stacking errors, but these ones are not suitable for the SCI scheme according to the authors. In this sense, von Papen (2011) exposes that SCI authors suggest to consider relative high errors (*e.g.* 5%), which can be explained as geological noise. Spies and Frischknecht (1991) claimed that the geological noise include all geological phenomena which result in incorrect layered-earth interpretations using quasi-static 1D models. As it was proposed in von Papen (2011), trials were done with different errors (*e.g.* between 1% and 5%) for the SCI application and no major discrepancies were found. Therefore, 1% of error was chosen for all the acquisition times. In addition, the same error values were used in the conventional 1D inversion schemes in order to fairly compare both results.

7.1.1 Occam inversion

The 1D Occam inversion was done for each station using a 10 Ωm starting model consisting of 30 layers with logarithmically equidistant layer thicknesses. The amount of layers was chosen after performing trials with models of 25 and 35 layers. No noticeable difference existed between the models, therefore, a 30 layers model avoid under-parameterization and shows an optimal computation time. The thickness of the first layer is 1 m and the depth of the last layer is 200 m. Thus, model parameterization is ensured at greater depths than the depth of investigation. Figure 7.1(a-c) shows the Occam inversion models obtained at stations SF-02, SF-04 and SF-16 for both regularizations: in green for the first order derivative and in black for the second order derivative. Similar results were obtained at the rest of the stations, which can be seen in the Appendix C.

7.1.2 Marquardt inversion

Marquardt inversion is useful to generate a model with minimum amount of layers. As it was already mentioned, the number of initial layers was derived from the Occam inverse models. In general, a three-layer model is sufficient to fit the data.

In Fig. 7.1(a-c), Marquardt inverse models obtained at stations SF-02, SF-04, and SF-16 are shown as an example, in red. At SF-02, the first conductive layer has a resistivity of 5 Ωm and a thickness of 4 m. A second resistive layer extends from 4 to 100 m and has a resistivity of 17 Ωm. The lowest layer is rather conductive with a resistivity value below 1 Ωm. At SF-04, the shallowest layer has a resistivity of 4 Ωm and a thickness of 6 m. The second layer has a resistivity of 15 Ωm and a thickness of 85 m. The lowest and most conductive layer has a resistivity of 0.5 Ωm. At SF-16, the first layer has a resistivity of 2 Ωm and a thickness of 3 m.

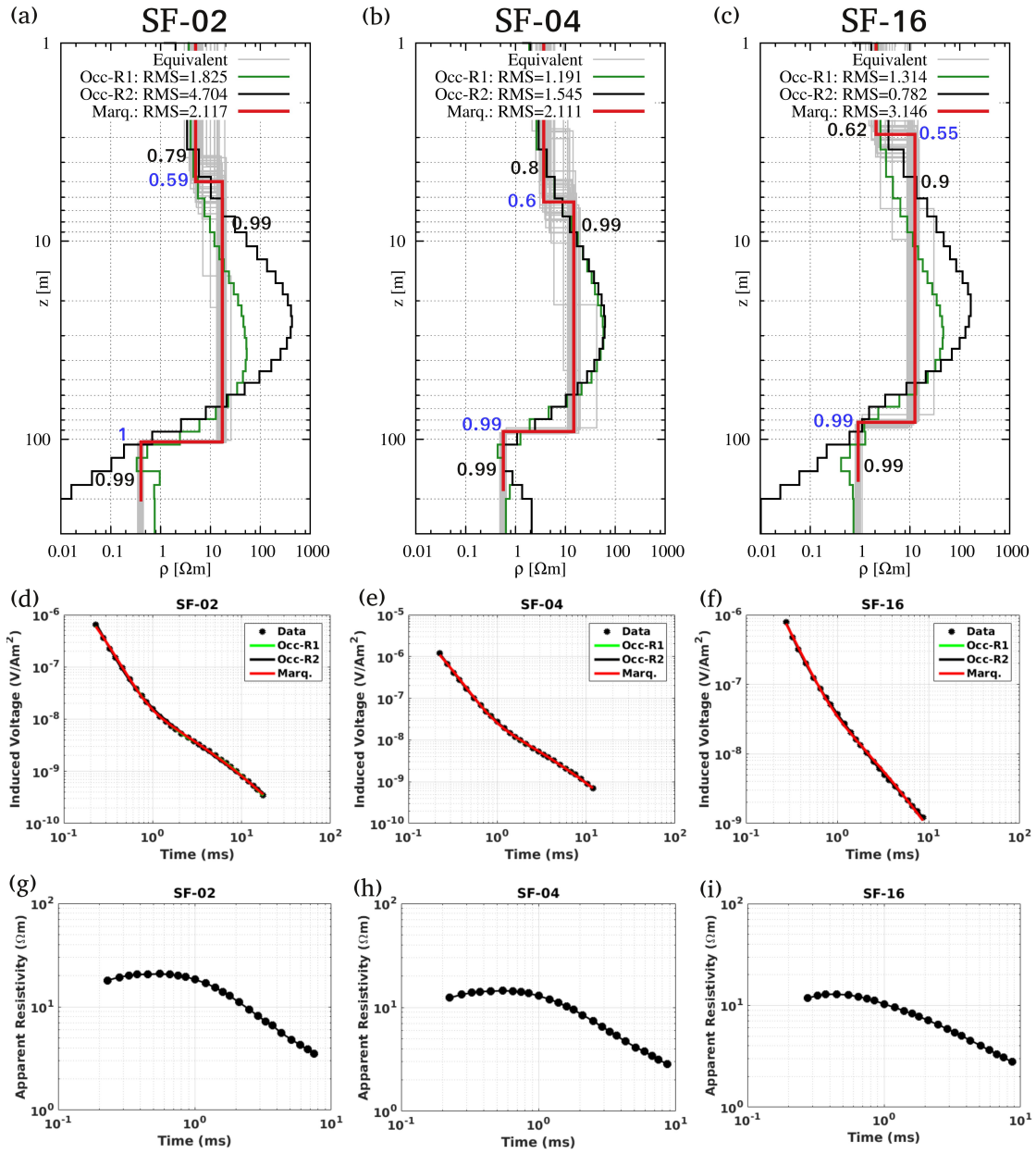

FIGURE 7.1: *(a-c) 1D Occam-R1/R2 (green and black), Marquardt (red) and Equivalent (gray) inverse models obtained at stations SF-02, SF-04, and SF-16. Parameter importances are marked in black for resistivities and in blue for depths. (d-f) Fitting between calculated data and observed data at stations SF-02, SF-04, and SF-16. (g-i) Late-time apparent resistivity transformations at stations SF-02, SF-04, and SF-16.*

The second layer is located between depths of 3 and 82 m, and has a resistivity of 13 Ωm. The deepest layer has a resistivity value below 1 Ωm. The three-layer behavior can also be distinguished in Fig. 7.1(g-i) where the late-time apparent resistivity transformations are displayed for the stations SF-02, SF-04, and SF-16. Furthermore, the characteristics of 1D Marquardt inversion models and late-time

apparent resistivity curves displayed in Fig. 7.1 are typical for all the measured soundings. The 1D inversion models at all TEM stations are displayed in Appendix C.

7.1.3 Resolution of model parameters

In order to reflect the model uncertainty and the quality of the inversion, equivalent models and parameter importances were obtained for the best fit Marquardt inversion model as described in section 3.2. On the one hand, when the equivalent models show high variability within a model parameter, this model parameter is not well resolved. On the other hand, an importance value close to 1 indicates that the model parameter is well-resolved (von Papen et al., 2013). Moreover, Lippert (2015) suggested that a model parameter is well-resolved for importances between 0.71 and 1, moderately resolved for importances of 0.5 to 0.7 or poorly resolved for importances smaller than 0.5.

Parameter importances and equivalent models are also shown in Fig. 7.1(a-c), at stations SF-02, SF-04 and SF-16. Black numbers represent the importances for resistivities and blue numbers for depths. Equivalent models are in light gray. At SF-02, the depth of the first layer's base is moderately resolved; it has an importance of 0.59 and the equivalent models show large variation. The rest of the model parameters have importances between 0.79 and 1, therefore they are well-resolved. At SF-04,the importance of the base's depth of first layer is 0.6 and the equivalent models show large variation, which indicate that this model parameter is moderately resolved. The rest of the model parameters are well-resolved; the importances are close to 1 and equivalent models display only small variations. At SF-16, the parameters of the first layer are moderately resolved, which is clearly visible by the large variation of the equivalent models and importances between 0.55 and 0.62. In contrast, the rest of the model parameters are well-resolved; the equivalent models show limited variations and the importances are close to 1.

7.1.4 Spatially Constrained Inversion of TEM data

Since conventional 1D inversion results are similar for all TEM soundings in the survey area, it was assumed that the shallow subsurface can be represented as a series of horizontal layers and no lateral resistivity changes were expected. Moreover, a 1D model assumption is valid in layered sedimentary areas where data is only slightly affected by 2D/3D resistivity structures (Newman et al., 1987; Sengpiel and Siemon, 2000). Thus, the TEM data is interpreted using a Spatially Constrained Inversion (SCI) scheme to derive a quasi 3D resistivity model of the survey area considering all the soundings.

As a first step of the SCI, the soundings are connected by applying a Delaunay Triangulation. Figure 7.2(a) shows the Delaunay triangulation of the TEM stations of the survey area. To define the strength of the constraints (see Equation 3.29), a reference distance B was set to the medium distance between the survey sta-

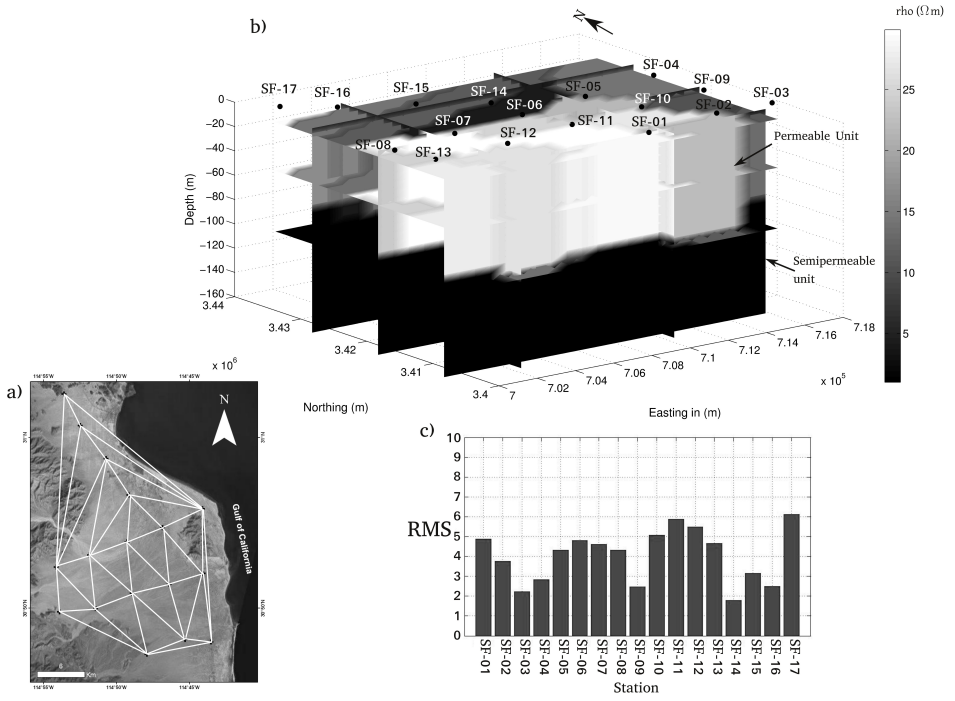

FIGURE 7.2: *(a) Map of the survey area displaying how the TEM soundings are connected by applying Delaunay triangulation. (b) Pseudo-3D model obtained after performing Spatially Constrained Inversion (SCI) to TEM data. Distribution of the stations are also displayed. Permeable and semipermeable units of the aquifer from San Felipe are indicated. (c) RMS values of the SCI models at all stations. Figure taken from Ruiz-Aguilar et al. (2018).*

tions. A weighting factor of $a = 1$ was used, so the distance dependence of the constraints was linear. After performing several routines with different values to estimate the optimal one, a strong reference constraint of $A = 10\%$ was used for all model parameters. 1D Marquardt inversion results were used as a starting model (3-layers) for the SCI scheme. In Fig. 7.2(b), SCI results are presented as a pseudo-3D resistivity model of the subsurface from the survey area. The surface layer shows variable thickness and resistivity values ranging from 5-10 m and 5-25 Ωm, respectively. The second layer extends up to a depth of $\sim$ 95 m with resistivities ranging from 15 to 30 Ωm, and correlates to the permeable unit of the aquifer from San Felipe. The deep conductive layer shows similar resistivity values ($\sim$ 1 Ωm) for the majority of the survey area and is correlated to the semipermeable unit of the aquifer.

Comparisons between SCI and Marquardt inverse models are displayed in Fig. 7.3. At station SF-02, the first layer of the SCI model shows a similar resistivity compared to the Marquardt model, but a difference of $\sim$ 2 m in thickness. The SCI second layer is slightly more resistive and extends up to a depth of 95 m, while the Marquardt's model second layer extends up to 105 m. The lowest layer has a slight greater resistivity in the SCI model ($\sim$ 1 Ωm). At station SF-04, the

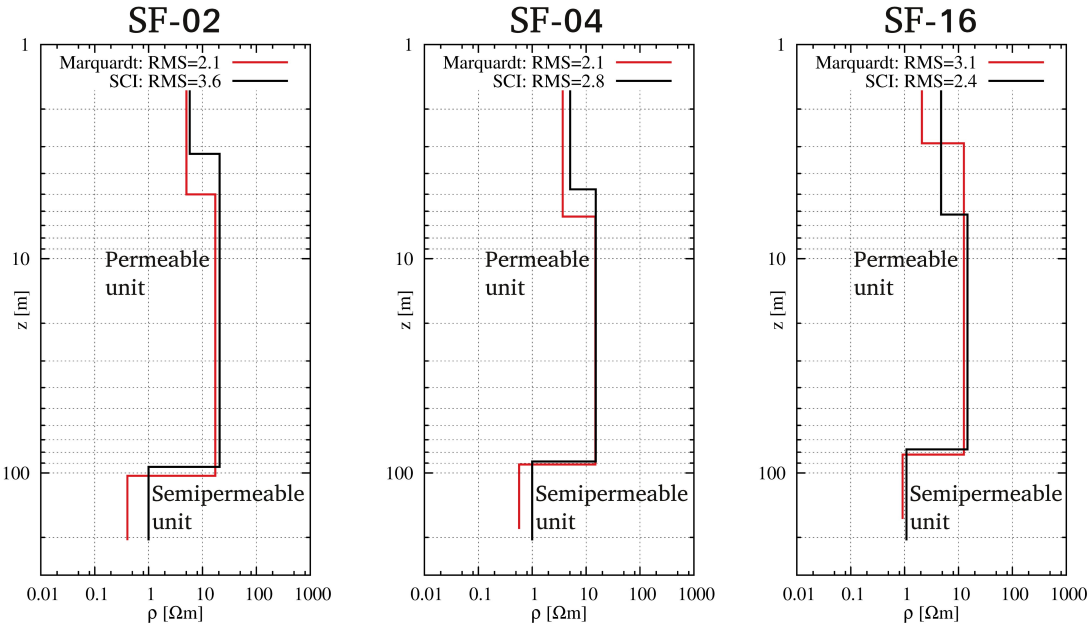

FIGURE 7.3: *Comparison between SCI inverted models and 1D Marquardt models at stations SF-02, SF-04 and SF-16. Permeable and semipermeable unit of the aquifer from San Felipe are indicated.*

SCI first layer has greater resistivity but smaller thickness than in the Marquardt model. The second layer has an identical resistivity and extends up to a similar depth in both models. The deepest SCI layer has a resistivity of 1 Ωm, while it has 0.5 Ωm in the Marquardt model. At station SF-16, the first layer of the SCI model has a resistivity of 5 Ωm and a thickness of 6 m, which are greater than in the Marquardt model. The second layer has identical resistivities ($\sim$ 14 Ωm) and extends up to similar depths in both models ($\sim$ 85 m). The lowest layer has a resistivity of $\sim$ 1 Ωm in the two models. Permeable and semipermeable units of the aquifer from San Felipe are marked in the Figure 7.3.

7.1.5 Geological interpretation of the shallow subsurface from San Felipe

Additional VES information

In CONAGUA (1989), the results of a Vertical Electrical Sounding (VES) survey campaign are reported which was carried out to investigate the conditions of the San Felipe-Punta Estrella aquifer. The soundings were acquired with Schlumberger configuration and the maximum AB/2 was of 1000 m. In Fig. 7.4, a profile constructed with the inversion results of 6 VES sites is deployed as an example. The VES profile is located in the central part of the survey area, between TEM stations SF-06 and SF-07.

In general, 4 different layers were interpreted. A shallow layer with resistivities of 46-300 Ωm and a thickness of $\sim$ 60 m which was correlated to sandstones of

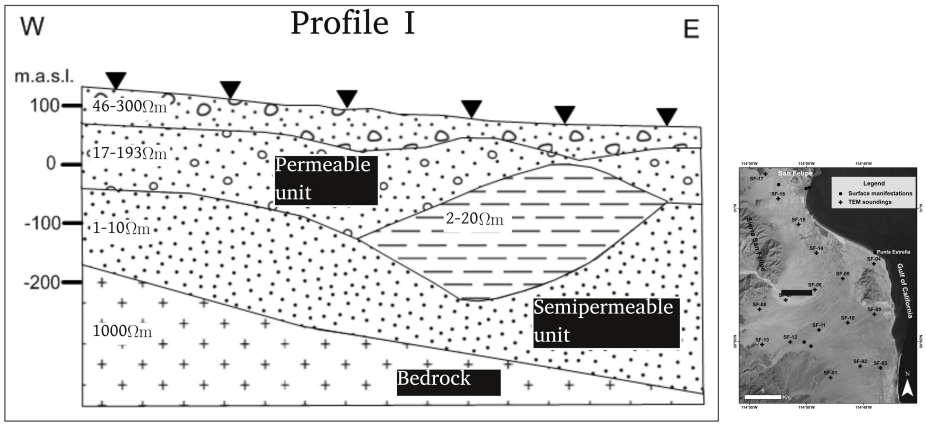

FIGURE 7.4: *Profile constructed with VES inversion models. It was redrawn from CONAGUA (1989). Location of the profile is indicated on the map.*

coarse grains and gravels. The second layer with resistivities ranging from 17-193 Ωm and a thickness of $\sim$ 100 m was also interpreted as sandstones and gravels, but of fine grains. A third conductive layer with resistivities of 1-10 Ωm and a thickness of $\sim$ 130 m was correlated to sediments of fine grain saturated of water with high content of mineral salts and geothermal waters. The lowest layer has a resistivity of 1000 Ωm and was interpreted as intrusive igneous rocks. In the eastern part of the profile, a clay layer located between the second and third layer was also mapped, with resistivites of 2-20 Ωm and an average thickness of $\sim$ 120 m. This clay layer is only detected in few areas by the VES data (CONAGUA, 1989). Permeable and semipermeable unit of the aquifer from San Felipe are marked in the profile (Fig. 7.4).

Interpretation of TEM inversion models

The interpretation of the TEM inversion models is based only on geological, hydrogeological and former VES information, as borehole data is not available for the survey area. The first and second layer can be correlated to the Pleistocene alluvial sediments that are filling San Felipe's valley. Resistivities of sediments are known to be strongly dependent on the saturation conditions, the salinity of the pore fluids, and the clay content (Archie, 1942; Knight and Endres, 2005). Therefore, the resistivity values of the second layer may be related to sediments containing freshwater and representing the permeable unit of the aquifer from San Felipe. The last conductive layer can be associated to the semipermeable unit where the high conductivity values may be due to the clayed sediments and high salinity. This assumption is based on CONAGUA (2015) where it is reported that the semipermeable unit has a high concentration of fluor which might be associated to thermal waters. Analyzing the equivalent models and parameter importances, it is concluded that the surface layer is not well resolved. Furthermore, due to the characteristics of acquisition, the first few meters cannot be detected

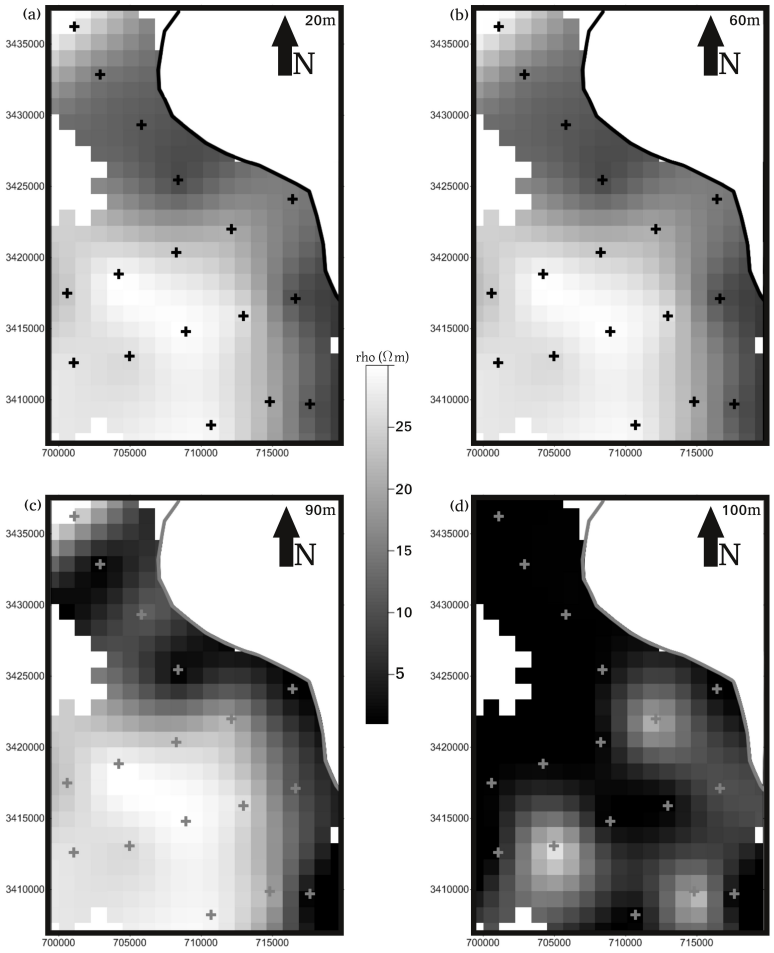

FIGURE 7.5: *Resistivity depth slices obtained with Spatially Constrained Inversion (SCI), for depths of (a) 20 m, (b) 60 m, (c) 90 m and (d) 100 m. Figure taken from Ruiz-Aguilar et al. (2018).*

and depths of investigation after Spies (1989) range from 150 to 160 m.

In Fig. 7.5, SCI inversion results are displayed as resistivity slices for depths of 20, 60, 90 and 100 m for the whole survey area. In Fig. 7.5(a-c), a resistive area is located in the central part of the valley corresponding to the permeable unit of the aquifer. More conductive zones shown in the eastern and northern parts are also related to the permeable unit of the aquifer, but with more salinity in the water. CONAGUA (2015) reported high salinity in the extracted water of the wells located near the shoreline which matches to the areas with lower resistivities. Furthermore, the variability in the conductivity at the depths slices shown (Figs. 7.5(a-c)), is mainly related to variations in groundwater quality rather than material type. In Fig. 7.5(d), the survey area is mainly conductive which is related to the semipermeable unit of the aquifer. Three resistive features are displayed representing the transition between permeable and semipermeable units of the aquifer in those areas.

In Fig. 7.6, two profiles constructed with SCI models are displayed. The location

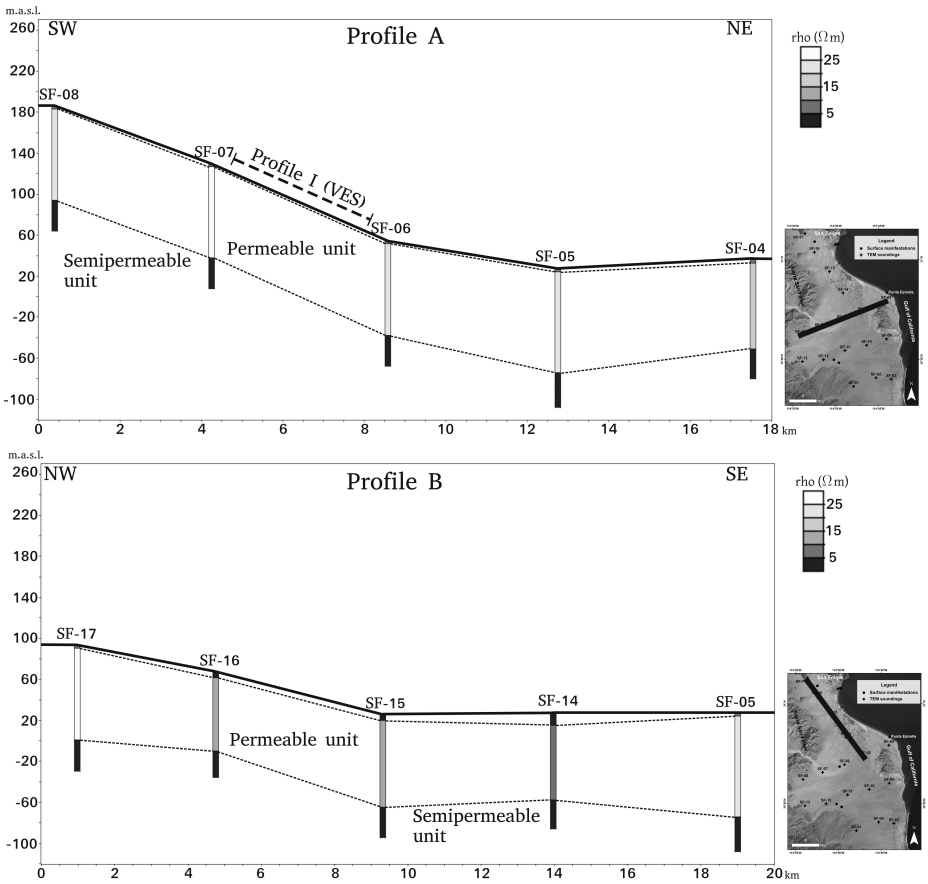

FIGURE 7.6: *Profiles constructed with Spatially Constrained Inversion models. Permeable and semipermeable units of the aquifer from San Felipe are marked. Location of the profiles in the survey area is shown on the maps. Projection of Profile I (VES) onto Profile A is also shown. Figure taken from Ruiz-Aguilar et al. (2018).*

of the profiles can be seen on the map that is shown. In both profiles, a moderate conductive surface layer overlies a resistive unit. This permeable unit is underlain by a conductive layer (semipermeable unit) which starts appearing at depths >90 m. It can be distinguished that the permeable unit has more conductive values in profile B than in profile A which is due to the high salinity concentration in areas nearer to the shoreline. In general, permeable and semipermeable units of the aquifer show continuity along the entire two profiles which agrees to the information reported in CONAGUA (2015). Moreover, a good agreement exists between profile A and profile I of Fig. 7.4. The surface layer of profile I has higher resistivities than profile A, but it must be pointed out that this layer has a poor sensitivity in the TEM models. The permeable unit is overlain by the surface layer in both profiles (profile I and A) with similar resistivities. The conductive semipermeable unit is also mapped in the two profiles, appearing at larger depths in profile I.

7.1.6 Summary of the 1D inversion of TEM data

The different 1D inversion schemes applied to TEM data were useful to describe the shallow part of the subsurface from survey area. Moreover, an updated description of San Felipe's aquifer was possible to achieve. The main results of this section are summarized as follows:

- The 1D Occam and Marquardt inversion models displayed a similar behavior at all TEM stations where two layers could be correlated to the aquifer from San Felipe.
- Based on the assumption that the survey area is located over horizontal layered sediments at shallow depths and the similarity of conventional 1D TEM inversion models, a SCI scheme was applied to the data.
- A pseudo-3D model of the subsurface was derived with the SCI inversion models and permeable and semipermeable units of San Felipe's aquifer were identified.
- The permeable unit shows a thickness ranging from 60 to 80 m; it is in the southeastern part where it shows smaller values of thickness.
- Higher conductivity values of the permeable unit were identified in the zones nearer to the shoreline indicating a high salinity in the groundwater.
- A pseudo-2D section constructed with SCI inverse models was compared to the cross section generated with VES inversion results and a good correlation exists between the interpreted layers.
- Due to the reached depths of investigation, TEM soundings are not able to map the bedrock of the aquifer.

7.2 1D inversion of MT data

Similar to the 1D inversion of TEM data (section 7.1), Occam and Marquardt techniques were applied to the MT data. Both regularizations of Occam method are firstly applied and thus, a resistivity starting model is derived to perform the Marquardt inversion. An error floor of 2.5% was used for apparent resistivities and of 10% for phases.

7.2.1 Occam inversion

The 1D Occam inversion was performed at each station using a 10 Ωm starting model. After performing trials with different starting models, a model of 50 layers with logarithmically equidistant layer thicknesses was chosen. The thickness of the first layer is 50 m and the depth of the last layer is 20 km. Therefore, the model parameterization is ensured at greater depths than the depth of investigation. Figure 7.7(a-c) displays the Occam inverse models obtained at stations

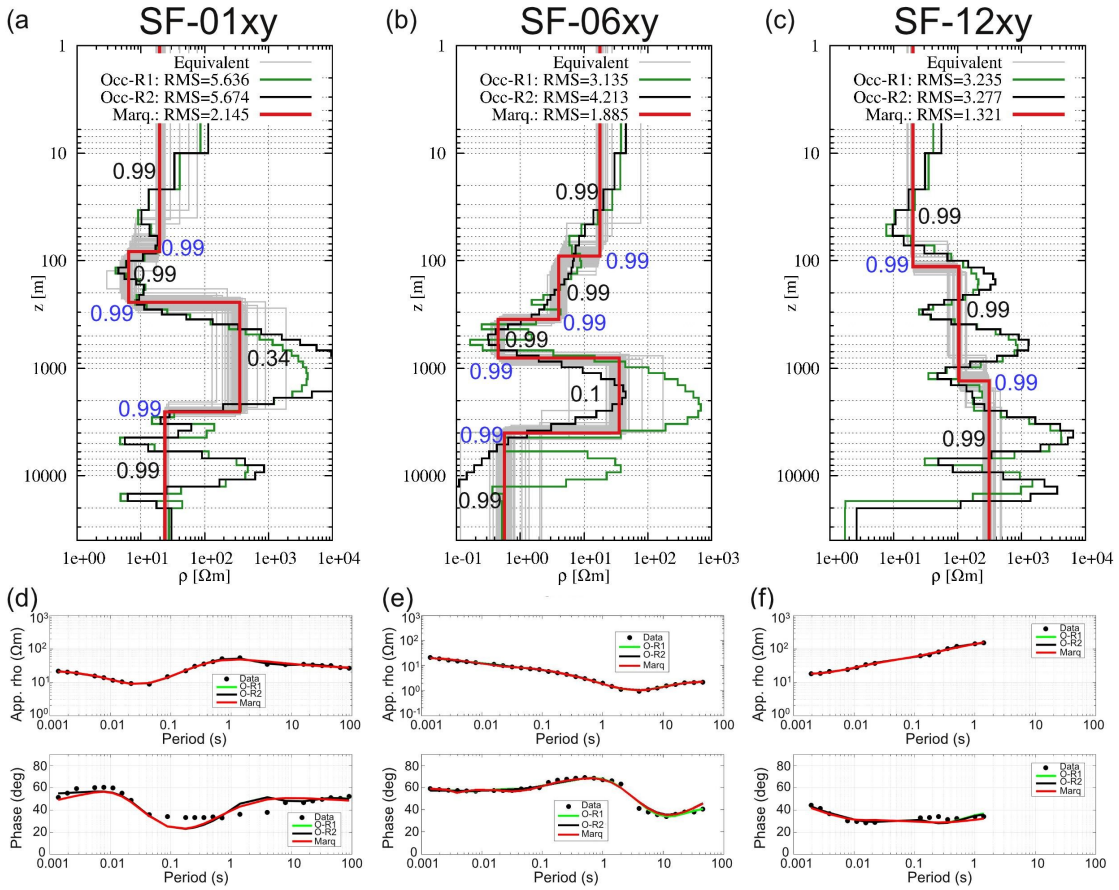

FIGURE 7.7: *(a-c) 1D Occam-R1/R2 (green and black), Marquardt (red) and Equivalent (gray) inverse models obtained at stations SF-01, SF-06, and SF-12 for the XY component. Parameter importances are marked in black for resistivities and in blue for depths. (d-f) Fitting between calculated data and observed data at stations SF-01, SF-06, and SF-12. Depths of investigation after Spies (1989) are SF-01 = 36.5km, SF-06 = 7.4km and SF-12 = 10.9km.*

SF-01, SF-06 and SF-12 for the XY component as an example. Both regularizations are shown, in green for first order derivative and in black for the second order derivative. Whereas figure 7.8(a-c) shows Occam inversion models for YX component and both regularizations, at stations SF-08, SF-11 and SF-16. The Occam inversion models obtained at the rest of stations can be seen in the Appendix E.

7.2.2 Marquardt inversion

As it has been already mentioned in subsection 7.1.2, Marquardt inversion is useful to generate a model with minimum amount of layers. The starting models to perform Marquardt inversion were derived from the Occam inverse models.

In Fig. 7.7(a-c), Marquardt inverse models obtained at stations SF-01, SF-06 and SF-12 for the XY component are shown in red as an example. At SF-01, a four-

layer model is sufficient to fit the data. The first layer has a resistivity of 19 Ωm and a thickness of 82 m. A second conductive layer extends from 82 to 243 m and has a resistivity of 6 Ωm. The third layer is rather resistive with 353 Ωm and a thickness of 2540 m. The lowest layer has a resistivity value of 23 Ωm. At SF-06, a five-layer model is needed to fit the data. The shallowest layer has a resistivity of 17 Ωm and a thickness of 90 m. The second layer has a resistivity of 4 Ωm and a thickness of 260 m. A third conductive layer extends from 350 to 802 m and has a resistivity value below 1 Ωm. The fourth and most resistive layer has a resistivity of 35 Ωm and a thickness of 3199 m. The lowest conductive layer has a resistivity of 0.5 Ωm. At SF-12, a three-layer model is sufficient to fit the data. It must be pointed out that the outliers at longer periods of this sounding were removed (*i.e.* $<$3 s). The first layer has a resistivity of 19 Ωm and a thickness of 113 m. The second layer is located between depths of 113 and 1311 m and has a resistivity of 104 Ωm. The deepest layer is rather resistive with a resistivity value of 311 Ωm.

In Fig. 7.8(a-c), Marquardt inversion models obtained at stations SF-08, SF-11, and SF-16 for the YX component are displayed as an example, in red. At SF-08, a five-layer model is required to fit the data. The first layer has a resistivity of 26 Ωm and a thickness of 55 m. A second conductive layer extends from 55 to 140 m and has a resistivity of 7 Ωm. The third layer has a resistivity value of 27 Ωm and 736 m of thickness. The fourth and most resistive layer has a resistivity of 309 Ωm and extends from 736 to 2846 m. The deepest layer has a resistivity value of 16 Ωm. At SF-11, a four-layer model is sufficient to fit the data. The shallowest layer has a resistivity of 43 Ωm and a thickness of 49 m. The second layer has a resistivity of 12 Ωm and a thickness of 83 m. A third resistive layer extends from 132 to 3189 m and has a resistivity value of 67 Ωm. The lowest layer is rather conductive and has a resistivity of 0.2 Ωm. At SF-16, a four-layer model is also sufficient to fit the data. The first layer has a resistivity of 12 Ωm and a thickness of 40 m. The second layer is located between depths of 39 and 303 m, and has a resistivity of 4 Ωm. A third layer extends from 303 to 3016 m and has a resistivity of 15 Ωm. The deepest layer is rather conductive with a resistivity value of 1 Ωm.

7.2.3 Resolution of model parameters

Equivalent models and parameter importances were obtained for the best fit Marquardt inverse model and thus, the model uncertainty and the quality of the inversion is analyzed. As it has been mentioned before in the subsection 7.1.3, when the equivalent models show high variability within a model parameter, this parameter is poorly resolved. Whereas an importance value close to 1 indicates that the model parameter is well-resolved. The approach suggested by Lippert (2015) is used (as in subsection 7.1.3), where a model parameter is well-resolved for importances between 0.71 and 1, moderately resolved for importances of 0.5 to 0.7 or poorly resolved for importances smaller than 0.5.

In Fig. 7.7(a-c), parameter importances and equivalent models are shown at stations SF-01, SF-06 and SF-12 (XY component). Black numbers represent the im-

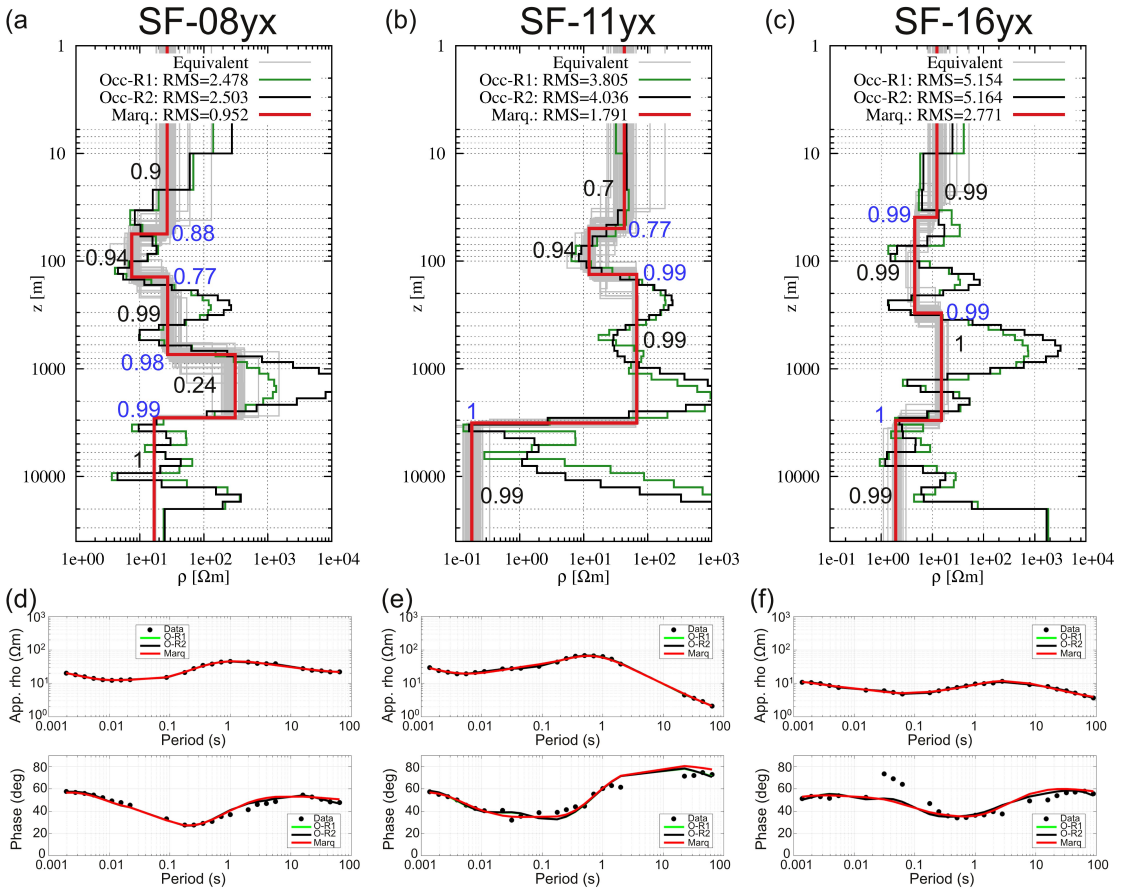

FIGURE 7.8: *(a-c) 1D Occam-R1/R2 (green and black), Marquardt (red) and Equivalent (gray) inverse models obtained at stations SF-08, SF-11, and SF-16 for the YX component. Parameter importances are marked in black for resistivities and in blue for depths. (d-f) Fitting between calculated data and observed data at stations SF-08, SF-11, and SF-16. Depths of investigation after Spies (1989) are SF-08 = 28.1km, SF-11 = 8.6km and SF-16 = 13.5km.*

portances for resistivities and blue numbers for depths. Equivalent models are in light gray. At SF-01, the resistivity of the third layer is poorly resolved, which is clearly visible by its decreased importance and large variation of the equivalent models. The rest of the model parameters have an importance of 0.99, therefore they are well resolved. At SF-06, the resistivity of the fourth layer is poorly resolved; it has an importance value of 0.1 and the equivalent models show large variations. While the rest of the model parameters are well resolved: equivalent models show limited variations and the importances are close to 1. At SF-12, the importances of all the model parameters are 0.99, indicating that they are well resolved. The equivalent models confirm the above mentioned by showing limited variations.

In Fig. 7.8(a-c), parameter importances and equivalent models are shown at stations SF-08, SF-11 and SF-16 (YX component). Black numbers represent the importances for resistivities and blue numbers for depths. Equivalent models are in

light gray. At SF-08, the resistivity of the fourth layer is poorly resolved; it has an importance value of 0.24 and the equivalent models show large variation. While the rest of the model parameters are well resolved; equivalent models show short variations and the importances are between 0.71 and 1. At SF-11, the resistivity of the first layer is moderately resolved; it has an importance of 0.7 and the equivalent models show large variation. The rest of the model parameters are well-resolved, with importances close to 1 and limited variation of the equivalent models. At SF-12, the importances of all model parameters are between 0.99 and 1, therefore they are well resolved.

7.2.4 Comparison of 1D MT and TEM inversion models

It is evident that MT and TEM inversion models can be compared only at shallow depths due to their different depths of penetration. In this sense, the second and third layer of the TEM inverse models are compared to the first and second layer of the MT inversion models. It is useless to compare the first layer of TEM inversion models because MT definitely does not have resolution at such depths.

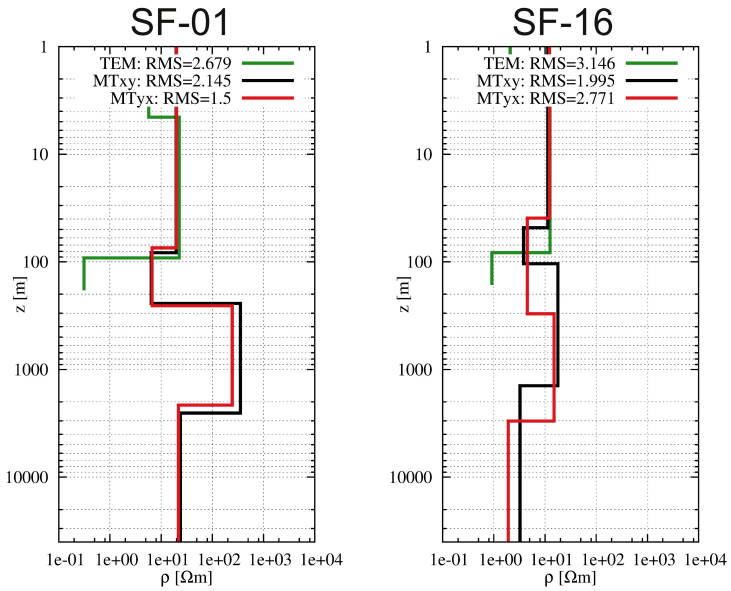

FIGURE 7.9: *Comparison between 1D MT and TEM inversion models at stations SF-01 and SF-16.*

In Fig. 7.9, comparisons between 1D MT and TEM inversion models at two selected stations are shown as an example. At station SF-01, the first layer of the MT inverse models show similar resistivity compared to the second layer of the TEM inversion model. A slight difference exists on the depth of the subsequent conductive layer (second layer in the MT inversion models and third layer in the TEM inverse model), $\sim$ 10 m between MTxy and TEM inverse model, while $\sim$ 17 m between MTyx and TEM inversion models. The resistivity of this conductive layer is clearly different between MT inverse models and TEM inversion model,

$\sim$ 6 Ωm in the MT models and 0.3 Ωm in the TEM model. At SF-16, the resistivities of MT models first layer and TEM model second layer are identical. The depth of the underlain conductive layer differs between the inverse models; it is located at 82 m in the TEM model, while at 48 m in MTxy model and at 39 m in MTyx model. The resistivity of this conductive layer is of $\sim$ 6 Ωm in the MT models, which is greater than in the TEM model.

7.3 2D inversion of MT data

Although the dimensionality analysis suggested that the subsurface structure is 1D and 3D, this section deals with the 2D inversion of MT data. The non-linear conjugate gradient (NLCG) algorithm (Rodi and Mackie, 2001) described in section 3.6 was applied for performing the 2D MT inversion routines. The version of this algorithm implemented in WingLink software package was used. At first, the impedance tensor of each station was rotated based on the geo-electric strike analysis carried out in subsection 5.2.4 and thus, the decouple on TM and TE mode was done. For the data in the E-polarization (TE mode) the electric currents flow parallel to the strike direction and for the B-polarization (TM mode) data, the electric currents flow perpendicular to the strike direction. Due to the low quality of VTF elements, the inversion runs including them showed poor results and therefore they are not presented in this section. For the 2D inversion of the MT data at the four different profiles, a 10 Ωm starting model was chosen after performing trials with different values and appraising their results. The 2D staggered grid for each profile's model was constructed such that the grid columns below the stations have a width of 0.5 skin depth. To investigate that the discretization of the models was optimal, a forward calculation to the 10 Ωm background models was performed and it was corroborated if at each station the response of such homogeneous half-space was obtained, *i.e.* apparent resistivities of 10 Ωm and phases of 45° for all the frequencies. In presence of static shift, downweighting of the apparent resistivities against the phases is a common procedure in 2D inversion (Tietze, 2012; Becken et al., 2011). In the 2D inversion of San Felipe data, however, the phases are downweigthed. The static shift effect observed in the MT field data was corrected based on the TEM data, therefore the more weight assigned to the apparent resistivities. The procedure explained in subsection 5.2.5 for correcting the static shift was also applied to the TE and TM apparent resistivity curves. Thus, error floors of 5% were assigned to the apparent resistivities and 10% to the phases for both modes. To find out a suitable regularization parameter such that neither the smoothing term nor the data misfit dominates in the cost function, the so-called L-curve was utilized (see Appendix F). A regularization parameter τ of 30 was optimal at the inversion of data from the four different profiles[1].

Figure 7.10 displays the results of the 2D inversion of MT data from the four dif-

[1]Note that τ is identical to the regularization parameter λ. It is referred as τ in this section to be consistent with Rodi and Mackie (2001).

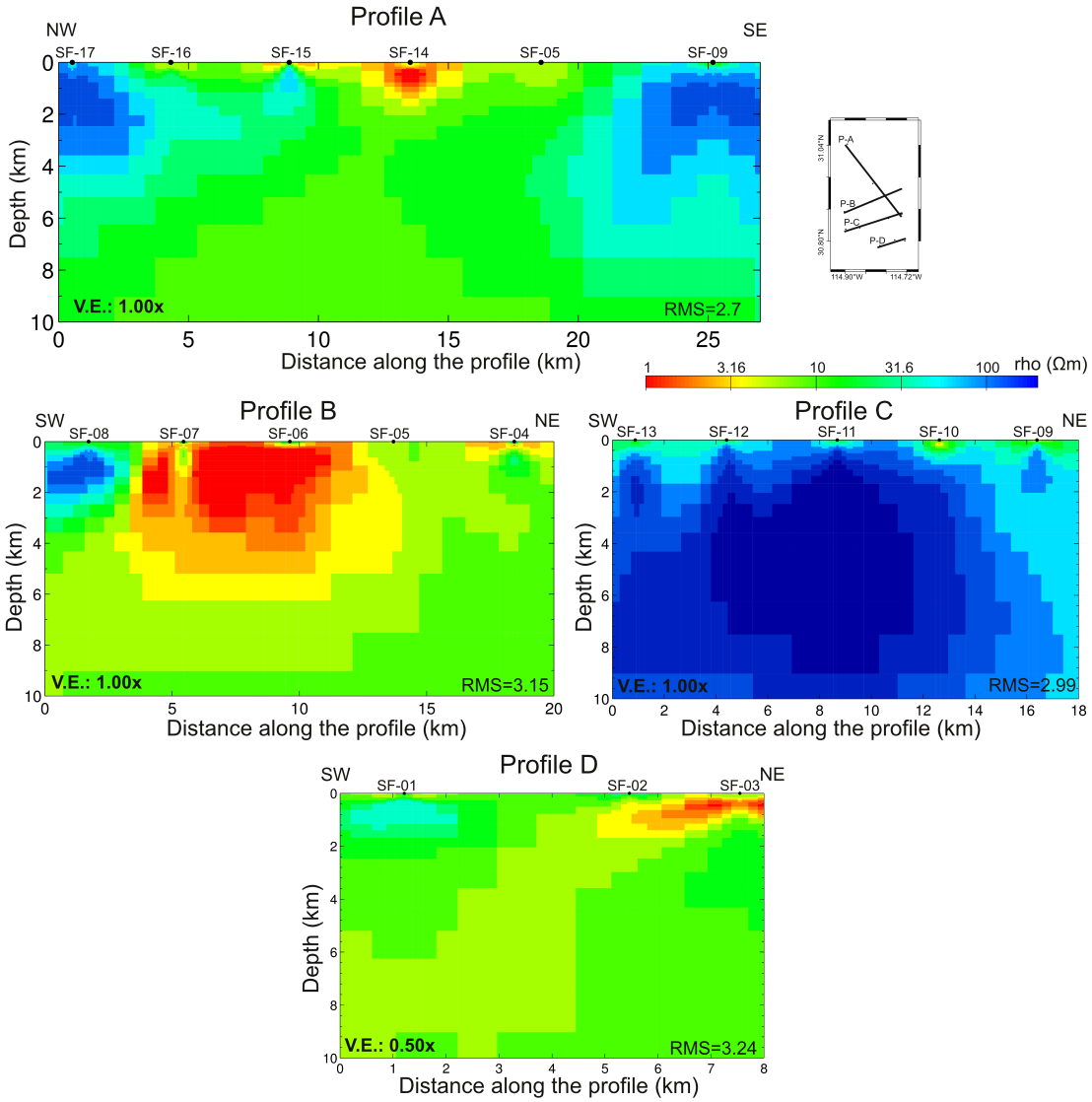

FIGURE 7.10: *Results of the 2D inversion of TE and TM data from the four different profiles.*

ferent profiles. At profile A, a resistor is distinguished in the northwestern part. This resistor extends from shallow depths to $\sim$ 5 km below station SF-17. In the central part of the profile, a conductor is derived from shallow depths to $\sim$ 1.5 km. Whereas in the southeastern area of the profile, a resistor is imaged with a thickness of $\sim$ 7 km. At the profile B, a resistor extends from depths of $\sim$ 500 m to 3 km in the southwestern part. In the central area, a conductor is imaged with a thickness of $\sim$ 6 km. Another conductor can be distinguished in the shallowest part of the northeastern area of the profile (below SF-04). This conductor has a thickness of $\sim$ 300 m. At profile C, a resistor is derived along the entire section and it shows a thickness of $\sim$ 10 km. Finally at profile D, a resistor is distinguished under the site SF-01 and it extends from depths of $\sim$ 300 m to 1.5 km. In the northeastern part of the profile, a conductor is derived at shallow depths.

This conductor is constrained by data from stations SF-02 and SF-03 and it has a thickness that varies from 500 to 1500 m.

As it was already mentioned, the dimensionality analysis suggested a 1D and 3D subsurface structure, therefore these 2D inversion results are not reliable for correlating them to the geological information. Nevertheless, the 2D inversion results are compared to the achieved 3D inverse model in the subsequent chapter. Furthermore, the geological interpretation based on MT data is also described in the following chapter.

Chapter No. 8

3D Inversion of Magnetotelluric data

This chapter deals with the three-dimensional inversion of MT data collected in San Felipe. Firstly, a theoretical overview of the used inversion algorithm is given. As it was showed with the modeling studies described earlier in this thesis, the input parameters for the 3D inversion must be systematically tested before achieving an optimal inverse model. The influence of these parameters are firstly analyzed on the inversion of the off-diagonal elements. Similar to section 6.6, the impact of the regularization and smoothing parameters are described only for the anti-diagonal components inversion. Whereas the influence of the data errors settings is investigated on the inversion of the off-diagonal, full impedance and full impedance-VTF components. A comparison between the inverse models obtained with each data set is done and the one with most reasonable results is used for further analyses.

Later on, sensitivity studies are carried out to determine the depth of investigation and reliability of the structures derived by the inversion. Afterwards, it is described how the TEM data is incorporated into the 3D inversion scheme of MT data. Thus, the 3D MT inversion is stabilized and its results are enhanced. Finally, the preferred 3D inversion model is correlated to the geological information of San Felipe.

8.1 3D MT inversion modeling

The inversion scheme implemented in ModEM software (Kelbert et al., 2014) is based on the minimization of the cost function:

$$\boldsymbol{\Phi} = \left(\boldsymbol{d} - \boldsymbol{d}'\right)^T \boldsymbol{C}_d^{-1} \left(\boldsymbol{d} - \boldsymbol{d}'\right) + \lambda \left(\boldsymbol{m}\right)^T \boldsymbol{C}_m^{-1} \left(\boldsymbol{m} - \boldsymbol{m}_0\right) \tag{8.1}$$

where $\boldsymbol{d}$ is the observed data, $\boldsymbol{d}'$ is the calculated data. The data errors are contained in the covariance matrix $\boldsymbol{C}_d$. The vector $\boldsymbol{m}$ contains the model parameters. A set of prior model parameters is contained in the vector $\boldsymbol{m}_0$. The matrix $\boldsymbol{C}_m$

is the model covariance which describes the model smoothness and λ is the so-called regularization or trade-off parameter.

In the ModEM algorithm, the data covariance $\boldsymbol{C}_d$ is a diagonal matrix which contains the inverse of the squared data errors. Note that $\boldsymbol{C}_d$ is identical to the matrix $\boldsymbol{W}_d^2$ described in section 3.1. The model covariance matrix $\boldsymbol{C}_m$ is constructed as a sequence of 1D smoothing and scaling operators (Tietze, 2012):

$$\boldsymbol{C}_m = \boldsymbol{C}_x \boldsymbol{C}_y \boldsymbol{C}_z \boldsymbol{C}_z^T \boldsymbol{C}_y^T \boldsymbol{C}_x^T \tag{8.2}$$

The 1D smoothing operators are block-diagonal:

$$\boldsymbol{C}_x = \begin{pmatrix} \boldsymbol{C}_{11}^x & & & \\ & \boldsymbol{C}_{21}^x & & \\ & & \ddots & \\ & & & \boldsymbol{C}_{N_y N_z}^x \end{pmatrix} \tag{8.3}$$

Likewise for $\boldsymbol{C}_y$ and $\boldsymbol{C}_z$. Each block $\boldsymbol{C}_{jk}^x$ is formed by an autoregression scheme:

$$\boldsymbol{C}_{jk}^x = \begin{pmatrix} 1 & & & \\ \alpha_x & 1 & & \\ \alpha_x^2 & \alpha_x & 1 & \\ \vdots & & & \ddots \\ \alpha_x^{Nx-1} & & \cdots & 1 \end{pmatrix} \tag{8.4}$$

The parameter α_x defines the model smoothness in x direction. Identical procedure is done for assigning the smoothness in y and z directions. The smoothing parameter is chosen between 0 and 1, where higher values results in smoother models. The cost function (eq. 8.1) is minimized using a nonlinear conjugate gradients inversion approach. The regularization parameter λ is selected to an initial value and it decreases during the inversion routine.

8.2 Off-diagonal elements inversion

As a first approach, 3D inversion of MT data from San Felipe is carried out only using the off-diagonal elements of the impedance tensor. Newman et al. (2008) found that including the on-diagonal elements of the impedance tensor degrades the performance of the 3D inversion because of their lower magnitudes. Furthermore, the inversion of only the off diagonal impedances represents a good practice to have a first image of the conductivity distribution and for identifying which parts of the inverse model are constrained by the anti-diagonal components.

8.2.1 Starting models

The selection of a suitable prior or background resistivity model is important in the 3D inversion scheme because it is the starting point for the optimization and

defines the penalty functional. In this regard, inversion runs with different starting models are firstly performed in order to select the most appropriate one for further interpretations. The starting models consisted of a homogeneous half-space with 1, 10, 30 and 100 Ωm. The Pacific ocean and Gulf of California were embedded in all the models. The 3D finite difference grid contains $54 \times 50 \times 56$ nodes in the x, y and z directions, respectively. As it was demonstrated in the modeling investigation described in section 6.3, a mesh with cells 1000 m sided within the data coverage part is the most suitable for the San Felipe field data. The first vertical layer has a thickness of 15 m and the subsequent layers were increased by a factor of 1.2. Since the terrain slopes in the survey area are less than 1°, topography is not included. Thus, inversion runs were carried out to the off-diagonal data set and using the four different background resistivity models as starting point. All the runs were performed with the same input parameters. Data errors were set to 5% of $|Zxy * Zyx|^{1/2}$.

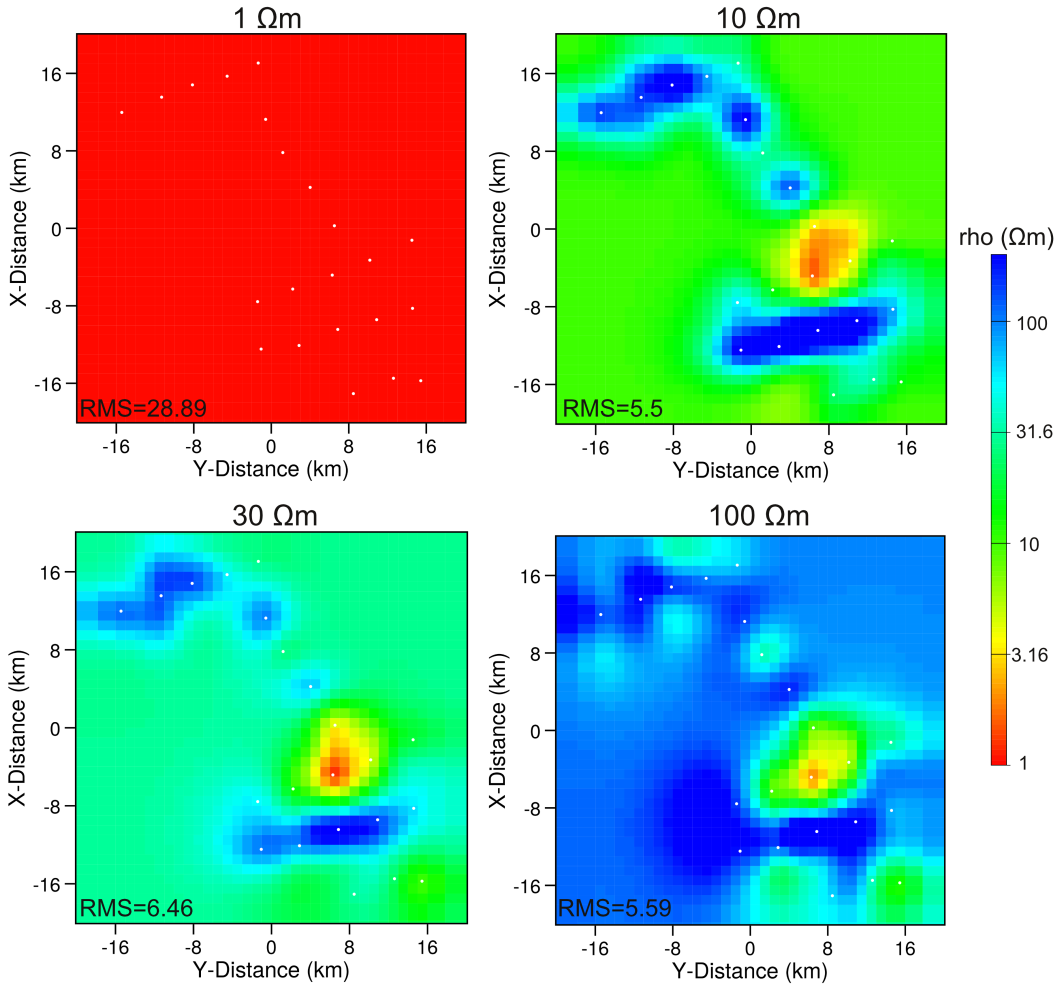

FIGURE 8.1: *Results of the off-diagonal elements inversion with four different starting models presented as resistivity slices at depths of ∼ 1.8 km. The MT stations are marked with white dots.*

The results of the four different inversion trials are displayed in Fig. 8.1 as resistivity slices at depths of $\sim$ 1800 m. It is clearly visible that the inversion with a starting model of 1 Ωm was not successful, the resistivity values remained at the same level not only outside of the survey area but also within it. At the iteration 0 (*i.e.* forward modeling) the misfit was of 29.7 and after 11 iterations the inversion process finished with a RMS of 28.89.

TABLE 8.1: *Initial and final RMS values of the off-diagonal inversion trials with different starting models.*

Starting Model	Initial RMS	Final RMS
1 Ωm	29.7	28.89
10 Ωm	19.15	5.5
30 Ωm	28.24	6.46
100 Ωm	67.29	5.59

Moreover, the quasi-minimum residual (Kelbert et al., 2014) iterative forward solver could not find a minimum at each inversion iteration with the used starting model. In contrast, the inversion with the 10 Ωm background model shows a more feasible result. The starting misfit was of 19.15 and after 24 iterations a RMS of 5.5 was reached. At the depth slice obtained of this inversion model (Fig. 8.1), resistive and conductive bodies can be distinguished within the survey area. Whereas identical resistivities to the starting model remained outside of the data coverage. The inversion run with a 30 Ωm starting model finished after 20 iterations and the misfit decreased from 28.24 to 6.46 (Table 8.1). Similar to the results of the inversion with the 10 Ωm background model, resistive and conductive bodies are also distinguished in the depth slice of this inverse model. Finally, the inversion trial with the 100 Ωm starting model showed an initial misfit of 67.29 and it decreased to 5.59 after 29 iterations.

In general, the inversion results show that the resistivities of the used starting model remain in areas where data coverage is insufficient. An exception is the inversion of the 1 Ωm background model, but it has been already pointed out that the forward solver could not find a minimum during the divergence correction. In this sense, the tolerance of the quasi-minimum residual (QMR) iterative solver could be modified to get a different result, but then it would not be comparable to the other inversion runs. Furthermore, the rest of the runs showed reasonable results and therefore, the QMR tolerance was kept at the same value.

As it can be distinguished in Table 8.1, the different inversion trials reached comparable RMS values, except the inversion with a 1 Ωm starting model which shows a RMS of 28.89. To decide which model is more suitable as a starting point for the optimization, the initial misfit was used as a reference. In this regard, the 10 Ωm starting model showed the lowest RMS at the iteration 0 of the inversion run (*e.g.* 19.15) and therefore, it was taken as the prior model for the subsequent inversion routines.

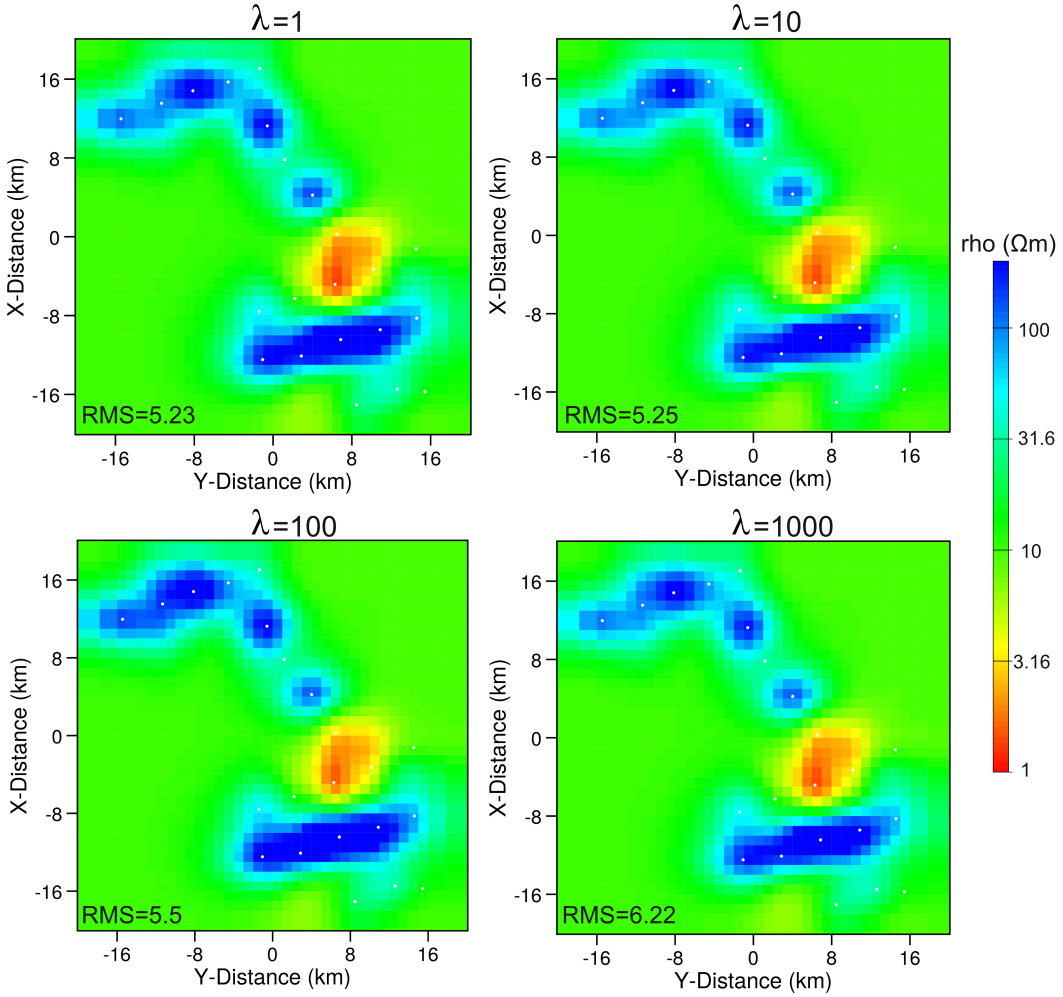

FIGURE 8.2: *Results of the off-diagonal elements inversion with different λ values presented as resistivity slices at depths of $\sim$ 1.8 km. The MT stations are marked with white dots.*

8.2.2 Regularization parameter λ

The trade-off parameter λ defines the balance between data fit and model smoothness. This regularization parameter is selected by the user and it decreases during the inversion routine. Similar to the modeling study described in subsection 6.6.1, trials with initial λ values of 1, 10, 100 and 1000 were carried out to assess the different inverse models. A 10 Ωm half-space starting model was utilized at all the runs (with the Pacific ocean and Gulf of California embedded). Data errors were set to 5% of $|Zxy * Zyx|^{1/2}$. The rest of the input parameters were identical for all the trials.

Figure 8.2 shows the results of the four different inversion trials as resistivity slices at depths of $\sim$ 1800 m. No remarkable differences are noticed in the conductivity distribution of the four inverse models. However, the differences are more notorious in the data misfit (Fig. 8.3). The inversion with the highest reg-

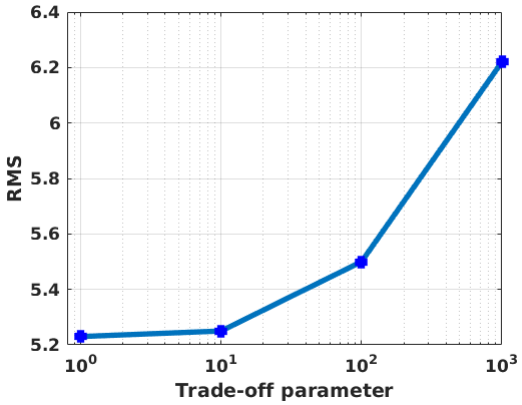

λ	RMS
1	5.23
10	5.25
100	5.5
1000	6.22

FIGURE 8.3: *Final RMS values of the off-diagonal inversion trials with different starting values for the regularization parameter.*

ularization parameter ($\lambda = 1000$) reached a RMS of 6.22. Whereas the inversion run of the lowest trade-off parameter ($\lambda = 1$) showed a final RMS of 5.23. These results make sense, when the regularization parameter is set to an initial high value the smoothing is more dominant than with a lower λ value. While the data misfit is more relevant when the initial trade-off parameter is set to a lower value. For instance, the graph of Fig. 8.3 illustrates that the data misfit is lower at decreased values of λ. A starting value for the regularization parameter of 100 was taken for the subsequent inversions because it shows an acceptable RMS and its relative high value also gives importance to the model smoothness.

8.2.3 Model Coviarance parameter

As it was earlier mentioned in this thesis, the model covariance α describes the model smoothness and can be independently defined along the three different directions. The procedure described in the modeling investigation of subsection 6.6.2 is here followed, where inversion trials with isotropic α values of 0.1, 0.3, 0.5, 0.7 and 0.9 are performed to evaluate the impact of the smoothing parameter. A 10 Ωm half-space starting model was utilized at all the trials (with the Pacific ocean and Gulf of California embedded). The trade-off parameter λ was set to an initial value of 100. Data errors were set to 5% of $|Zxy * Zyx|^{1/2}$.

The inversion results of all the trials are displayed in Fig. 8.4 as resistivity slices at depths of $\sim$ 1800 m. The differences between the inverse models due to the used smoothing parameter are notorious. The inversion model of $\alpha = 0.1$ shows mainly local resistivity bodies nearby the stations. At the inverse model of $\alpha = 0.3$, the smoothness is high enough to connect the model parameters of cells further to the MT sites. At the inversion model with $\alpha = 0.5$, the resistivity bodies show greater dimensions due to higher value of the smoothing parameter. The inversion model slice of $\alpha = 0.7$ displays a connected large scale resistive body, but the separation between the stations area from the north and south is roughly 20 km and consequently, the model parameters within this data gap have zero

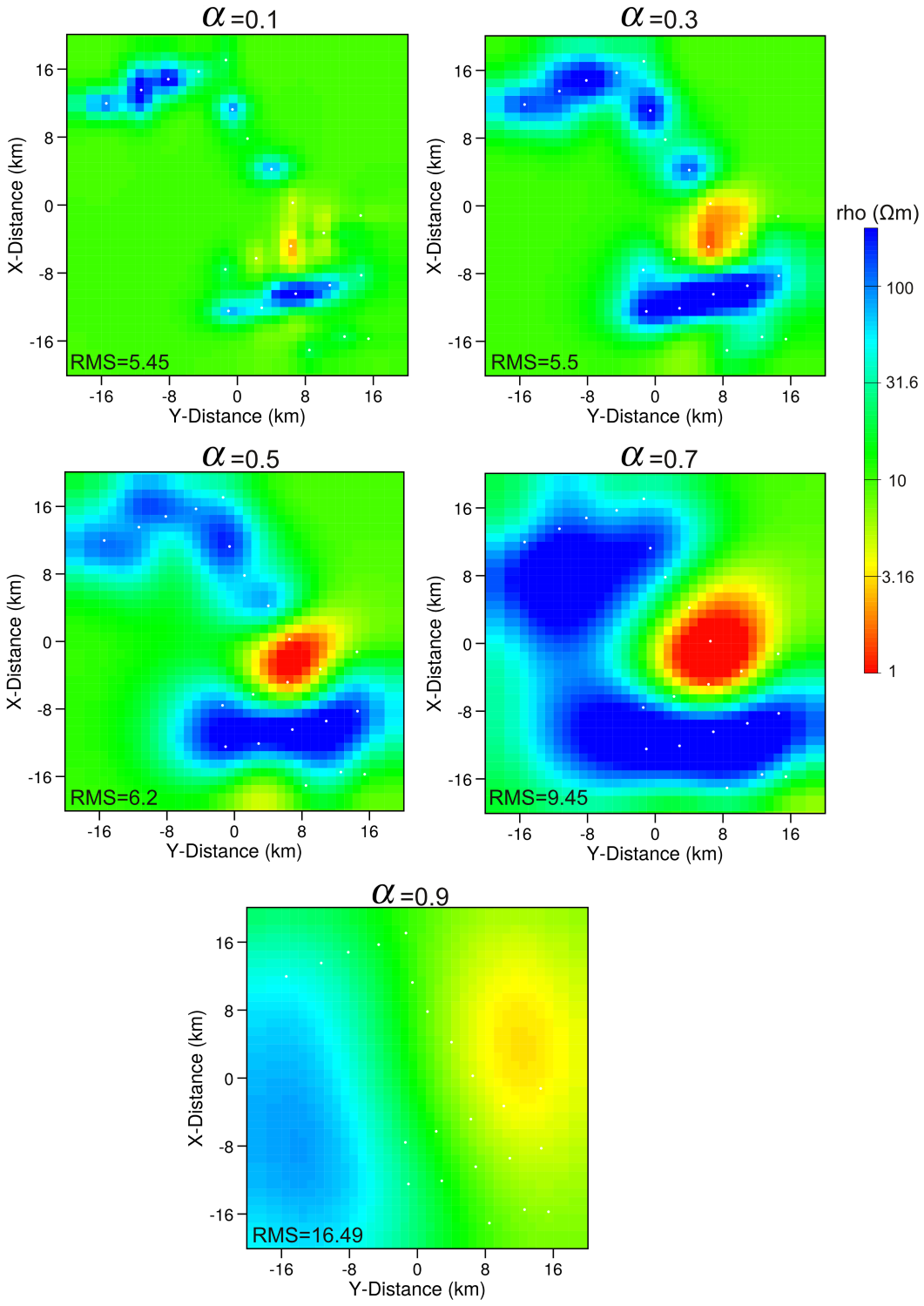

FIGURE 8.4: *Results of the off-diagonal elements inversion with different α values presented as resistivity slices at depths of ∼ 1.8 km. The MT stations are marked with white dots.*

sensitivities. The conductive body also displays greater dimensions and extends

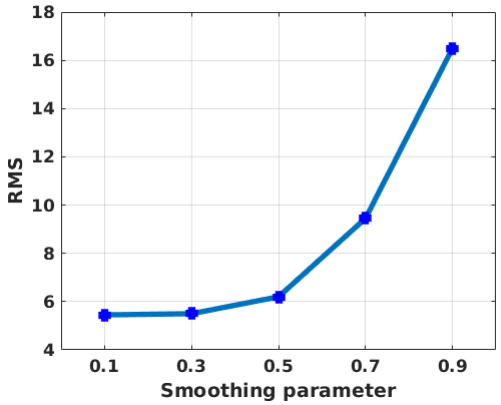

α	RMS
0.1	5.45
0.3	5.5
0.5	6.2
0.7	9.45
0.9	16.49

FIGURE 8.5: *Final RMS values of the off-diagonal inversion trials with different smoothing parameters.*

to areas where data coverage is inexistent. Finally, the inversion model of $\alpha = 0.9$ shows a completely different conductivity distribution where a resistive area is distinguished in the western part and a conductive zone in the eastern area. These two features are outside of the stations coverage, therefore this inversion result is not plausible.

Figure 8.5 shows the RMS values obtained at each inversion run. The higher the smoothing parameter is, a higher RMS is then obtained. A compromise between the data misfit and the model smoothness must be taken into account, therefore a value of $\alpha = 0.3$ was taken because it showed an acceptable RMS and a reasonable model smoothness.

8.2.4 Data errors

As it was demonstrated in the modeling investigation of subsection 6.6.3, data error settings is also an important input inversion parameter that must be systematically tested to define the most suitable for the given data set. In this thesis, the data errors were set relative to the mean of the off-diagonal impedances $|Zxy * Zyx|^{1/2}$ (Meqbel, 2009; Patro and Egbert, 2011; Tietze, 2012). Thus, trials with different data errors were carried out, which were varied from 1% to 30% of $|Zxy * Zyx|^{1/2}$. Identical inversion input parameters were set at all the inversion runs: a initial trade-off parameter of 100, a smoothing parameter of 0.3 and a 10 Ωm homogeneous half-space (with the Pacific ocean and gulf of California embedded) as a starting model. Considering the final RMS obtained at each trial, inversion runs with errors of 1% and 2% show huge data misfit (Fig. 8.6). While runs with errors of $\geq$ 10% present low misfit, which it is expected[1].

In addition, the results of inversion runs with data errors of 1, 3, 5 and 30 % are shown in Fig. 8.7 as resistivity slices at depths of $\sim$ 1800 m. The inverse models

[1]From the equation to calculate the RMS, a lower RMS value results if high data errors are used.

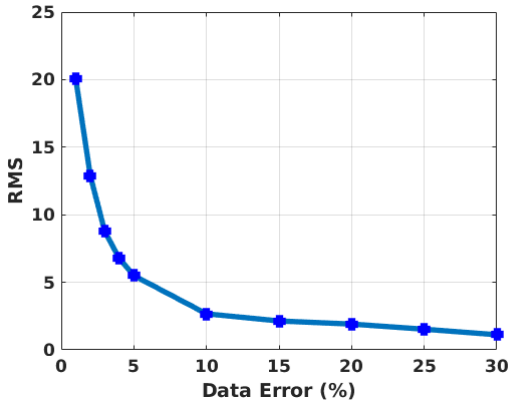

FIGURE 8.6: *Final RMS values of the off-diagonal inversion trials with different data errors. Note that data errors were set relative to the mean of the off-diagonal impedances* $|\mathrm{Zxy} * \mathrm{Zyx}|^{1/2}$.

with data errors of 3, 5 and 30 % show roughly similar conductivity distribution. In contrast, a different resistivity distribution is displayed at the inverse model of 1% of data error. At this inverse model, the northern resistive body has greater dimensions, the central conductor also shows greater dimensions. The southern resistor extends a bit further to the south and displays greater dimensions as well. A suspicious conductive body is distinguished at the southern part, which is not feasible because it is located outside of the MT stations coverage and therefore the model parameters in this area have zero or minimum sensitivities. The main diagonal elements are important for imaging off profile structures (Siripunvaraporn et al., 2005), consequently this conductor outside of the data coverage derived from the inversion of the anti-diagonal impedances is not reliable. Moreover, a similar result was obtained in the modeling investigation of subsection 6.6.3 where the off-diagonal elements inversion with data errors of 1% also derived structures outside of the data coverage with resistivities four times smaller than the resistivity of the starting model.

The slices of the inversion models of 3 and 5 % of data errors are quite similar, only the southern suspicious conductor is slightly more vanished at the inverse model with 5 % of data error. The inverse model of 30 % of data error shows the features with shorter dimensions because part of the information contained in the Z_{xy} and Z_{yx} components is lost due to the high data error setting. In this sense, the data errors of 5 % were taken for the subsequent inversions because it seems that no information is lost while reaching an acceptable RMS of 5.5.

Thereby, the preferred model for the off-diagonal elements inversion is the one obtained with 10 Ωm background model (Pacific ocean and Gulf of California are embedded), $\lambda = 100$, $\alpha = 0.3$ (at all directions) and data errors set to 5 % of $|\mathrm{Zxy} * \mathrm{Zyx}|^{1/2}$.

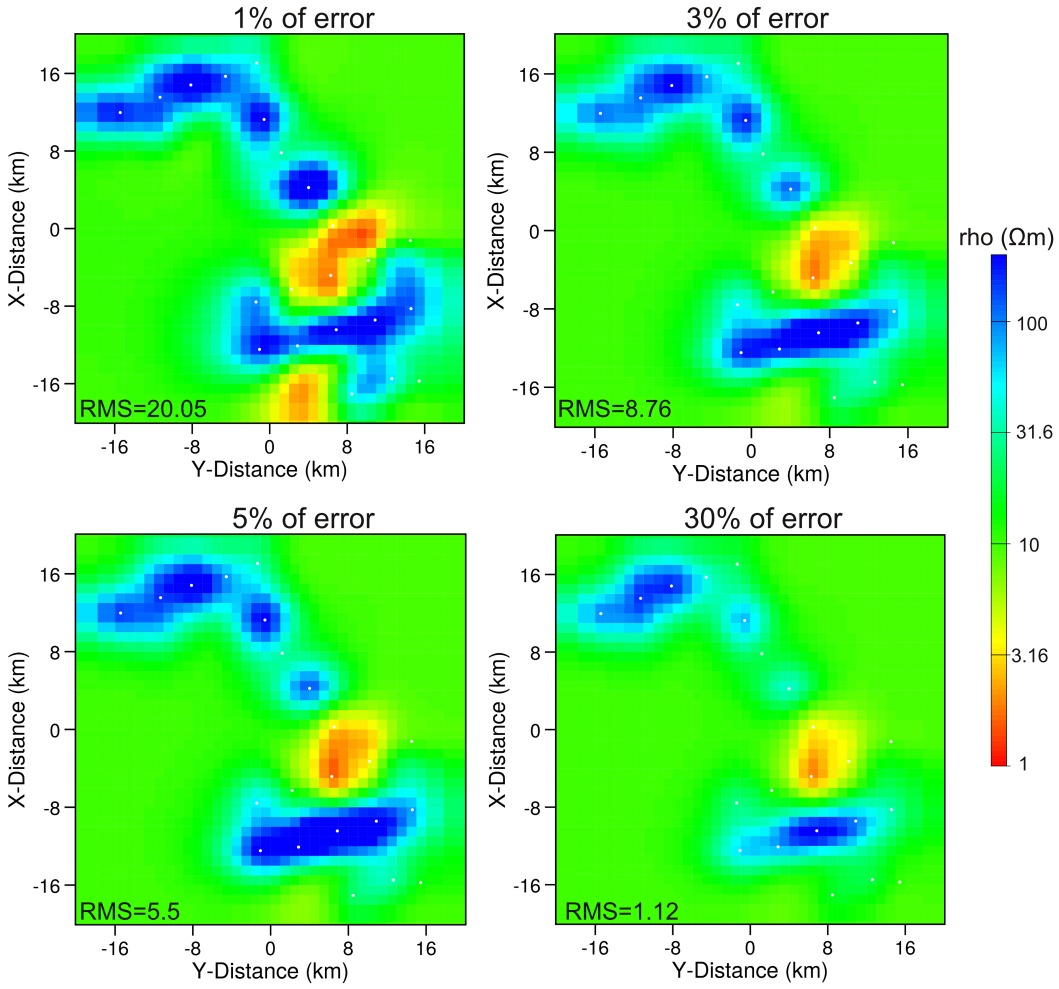

FIGURE 8.7: *Results of the off-diagonal elements inversion with different data errors presented as resistivity slices at depths of ∼ 1.8 km. The MT stations are marked with white dots. Note that data errors were set relative to the mean of the off-diagonal impedances* $|\mathrm{Zxy} * \mathrm{Zyx}|^{1/2}$.

8.3 Full impedance tensor inversion

Similar to section 8.2, trials were carried out to evaluate the impact of the input parameters on the inversion of the full impedance tensor. The inversion runs with different λ and α values showed identical results to the ones obtained with the off-diagonal impedances inversion, so that only the inversion trials results with different data errors are discussed in this section.

8.3.1 Data errors

To investigate the influence of the data errors on the inversion of the full impedance tensor several trials were carried out varying only the errors of the main diagonal elements. The data errors for Z_{xy} and Z_{yx} components were set to 5 %

of $|Zxy * Zyx|^{1/2}$, since reasonable results were obtained during the inversion of the off-diagonal elements with such errors (see subsection 8.2.4). Whereas for the main diagonal components, data errors were varied from 1 to 30 % of $|Zxy * Zyx|^{1/2}$. It is obvious that lower values than 5 % would give more weight to the noisy main diagonal elements and thus information of the off-diagonal components might be lost, however they were considered in order to investigate their inversion output.

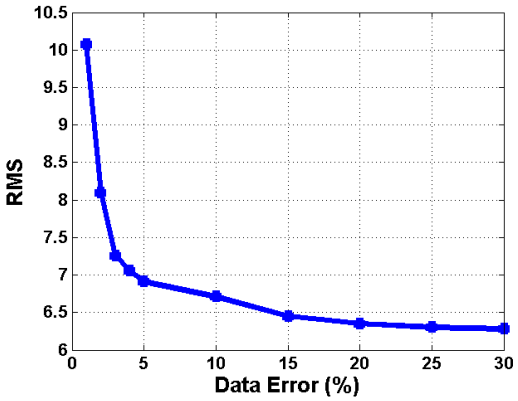

FIGURE 8.8: *Final RMS values of the full impedance inversion trials with different data errors. Note that data errors were set relative to the mean of the off-diagonal impedances* $|Zxy * Zyx|^{1/2}$ *and only the errors for the main diagonal components were varied.*

Figure 8.8 displays a graph where the final RMS values obtained at each inversion trial of the different data error settings are plotted. As it is expected, the inversion trial with data errors of 30 % for the main diagonal components of the impedance tensor shows the best data misfit, while the trials with data errors $< 5\%$ display higher RMS's.

The results of four inversion runs are shown in Fig. 8.9 as resistivity slices at depths of $\sim$ 1800 m. At the inverse model with 1% of data errors, the derived bodies display greater dimensions than in the rest of the inversion models and suspicious conductors are obtained within and outside of the data coverage. The northern resistor is imaged several kilometers further from the MT profile located at this area, which is unreliable. Taking into account that no additional MT stations exist north to such profile and based on the fact that a single profile can image off-profile structure up to $\sim$3 km further from the profile with the given conditions (see Appendix G), the dimensions of this resistor are unreliable. Similarly the resistor located in the central part shows large dimensions and no profile exists parallel to the one situated above such a resistive body. Therefore, the inversion trial with 1% of data errors does not show a reasonable result. At the inversion model with 5% of data errors, the bodies display shorter dimensions and the suspicious conductors within the stations coverage are vanished. Only a conductor south from the survey area is still derived, but with increased resistivity.

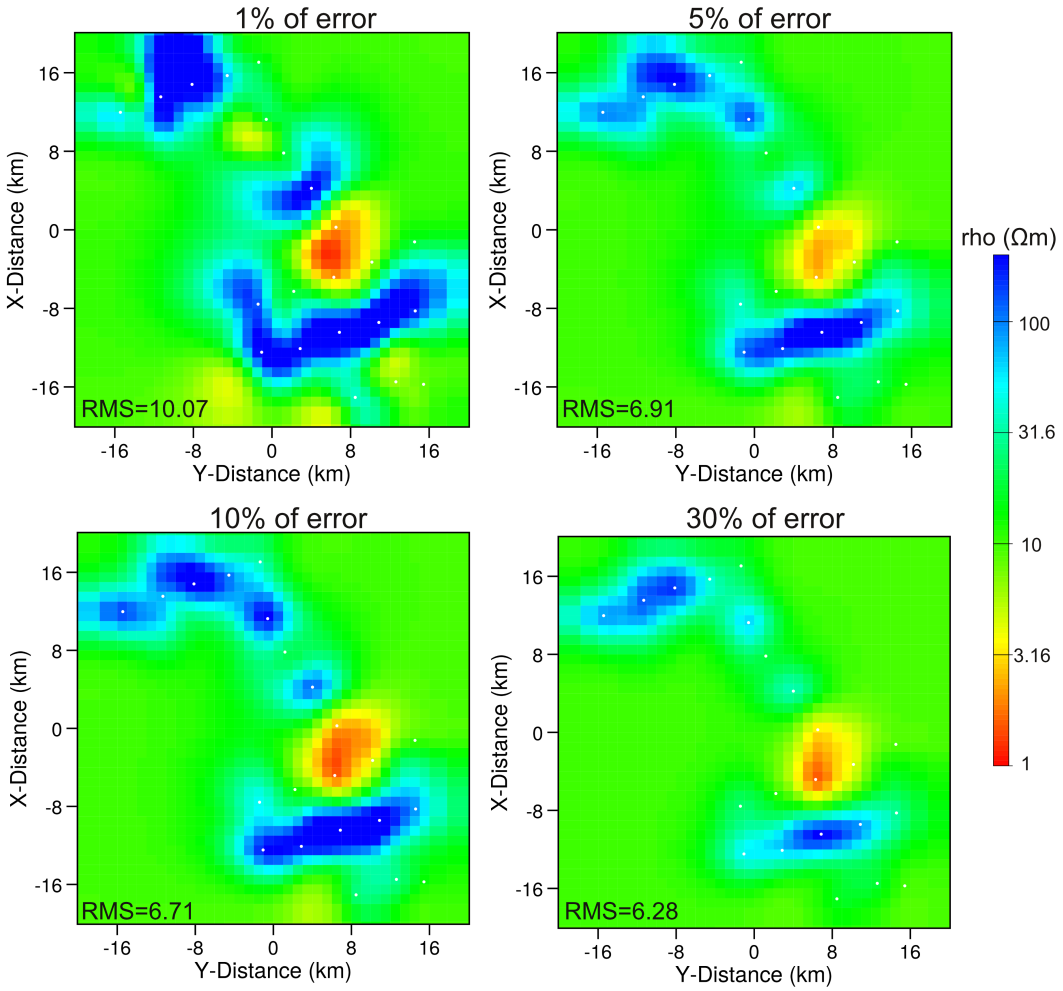

FIGURE 8.9: *Results of the full impedance elements inversion with different data errors presented as resistivity slices at depths of ∼ 1.8 km. The MT stations are marked with white dots. Note that data errors were set relative to the mean of the off-diagonal impedances* $|\mathrm{Zxy} * \mathrm{Zyx}|^{1/2}$ *and only the errors for the main diagonal components were varied.*

The northern resistor shows now greater dimensions to the southeast direction but within the data coverage. The dimensions of the central resistor are also decreased. At the inversion model with 10% of data errors, the resistive bodies have similar dimensions to the ones of the 5% data errors, however, the conductive structure is differently derived. This conductor shows now greater dimensions but restricted to the data coverage. At the inverse model with 30% of data errors the bodies show shorter dimensions, which it is expected due to the loss of information while severely downweighting the main diagonal impedances. Thereby, the preferred model for the full impedance elements inversion is the one obtained with data errors set to 5 % of $|\mathrm{Zxy} * \mathrm{Zyx}|^{1/2}$ for the anti-diagonal and 10 % for the main diagonal components.

8.4 Full impedance tensor and VTF elements inversion

As section 8.3, only the results of varying the data errors at inversion trials of the full impedance tensor and VTF elements are discussed. Inversion runs varying the regularization and smoothing parameters showed identical results to the ones discussed in the off-diagonal elements inversion.

8.4.1 Data errors

For this case inversion trials were carried out varying only the data errors of the VTF elements from 1 to 30% to evaluate their influence on the inversion models. Whereas the data errors for the off-diagonal components were set to 5 % and the main diagonals to 10 % of $|Zxy * Zyx|^{1/2}$ at all the inversion runs because with such error settings the most reasonable inverse model was obtained for the full impedance inversion (see subsection 8.3.1).

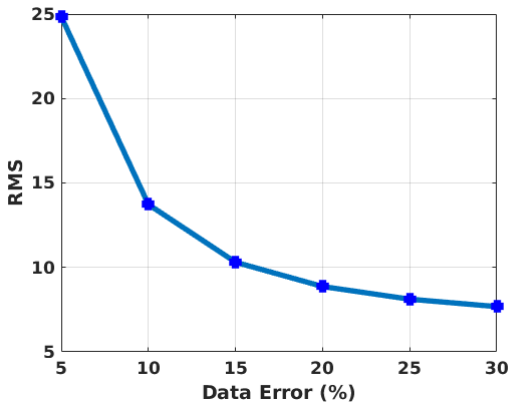

FIGURE 8.10: *Final RMS values of the full impedance and VTF inversion trials with different data errors. Note that only the data errors of the VTF elements were varied and set to constant values.*

The RMS reached at each trial can be distinguished in the graph of Fig. 8.10. In general, all the inversion runs ended with a high data misfit due to the poor quality of the VTF data (see appendix D). Figure 8.11 displays the conductivity slices extracted from the inversion models with VTF data errors of 5 and 30%. It can be observed that the main difference between both inverse models is the size of the conductive structure, which it is not a surprise given that VTF data are sensitive to conductors. This conductive structure has greater dimensions at the inversion model with data errors of 30%.

Based on the data misfit, the inversion model with data errors of 30% is taken for a comparison with the off-diagonal and full impedance inverse models.

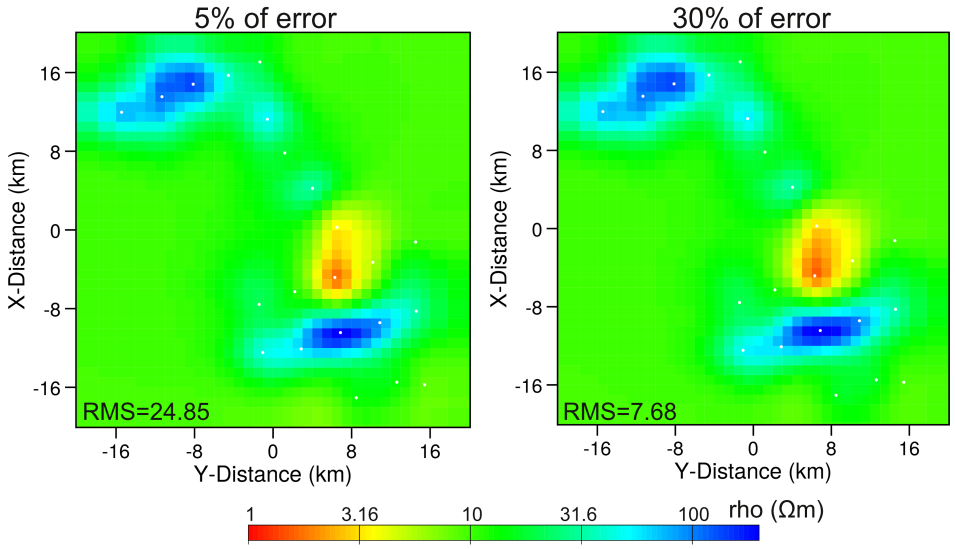

FIGURE 8.11: *Results of the full impedance-VTF elements inversion with different data errors presented as resistivity slices at depths of ∼ 1.8 km. The MT stations are marked with white dots. Note that only the data errors of the VTF elements were varied and set to constant values.*

8.5 Comparison between 3D inversion models

The differences between the preferred off-diagonal, full impedance and full impedance-VTF elements inversion models are pointed out in this section. These inverse models are shown in Fig. 8.12 as conductivity slices at depths of ∼ 1.8 km. Besides of having the highest RMS, the full impedance-VTF elements inversion model shows the poorest resistivity distribution. Neither the resistors nor the conductor are derived as in the other two inverse models. It is clearly noticed that the resistors have shorter dimensions, while the conductor shows a different orientation (N-S). It can be concluded that including the VTF data of San Felipe degrades the quality of the 3D inversion output.

As a first impression the off-diagonal and full tensor inverse models have roughly a similar conductivity distribution, however, a few details come up. The northern resistor shows a little bit larger dimensions in the full impedance tensor inversion model. Its resistivity distribution is imaged at further distances from the profile in the north direction. Similarly the central resistive body is derived at further areas from the MT station whose data constrain such a resistor in the full tensor inverse model. At the southern resistor is not as evident but one can still recognize that it is imaged at further areas from the corresponding MT profile. Regarding the conductive structure, it has the same orientation (NE-SW) at both inverse models. However, it is also derived at further zones from the three MT stations whose data constrain such a conductor in the full tensor inversion model. Despite the worse RMS and clearer image of the conductor outside from the data coverage (*i.e.* an inversion artifact), the full impedance tensor inverse model displays the

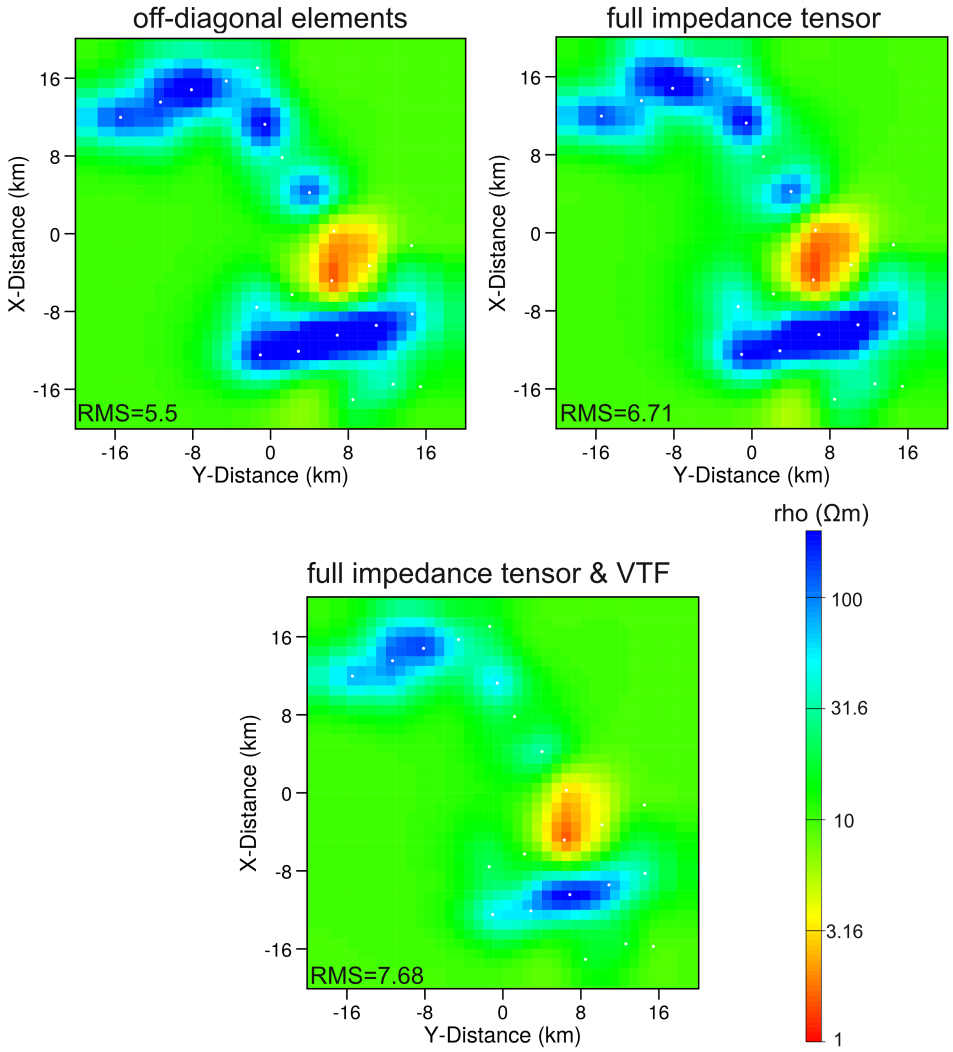

FIGURE 8.12: *Comparison of slices extracted from the preferred off-diagonal, full impedance and full impedance-VTF elements inversion models at depths of ∼ 1.8 km.*

most reasonable result and therefore, it will be taken for further analyses.

8.6 Sensitivity studies

The sensitivity investigations carried out in this section are aimed to determine the depth of investigation and for analyzing whether or not the structures derived from the 3D inversion are reliable.

8.6.1 Depth of investigation

The so called squeeze tests (Allen and Tromp, 2005) were applied to assess at which maximum depths the inverse model is sensitive to the data. In this way,

the model parameters are fixed below specific depths and inversion runs are carried out using the models with the fixed resistivities as starting points for the optimization. Thus, the influence of such constraints can be evaluated on the data misfit and conductivity distribution. The parameters of the full impedance inverse model were fixed to 10 Ωm (prior value) below depths of ∼ 1.8, 4.5 and 10 km. These depths were selected based on the resistivity bodies derived by the 3D inversion and the depths of investigation estimated after Spies (1989).

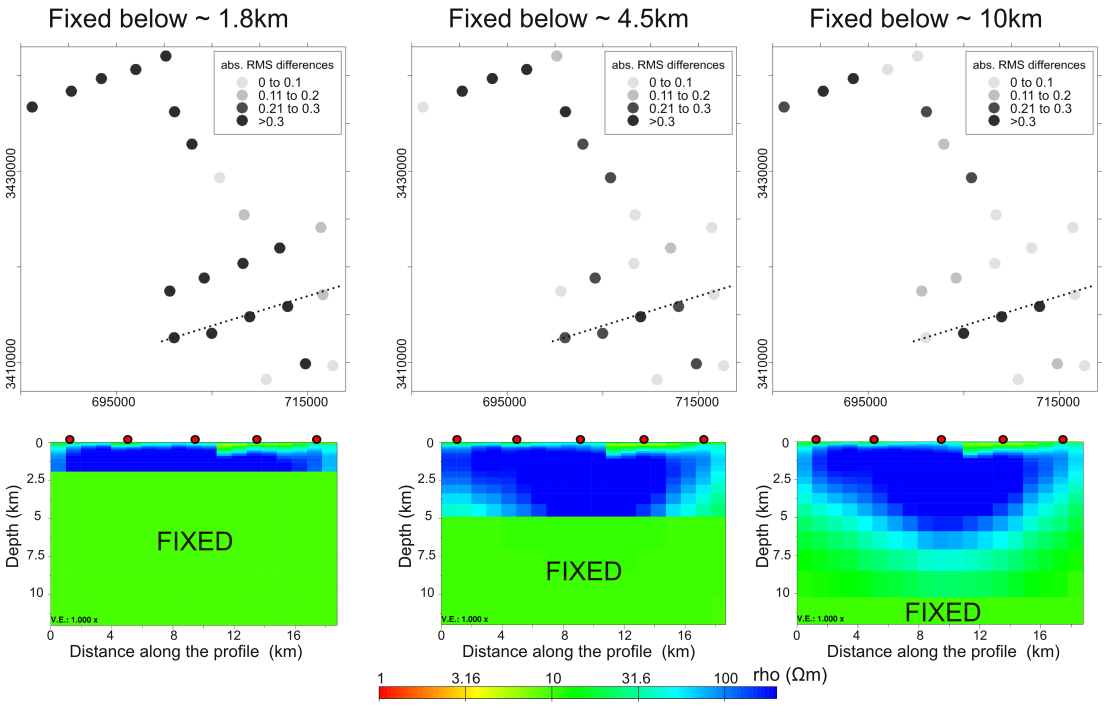

FIGURE 8.13: *Images of the upper panel display the absolute differences between the RMS of the unconstrained inversion and the RMS's obtained from the inversion runs with fixed resistivity on the used starting models. On the lower panel, profiles extracted from the three different inversion models are shown. The location of the profiles are displayed with dashed lines on the images of the upper panel. MT sites are represented with red dots on the profiles.*

Figure 8.13 shows the results of the inversion runs using the above mentioned models with frozen resistivity as prior models. The deviations of the data misfit from the unconstrained inversion are displayed on the upper panel (*i.e.* absolute differences between the RMS obtained with the unconstrained inversion and the RMS's reached at the constrained inversion runs). The images of the lower panel display profiles extracted from the inversion models. At the shallowest depth, the RMS's strongly deviate from the ones obtained with the unconstrained inversion at almost all the stations. A total of 16 soundings show absolute RMS differences greater than 0.3, indicating that deeper structure is required by the data. At medium depths (∼ 4.5 km), 12 stations display absolute RMS differences greater than 0.2, which indicate that deeper structure is still needed by the data of these

soundings. In contrast, eight stations have absolute RMS differences less than 0.1, so that the data of these sites are not requiring deeper structure. Longer period data of such sites were removed due to noise and additionally the presence of a conductive structure in this area reduces the depth of investigation, therefore these stations show less absolute RMS differences than the rest of the soundings. Whereas at depths of $\sim$ 10 km, the majority of the soundings are approaching to the data misfit levels obtained with the unconstrained inversion. Ten sites are showing absolute RMS differences less than 0.1 and four sites less than 0.2, which indicate that data do not need deeper structure. From the skin depth formula, a greater penetration depth exists when the medium is more resistive, thereby the parts of the inverse model where resistors were effectively detected are showing sensitivities at greater depths than the areas where conductors are derived. For instance, data of the selected profile are imaging a resistive structure and therefore some soundings contained in such profile are still displaying considerable RMS deviations at the inversion result with the model parameters fixed below $\sim$ 10 km. Nevertheless, it is concluded that the majority of MT data from San Felipe are resolving structure up to depths of 10 km.

8.6.2 Reliability of the derived resistivity distribution

Feasibility studies were carried out to test for artifacts generated from the 3D inversion. In this sense, a synthetic model was constructed containing the main features that were identified on the inverse model. The images from the left column of Fig. 8.14 are resistivity slices at selected depths extracted from the above mentioned synthetic model. A forward modeling was applied to this model and the calculated data were used for the inversion. The images from the right column in Fig. 8.14 are the corresponding slices extracted from the inverse model. In general, all the bodies were successfully derived by the inversion routine. At depths from $\sim$ 0.3 to 0.4 km, the southwestern part of the northernmost resistor was not possible to recover. An explanation might be that no more stations exist down to this area and therefore there are not data that can effectively constrain such part of the resistor. The northern conductor was successfully derived, with obvious reduced dimensions due to the lack of more data to constrain it. All the central resistors were retrieved, with a spatial distribution restricted to the proximity of the MT sites. Same for the central conductor, the inversion could derive it but with shorter dimensions. Whereas the southern conductor is derived with slightly larger dimensions to the eastern zone, which it is possible because of the closeness of the model parameters of this area to the rather conductive parameters representing the gulf of California. At depths from $\sim$ 0.9 to 1.1 km, all the resistors and the conductive structure were retrieved at areas restricted to the locations of the MT sites.

The southernmost conductor is clearly a remainder of the true conductive structure that is located up to depths of $\sim$ 800 m. At depths from $\sim$ 1.6 to 1.9 km, the northeast part of the northernmost resistor was not recovered by the inversion. Similarly the inversion routine could not derive the southern part of the

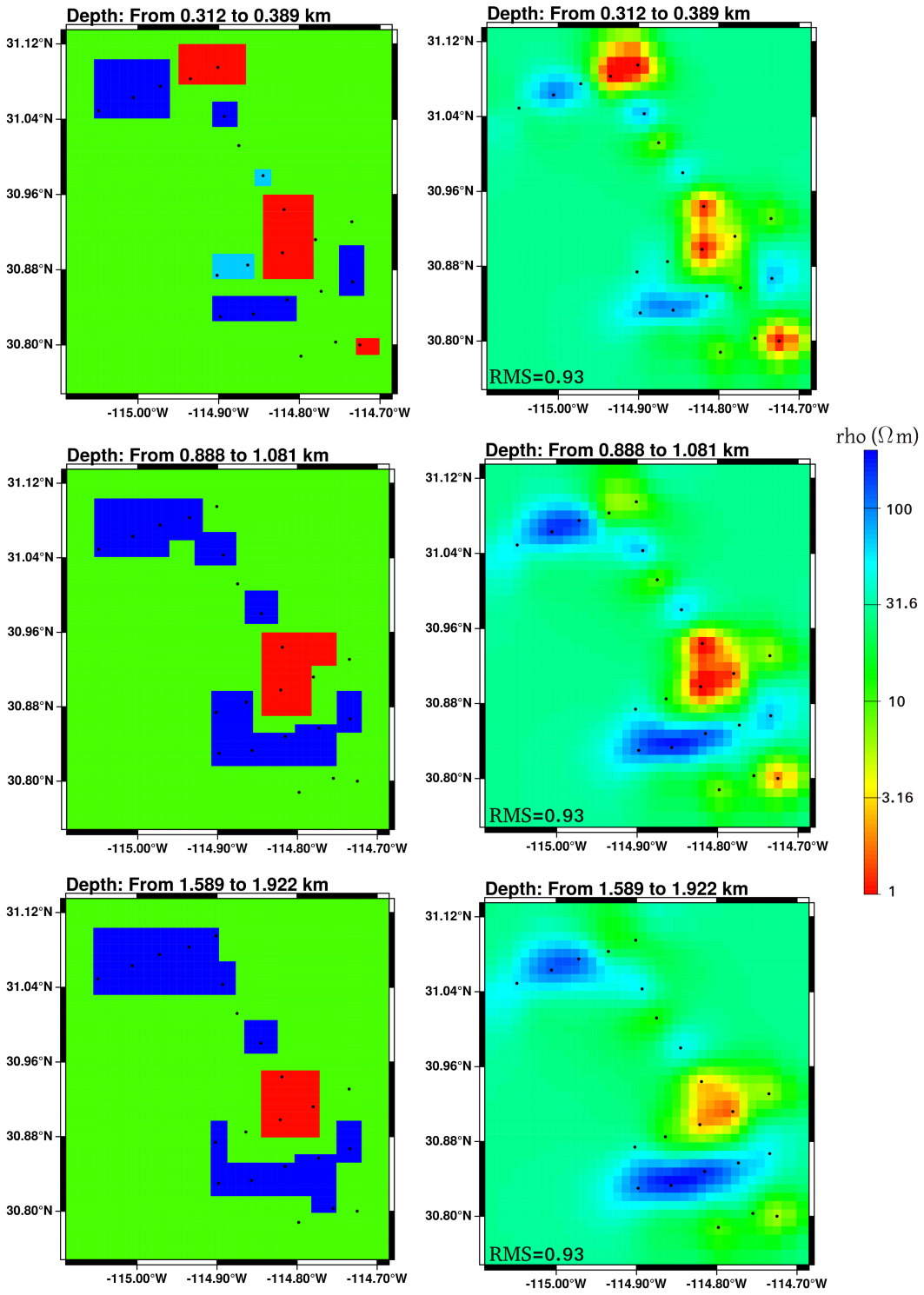

FIGURE 8.14: *Left column: conductivity slices extracted from the 3D synthetic model containing the main features derived from the inversion of field data. Right column: Results from the inversion of data calculated from the synthetic model shown on the left panel.*

southernmost resistive body. Regarding the central conductive structure, it was only retrieved on areas of the model that are sensitive to the data. Thereby, these results are taken into account for further interpretations of the achieved inverse model.

8.7 Comparison of 1D, 2D and 3D inversion models

To illustrate the advantages of the 3D MT inversion, its results are compared with 1D and 2D inversion models in this section. Figure 8.15 displays the 2D inversion model obtained at profile A and the corresponding cross section extracted from the 3D inversion model. One dimensional inverse models obtained at three stations that are part of such profile are also shown. The differences between the 2D and 3D inversion models are notorious. The resistor derived under the station SF-17 has a greater thickness in the 2D inversion model, whereas the resistor under SF-15 has greater dimensions at the 3D inverse model. At both inversion models, the above mentioned resistors seem to be connected in the area below soundings SF-15 and SF-16. The central conductor is imaged from depths of $\sim$ 300 m to 5 km in the 3D inverse model, while at the 2D inversion model such conductor is derived from the shallowest depths up to $\sim$ 2 km. This central conductor extends laterally below stations SF-05 and SF-14 in the 3D inverse model, contrary to the 2D inversion model where such conductor is constrained only by data of SF-14. The resistor derived below station SF-09 has a greater thickness and lateral extension in the 2D inversion model. On the other hand, resistive layers are distinguished up to depths of $\sim$ 7 km in the 1D inverse model obtained at station SF-17. At SF-14, conductive layers are derived from depths of $\sim$ 300 m. Finally at the 1D inverse model obtained station SF-09, the resistive layers extend from $\sim$ 70 m to 6 km.

Although the main robust features are imaged with the 2D and 3D inversion (*e.g.* the two resistors and one conductor in profile A of Fig. 8.15), the above described differences can lead to a misinterpretation. As it has been demonstrated with the dimensionality analysis the subsurface structure is 1D and 3D, therefore the 2D inversion models are not properly characterizing the resistivity distribution. Ledo et al. (2002) concluded that the interpretation of 3D datasets with 2D techniques may be valid if the finite strike extent of a 3D structure located below the profile is greater than about one-half of a skin depth. In this sense, the 2D inversion of data from profile A (Fig. 8.15) might be valid only if we consider the central conductor derived by the 3D inversion (see Fig. 8.12) as the true conductive 3D structure with a finite strike extent of $\sim$ 6 km and assuming a skin depth of 1.6 km approximately[2]. However, the above mentioned is only a speculation because the true finite strike of such conductor is unknown. In addition, one must take into account that in the 2D inversion modeling of San Felipe data the gulf of

[2]This value for the skin depth was obtained by assuming 1 s as the period of maximum induction in such conductive structure and considering the resistivity value of 10 Ωm used for the starting models on the 2D and 3D inversion schemes.

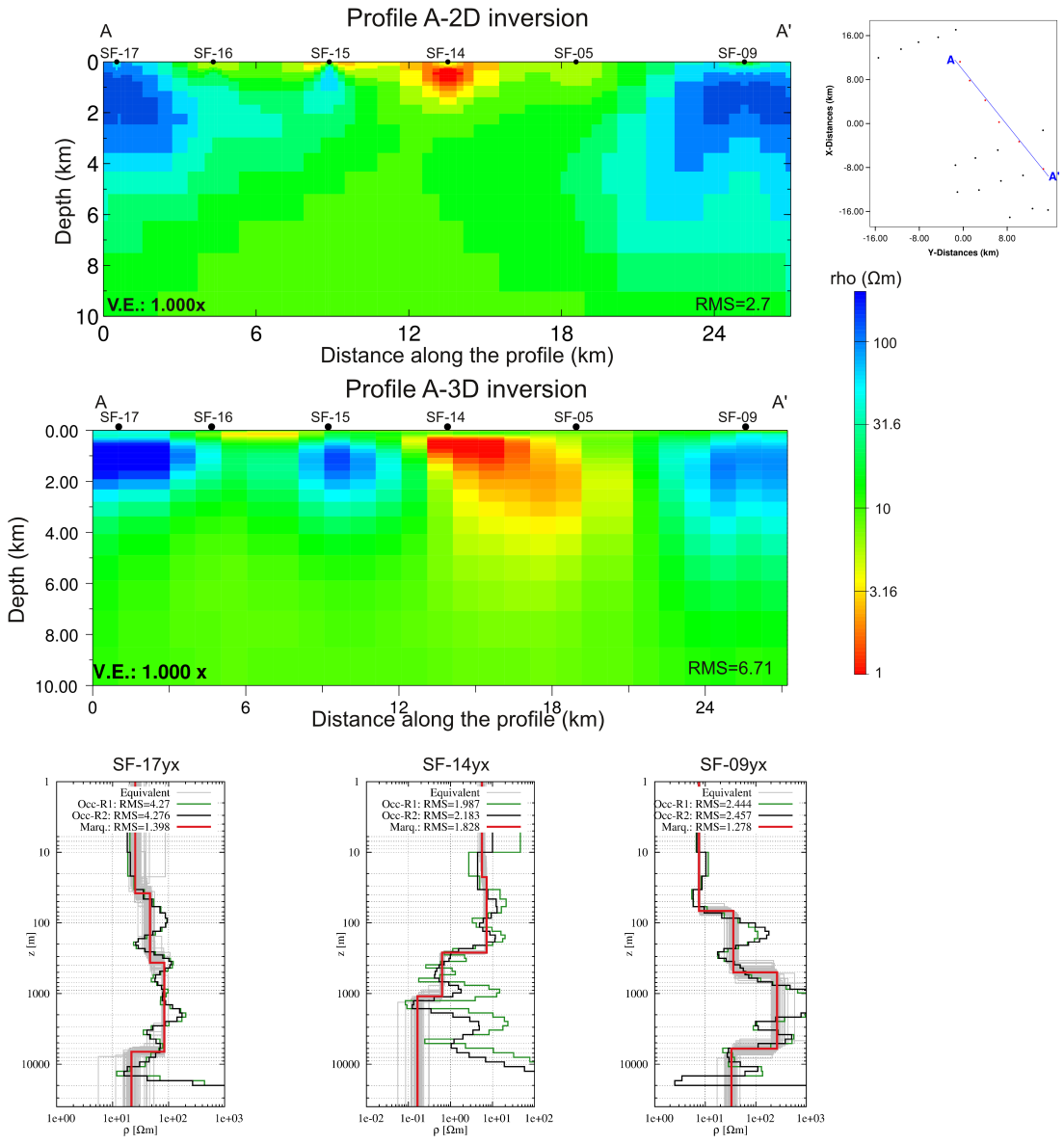

FIGURE 8.15: *Comparison between 3D, 2D and 1D MT inversion models. The lowest panel show 1D inversion models obtained at three stations that are part of the profile A.*

California cannot be added to the model as accurate as it can be done in the 3D inversion modeling.

Despite the similarities between the 1D and 3D inversion models at shallow parts, it is clear that at greater depths differences exist which may be attributed to the less resolution of the 3D inversion. In this sense, Cumming and Mackie (2010) pointed out that 1D inversion has more resolution at depths than the 3D inversion, which it is clearly seen by the greater thicknesses of the lowest resistive layers in the 1D inverse models obtained at stations SF-09 and SF-17 (Fig. 8.15) in comparison to the thicknesses of the resistors imaged at the 3D inversion model

below the same stations.

Thereby, it can be concluded that the 1D and 3D inverse models of San Felipe show the most reliable features. Although a loss of resolution at greater depths is distinguished at the 3D inversion models, the use of additional geophysical information enhance the 3D inversion results as it is demonstrated in the subsequent section.

8.8 Inversion of MT data including additional geophysical information

As it has been earlier mentioned in this thesis, TEM data would not only be used to correct the static shift effect of MT data but also to constrain the 3D MT inversion. The strategies to incorporate the information derived from TEM data are explained in this section. On the one hand, a constrained 3D inverse model was achieved by fixing model parameters based on the resistivity model obtained from the Marquardt inversion of the TEM data (see subsection 7.1.2). On the other hand, information of the resistivity model derived with the Spatially Constrained Inversion (SCI) of TEM data in subsection 7.1.4 was incorporated into a model used as a starting point for the optimization on the 3D inversion of MT data. It is important to point out that the second approach does not represent a constrained inversion. The model parameters were not fixed and the TEM information was only used as *a priori*. Figure 8.16 shows conductivity slices at depths between 81

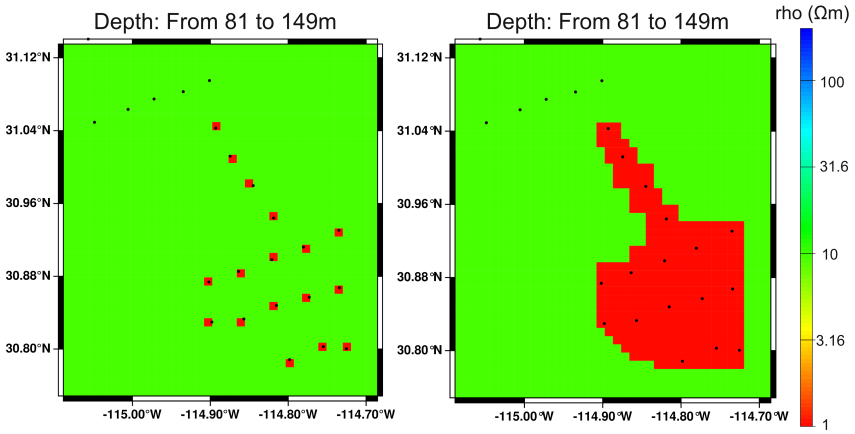

FIGURE 8.16: *Illustration of the applied strategies to incorporate the TEM information into the 3D MT inversion. The left image displays a resistivity slice extracted from a 10 Ωm 3D model where the model parameters under the stations are fixed to the resistivity values obtained from the TEM Marquardt inverse models. The right image shows a conductivity slice extracted from a 10 Ωm 3D model where the model parameters within the survey area are set to the resistivity values obtained from the Spatially Constrained Inversion of TEM data. Note that in both cases the model parameters of the northern area are neither fixed nor set to a resistivity value because TEM data do not exist in this zone.*

and 149 m to illustrate how the TEM information was incorporated. The resistivity slice of the left image shows the case for the constrained inversion, where the model parameters containing the stations are fixed to 1 Ωm at such depths. Whereas the conductivity slice of the right panel displays the case for the inversion with *a priori* information: the model parameters within the survey area are set (not fixed) to the resistivity obtained from the SCI of TEM data.

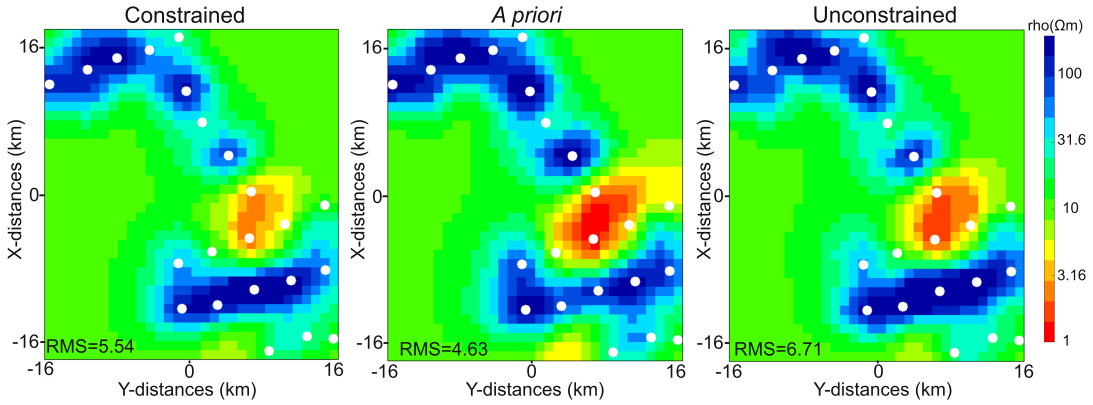

FIGURE 8.17: *Resistivity slices extracted from the models resulted from the constrained inversion and the inversion with a priori information. The conductivity slice extracted from the unconstrained inverse model is also displayed for comparison. MT sites are marked with white dots.*

Results of the constrained inversion and the inversion with *a priori* information are shown in Fig. 8.17 as conductivity slices at depths of $\sim$ 1.8 km. A resistivity slice extracted from the unconstrained inverse model is also displayed for comparison.[3] Different resistivity distribution can be distinguished at each inverse model, which is expected given that the 3D MT inversion is a strongly ill-posed problem. At the constrained inverse model, the resistors show shorter dimensions than at the unconstrained inversion model. In contrast, the central conductive structure is derived with similar dimensions at both inversion models (constrained and unconstrained). At the *a priori* inverse model the resistors are clearly better defined and show greater dimensions than at the unconstrained and constrained inverse models. The central conductor is also derived with greater dimensions. Besides showing the lowest data misfit, the inversion with *a priori* information derives a better defined conductivity distribution. However, the southern conductor (inversion artifact) located outside of the data coverage is more visible in the *a priori* inverse model.

To better visualize the discrepancies between the inverse models, relative differences were computed and are shown in Fig. 8.18. The left image displays the relative differences between the constrained and unconstrained inverse models. It can be distinguished that the major discrepancies are on the area of the south-

[3]The inversion with *a priori* information is an unconstrained inversion too, but for simplicity it is referred as *a priori* inverse model. Whereas the unconstrained inversion model is referring to the one without including TEM information.

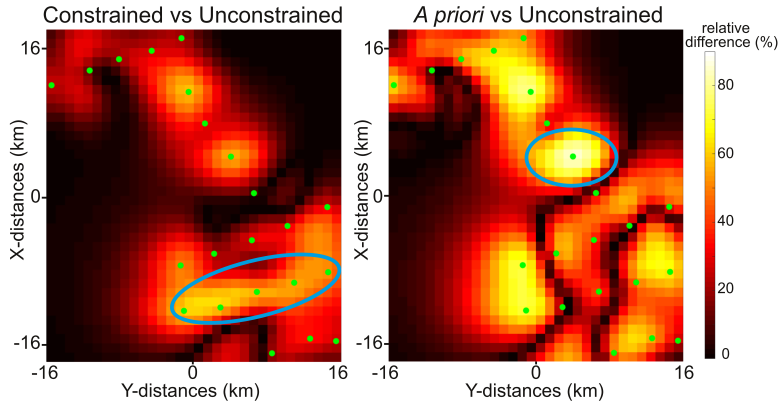

FIGURE 8.18: *Left image: Relative differences between the constrained and unconstrained inverse models. Right image: Relative differences between the a priori and unconstrained inverse models. MT sites are marked with green dots at both images.*

ern resistor (labeled with a circle). In contrast, the area of the central conductor has minimal discrepancies. The relative differences between the *a priori* and unconstrained inverse models are shown on the right image of Fig. 8.18. The circle is indicating the area with major discrepancies, which is where the central resistor is derived. Some parts of the northern and southern resistors are also showing high relative differences ($\sim$ 70%). In addition, the zone of the central conductor is displaying slightly high relative differences ($\sim$ 40%).

Results of the constrained inversion and the inversion with *a priori* information are now displayed as cross sections in Fig. 8.19. A profile extracted from the unconstrained inverse model is also shown for comparison. The location of the selected profile can be seen on the map from the lowest panel. At the constrained inversion model the resistor has slightly shorter dimensions than at the unconstrained inverse model. It is located up to similar depths at both models but it is imaged at larger distances along the profile with the unconstrained inversion. Regarding to the conductor, it has a smaller size at the constrained inversion model than at the unconstrained inverse model. It is poorly imaged under the station SF-05 and it reaches shallower depths (*e.g.*$\sim$ 2 km) under the sounding SF-06 at the constrained inverse model. At the *a priori* inverse model, in contrast, both bodies -resistor and conductor- are imaged with larger dimensions than at the unconstrained inversion model. The resistor is clearer imaged up to depths of 6 km under the site SF-08 and it extends laterally to the center of the profile with greater thickness. It also appears at shallower depths below the station SF-07. The conductor has a larger lateral extension, it appears at the center of the profile and it is dipped under the site SF-04. In fact, data of site SF-04 are detecting a conductor (see appendix D).

Figure 8.20 shows a comparison of the fitting between observed data and calculated data generated from each inversion routine at two selected stations. In general, it is clear that the inversion with *a priori* information displays the best data fitting at both soundings. Specially at greater periods, the fitting of *a priori* is

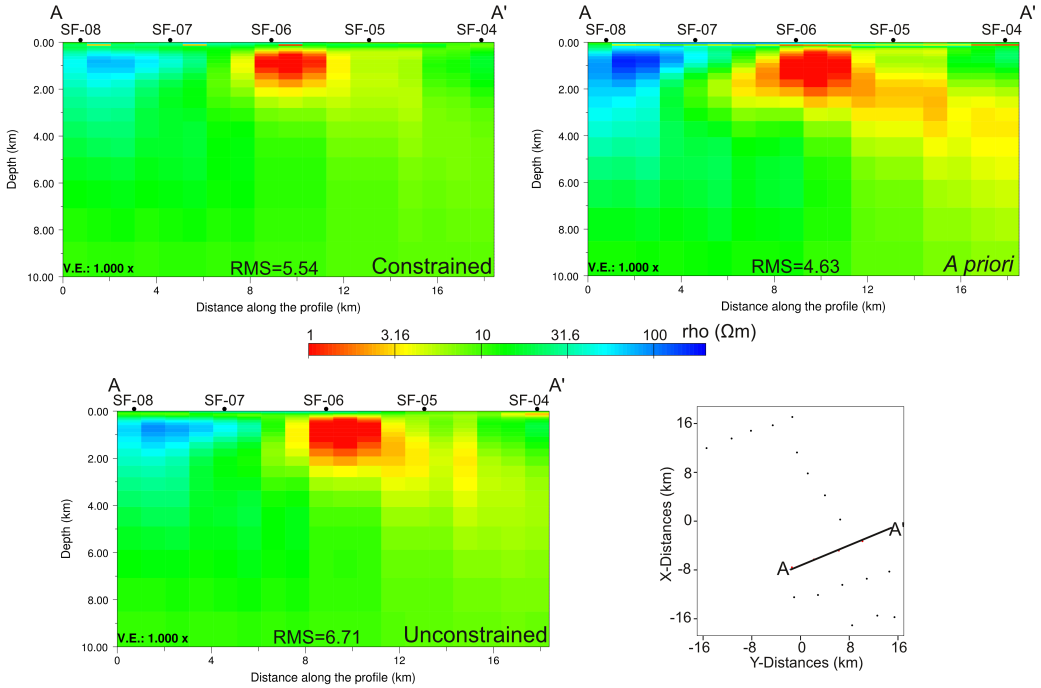

FIGURE 8.19: *Profiles extracted from the 3D models resulted of the constrained inversion and the inversion with a priori information. A profile extracted from the unconstrained inverse model is also displayed for comparison. Location of the profile A-A' is shown on the map from the lowest panel.*

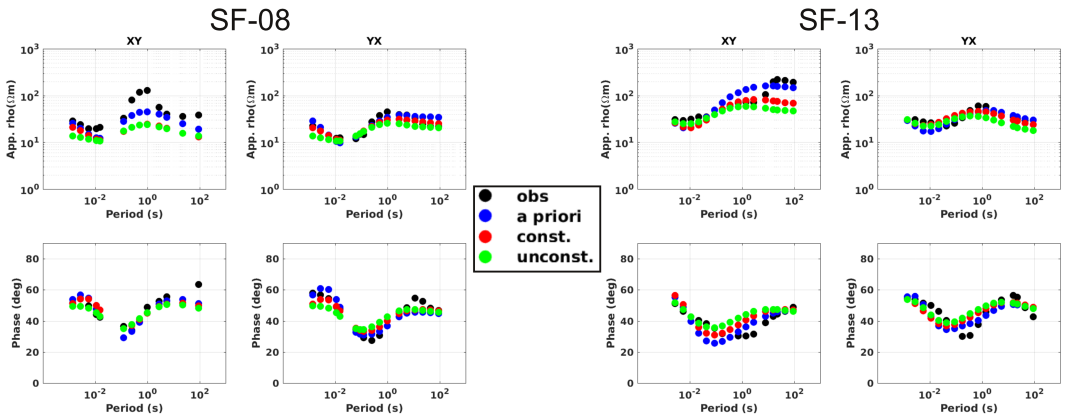

FIGURE 8.20: *Fitting between observed data and calculated data generated from the constrained inversion, inversion with a priori information and unconstrained inversion routines at stations SF-08 and SF-13.*

remarkably better than the ones of the constrained and unconstrained inversion, being more evident on the apparent resistivity curve of the XY component at station SF-13.

Thus, the inversion with *a priori* information has been proved as deriving the most reasonable results. Although the southern conductor (inversion artifact) located outside of the data coverage is more visible on the *a priori* inverse model,

this inversion model shows the lowest data misfit and most complete image of the subsurface. Thereby, it will be used for the subsequent interpretations.

8.9 Preferred inversion model

As it was previously discussed, the inversion with *a priori* information showed the most reasonable results and therefore its derived conductivity model is chosen as the preferred inverse model and a description of it is given in this section. Resistivity slices extracted from this preferred inversion model are displayed in Fig. 8.21. Based on the modeling and sensitivity studies earlier explained in this thesis, only the parts of the inverse model that showed to be reliable are described in this section (*i.e.* only the resistivity distribution derived within the data coverage).

In general, the resistivity bodies have shorter dimensions and seem to be local features at shallow depths (*e.g.* $\sim$ 220 m). Due to the distances between the stations, the information of the penetrated EM waves recorded at each site cannot be interconnected at such depths and consequently the derived bodies are isolated. At shallow depths, a conductor is observed in the northern part of the survey area, extending up to depths of $\sim$ 540 m. Another shallow conductor can be distinguished under the southeastern station up to depths of $\sim$ 800 m. A resistor is imaged at the northern zone, it is derived separately under the northernmost profile and below the closest station of the perpendicular profile at shallow depths. This resistor is connected at depths of $\sim$ 800 m and its size increases in the deeper slices. For instance, it shows the greatest dimensions at depths of $\sim$ 2.1-3.1 km. A central conductive structure can be distinguished from shallow depths of $\sim$ 350 m up to $\sim$ 5.4 km. This conductor is N-S oriented up to depths of $\sim$ 800 m, where it starts to deviate until showing a NE-SW orientation at depths of $\sim$ 1.5 km. A central resistor is also mapped north from the above described conductive structure. This resistor seems to be connected to the northern resistive body at medium depths ($\sim$ 1.5 km). Finally, another resistor is imaged in the southern part of the survey area. It appears at shallow depths and it can be still distinguished at depths of $\sim$ 10 km. As it was pointed out on the squeeze tests (see subsection 8.6.1), data are detecting structure up to 10 km only at some parts of the models. These parts can be recognized at the deepest slice where the northern and southern resistors are slightly imaged.

Figure 8.22 shows profiles extracted from the preferred 3D inversion model. At profile 1, the resistor labeled as R1 displays a thickness of almost 8 km and it is laterally imaged along the entire profile. Its minimal thickness can be distinguished in the NE part under the station P14, where it extends to depths from 1 to 6.5 km approximately. At this part of the profile, a conductor (C1) is overlain the resistor R1 with a thickness that ranges from $\sim$ 800 to 1000 m. This conductor C1 is constrained by the data of stations P13 and P14, at the NE part of the profile. At profile 2, a resistive body labeled as R2 is imaged below soundings SF-07 and SF-08. R2 body reaches depths of $\sim$ 6 km under the station SF-08 and

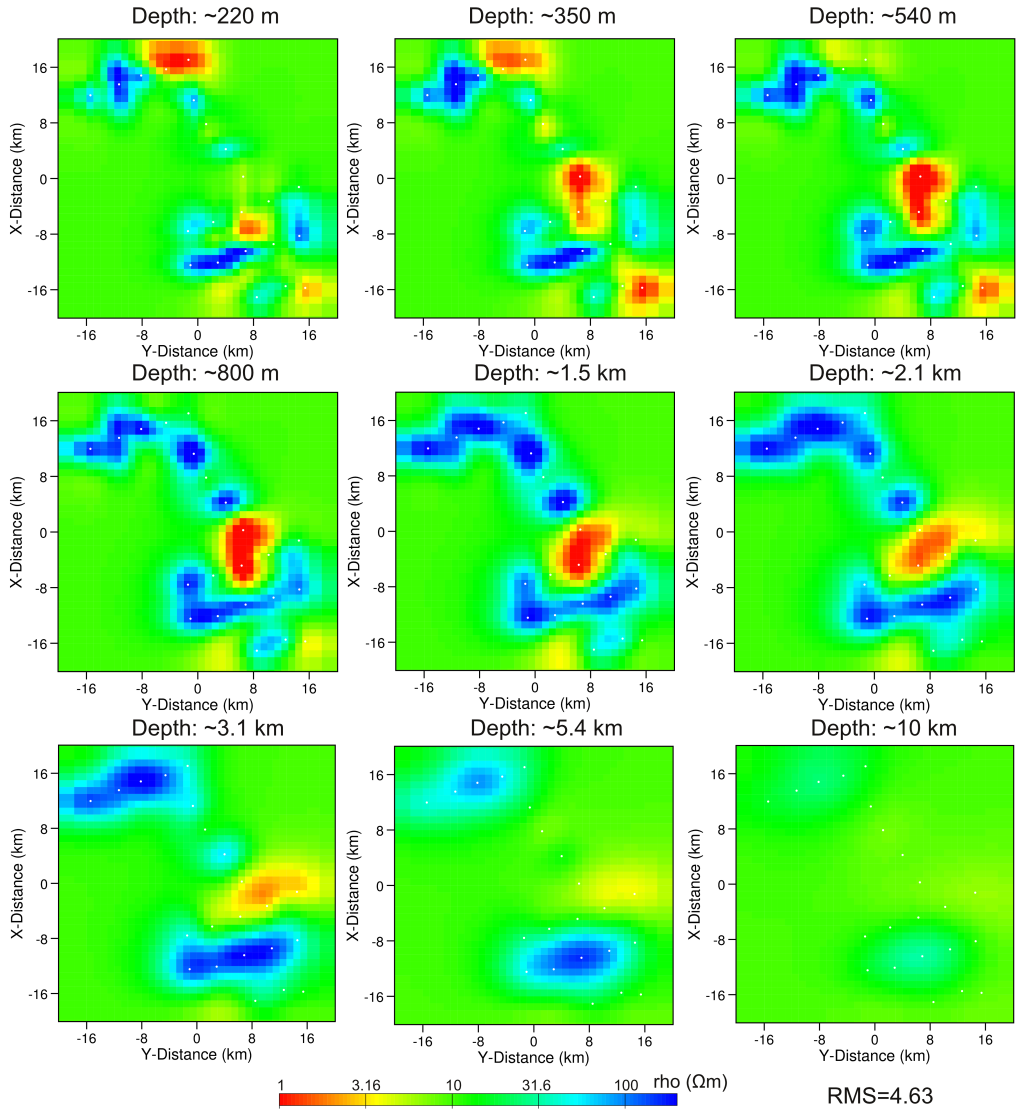

FIGURE 8.21: *Resistivity slices extracted from the preferred inversion model. MT sites are marked with white dots.*

its thickness decreases down to $\sim$ 1 km below the site SF-07. A conductor labeled as C2 is imaged at the central part and it extends laterally up to end of the profile. It is located at shallow depths in the center of the profile, showing a thickness of $\sim$ 3 km under the site SF-06. C2 is dipped below station SF-04 and it extends from depths of 2 to 6 km approximately. At profile 3, a huge resistive body (R3) is distinguished along the entire profile with a thickness that ranges from $\sim$ 5 km to 10 km. It is in the NE part of the profile where R2 has its minimal thickness, it extends from $\sim$ 300 m to 6 km under the sounding SF-09. At profile 4, two conductivity bodies are imaged and labeled as R2 and C3. The resistor R2 extends laterally below stations SF-01 and SF-02. It appears at shallow depths of $\sim$ 300 m under the site SF-01 and it is dipped under sounding SF-02 where it extends at depths from 600 m to 2.5 km approximately. The conductor C3 is located in the

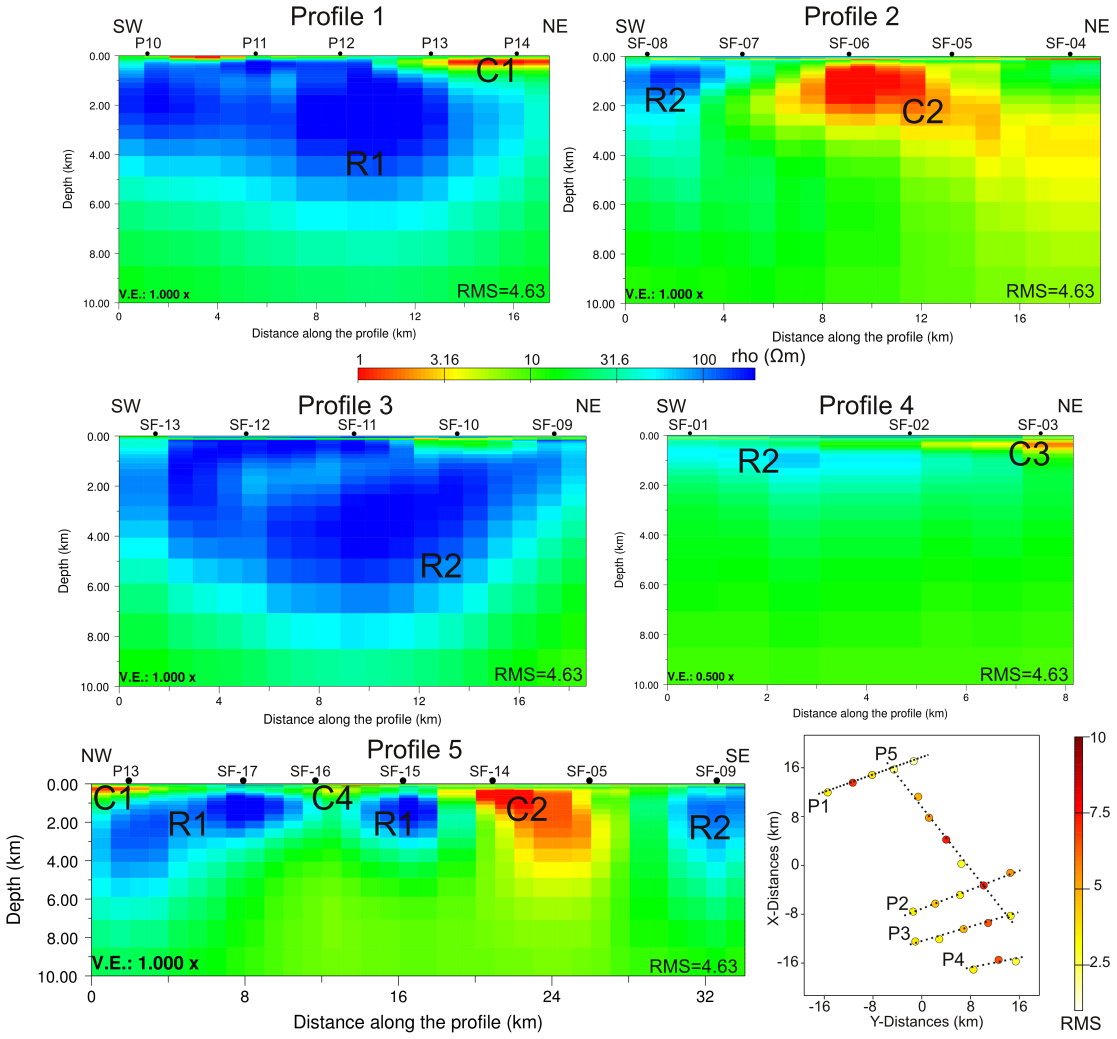

FIGURE 8.22: *Profiles extracted from the preferred 3D inversion model. Locations of the profiles can be distinguished on the map, where the RMS obtained at each station is also plotted.*

NE part and it extends laterally to the center of the profile, under the site SF-02. It shows a thickness of $\sim$ 800 m. Profile 5 is approximately perpendicular to the rest of the profiles, so that only one conductor was labeled as a new body (C4). C4 is located in the center of the profile at shallow depths, below stations SF-15 and SF-16. It has a maximum thickness of $\sim$ 1 km. In the NW zone of the profile, C1 is imaged at shallows depths and its thickness ranges from $\sim$ 500 m to 1.5 km. R2 is underlain the conductor C1 and it appears at depths of 1.5 km under the site P13, being in this part of the profile where it reaches maximum depths of $\sim$ 10 km. R1 is emerging at shallower depths below the sounding SF-17, showing a thickness of $\sim$ 4 km in this zone. The resistive body under station SF-15 is also considered as R1, although it is not completely clear if a connection exists due to the lack of data for constraining the resistor between sites SF-15 and SF-16. R1 displays a thickness of $\sim$ 3 km below SF-15. The conductive structure C2 is located under

the soundings SF-05 and SF-14. It is imaged from shallow depths up ∼ to 6.5 km. Finally, R2 can be seen in the SE area of the profile, being constrained by data of station SF-09. It shows a thickness of ∼ 7 km.

8.9.1 Correlation of the preferred inversion model to geological information

The resistivity distribution of the preferred 3D inverse model is now correlated to the geology of the survey area described in section 4.2. In this regard, the resistive bodies R1 and R2 (Fig. 8.22) are correlated to batholithic rocks and prebatholitic metasedimentary rocks that build the basement of the area. Whereas the conductive structures C1, C3 and C4 (Fig. 8.22) represent the alluvial sediments that fill the basins. At profile 5 (Fig. 8.22) it can be distinguished that C1 and C4 are quite similar structures and they are comparable to C3 which is imaged at profile 4. Due to their geometries and conductivities, they clearly represent sedimentary basins. Conductive structure C2 also displays similar geometry up to depths of ∼ 1.5 km, which can be seen for instance at profile 5 (Fig. 8.22). It shows, however, a different behavior at greater depths: it is dipped down to ∼ 6 km and no resistor is underlain it, as the cases of the others conductors. Therefore C2 is interpreted as a sedimentary basin at its shallow part and it is a fault zone with geothermal fluids after depths of ∼ 1.5 km. C2 seems to have a sub-vertical shape at depths greater than ∼ 1.5-2 km and it is imaged down to ∼ 6-6.5 km with the data acquisition characteristics (Fig. 8.22), but it might continue to deeper parts. If this hypothesis is true, there could be a deeper zone with metamorphism fluids which go up through faults.

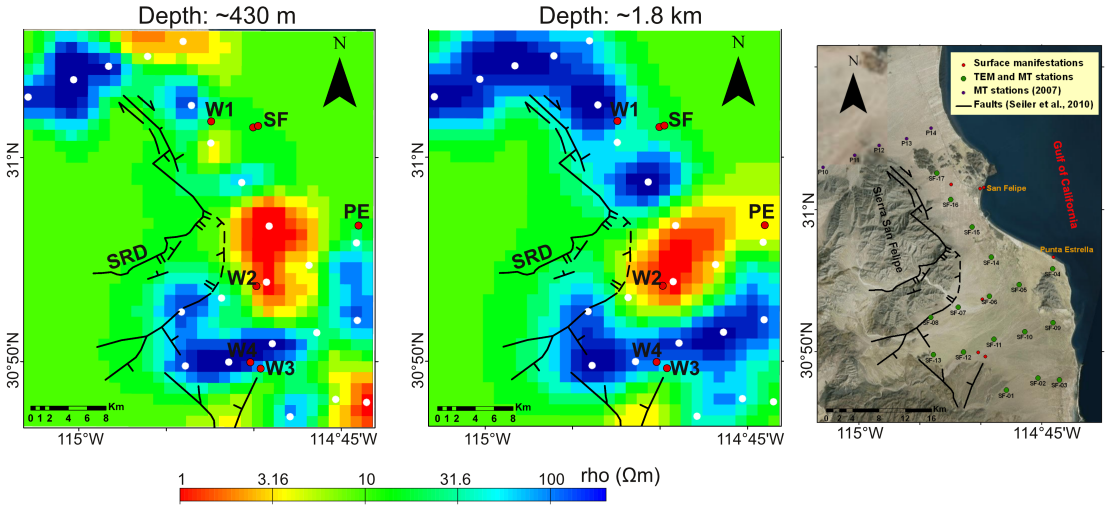

FIGURE 8.23: *Resistivity slices extracted from the preferred 3D inversion model. Faults and geothermal surface manifestations are plotted on the slices. White and red dots represent the MT sites and surface manifestations, respectively.*

The faulting system of Santa Rosa detachment (SRD) is plotted on two conduc-

tivity slices extracted from the 3D preferred inversion model at selected depths in Fig. 8.23. Geothermal surface manifestations and MT stations are displayed with red and white dots, respectively. At depths of $\sim$ 430 m the conductor C2 has a N-S orientation and it is clearly visible how the SRD delimits the western part of such a structure. This image confirms that the SRD controls the sedimentary basin of the eastern area of Sierra San Felipe, as Seiler et al. (2010) suggested. At the same depth, the rest of the conductive structures interpreted as sedimentary basins are also mapped. Their orientations are not possible to infer due to the lack of MT data to constrain the northern and southern parts of the model. At depths of $\sim$ 1.8 km the C2 conductor shows a different orientation, it is now NE-SW oriented, while the rest of the conductive structures are not imaged anymore.[4] The above mentioned is a first indicator to support the hypothesis that the deeper part of C2 ($>$1.5 km) is a fault zone that is linked to the sedimentary basin. In addition, the deeper part of C2 has an orientation approximately parallel to the two NE-SW faults of the SRD that are plotted. These plotted faults were identified at the surface, but they might continue in the subsurface of the survey area and therefore C2 may be interpreted as a fault zone.

Fault zone conductors have been imaged with Magnetotellurics in several studies, *e.g.* Ritter et al. (2003, 2005), Unsworth and Bedrosian (2004), Becken et al. (2011) and Desissa et al. (2013). Recently, Meqbel et al. (2016) have investigated a fault zone below the Dead Sea Basin and found a sub-vertical conductive channel which was attributed to deep geothermal fluids due to metamorphism in the crust. In this regard, the San Felipe survey area is also an active extensional terrain and therefore it is plausible that the deeper part of the conductive structure C2 is a fault zone with fluids. Nevertheless, additional long period MT soundings are necessary to map deeper parts of this structure and thus it could confirm if the conductor is also linked to the lower crust and represents an upward migration of deep fluids.

Another characteristic of the deeper part of the C2 conductor is that it is located within the area where some of the geothermal surface manifestations are identified. For instance W2, which is a water well with high temperature (Fig. 8.23). CONAGUA (2015) reported that water of the wells from San Felipe has a high concentration of fluor which might be associated to thermal waters. Thereby, the deeper part of the C2 conductor might be a fault zone with fluids of high temperature and it is heating the upper layers as the aquifer contained in the sedimentary basin. According to the catalog of geothermal play types based on geological settings introduced by Moeck (2014), the San Felipe geothermal system fits into the non-magmatic convection-dominated geothermal play. These extensional terrain geothermal systems can be purely fault controlled if heat convection occurs along the fault or fault-leakage controlled when the fluid leaks from the fault into a permeable concealed layer (Moeck, 2014). To determine whether the San Felipe geothermal system is fault or fault-leakage controlled, additional MT soundings

[4]Only a conductor outside of the data coverage is derived, but it is considered as an inversion artifact and therefore it is not interpreted.

are required focusing in the area where the C2 conductive structure is imaged.

8.10 Summary of the 3D MT inversion

The results of this chapter are summarized as follows:

- Systematical trials with different inversion input parameters were useful to select the most suitable ones for the inversion of San Felipe magnetotelluric data set.
- The 3D inversion of the full impedance tensor elements derived conductivity bodies with slightly greater dimensions and a poorer data fit was obtained in comparison to the off-diagonal components inversion.
- Due to the low quality of the VTF's elements, including them in the inversion of San Felipe data led to a poor result.
- The 3D inversion of San Felipe MT data is resolving the subsurface structure up to depths of $\sim$ 10 km.
- The three-dimensional inversion model showed less resolution at greater depths in comparison to the 1D and 2D inverse models.
- Including the TEM information enhanced the results of the 3D MT inversion. A better RMS was achieved and the resolution at greater depths increased. From the two applied approaches, the incorporation of the features from the pseudo-3D conductivity model generated with the SCI of TEM data as *a priori* information into the 3D MT inversion scheme showed to be superior.
- A conductive structure was derived in the central part of the survey area which is interpreted as a sedimentary basin at its shallow part and as a fault zone with geothermal fluids at depths greater than 1.5 km.

Chapter No. 9

Conclusion and Outlook

The EM methods applied in this thesis were effective to locate a zone within San Felipe's area with geothermal potential. Additionally, an updated description of the aquifer San Felipe-Punta Estrella was achieved by using the inversion models obtained from the TEM data. In this regard, conventional 1D inversion models displayed a similar behavior at all TEM stations where two layers could be correlated to the aquifer. Based on the assumption that the survey area is located over horizontal layered sediments and the similarity of 1D TEM inversion models, SCI scheme was applied to the TEM data. A pseudo-3D model of the subsurface was derived with the SCI results and permeable and semipermeable units of the aquifer were identified. The permeable unit shows a thickness ranging from 60 to 80 m. It is in the southeastern part where the permeable unit shows smaller values of thickness. The semipermeable unit extends up to depths of 90-100 m. SCI results were also presented as resistivity depth slices and thus, higher conductivity values of the permeable unit were identified in the zones nearer to the shoreline indicating a high salinity in the groundwater. Resistivity cross sections were constructed to show the lateral continuity of the aquifer. A profile was compared to the cross section generated with VES inversion results and a good correlation exists between the interpreted layers.

Because of logistical issues, it was not possible to set up a remote reference MT station during the field survey. Therefore the application of a robust processing scheme was fundamental in order to estimate better magnetotelluric transfer functions. Although the quality of the VTF's was poor for almost all stations, it was possible to utilize the information from some periods and the induction vectors suggested a ocean effect due to the proximity of the survey area to the gulf of California. A dimensionality analysis was carried out based on the phase tensors, which suggested a 1D subsurface structure for periods shorter than 0.5 s and a 3D structure for longer periods. MT data from San Felipe were not severely affected by static shift, however, a correction was done using the TEM information priorly to the inversion of MT data. Despite that using TEM measurements

to correct static shift is questionable, this approach showed to be effective on the correction of San Felipe MT data. A reason might be that the shallow subsurface of the survey area consists of horizontal layered sediments, so that a 1D model assumption is valid and therefore TEM data are not distorted. TEM data can be affected by large lateral contrasts and/or by materials that can produce induced polarization effects (Cumming and Mackie, 2010), but it was not the case for San Felipe TEM data.

The 3D MT modeling studies carried out in this thesis provided useful insights that were later considered for the three-dimensional inversion of magnetotelluric data from San Felipe. In that respect, it was found that a fine discretization is not necessary when a considerable great separation between MT sites exists as it is the case for San Felipe data. A finer mesh can lead to improve the data misfit as Meqbel et al. (2014) showed in their example, however, this statement must be carefully taken. For sake of a lower RMS, it is not valid to use a fine discretization when the separation between the MT stations is huge because inversion artifacts might appear which lead to a misinterpretation. Therefore, modeling studies are advisable to find out the best grid discretization for the 3D inversion of a particular data set.

An advantage of the 3D inversion is that data from scattered MT stations can be easily inverted without data projection onto a profile as in 2D MT inversion (Siripunvaraporn, 2011). However, the modeling studies carried out in this thesis demonstrated that a distribution of stations as a regular grid is needed in order to derive undistorted target structures with the 3D MT inversion. Nevertheless, it is challenging to acquire data on a regular sites distribution due to obstacles that could exist in the survey area (*e.g.* inaccessibility to some areas, land permissions, abrupt topography, etc.).

The induction arrows displayed a presumably ocean effect caused by the gulf of California, therefore a 3D modeling study was performed in order to investigate the veracity of this hypothesis. The results of such modeling investigation indicated that a conductor under the gulf of California is required in order to cause a similar effect as the observed in field data. Moreover, this conductor is geologically correlated to the conductive sediments that normally exist below the sea-floor.

A main aspect of this thesis was the application of 3D inversion to San Felipe MT data. The most obvious and simple advantage of 3D inversion is that the Earth is three-dimensional, therefore a 2D earth model cannot be used to explain the 3D Earth (Siripunvaraporn, 2011). However, it is important as a code user to be aware of how the algorithm works and what the requirements are (Miensopust, 2017). In this sense, the inversion trials by systematically varying the inversion input parameters were useful in order to evaluate their impact and thus, find out the most suitable ones for the inversion of San Felipe MT data. In the inversion of both data sets - synthetic and field data - the smoothing parameter and data errors showed to have the highest impact on the inversion output. It can be concluded that the selection of the smoothing parameter involves a compromise between a

better data fit and the derivation of inversion artifacts. Furthermore, the determination of the smoothing parameters depend of the chosen discretization and therefore in the distances between stations and distribution of the soundings. In regards to the data errors, smaller values led to better retrieve the target structure in the inversion of synthetic data but regions with decreased resistivities outside of the data coverage were derived. It seems that the cost of giving more weight to the data is reflected in the occurrence of inversion artifacts outside of the data coverage.

Even tough including the main diagonal elements might lead to degrade the 3D MT inversion (essentially in terms of data fit), the target structures can be better derived. This conclusion is valid for the case of inverting synthetic data, where the true structure is known. In the inversion of San Felipe MT data, the conductivity bodies were derived with slightly greater dimensions on the inversion of the full impedance tensor but the global RMS increased in comparison to the inversion of the off-diagonal elements. Nevertheless the output of the full impedance tensor inversion was taken for the subsequent interpretations and sensitivity studies were carried out to determine the reliability of the derived resistivity bodies. In respect to the inversion of the field tipper data, including them within the inversion scheme drove to a poor result due to their low quality.

In comparison to the 1D and 2D inversion models, the three-dimensional MT inverse model showed less resolution at greater depths. By incorporating the TEM inversion modeling results, however, the 3D inversion could image San Felipe's subsurface with a better resolution at greater depths. In this regard, the applied first approach consisted of fixing model parameters based on the resistivity model derived from the Marquardt inversion of TEM data and thus, a 3D MT constrained inversion model was achieved. In the second approach, information of the pseudo-3D resistivity model derived with the Spatially Constrained Inversion (SCI) of TEM data was incorporated into a model used as a starting point for the optimization on the 3D inversion of MT data. Both approaches yielded in better results, but the second one demonstrated to be superior and therefore its result was taken as the preferred inversion model.

The preferred 3D inversion model was correlated to the geological information of the survey area. The conductive structure derived in the central part of the survey area was interpreted as a sedimentary basin at its shallow part and as a fault zone with geothermal fluids at depths greater than 1.5 km. This conductor is imaged up to depths of 6 km but it might continue to deeper parts containing metamorphism fluids which go up through the faults. However, additional long-period MT soundings are necessary to map deeper parts of this conductive structure and thus, it could be confirmed whether or not the conductor is linked to the lower crust and represents an upward migration of deep fluids. In order to define whether the San Felipe geothermal system is fault or fault-leakage controlled, a new MT survey is required focusing in the area of the central conductor.

Bibliography

Allen, R. M. and Tromp, J. (2005). Resolution of regional seismic models: Squeezing the Iceland anomaly. *Geophysical Journal International*, 161(2):373–386.

Arango-Galván, C., Prol-Ledesma, R. M., and Torres-Vera, M. A. (2015). Geothermal prospects in the Baja California Peninsula. *Geothermics*, 55:39–57.

Archie, G. E. (1942). The electrical resistivity log as an aid in determining some reservoir characteristics. *Transactions of the American Institute of Mining and Metallurgical Engineers*, 146:54–62.

Atwater, T. (1970). Implications of plate tectonics for the Cenozoic tectonic evolution of western North America. *Geological Society of America Bulletin*, 81(12):3513–3536.

Auken, E. and Christiansen, A. V. (2004). Layered and laterally constrained 2d inversion of resistivity data. *Geophysics*, 69(3):752–761.

Beaton, A. and Tukey, J. (1974). The fitting of power series, meaning polynomials, allustrated on band-spectroscopic data. *Technometrics*, 16:147–185.

Becken, M., Ritter, O., Bedrosian, P. A., and Weckmann, U. (2011). Correlation between deep fluids, tremor and creep along the central San Andreas fault. *Nature*, 480(7375):87–90.

Bertani, R. (2010). Geothermal Power Generation in the World 2005-2010 Update Report. In *Proceedings World Geothermal Congress 2010*.

Bertani, R. (2015). Geothermal Power Generation in the World 2010-2014 Update Report. In *Proceedings World Geothermal Congress 2015*.

Cagniard, L. (1953). Basic theory of magneto-telluric method of geophysical prospecting. *Geophysics*, 18:605–635.

Caldwell, T. G., Bibby, H. M., and Brown, C. (2004). The magnetotelluric phase tensor. *Geophysical Journal International*, 158(2):457–469.

Chave, A. D. and Weidelt, P. (2012). The theoretical basis for electromagnetic induction. In Chave, A. D. and Jones, A. G., editors, *The Magnetotelluric Method: Theory and Practice*, pages 19–49. Cambridge University Press.

Christiansen, A. V., Auken, E., and Sørensen, K. (2006). The transient electromagnetic method. In Kirsch, R., editor, *Groundwater Geophysics: A Tool for Hydrogeology*. Springer.

CONAGUA (1989). Estudio geofísico complementario al estudio de evaluación de disponibilidad y calidad del agua subterránea en la zona sur del valle de San Felipe, B.C.N. Report P-24, Subdirección General Técnica, Gerencia de Aguas Subterráneas, Subgerencia de Evaluación y Ordenamiento de Acuíferos.

CONAGUA (2015). Actualización de la disponibilidad media anual de agua en el acuífero San Felipe-Punta Estrella (0222), Estado de Baja California. Report P-29, Subdirección General Técnica, Gerencia de Aguas Subterráneas, Subgerencia de Evaluación y Ordenamiento de Acuíferos.

Constable, S. C., Parker, R. L., and Constable, C. G. (1987). Occam's inversion: a practical algorithm for generating smooth models from EM sounding data. *Geophysics*, 52(3):289–300.

Cumming, W. and Mackie, R. (2010). Resistivity Imaging of Geothermal Resources using 1D, 2D and 3D MT Inversion and TDEM Static Shift Correction Illustrated by a Glass Mountain Case History. In *Proceedings World Geothermal Congress 2010*. Bali, Indonesia.

Delaunay, B. (1934). Sur la sphere vide. In *Bulletin of Academy of Sciences of the USSR 7*, pages 793–800.

Desissa, M., Johnson, N. E., Whaler, K., Hautot, S., Fisseha, S., and Dawes, G. (2013). A mantle magma reservoir beneath an incipient mid-ocean ridge in Afar, Ethiopia. *Nature Geoscience*, 6(10):861–865.

Dickson, M. H. and Fanelli, M. (2004). What is geothermal energy? `https://www.geothermal-energy.org/what_is_geothermal_energy.html`.

Egbert, G. D. (2006). Efficient Inversion of Multi-frequency and Multi-Source Electromagnetic Data. Final project report, College of Oceanic and Atmospheric Sciences, Oregon State University.

Egbert, G. D. and Booker, J. R. (1986). Robust estimation of geomagnetic transfer functions. *Geophysical Journal International*, 87(1):173–194.

Egbert, G. D. and Kelbert, A. (2012). Computational recipes for electromagnetic inverse problems. *Geophysical Journal International*, 189(1):251–267.

Erdoğan, E. and Candansayar, M. E. (2017). The conductivity structure of the Gediz Graben geothermal area extracted from 2D and 3D magnetotellutic inversion: Synthetic and field data applications. *Geothermics*, 65:170–179.

Farquharson, C. G. and Oldenburg, D. W. (2004). A comparison of automatic techniques for estimating the regularization parameter in non-linear inverse problems. *Geophysical Journal International*, 156(3):411–425.

Fitterman, D. V. and Anderson, W. L. (1987). Effect of Transmitter Turn-Off Time on Transient Soundings. *Geoexploration*, 24:131–146.

Fletcher, J. M., Grove, M., Kimbrough, D., Lovera, O., and Gehrels, G. E. (2007). Ridge-trench interactions and the Neogene tectonic evolution of the Magdalena shelf and southern Gulf of California: Insights from detrital zircon U-Pb ages from the Magdalena fan and adjacent areas. *Geological Society of America Bulletin*, 119(11-12):1313–1336.

Flores-Armenta, M., Ramíres-Montes, M., and Morales-Alcalá, L. (2014). Geothermal Activity and Development in México-Keeping the Production Going. In *Short Course VI on Utilization of Low- and Medium-Enthalpy Geothermal Resources and Financial Aspects of Utilization*.

Gamble, T., Goubau, W., and Clarke, J. (1979). Magnetotellurics with a remote magnetic reference. *Geophysics*, 44(1):53–68.

Grayver, A. V. (2013). *Three-dimensional controlled-source electromagnetic inversion using modern computational concepts*. PhD thesis, Freie Universität Berlin.

Gutiérrez-Negrín, L. C. A., Maya-González, R., and Quijano-León, J. (2010). Current Status of Geothermics in Mexico. In *Proceedings World Geothermal Congress 2010*. Bali, Indonesia.

Gutiérrez-Negrín, L. C. A., Maya-González, R., and Quijano-León, J. (2015). Present Situation and Perspectives of Geothermal in Mexico. In *Proceedings World Geothermal Congress 2015*.

Heise, W. and Pous, J. (2003). Anomalous phases exceeding 90° in magnetotellurics: anisotropic model studies and a field example. *Geophysical Journal International*, 155(1):308–318.

Huber, P. J. (1981). *Robust Statistics*. Wiley, New York, USA.

Ichihara, H. and Mogi, T. (2009). A realistic 3-D resistivity model explaining anomalous large magnetotelluric phases: the L-shaped conductor model. *Geophysical Journal International*, 179(1):14–17.

Jiracek, G. R. (1990). Near-surface and topographic distortions in Electromagnetic Induction. *Surveys in Geophysics*, 11:166–203.

Junge, A. (1990). Robust estimation of bivariate transfer functions. In Haak, V. and Homilus, H., editors, *Protokoll Kolloquium Elektromagnetische Tiefenforschung*, pages 75–86. DGG, Hornburg, Germany.

Junge, A. (1992). On the effective number of degrees of freedom in magnetotelluric transfer function estimation. In Haak, V. and Homilus, H., editors, *Protokoll Kolloquium Elektromagnetische Tiefenforschung*, pages 75–86. DGG, Borkheide, Germany.

Junge, A. (1994). *Induced telluric fields - new observations in North Germany and the Bramwald*. Habilitation Thesis, Faculty of Physics, University of Göttingen, Germany.

Junge, A. (1996). Characterization of and correction for cultural noise. *Surveys in Geophysics*, 17:361–391.

Kaufman, A. A. and Keller, G. V. (1981). The Magnetotelluric Sounding Method. In Banks, R., editor, *Methods in Geochemistry and Geophysics*, volume 15. Elsevier Scientific, Amsterdam.

Kelbert, A., Meqbel, N., Egbert, G. D., and Tandon, K. (2014). ModEM: A modular system for inversion of electromagnetic geophysical data. *Computers and Geosciences*, 66:40–53.

Key, K. (2012). Is the fast Hankel transform faster than quadrature? *Geophysics*, 77(3):F21–F30.

Knight, R. J. and Endres, A. L. (2005). An Introduction to Rock Physics Principles for Near-Surface Geophysics. In Butler, D. K., editor, *Near-Surface Geophysics*, pages 31–70. Society of Exploration Geophysicists, Tulsa.

Krings, T. (2007). The influence of Robust Statistics, Remote Reference, and Horizontal Magnetic Transfer Functions on data processing in Magnetotellurics. Master's thesis, University of Münster.

Ledo, J., Queralt, P., Martí, A., and Jones, A. G. (2002). Two-dimensional interpretation of three-dimensional magnetotelluric data: an example of limitations and resolution. *Geophysical Journal International*, 150:127–139.

Levenberg, K. (1944). A method for the solution of certain nonlinear problems in least squares. *Quarterly of Applied Mathematics*, 2:164–168.

Lilley, F. E. M. and Weaver, J. T. (2003). Phases greater than 90° in MT data: Analysis using dimensionality tools. *Journal of Applied Geophysics*, 70(1):9–16.

Lines, L. and Treitel, S. (1984). A review of least-squares inversion and its application to geophysical problems. *Geophysical Prospecting*, 32(2):159–186.

Lippert, K. (2015). *Detektion eines submarinen Aquifers vor der Küste Israels mittels mariner Long Offset Transient-elektromagnetischer Messung*. PhD thesis, University of Cologne, Germany.

Marquardt, D. W. (1963). An Algorithm for Least-Squares Estimation of Nonlinear Parameters. *Journal of the Society for Industrial and Applied Mathematics*, 11(2):431–441.

Martín-Barajas, A. (2000). Volcanismo y extensión en la provincia extensional del Golfo de California. *Boletín de la Sociedad Geológica Mexicana*, 53(1):72–83.

Meju, M. A. (1994). *Geophysical Data Analysis: Understanding Inverse Problem in Theory and Practice*. Society of Exploration Geophysicists.

Menke, W. (1984). *Geophysical data analysis: discrete inverse theory*. Academic Press inc.

Meqbel, N. (2009). *The electrical conductivity structure of the Dead Sea Basin derived from 2D and 3D inversion of magnetotelluric data*. PhD thesis, Freie Universität Berlin.

Meqbel, N., Egbert, G., Wannamaker, P., Kelbert, A., and Schultz, A. (2014). Deep electrical resistivity structure of the northwestern U.S. derived from 3-D inversion of USArray magnetotelluric data. *Earth and Planetary Science Letters*, 402:290–304.

Meqbel, N., Wckmann, U., Muñoz, G., and Ritter, O. (2016). Crustal metamorphic fluid flux beneath the Dead Sea Basin: constraints from 2-D and 3-D magnetotelluric modelling. *Geophysical Journal International*, 207:1609–1629.

Miensopust, M. P. (2017). Application of 3-D Electromagnetic Inversion in Practice: Challenges, Pitfalls and Solution Approaches. *Surveys in Geophysics*, 38:869–933.

Moeck, I. S. (2014). Catalog of geothermal play types based on geologic controls. *Renewable and Sustainable Energy Reviews*, 37:867–882.

Mosegaard, K. and Sambridge, M. (2002). Monte Carlo analysis of inverse problems. *Inverse problems*, 18:29–54.

Munkholm, M. and Auken, E. (1996). Electromagnetic noise contamination on transient electromagnetic soundings in culturally disturbed environments. *Journal of Environmental Engineering Geophysics*, 1(2):119–127.

Muñoz, G. (2014). Exploring for Geothermal Resources with Electromagnetic Methods. *Surveys in Geophysics*, 35:101–122.

Nabighian, M. N. and Macnae, J. C. (1991). Time domain electromagnetic prospecting methods. In Nabighian, M. N., editor, *Electromagnetic Methods in Applied Geophysics*, volume 2(A), pages 427–509. Society of Exploration Geophysicists, Tulsa, Oklahoma.

Newman, G. A. (1989). Deep transient electromagnetic soundings with a grounded source over near-surface conductors. *Geophysical Journal International*, 98(3):587–601.

Newman, G. A., Anderson, W. L., and Hohmann, G. W. (1987). Interpretation of transient electromagnetic soundings over three-dimensional structures for the central-loop configuration. *Geophysical Journal International*, 89(3):889–914.

Newman, G. A., Gasperikova, E., Hoversten, G. M., and Wannamaker, P. E. (2008). Three-dimensional magnetotelluric characterization of the Coso geothermal field. *Geothermics*, 37:369–399.

Pamplona-Pérez, U. (2007). Perfil Magnetotelúrico a través de la Sierra San Pedro Mártir, Baja California, México. Master's thesis, Centro de Investigación Científica y de Educación Superior de Ensenada.

Patro, P. K. and Egbert, G. D. (2011). Application of 3-D inversion to magnetotelluric profile data from the Deccan Volcanic Province of Western India. *Physics of the Earth and Planetary Interiors*, 187:33–46.

Pellerin, L. and Hohmann, G. W. (1990). Transient electromagnetic inversion: A remedy for magnetotelluric static shifts. *Geophysics*, 55(9):1242–1250.

Pellerin, L., Johnston, J. M., and Hohhmann, G. W. (1996). A numerical evaluation of electromagnetic methods in geothermal exploration. *Geophysics*, 61(1):121–130.

Petry, H. (1987). Transient elektromagnetische Tiefensondierungen- Modellrechnungen und Inversion. Master's thesis, University of Cologne.

Pirttijärvi, M. (2010). *JOINTEM Users' Guide*. University of Oulu, Department of Physics, Oulu, FI.

Piña-Varas, P. and Dentith, M. (2017). Magnetotelluric Data from the Southeastern Capricorn Orogen, Western Australia: An Example of Widespread Out-of-Quadrant Phase Responses Associated with Strong 3-D resistivity Contrasts. *Geophysical Journal International*, 212:1022–1032.

Polak, E. (1971). *Computational methods in optimization: A unified approach:*. Academic Press.

Quijano, J. L. and Gutiérrez-Negrín, L. C. A. (2005). Update of Geothermics in Mexico. In *Proceedings World Geothermal Congress 2005*.

Ritter, O., Hoffmann-Rothe, A., Bedrosian, P. A., Weckmann, U., and Haak, V. (2005). Electrical Conductivity images of active and fossil fault zones. *Geological Society London Special Publications*, 245(1):165–186.

Ritter, O., Junge, A., and Dawes, G. (1998). New equipment and processing for magnetotelluric remote reference observations. *Geophysical Journal International*, 132:535–548.

Ritter, O., Ryberg, T., Weckmann, U., Hoffmann-Rothe, A., Abueladas, A., Garfunkel, Z., and Group, D. R. (2003). Geophysical images of the Dead Sea Transform in Jordan reveal an impermeable barrier for fluid flow. *Geophysical Research Letters*, 30(14):861–865.

Rodi, W. and Mackie, R. L. (2001). Nonlinear conjugate gradients algorithm for 2-d magnetotelluric inversion. *Geophysics*, 66(1):174–187.

Ruiz-Aguilar, D., Tezkan, B., and Arango-Galván, C. (in press 2018). Exploration of the aquifer of San Felipe's geothermal area (Mexico) by Spatially Constrained Inversion of Transient Electromagnetic data. *Journal of Environmental and Engineering Geophysics*.

Scholl, C. (2005). *The influence of multidimensional structures on the interpretation of LOTEM data with one-dimensional models and the application to data from Israel*. PhD thesis, University of Cologne.

Seiler, C., m. Fletcher, J., Quigley, M. C., Gleadow, A. J., and Kohn, B. P. (2010). Neogene structural evolution of the Sierra San Felipe, Baja California: evidence for protogulf transtension in the Gulf Extensional Province? *Tectonophysics*, 488:87–109.

Sengpiel, K. and Siemon, B. (2000). Advanced inversion methods for airborne electromagnetic exploration. *Geophysics*, 65:1983–1992.

Simpson, F. and Bahr, K. (2005). *Practical Magnetotellurics*. Cambridge University Press.

Siripunvaraporn, W. (2011). Three-Dimensional Magnetotelluric Inversion: An Introductory Guide for Developers and Users. *Surveys in Geophysics*, 33:5–27.

Siripunvaraporn, W., Egbert, G., and Lenbury, Y. (2002). Numerical accuracy of magnetotelluric modeling: A comparison of finite difference approximations. *Earth Planets Space*, 54:721–725.

Siripunvaraporn, W., Egbert, G., and Uyeshima, M. (2005). Interpretation of two-dimensional magnetotelluric profile data with three-dimensional inversion: synthetic examples. *Geophysical Journal International*, 160:804–814.

Spies, B. R. (1989). Depth of investigation in electromagnetic sounding methods. *Geophysics*, 54(7):872–888.

Spies, B. R. and Frischknecht, C. F. (1991). Electromagnetic Sounding. In Nabighian, M. N., editor, *Electromagnetic Methods in Applied Geophysics*, volume 2(A), pages 285–426. Society of Exploration Geophysicists, Tulsa, Oklahoma.

Sternberg, B. K., Washburne, J. C., and Pellerin, L. (1988). Correction for the static shift in magnetotelurics using transient electromagnetic soundings. *Geophysics*, 53(11):1459–14680.

Streich, R. (2009). 3D finite-difference frequency-domain modeling of controlled-source electromagnetic data: direct solution and optimization for high accuracy. *Geophysics*, 74(5):F95–F105.

Swidinsky, A., Hölz, S., and Jegen, M. (2012). On mapping seafloor mineral deposits with central loop transient electromagnetics. *Geophysics*, 77(3):E171–E184.

Swift, C. M. (1967). *A magnetotelluric investigation of an electrical conductivity anomaly on the southwestern United States*. PhD thesis, Massachusetts Institute of Technology.

Tezkan, B. (1999). A review of enviromental applications of quasi-stationary electromagnetic techniques. *Surveys in Geophysics*, 20:279–308.

Thiel, S., Heinson, G., Gray, D., and Gregory, R. T. (2009). Ophiolite emplacement in NE Oman: constraints from magnetotelluric sounding. *Geophysical Journal International*, 176(3):753–766.

Tietze, K. (2012). *Investigating the electrical conductivity structure of the San Andreas fault system in the Parkfield-Cholame region, central California, with 3D magnetotelluric inversion*. PhD thesis, Freie Universität Berlin.

Tikhonov, A. N. (1950). On determining electrical characteristics of the deep layers of the Earth's crust. *Doklady*, 73:295–297.

Unsworth, M. and Bedrosian, P. (2004). On the geoelectric structure of major strike-slip faults and shear zones. *Earth Planets Space*, 56(12):1177–1184.

Viezzoli, A., Christiansen, A. V., Auken, E., and Sørensen, K. (2008). Quasi-3D modeling of airborne TEM data by spatially constrained inversion. *Geophysics*, 73(3):105–113.

von Papen, M. (2011). Spatial Constrained Inversion von In-Loop TEM Daten zur Bestimmung der Grundwasserkontamination in Roorkee, Indien. Master's thesis, University of Cologne.

von Papen, M., Tezkan, B., and Israil, M. (2013). Characterization of an aquifer in Roorkee, India using the Spatially Constrained Inversion of in-loop TEM data. *Near Surface Geophysics*, 11(1):85–94.

Vozoff, K. (1991). The Magnetotelluric Method. In Nabighian, M. N., editor, *Electromagnetic Methods in Applied Geophysics*, volume 2. Society of Exploration Geophysicists, Tulsa, Oklahoma.

Ward, S. and Hohmann, D. L. B. (1988). Electromagnetic Theory for Geophysical Applications. In Nabighian, M. N., editor, *Electromagnetic Methods in Applied Geophysics*, volume 2, pages 131–308. Society of Exploration Geophysicists, Tulsa, Oklahoma.

Weaver, J. T. (1994). *Mathematical methods for geo-electromagnetic induction*. Taunton, Somerset, England : Research Studies Press, New York, USA.

Weckmann, U., Magunia, A., and Ritter, O. (2005). Effective noise separation for magnetotelluric single site data processing using a frequency domain selection scheme. *Geophysical Journal International*, 161:635–652.

Weidelt, P. (1986). *Einführung in die elektromagnetische Tiefenforschung*. Lecture Technische Universät Braunschweig.

Weidelt, P. and Kaikkonen, P. (1994). Local 1-D interpretation of magnetotelluric B-polarization impedances. *Geophysical Journal International*, 117:733–748.

Wiese, H. (1962). Geomagnetische Tiefentellurik Teil II: Die Streichrichtung der untergrundstrukturen des elektrischen Widerstandes, erschlossen aus geomagnetischen Variationen. *Geofisica pura e applicata*, 52(1):83–103.

Williams, C. F., Reed, M. J., and Anderson, A. F. (2011). Updating the classification of geothermal resources. In *Proceedings 36th Workshop on Geothermal Engineering*. Stanford, California.

Yee, K. (1966). Numerical solution of initial boundary value problems involving Maxwell's equations in isotropic media. *IEEE Transactions on Antennas and Propagation*, 14(3):302–307.

Yogeshwar, P. (2014). *A resistivity-depth model of the central Azraq basin area, Jordan: 2D forward and inverse modeling of time domain electromagnetic data*. PhD thesis, University of Cologne.

List of Figures

List of Tables

Appendices

Appendix A

Stations coordinates

In the following Appendix the stations coordinates are displayed.

TABLE A.1: *Locations of the MT and TEM soundings used for this thesis. Coordinates are in the Universal Transverse Mercator (UTM) system, within UTM zone 11.*

Station	Easting (m)	Northing (m)	Altitude (m)
SF-01	710684	3408219	103
SF-02	714799	3409882	46
SF-03	717631	3409687	19
SF-04	716421	3424113	38
SF-05	712113	3421976	28
SF-06	708260	3420365	55
SF-07	704204	3418851	130
SF-08	700592	3417486	187
SF-09	716627	3417111	22
SF-10	712942	3415869	51
SF-11	708939	3414790	83
SF-12	704968	3413061	131
SF-13	701048	3412618	198
SF-14	708381	3425443	28
SF-15	705800	3429340	26
SF-16	702908	3432864	68
SF-17	701071	3436247	94
P10	686211	3436734	487
P11	690289	3438381	279
P12	693450	3439699	373
P13	697031	3440655	174
P14	700194	3442060	98

Appendix B

1D TEM Forward Modeling

This Appendix deals with a 1D TEM modeling comparison between the forward solution of a central loop and single loop configuration. This short study was done to validate the use of EMUPLUS, because this software has implemented the forward calculation for a central loop TEM configuration and the San Felipe data was acquired with single loop configuration.

Firstly, a forward calculation of a 10 Ωm homogeneous half-space was done with the central and single loop configuration. The software JOINTEM (Pirttijärvi, 2010) was utilized for the single loop case and EMUPLUS for the central loop. A 50 x 50 m^2 transmitter was used, with an injected current of 9 A and ramp time of 115 μs. Thus, synthetic data were calculated from 1 to 70 ms, which is the time range of the data acquired in San Felipe. Figure B.1(a) shows the synthetic transient responses for the coincident and single loop. It is clear that the transients are different at short acquisition times, *e.g.* $t < 3$ ms. The relative difference of these two transients is 9%. In addition, synthetic data were also calculated for a time range from 2 to 20 ms, which was the range that prevailed after removing the data that reached the noise level and therefore, all the data used for the inversion have roughly this time range. These transients are shown in Fig. B.1(c), where differences between them exist at $t < 3$ ms. The relative difference between these calculated transients is 8%.

TABLE B.1: *Parameters of the model A used for a 1D TEM forward calculation.*

Layer No.	Resistivity (Ωm)	Thickness (m)
1	5	5
2	20	90
3	1	0

Similarly, a forward calculation was done to a second model (Table B.1) with central loop and single loop configuration. Table B.1 shows the parameters of

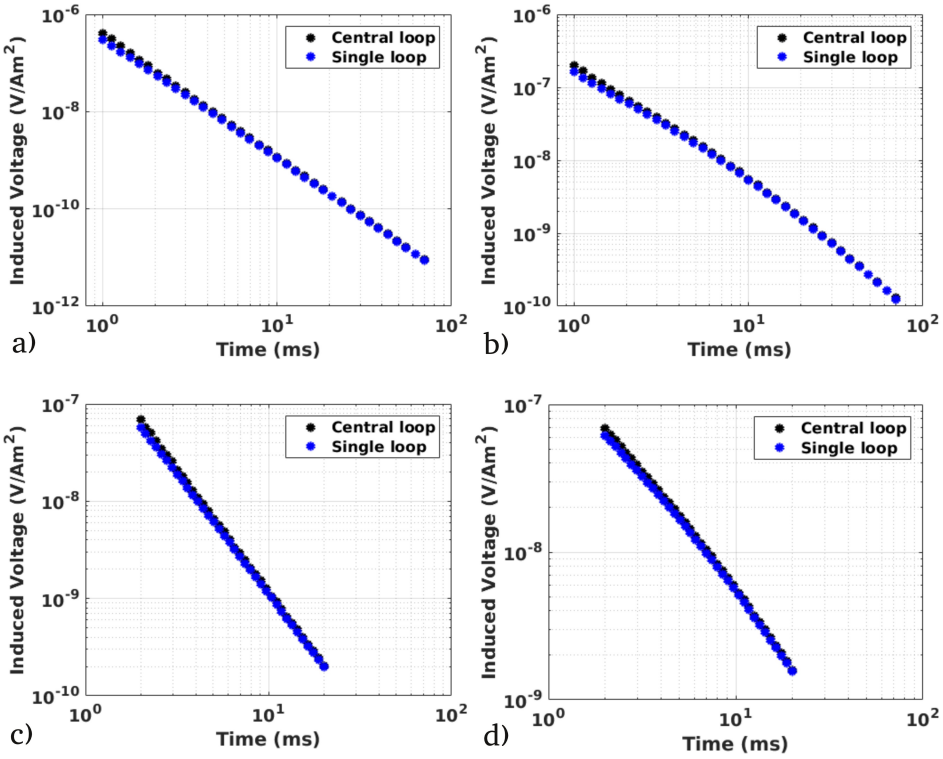

FIGURE B.1: *Transient responses. (a) Transient calculated from the 10 Ωm homogeneous half-space model between 1 and 70 ms. (b) Transient calculated from the Model A between 1 and 70 ms. (c) Transient calculated from the 10 Ωm homogeneous half-space model between 2 and 20 ms. (d) Transient calculated from the Model A between 2 and 20 ms.*

model A. Identical characteristics of the transmitter earlier described were used. At first, synthetic data were calculated for a time range from 1 to 70 ms. Figure B.1(b) displays these transient responses; major differences between them exist at $t < 2$ ms and they have a relative difference of 6%. Moreover, synthetic transients were calculated for a time range from 2 to 20 ms, too. These transients responses are displayed in Fig. B.1(d), where differences are mainly observed from 2 to 3 ms. The relative difference between the transients is 5%.

Thereby, it is concluded that the differences between the solution for a central and single loop are mainly at short acquisition times (*e.g.* $t < 2$ ms). Furthermore, for the time range (2-20 ms) of the data that are used in the 1D inversion of this thesis, the differences are minimal.

Appendix C

1D TEM inversion models

This appendix shows the 1D TEM inversion models at all the stations and the corresponding fit between observed data and calculated data.

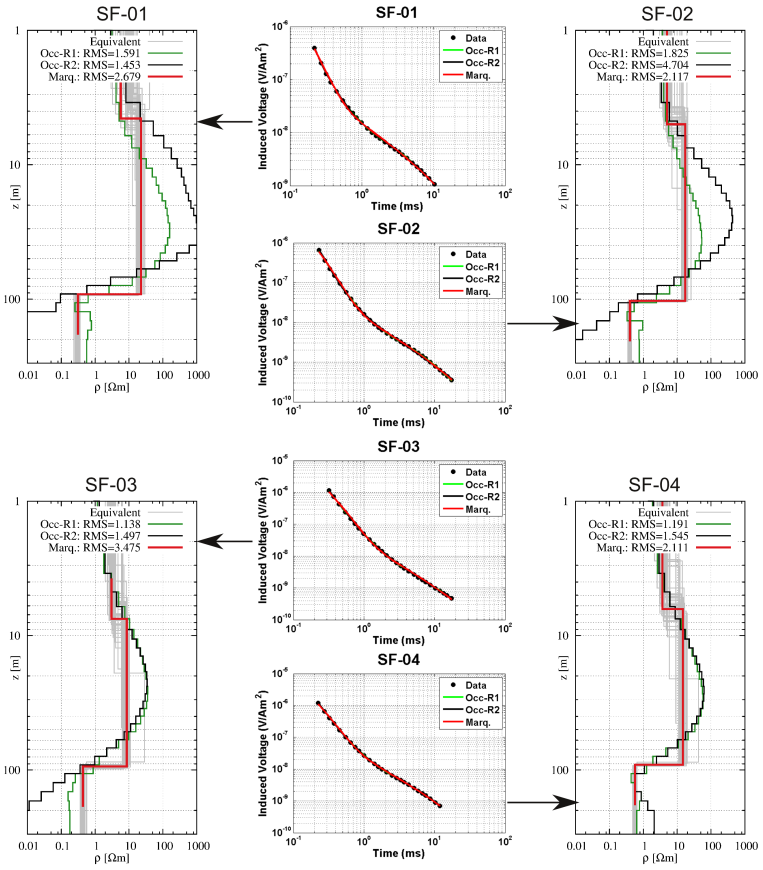

FIGURE C.1: *1D TEM Occam-R1/R2 (green and black), Marquardt (red) and Equivalent (gray) inversion models for stations SF-01 to SF-04.*

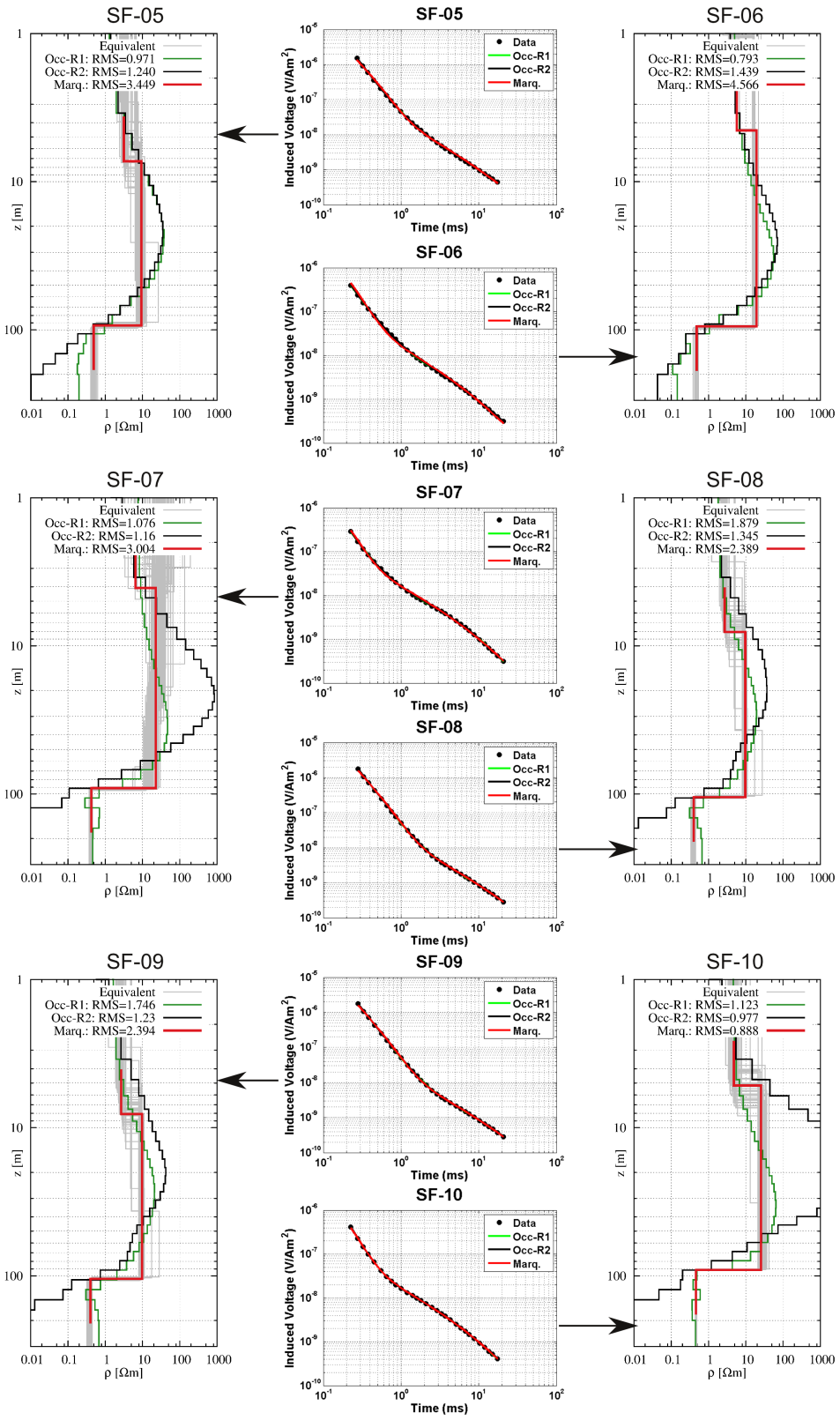

FIGURE C.2: *1D TEM Occam-R1/R2 (green and black), Marquardt (red) and Equivalent (gray) inversion models for stations SF-05 to SF-10.*

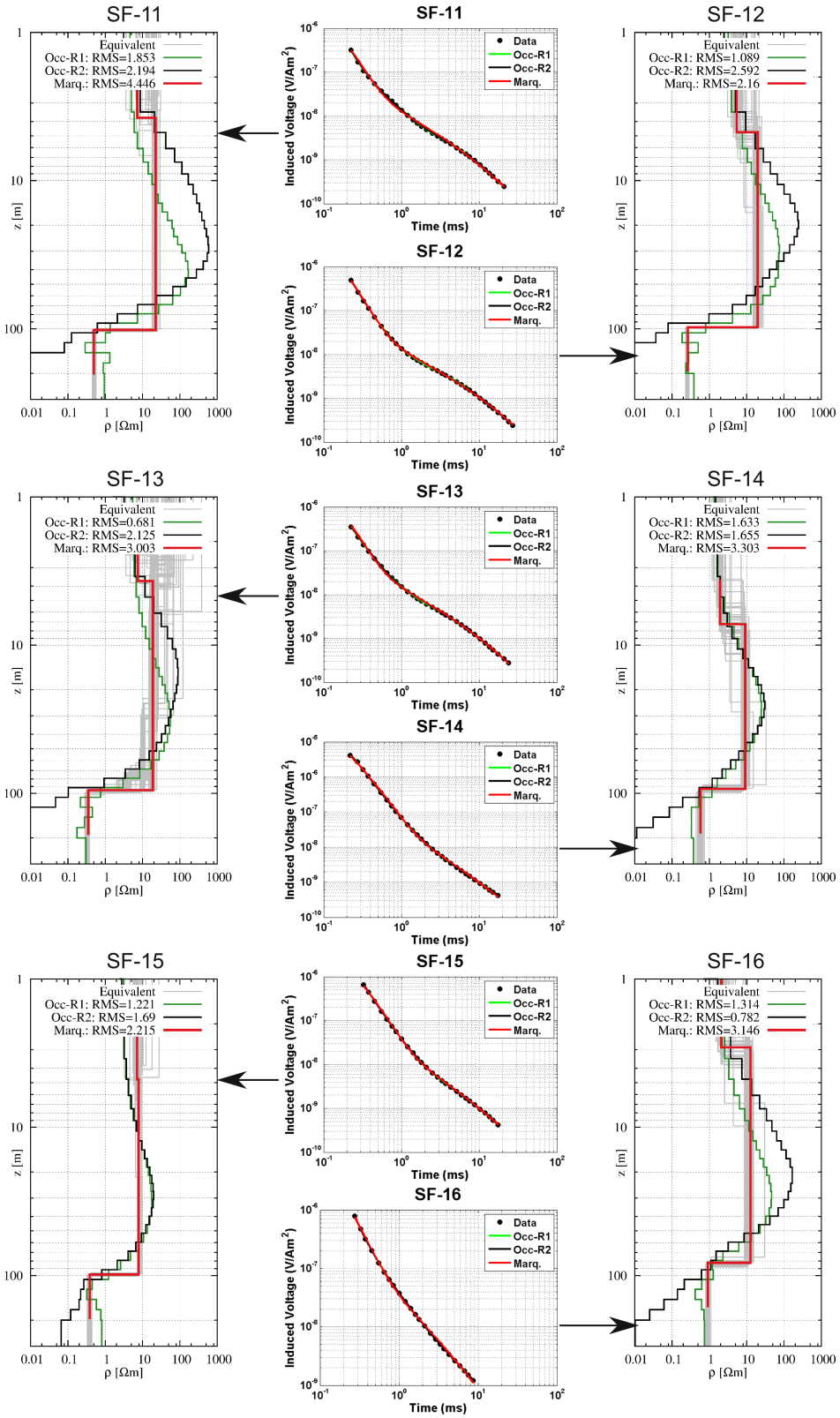

FIGURE C.3: *1D TEM Occam-R1/R2 (green and black), Marquardt (red) and Equivalent (gray) inversion models for stations SF-11 to SF-16.*

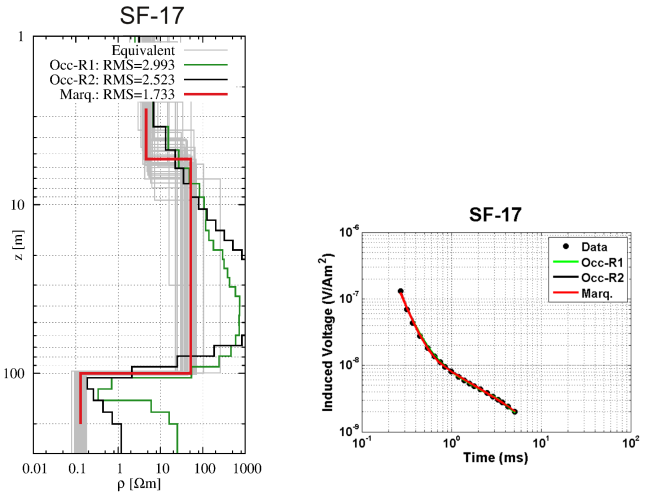

FIGURE C.4: *1D TEM Occam-R1/R2 (green and black), Marquardt (red) and Equivalent (gray) inversion models for station SF-17.*

Appendix D

MT Transfer functions

This Appendix shows the MT transfer functions obtained at each station.

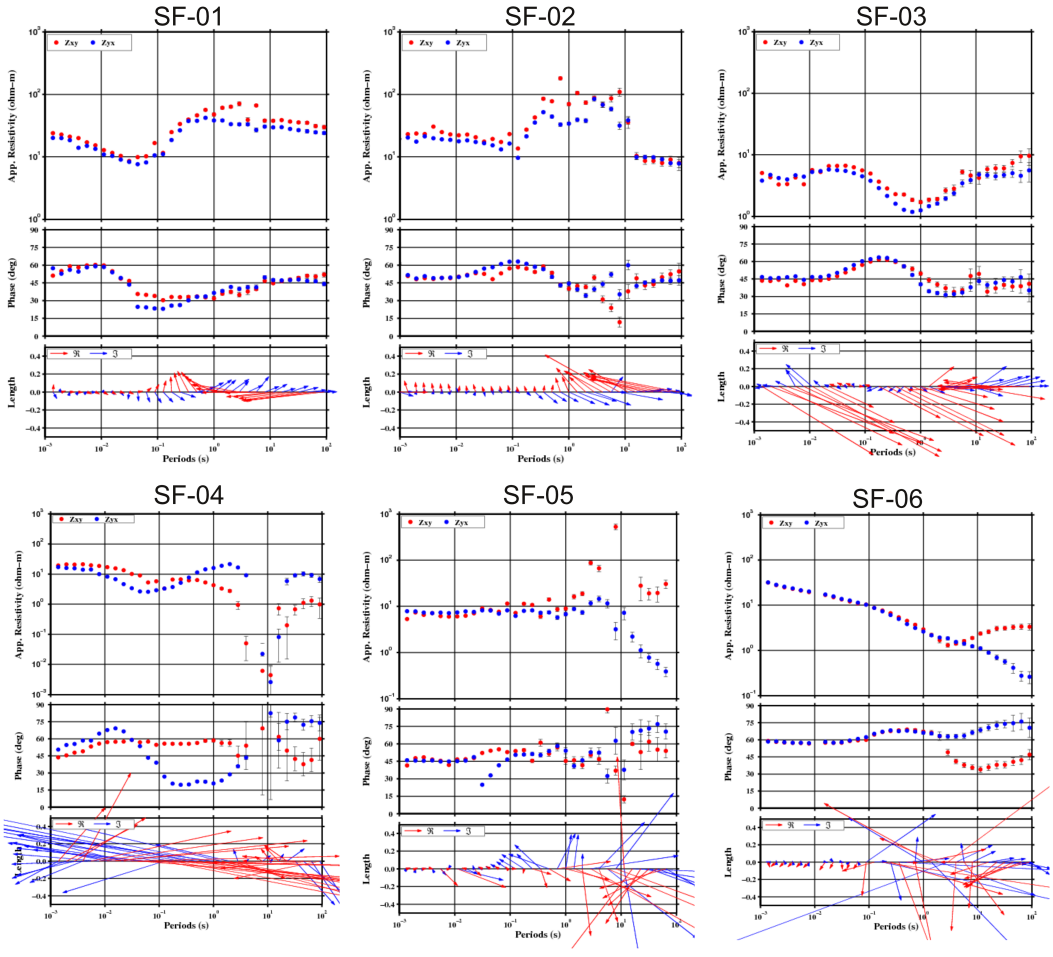

FIGURE D.1: *MT transfer functions obtained at stations SF-01 - SF-06.*

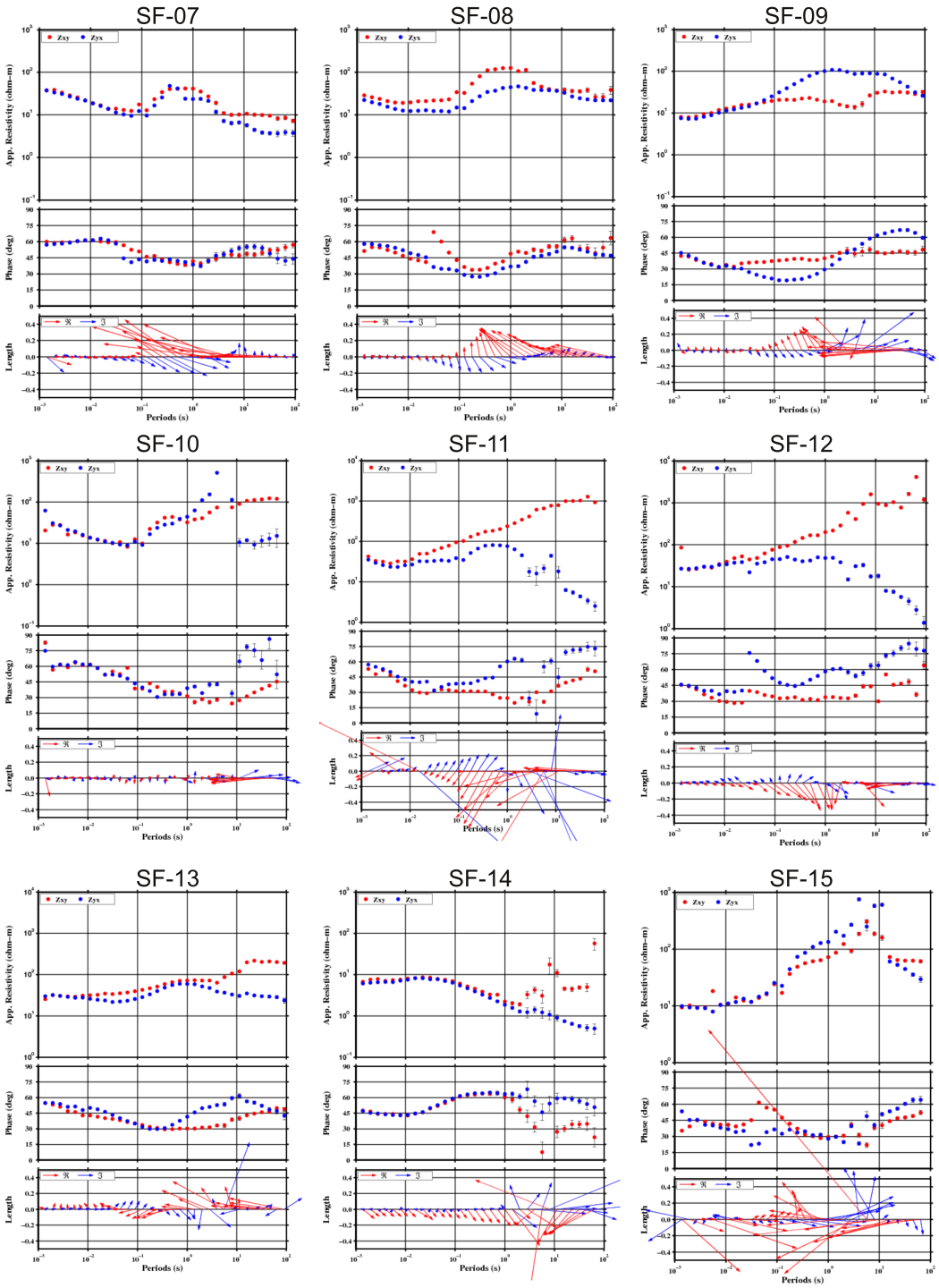

FIGURE D.2: *MT transfer functions obtained at stations SF-07 - SF-15.*

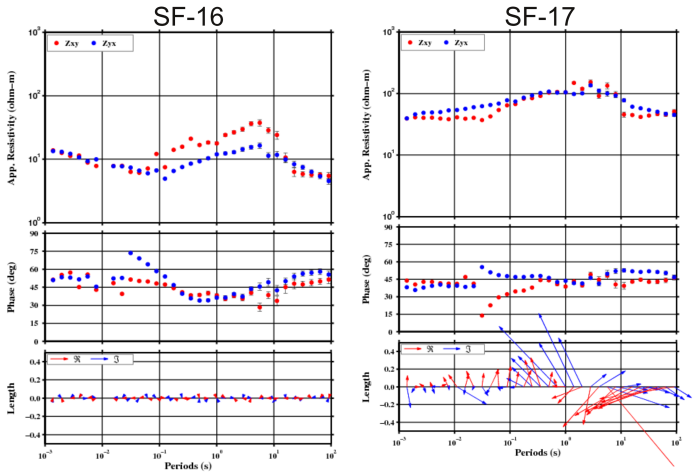

FIGURE D.3: *MT transfer functions obtained at stations SF-16 - SF-17.*

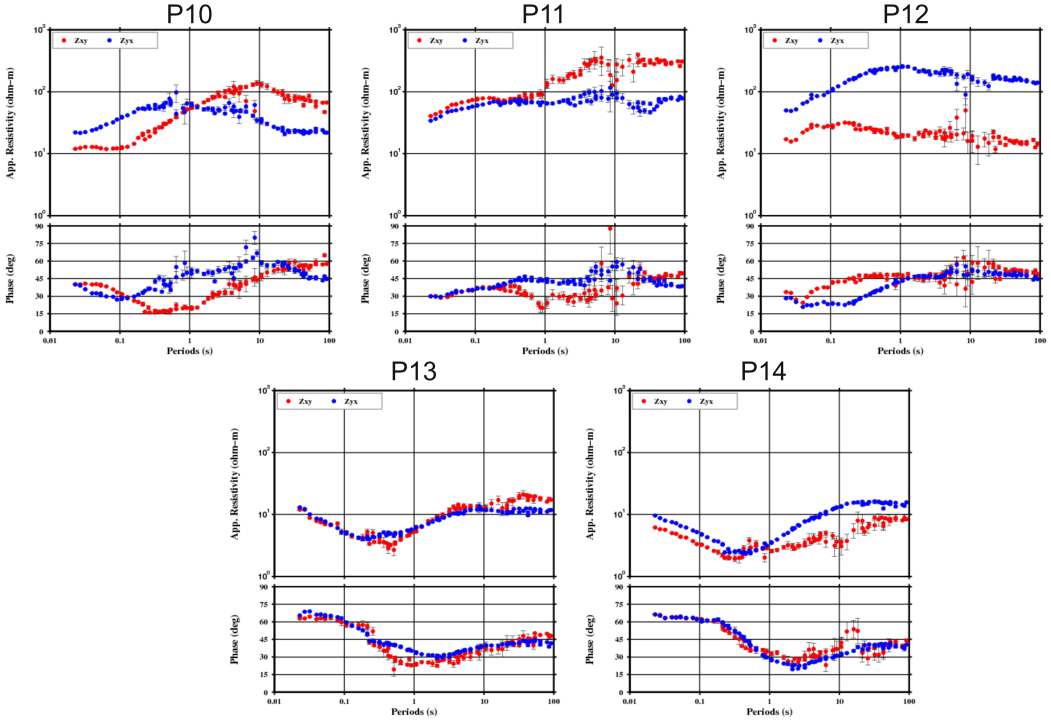

FIGURE D.4: *MT transfer functions obtained at stations P10 - P14. These soundings were used to generate a 2D inversion model by Pamplona-Pérez (2007) and they are only included in the 3D MT inversion scheme applied in this thesis.*

Appendix E

1D MT inversion models

This Appendix shows the 1D MT inversion models at all the stations.

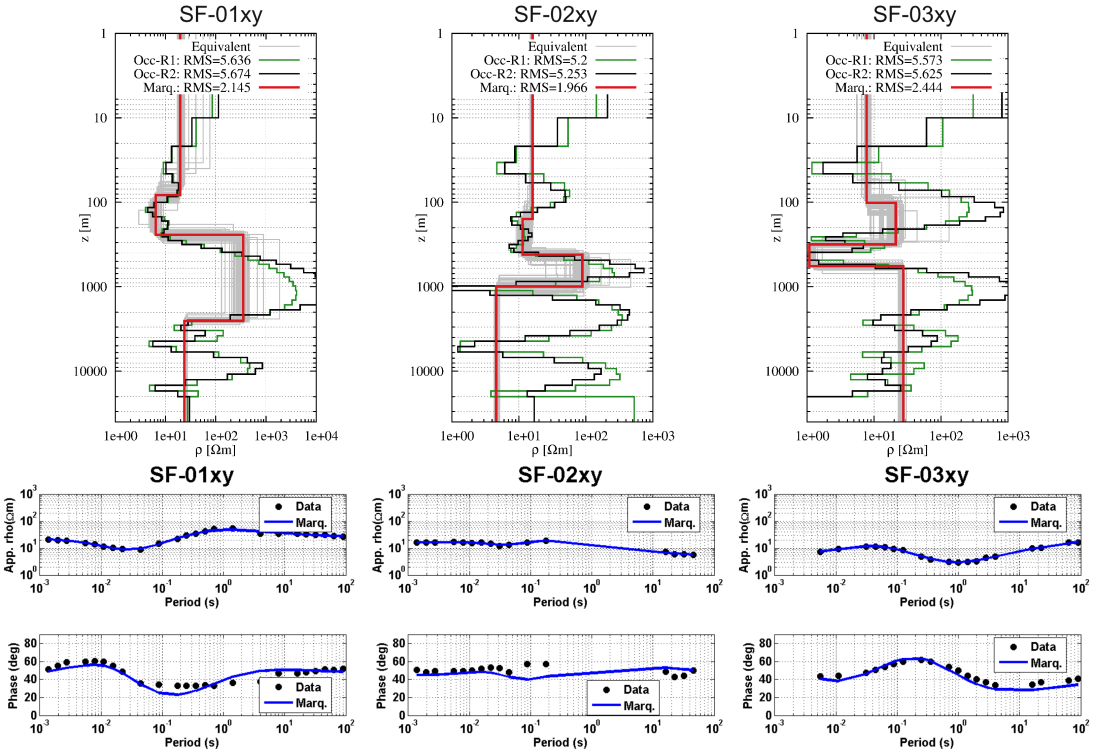

FIGURE E.1: *1D MT Occam-R1/R2 (green and black), Marquardt (red) and Equivalent (gray) inversion models for the XY component of stations SF-01 to SF-03.*

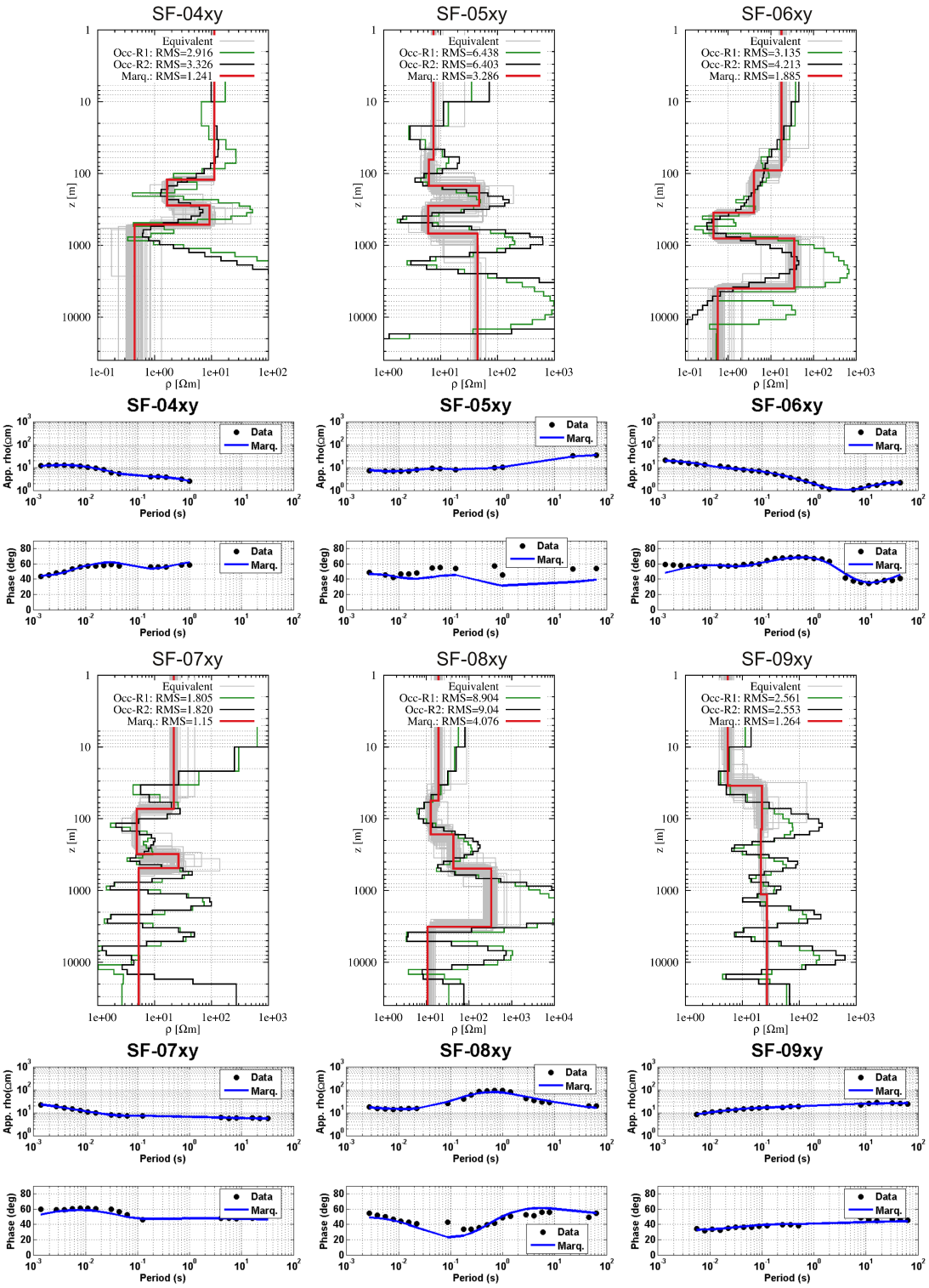

FIGURE E.2: *1D MT Occam-R1/R2 (green and black), Marquardt (red) and Equivalent (gray) inversion models for the XY component of stations SF-04 to SF-09.*

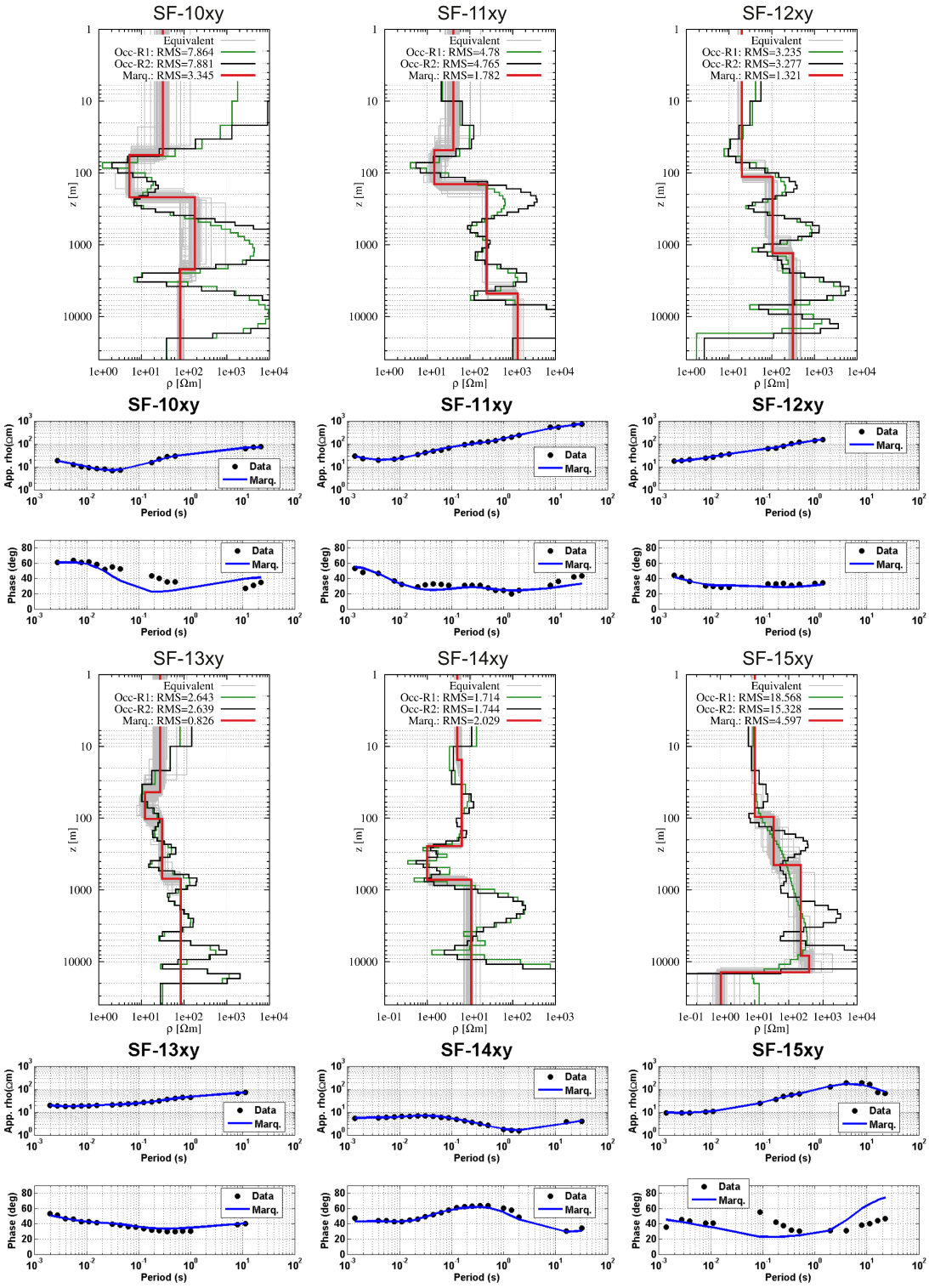

FIGURE E.3: *1D MT Occam-R1/R2 (green and black), Marquardt (red) and Equivalent (gray) inversion models for the XY component of stations SF-10 to SF-15.*

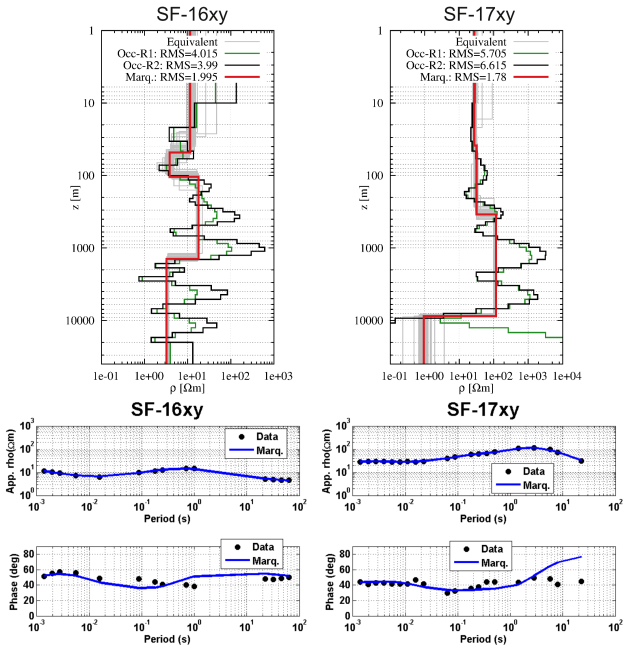

FIGURE E.4: *1D MT Occam-R1/R2 (green and black), Marquardt (red) and Equivalent (gray) inversion models for the XY component of stations SF-16 to SF-17.*

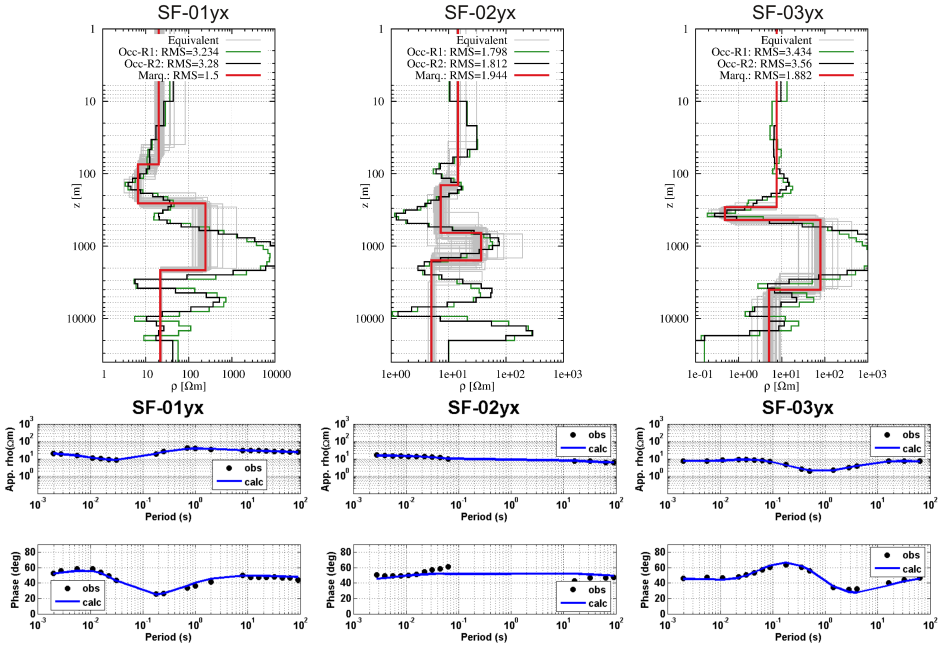

FIGURE E.5: *1D MT Occam-R1/R2 (green and black), Marquardt (red) and Equivalent (gray) inversion models for the YX component of stations SF-01 to SF-03.*

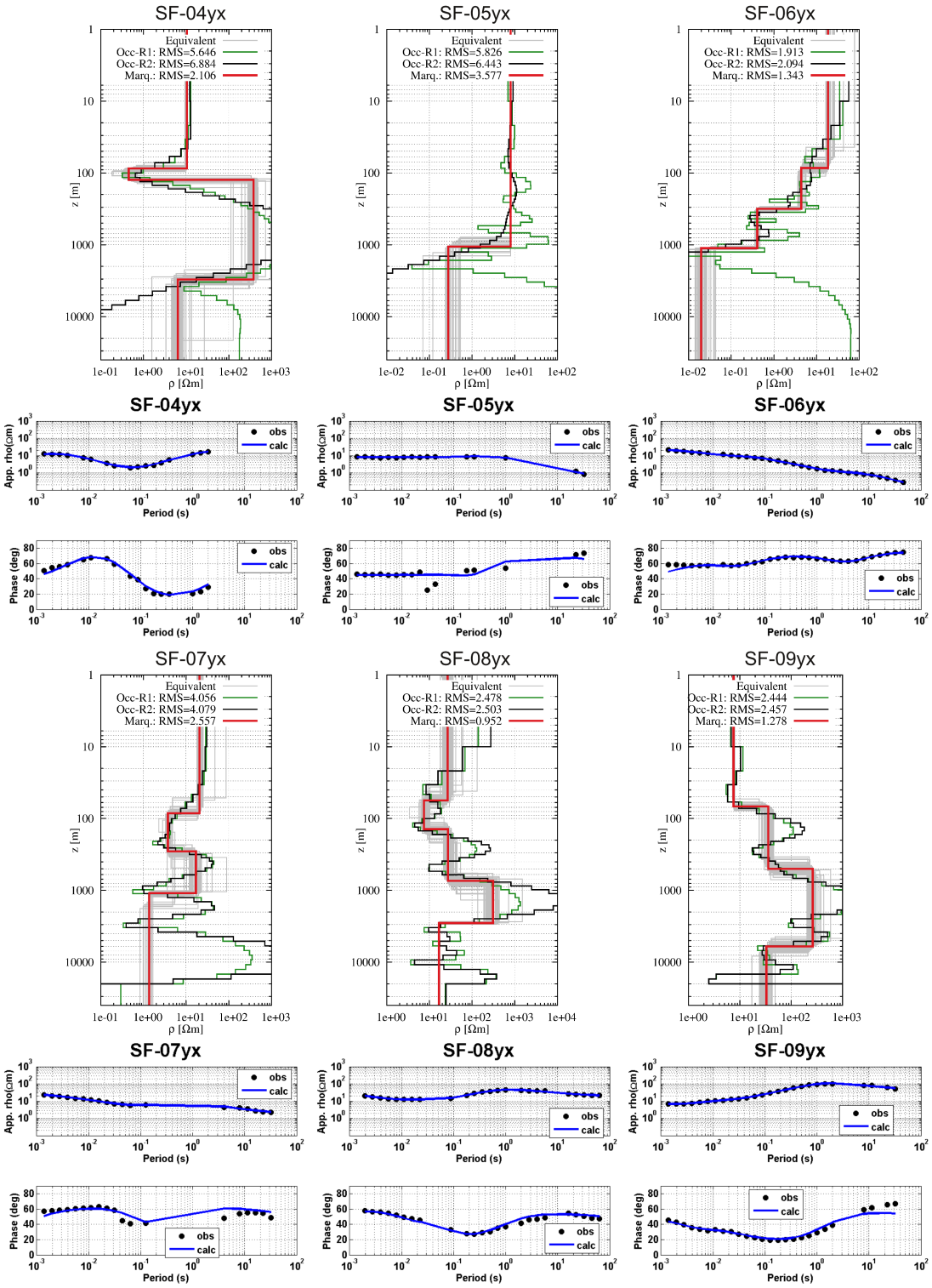

FIGURE E.6: *1D MT Occam-R1/R2 (green and black), Marquardt (red) and Equivalent (gray) inversion models for the YX component of stations SF-04 to SF-09.*

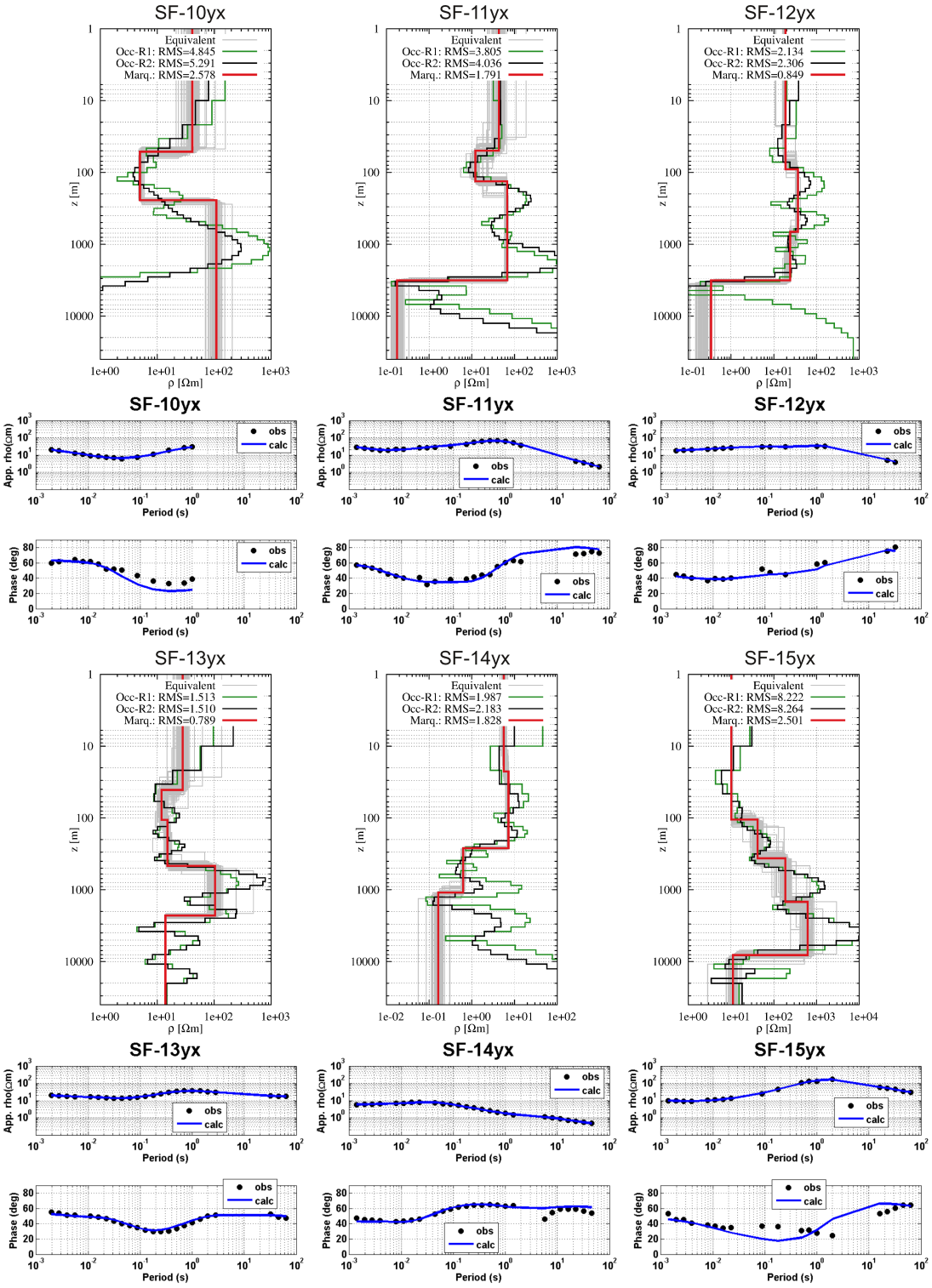

FIGURE E.7: *1D MT Occam-R1/R2 (green and black), Marquardt (red) and Equivalent (gray) inversion models for the YX component of stations SF-10 to SF-15.*

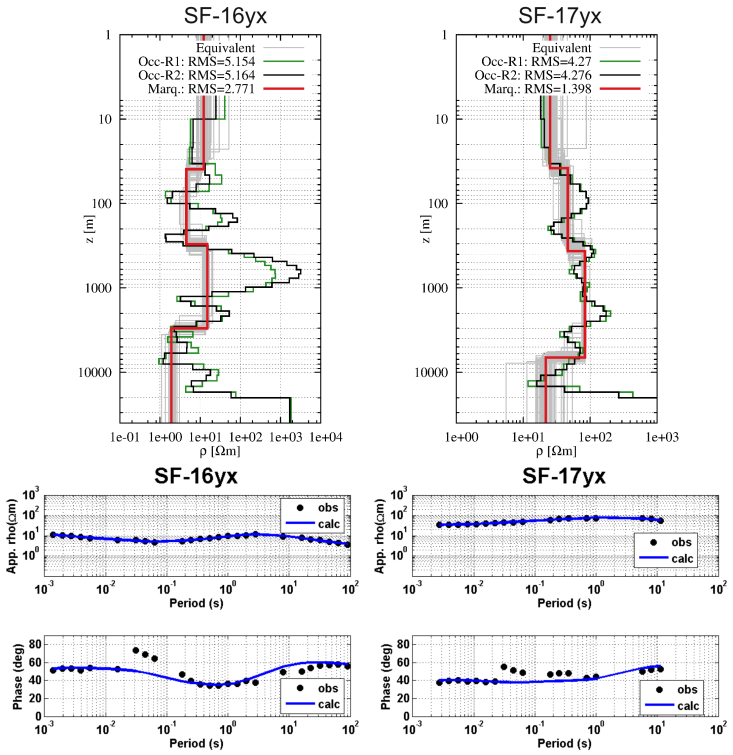

FIGURE E.8: *1D MT Occam-R1/R2 (green and black), Marquardt (red) and Equivalent (gray) inversion models for the YX component of stations SF-16 to SF-17.*

Appendix F

Additional information from the 2D MT inversion

This Appendix shows additional information in regards to the 2D inversion of magnetotelluric data. Figure F.1 displays the L-curves computed to find out a suitable regularization parameter for the 2D MT inversion of data from the four different profiles. It can be distinguished that at the inversion of data from the four different profiles a regularization parameter of 30 ensures that neither the model smoothness nor the data fit dominates in the penalty function.

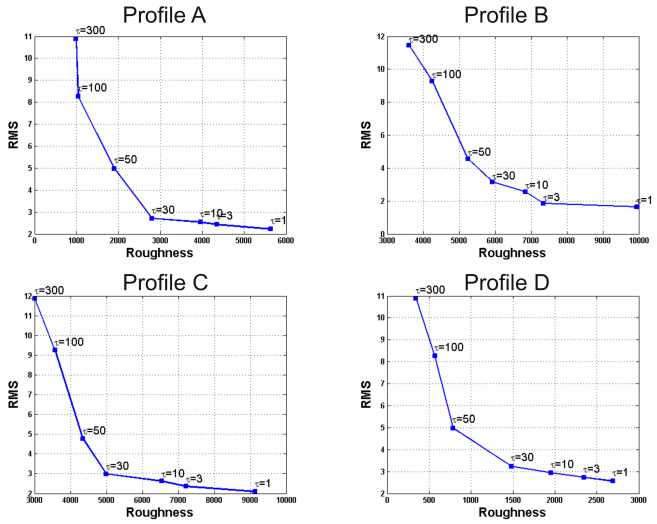

FIGURE F.1: *L-curves computed to select a suitable regularization parameter for the 2D inversion of data from the four different profiles.*

Figures F.2-F.5 show the fit between observed and calculated data from the 2D inversion.

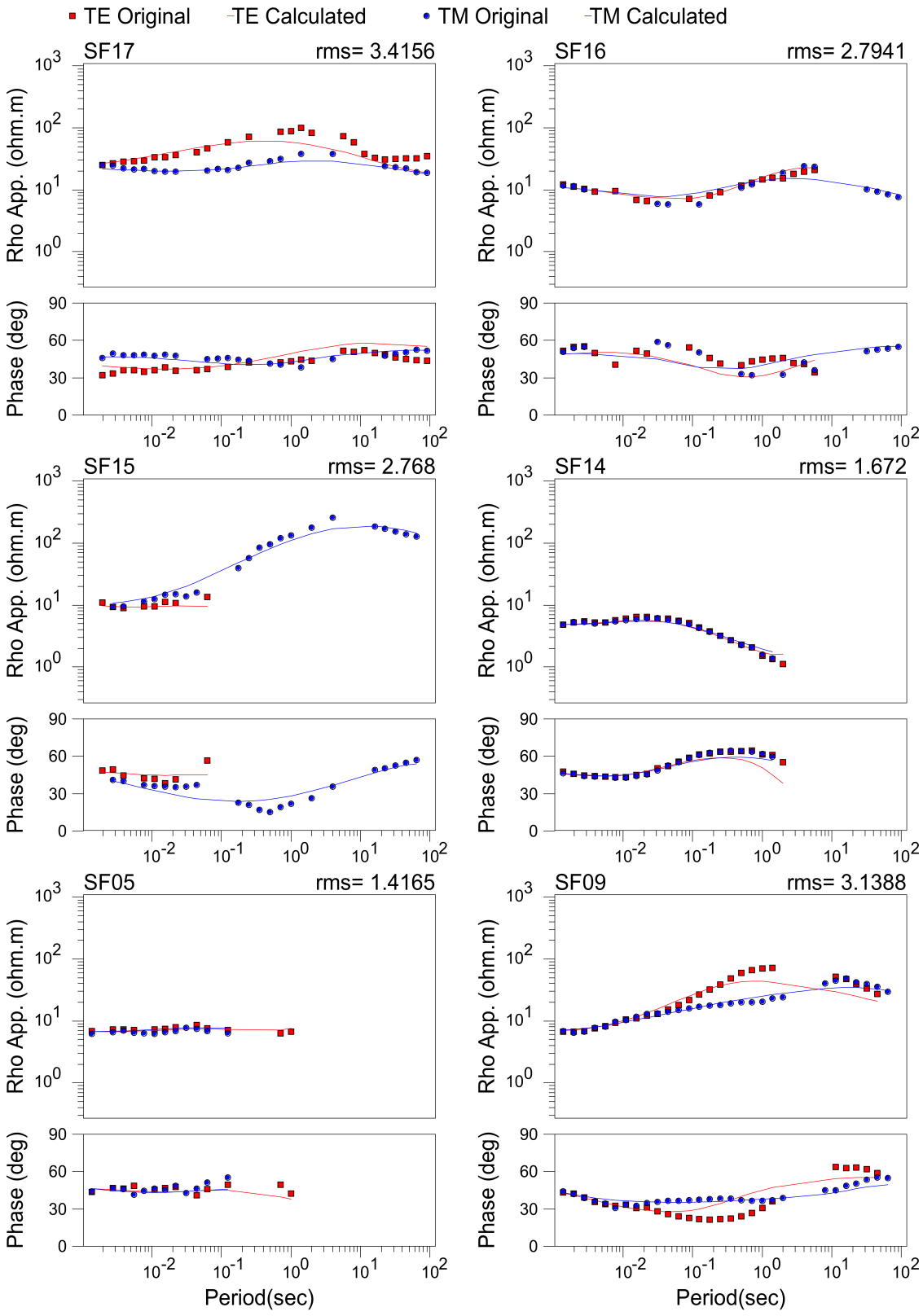

FIGURE F.2: *Fit between observed and calculated data from the 2D inversion for profile A.*

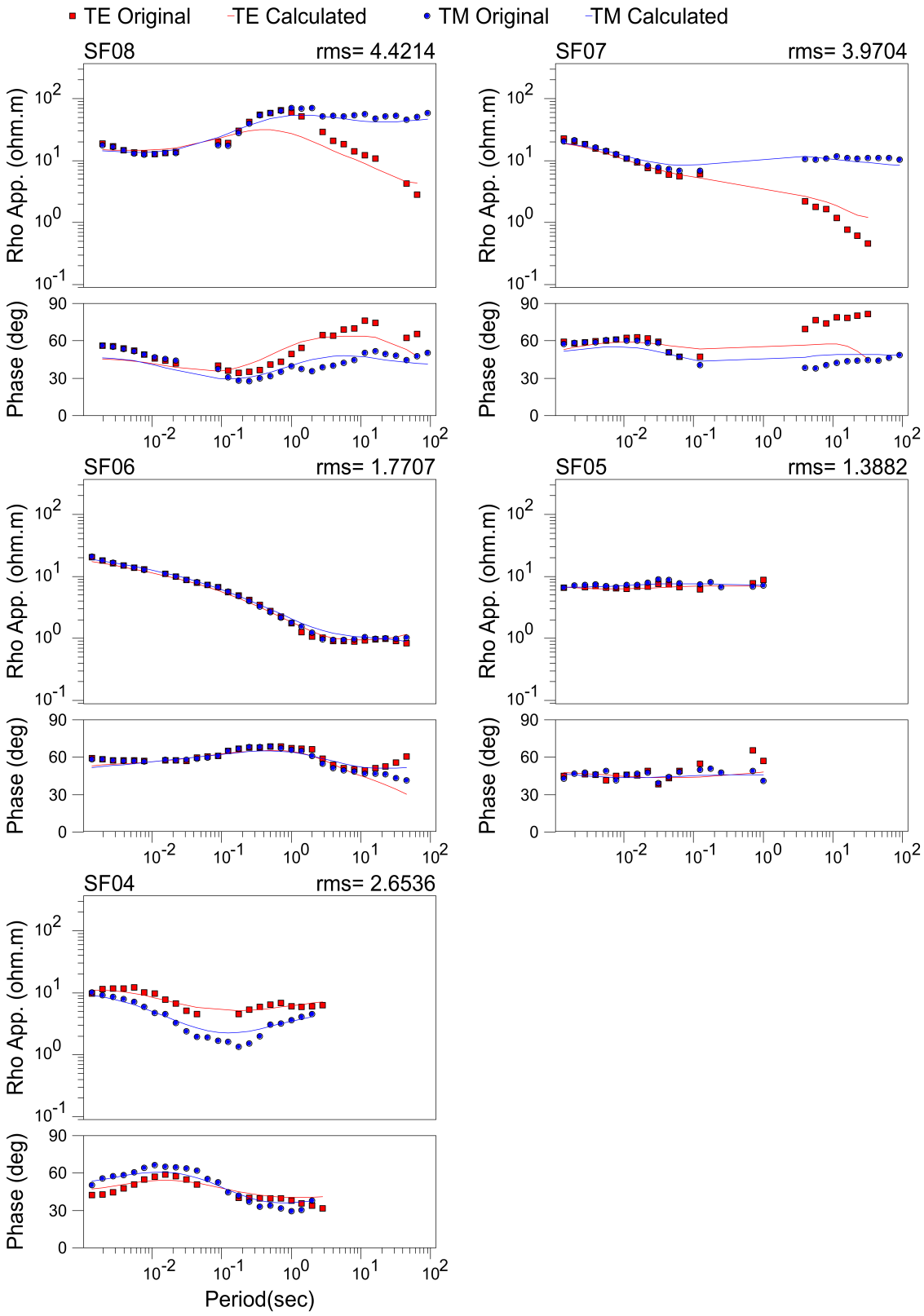

FIGURE F.3: *Fit between observed and calculated data from the 2D inversion for profile B.*

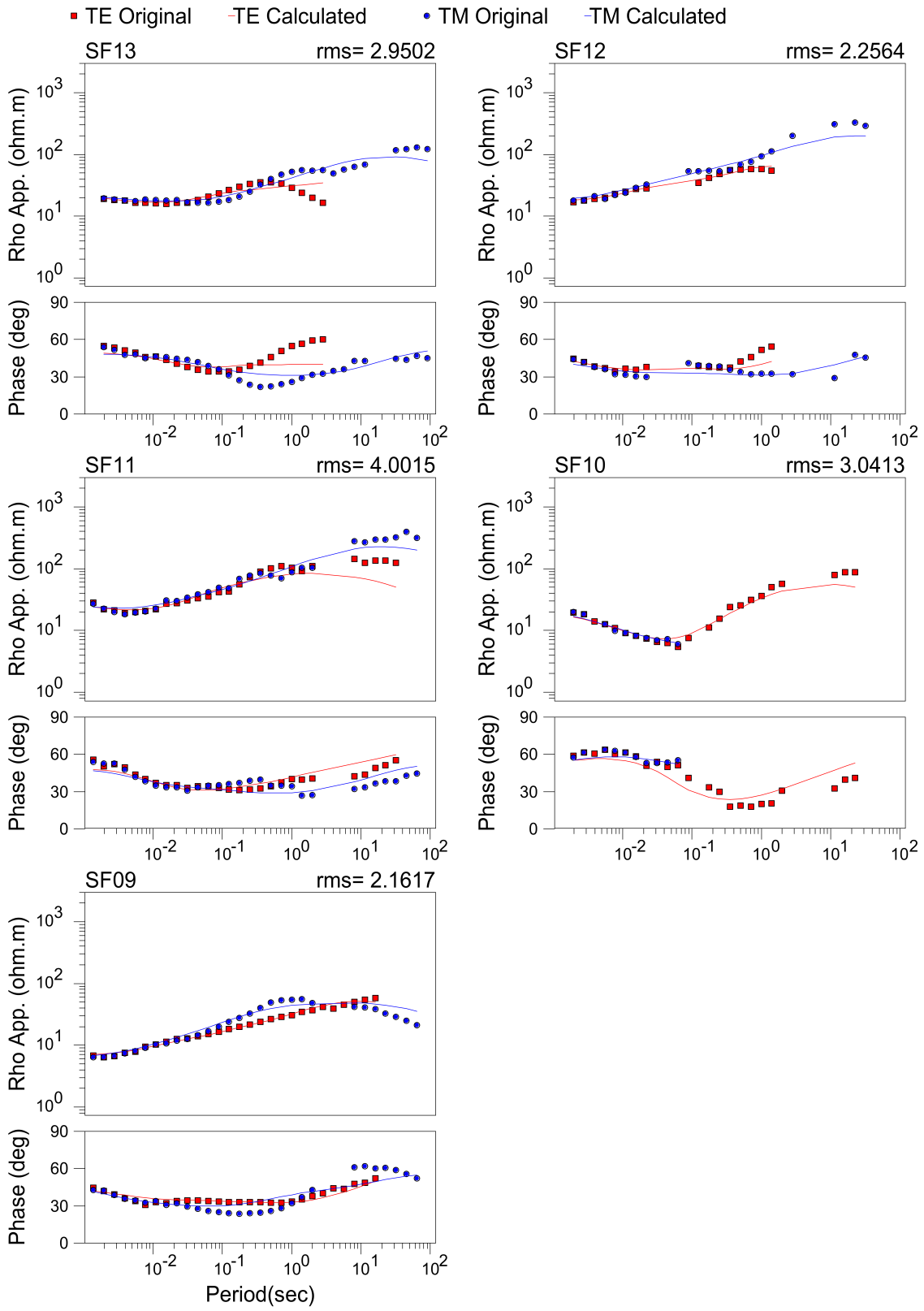

FIGURE F.4: *Fit between observed and calculated data from the 2D inversion for profile C.*

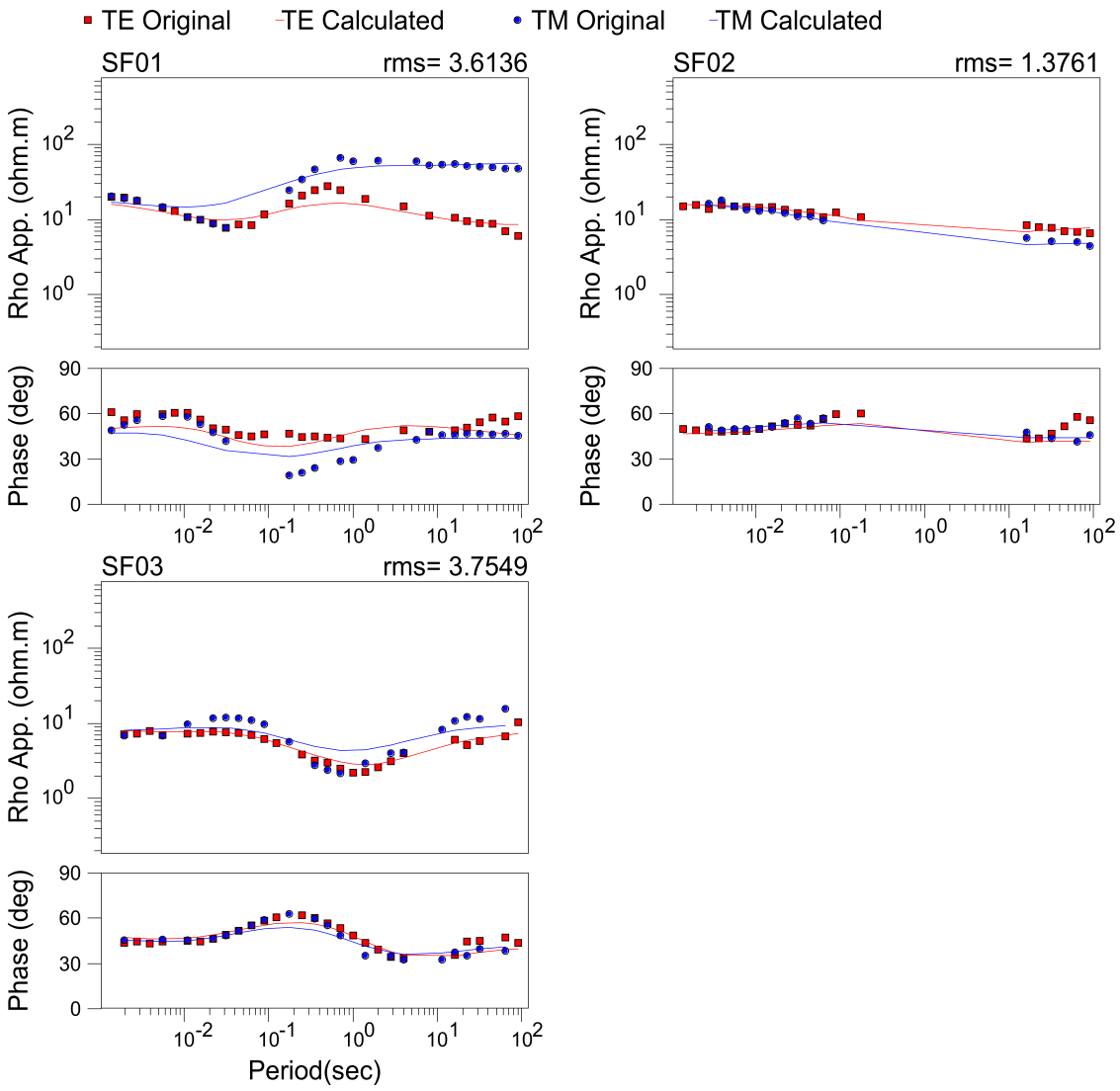

FIGURE F.5: *Fit between observed and calculated data from the 2D inversion for profile D.*

Appendix G

Additional 3D modeling studies

Two additional 3D modeling investigations are described in this Appendix. The first one is to analyze the detectability of a structure between two MT profiles and the second one shows how a structure is imaged with a single profile.

Structure between two profiles

The detectability of a buried structure located between two MT profiles is tested with the 3D inversion of synthetic data. In this sense, a 3D model was generated consisting of a 1 Ωm conductor embedded in a 100 Ωm host geology (upper image of Fig. G.1). Dimensions of the conductive body are of 2 x 16 x 1.328 km. Same conditions that in San Felipe's area were set, where the gulf of California and Pacific ocean are included. A total of 10 MT sites were deployed along the two profiles. Distances between stations are 4 km.

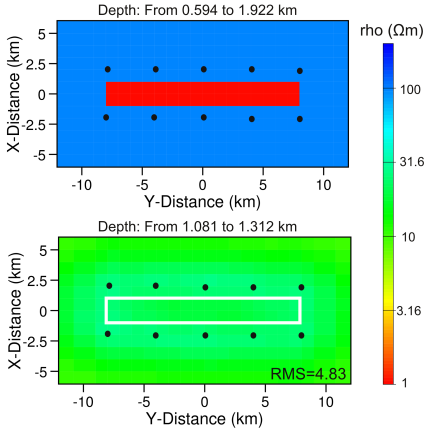

FIGURE G.1: *Upper image shows the conductor embedded in a 100 Ωm host geology. On the lower image the inversion result is displayed as a resistivity slice, the white lines represent the actual position of the conductor. The MT sites are marked with the black dots.*

Thus, a 3D forward modeling was applied. The full impedance tensor elements and VTF components were calculated for 21 frequencies in the range from 1000 Hz to 0.01 Hz. Subsequently, the calculated data were used as input to perform a 3D inversion. A 10 Ωm starting model was utilized (including the 0.3 Ωm of Pacific ocean and gulf of California). Data errors were set to 5% of $|Zxy * Zyx|^{1/2}$ for the impedance tensor elements and a constant value of 0.05 for the VTF. The lower image of Fig. G.1 displays the inversion result as a resistivity slice at depths of ∼1.2 km. As it was expected, the inversion was unsuccessful to retrieve the conductor because none of the MT sites is located above it. Only its footprint can be slightly noticed in the inverse model. It is therefore demonstrated that structures derived with 3D MT inversion are reliable only if they are located under the data coverage. Hence, the structures obtained from the 3D inversion of the acquired MT data in San Felipe are interpreted if they are under the soundings, otherwise they are considered as inversion artifacts.

Structure under a single profile

At this investigation, the resolution obtained with a 3D inversion of a single MT profile data is analyzed. Siripunvaraporn et al. (2005) extensively studied the 3D inversion output of a MT profile data, hence it is only tested the case of a conductor under the MT profile with the same conditions of the field survey in San Felipe. In this sense, a 3D model with a conductive block embedded in a 100 Ωm host geology was created (upper image of Fig. G.2). The conductor has dimensions of 11 x 10 x 1.328 km. Five MT sites were deployed along the profile. Distances between the sites are of 4 km, as the mean spacing of the MT soundings acquired in San Felipe.

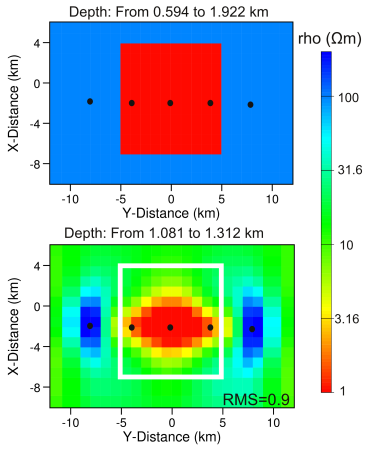

FIGURE G.2: *On the upper image, the conductive block embedded in a 100 Ωm host geology is shown. The lower image displays the inversion result as a resistivity slice where the white lines represent the actual position of the conductor. The MT sites are marked with the black dots.*

A forward modeling was applied to the above mentioned model. The full imped-

ance tensor and VTF elements were calculated for 21 frequencies in the range from 1000 Hz to 0.01 Hz. The synthetic data were used as input for the 3D inversion. Data errors were set to 5% of $|Zxy * Zyx|^{1/2}$ for the impedance tensor elements and a constant value of 0.05 for the VTF. A resistivity slice obtained from the inversion model is displayed on the lower image of Fig. G.2. The real position of the conductor is indicated with the white lines. It can be clearly distinguished that the corners of the conductive block are not recovered due to the absence of MT sites at those areas. With the given settings, the inversion could derive the resistivities of the conductor up to $\sim$3 km further from the center of the profile in the N-S direction. It is evident that additional profiles are required to constrain the full 3-D conductive block, however, it is demonstrated that a single profile can image nearby off-profile structure on similar conditions that San Felipe survey area.

Appendix H

3D inversion data fit

This Appendix shows the fit between calculated and observed data from the preferred 3D MT inversion model.

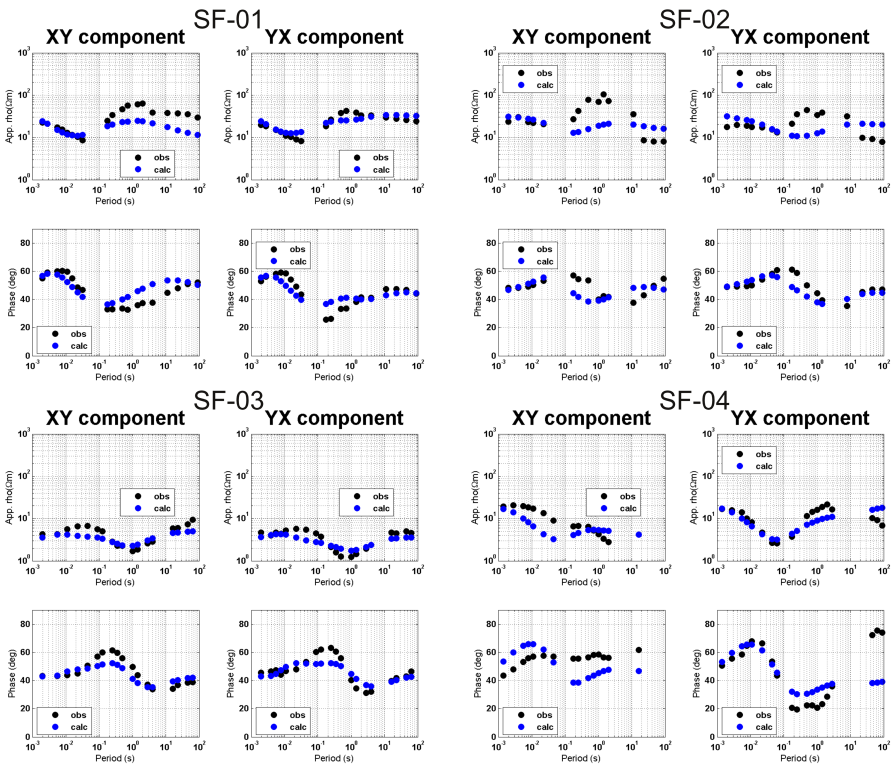

FIGURE H.1: *Fit between calculated and observed data from the preferred 3D inversion model at stations SF-01 - SF-04, for XY and YX components.*

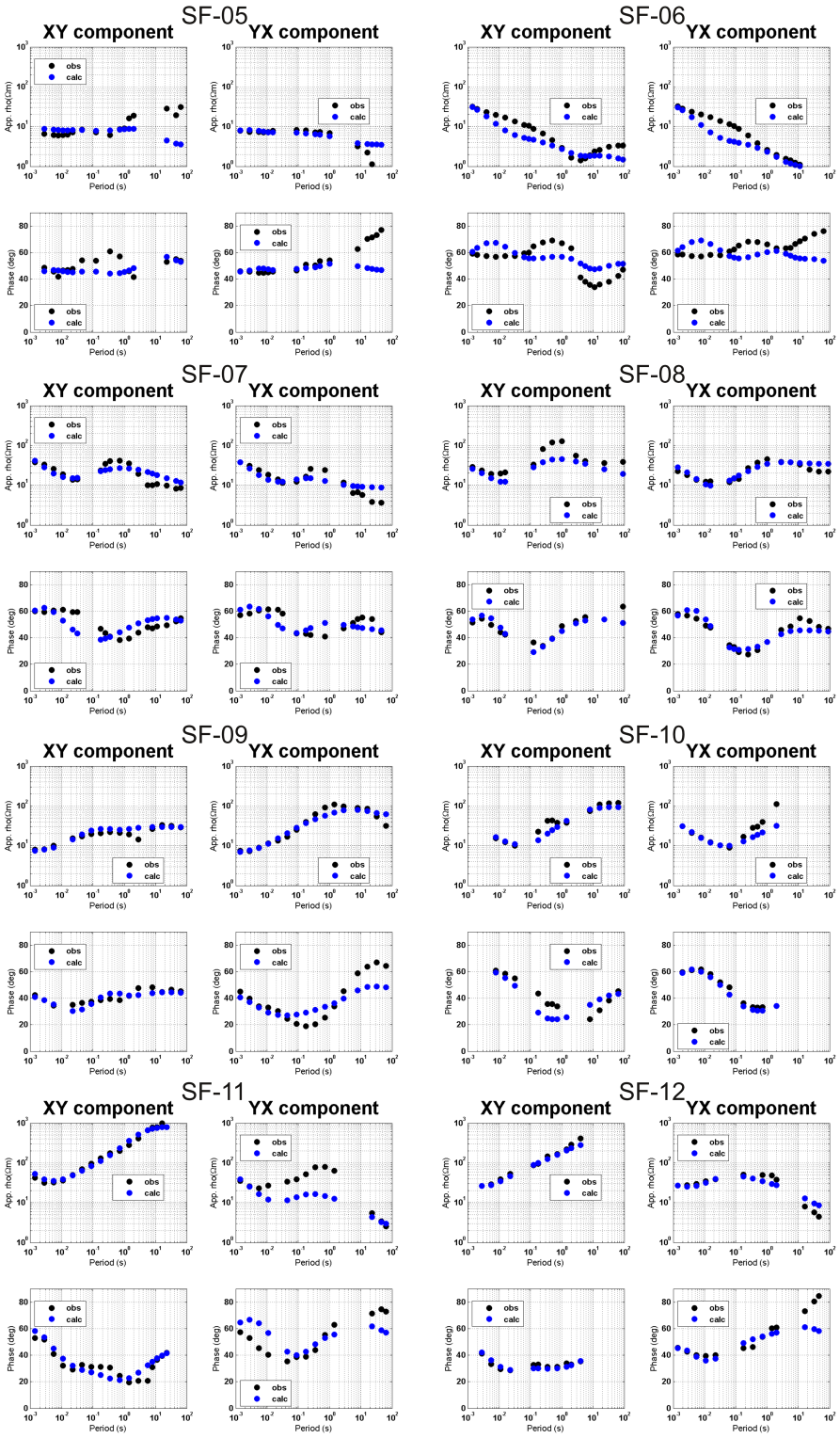

FIGURE H.2: *Fit between calculated and observed data from the preferred 3D inversion model at stations SF-05 - SF-12, for XY and YX components.*

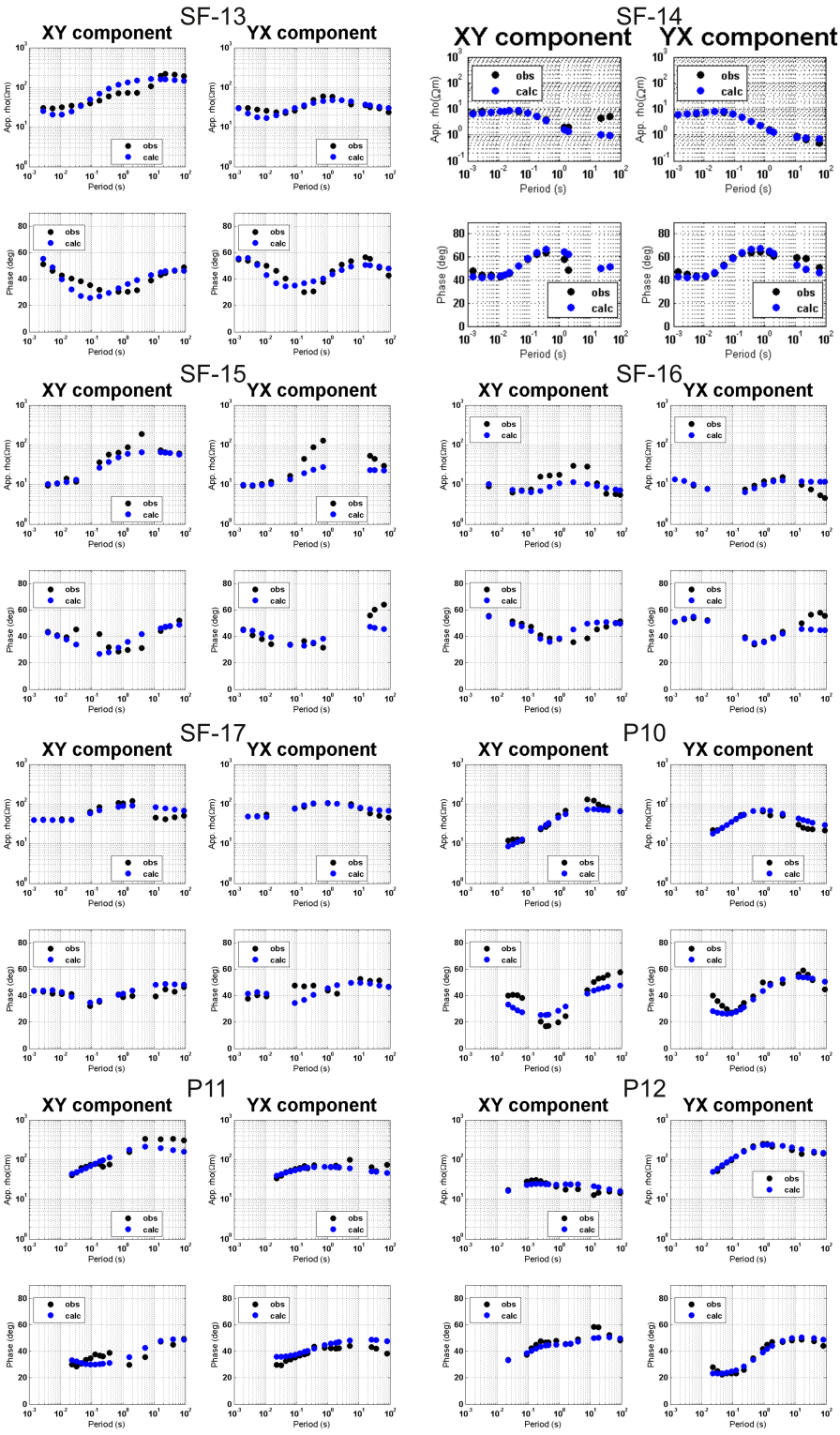

FIGURE H.3: *Fit between calculated and observed data from the preferred 3D inversion model at stations SF-13 - P12, for XY and YX components.*

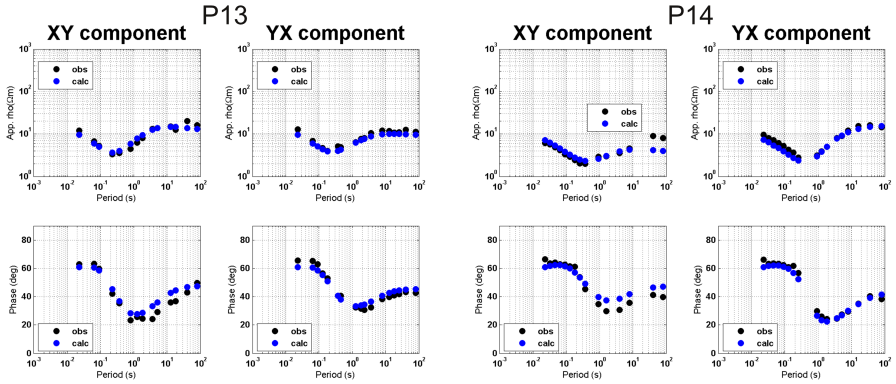

FIGURE H.4: *Fit between calculated and observed data from the preferred 3D inversion model at stations P13 - P14, for XY and YX components.*

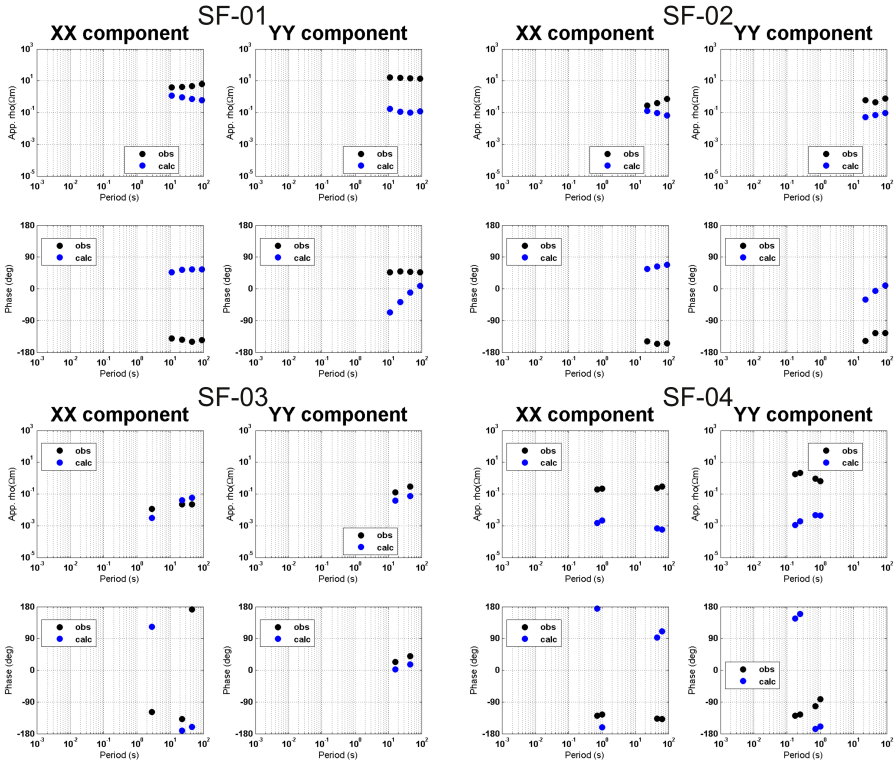

FIGURE H.5: *Fit between calculated and observed data from the preferred 3D inversion model at stations SF-01 - SF-04, for XX and YY components.*

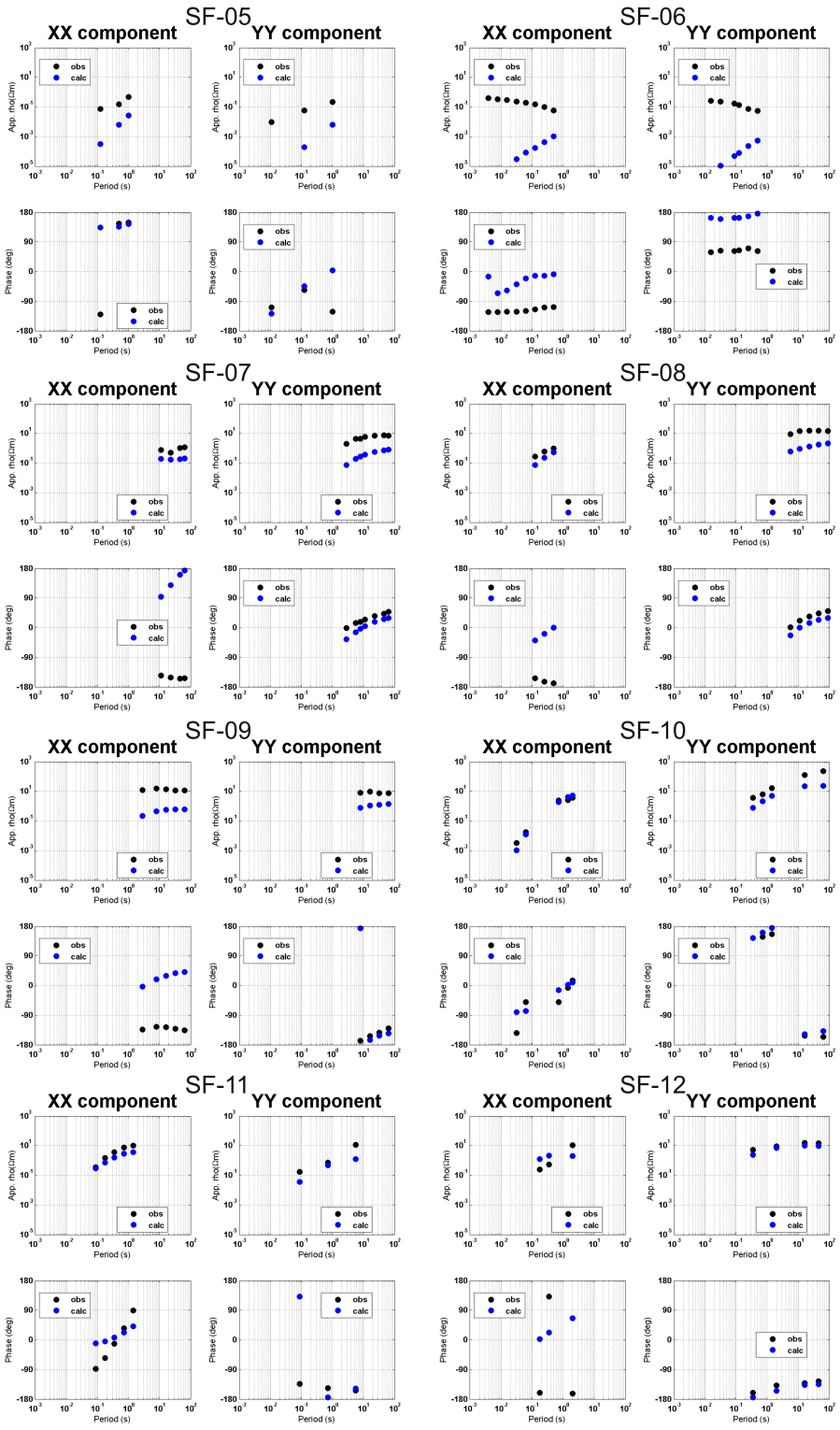

FIGURE H.6: *Fit between calculated and observed data from the preferred 3D inversion model at stations SF-05 - SF-12, for XX and YY components.*

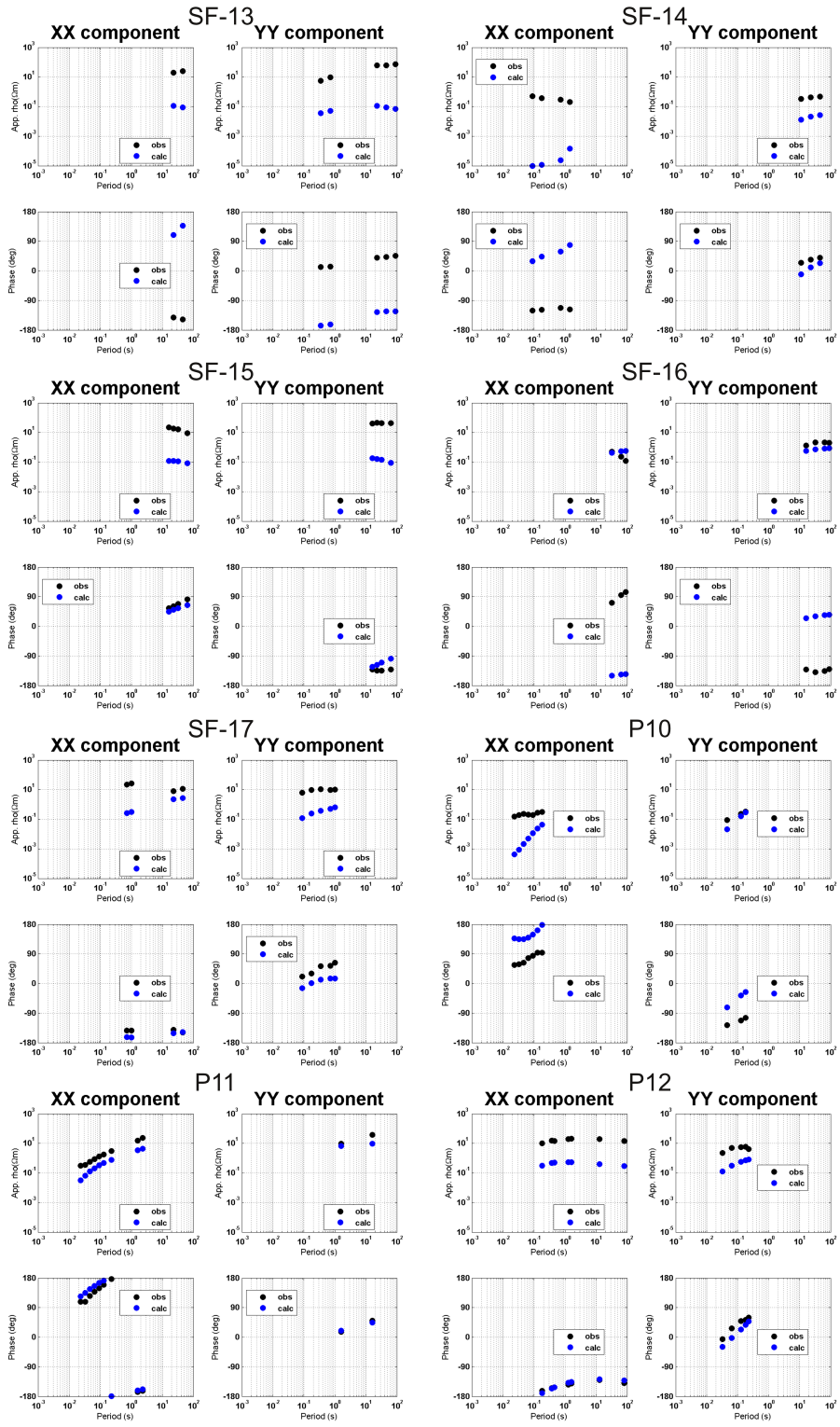

FIGURE H.7: *Fit between calculated and observed data from the preferred 3D inversion model at stations SF-13 - P12, for XX and YY components.*

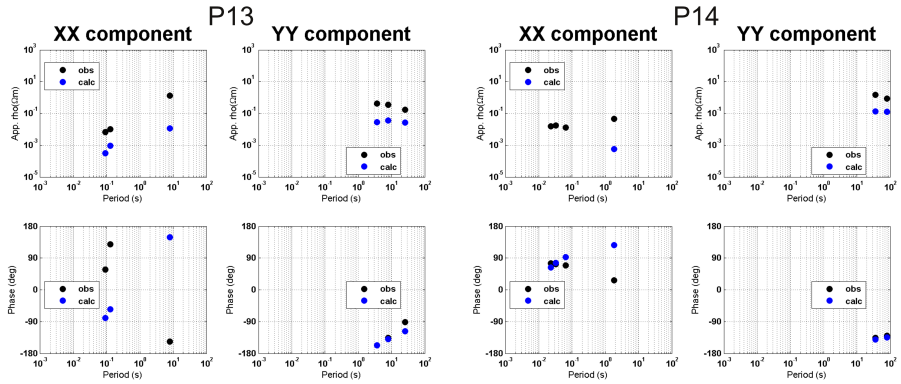

FIGURE H.8: *Fit between calculated and observed data from the preferred 3D inversion model at stations P13 - P14, for XX and YY components.*

Acknowledgments

I am deeply thankful to my PhD supervisor Prof. Dr. Bülent Tezkan who supported me during all the doctoral project and made this work possible. He kindly accepted to supervise my project and was always available for helping me whenever I needed.

I would like to thank Prof. Dr. Andreas Junge for appraising this thesis.

I acknowledge DAAD (Deutscher Akademischer Austauschdienst) for funding my doctoral project.

I am grateful to Dr. Rosa María Prol-Ledesma and Dr. Claudia Arango-Galván for allowing me to use the data from San Felipe in my doctoral project. In addition, I would like to acknowledge Dr. José Manuel Romo Jones for letting me use additional MT soundings collected near to San Felipe some years ago.

I would like to thank all my colleagues who helped to collect the field data in San Felipe: Gaby, Olaf, Miguel, Jaime, Jesús, Martin and Daniel. I am thankful to Óscar Castro and Zack Spica for also helping on the field survey and assisting me to drive during the long and nice road trip from Mexico city to San Felipe.

I acknowledge Dr. Naser Meqbel for providing me his 3D GridTools software. All the 3D forward and inversion modeling routines applied in this thesis were done with CHEOPS computing cluster which is provided by the Regional Computing Center (RRZK) of the University of Cologne. Therefore, I would like to thank them for the possibility to use CHEOPS and their assistance when it was needed.

I am thankful to Amir Haroon, Klaus Lippert, Wiebke Mörbe and Marc Seidel for proof-reading this thesis. I also thank Marc for correcting the German version of the Abstract.

I would like to thank all my colleagues of the Applied Geophysics working group from the IGM-University of Cologne for creating a

friendly working atmosphere.

I am greatly thankful to my parents Sofia and Rodolfo for always supporting me.

I am tremendously grateful to my wife Katya for her support in all the stages of my doctoral project. Without her help, the final phase of this work would have been more difficult.

Erklärung zur Dissertation

Ich versichere, dass ich die von mir vorgelegte Dissertation selbstständig angefertigt, die benutzten Quellen und Hilfsmittel vollständig angegeben und die Stellen der Arbeit - einschließlich Tabellen, Karten und Abbildungen -, die anderen Werken im Wortlaut oder dem Sinn nach entnommen sind, in jedem Einzelfall als Entlehnung kenntlich gemacht habe; dass diese Dissertation noch keiner anderen Fakultät oder Universität zur Prüfung vorgelegen hat; dass sie - abgesehen von unten angegebenen Teilpublikationen - noch nicht veröffentlicht worden ist sowie, dass ich eine solche Veröffentlichung vor Abschluss des Promotionsverfahrens nicht vornehmen werde.

Die Bestimmungen dieser Promotionsordnung sind mir bekannt. Die von mir vorgelegte Dissertation ist von Prof. Dr. Bülent Tezkan betreut worden.

Köln, Februar 2018.

Teilpublikationen:

Ruiz-Aguilar, D., Tezkan, B. and Arango-Galván, C. Exploration of the aquifer of San Felipe's geothermal area (Mexico) by Spatially Constrained Inversion of Transient Electromagnetic data. *Journal of Environmental and Engineering Geophysics*. In press 2018.